Terahertz Inspection Through FMCW Radar Developments and Advanced Imaging Approaches

Adrien Chopard

université de BORDEAUX

université de BORDEAUX

THÈSE PRÉSENTÉE

POUR OBTENIR LE GRADE DE

DOCTEUR
DE L'UNIVERSITÉ DE BORDEAUX

ECOLE DOCTORALE DES SCIENCES PHYSIQUES ET DE L'INGÉNIEUR

SPÉCIALITÉ LASER MATIÈRE NANOSCIENCES

Par **Adrien CHOPARD**

Terahertz Inspection Through FMCW Radar Developments and Advanced Imaging Approaches

Sous la direction de : **Patrick MOUNAIX**
Co-encadrant : **Jean-Paul GUILLET**

Soutenue le 07 Décembre 2021

Membres du jury :

M. **LAMPIN** Jean-François,	Directeur de recherche, IEMN, Lille	Rapporteur
M. **GARET** Frédéric,	Professeur, IMEP-LAHC, Chambéry	Rapporteur
Mme. **COQUILLAT** Dominique ,	Directrice de recherche, L2C, Montpellier	Examinatrice
Mme. **MANEUX** Cristell,	Professeure, IMS, Bordeaux	Présidente du jury
M. **STOLIDI** Adrien,	Docteur, CEA, List, Saclay	Invité
M. **GELLIE** Pierre,	Président, Lytid, Paris	Invité, Encadrant Industriel
M. **GUILLET** Jean-Paul,	Maître de conférences, IMS, Bordeaux	Co-Encadrant
M. **MOUNAIX** Patrick,	Directeur de Recherche, IMS, Bordeaux	Directeur de thèse

Abstract (EN)-

Following the recent evolutions of systems performances in the terahertz spectral range, this work reports on several instrumentation advances, intended as complementary tools for contactless Non-Destructive Testing. On the field of continuous wave sensing, even though optimal for the recovery of terahertz representations, standard single point focused imaging features an intrinsic recording time limitation. As an alternative, a transposition toward real-time imaging was undertaken. The development of a versatile galvanometric illumination process ensured the mitigation of intrinsic restraining factors in such a geometry. It ultimately led to reliable full-field imaging, up to the demonstration of enhanced real-time 3D tomographic inspection capabilities. Subsequently, the use of coherent sensing, through the detailed development of a FMCW (Frequency Modulated Continuous Wave) radar transceiver, operating in the 150 GHz frequency range, demonstrated nominal longitudinal sensing performances, based on a homodyne harmonic mixing scheme. Namely, the application of a normalization deconvolution procedure, along with a Phase Locked Loop stabilized architecture, ensure its reliable and consistent operation with high dynamic range measurement capabilities up to 100 dB and raw measurement rates up to 7.62 kHz. Those developments naturally led to applicative considerations with targeted Non-Destructive Testing oriented problematics. Namely, in parallel of volumetric inspection and specific instrumentation advances, the sensing capabilities for constactless thickness extraction on millimetric stratified sample geometries was obtained. Ultimately, with similar thickness and topological inspection aspirations, coherent wavefront sensing, through lensless focused imaging, was explored. It called on multi-plane phase retrieval and off-axis holography approaches, through single point sensing in the sub-terahertz range, and further transposed at 2.5 THz, with real-time recording.

Keywords: Terahertz; Millimeter-waves; Imaging; FMCW Radar; Non-Destructive Testing; Inspection; Sensing; Coherent Imaging.

Résumé (FR)-

Résultant des récents développements observables sur les performances de systèmes térahertz, ce manuscrit fait part d'avancées instrumentales, axées vers le domaine applicatif du contrôle non-destructif. Plus spécifiquement, pour les méthodes d'inspection par émission continue, les moyens standards d'imagerie point par point induisent de fortes contraintes temporelles de mesure. Dans le but d'y faire face, une transposition vers l'imagerie en temps réel a été entreprise. Le développement d'un procédé versatile d'éclairage galvanométrique permet de remédier aux principaux facteurs limitants intrinsèques d'une telle géométrie, pour arriver à des capacités d'imagerie plein champs optimisées ; allant jusqu'à la démonstration de reconstruction tomographiques 3D. Consécutivement, l'usage de méthodes de détection cohérente, au travers du développement détaillé d'une architecture radar FMCW (Frequency Modulated Continuous Wave), a été basée sur un mélange harmonique homodyne modulé en fréquence dans la gamme spectrale de 150 GHz. Elle a démontré des performances nominales de mesures longitudinale. En particulier, l'emploi d'une PLL (Phase Locked Loop) garantissant la stabilité du transceiver, complétée d'une approche algorithmique de déconvolution par normalisation, assure des performances d'utilisation accrues avec une plage dynamique atteignant 100 dB, tout en pouvant octroyer une cadence de mesure allant jusqu'à 7.62 kHz. Ces développements ont naturellement mené à des thématiques applicatives d'inspection volumique pour le contrôle sans contact. En particulier, la pertinence envers la problématique de mesure d'épaisseur sur échantillons millimétriques stratifiés a été établie. Finalement, motivée par de similaires considérations de contrôle topologiques, la reconstruction cohérente de fronts d'ondes, par imagerie sans lentille, a été transposée dans le domaine térahertz. Cette thématique a fait appel aux méthodes d'holographie hors-axe et de reconstruction de phase itérative, par l'usage d'imagerie point par point dans le domaine sub-térahertz, puis converties vers pour une implémentation en temps réel à 2.5 THz.

Mots Clefs: Terahertz; Ondes Millimetriques; Radar FMCW; Contrôle Non-Destructif; Imagerie; Inspection, Imagerie Cohérente.

Université de Bordeaux
Laboratoire de l'Intégration du Matériau au Système (IMS)
UMR CNRS 5218, F-33400 Talence, France

Contents

List of Figures

List of Tables

Acknowledgments

Grâce à l'aspect pluridisciplinaire, académique et industriel de ma thèse, j'ai eu la chance de travailler dans un environnement très évolutif en collaborant avec des collègues spécialisés dans des champs expertises multiples. Ces rencontres et échanges m'ont ainsi permis de développer des connaissances larges au sein d'un domaine technologique en plein essor. Je souhaite donc remercier toutes les personnes m'ayant apporté soutien et savoir tout au long de cette étape.

Je tiens ainsi, tout particulièrement, à remercier en premier lieu Dr. Patrick MOUNAIX pour cette opportunité et l'encadrement fourni au cours de ces travaux de thèse, ayant fait preuve d'un investissement sans faille. Au même titre, je remercie Dr. Jean-Paul GUILLET pour son accompagnement et sa supervision, avec toujours cette capacité à aiguiller les avancées.

La démarche collaborative de ce travail m'amène bien entendu à remercier à égale mesure l'encadrement au sein de Lytid. En particulier, Pierre GELLIE et Jean-Charles ROCHE qui ont su construire un cadre de travail motivant et cultiver un engouement autour de toutes les thématiques abordées, et sans qui cette opportunité n'aurait jamais été rendue possible. Je vous remercie ainsi pour tous les enseignements qui ont découlés de cette expérience fructueuse d'un point de vue personnel.

Je tiens à montrer ma gratitude envers Dr. Frédéric GARET et Dr. Jean-Francois LAMPIN pour avoir accepté d'évaluer mon travail en tant que rapporteurs, ainsi que Dr. Dominique COQUILLAT, Dr. Cristell MANEUX et Dr. Adrien STOLIDI, pour le temps consacré à l'examination de ce manuscrit en tant que membres du jury.

Plus largement, dans mon entourage professionel, je souhaite remercier toute l'équipe Lytid au travers d'Anna, Hanah, Hugo, Sébastien et Thibault, qui ont engendré de nombreux échanges et participé à l'aboutissement de ces travaux, ainsi que l'ensemble des membres de l'équipe de recherche Laser de l'IMS avec Damien BOGOURD et Frédéric DARRACQ. Il m'est important de dédier une mention particulière à Frédéric FAUQUET pour sa présence et l'aide indiscutable qu'il m'a apportée au cours de ces 3 années dans la réalisation pratique de mes travaux.

I would also like to thank Prof. Olga SMOLYANSKAYA and Prof. Nikolay PETROV, with whom a fruitful collaboration has been initiated with ITMO university Saint-Petersburg. De manière analogue, je fais écho à une succincte collaboration plus industrielle, qui je l'espère pourra se pérenniser, avec Joyce BOU-SLEIMAN, Arnaud SUSSET et Pierre FAUCHE.

A warm gratitude also goes to Dr. Qin WANG, and Dr. Ingemar PETERMANN for their teachings and the knowledge they shared with me during my stay in Stockholm among RISE Acreo's team, prior to this PhD work.

Je souhaite aussi accorder une attention à tous les étudiants que j'ai eu l'occasion de côtoyer et encadrer, avec Antoine, Clément, Thomas, Pierre-Louis et François, participant à leur échelle aux avancées observées. Plus specifiquement, merci à Barnabé, grâce à qui, une collaboration proche et impliquée a permis la mise en œuvre de nombreuses démonstrations applicatives sur ces travaux.

Ce dernier me permet ainsi de faire une parfaite transition vers toutes les relations amicales que la thèse m'a offertes avec Justin, Djeber, Matthieu, Ruben, Romain, Florent, Marine et Thomas, Soumaya, Marco, Ghyslain, Olivia et Moses. Un grand merci à MingMing, Quentin et Jean-Baptiste pour leur soutien apporté dès les premiers jours de ma thèse et tous les bons moments passés depuis notre arrivée en cette belle région Bordelaise.

Au-delà de ces rencontres récentes, je souhaite aussi vivement remercier mes amis de longue

date avec Julien et Mégane, Jean et Lucie, ... ou encore autant d'amis émanant de classes préparatoires avec Pierre-Alexis et Julie, Sebastien et Julie, Loïc, Arthur, Francis et Quentin.

Je dédie aussi naturellement d'infinis et très sincères remerciements à tout mon entourage familial. En particulier, un grand merci à mes parents qui m'ont transmis leurs valeurs, m'ont toujours accompagné tout au long de mes études jusqu'à ce point, et m'ont appris à fournir le meilleur de mes capacités. Merci aussi à Elise et Etienne, ma grande sœur et mon petit frère, avec qui d'excellents souvenirs restent et se construisent. Mes pensées incluent évidemment mes grands-parents qui, depuis mon enfance, m'ont fait vivre de magnifiques expériences enrichissantes.

Un remerciement tout particulier va aussi à la famille de ma chère Margaux, avec une attention spéciale pour le soutien que sa maman, Lydie, et sa grand-mère, Berthe, nous ont apporté.

J'en viens ainsi à l'ultime remerciement qui est dédié à Margaux, avec tant de belles choses vécues au cours de ces 10 ans. Je retiens tout particulièrement les voyages, que ce soit l'Equateur, l'Italie ou la Suède, mais aussi les découvertes quotidiennes que nous avons partagées et celles qui restent à venir. Je souhaite te remercier de tout cœur pour ta présence et ton soutien inconditionnel au cours de cette étape.

Acronyms

A

ADC: Analog-to-Digital Converter;

AXI: Advanced eXtensible Interface;

B

BPF: Band-Pass Filter ;

BRAM: Block RAM;

BS: Beam Splitter;

BW: Bandwidth;

C

CW: Continuous Wave;

CT: Computed Tomography;

D

DAC: Digital-to-Analog Converter;

DAQ: Data Acquisition;

dB: Decibels;

DDS: Direct Digital Synthesizer;

DFB: Distributed feedback;

DMA: Direct Memory Access;

DR: Dynamic Range;

DOF: Depth Of Field;

F

FET: Field Effect Transistor;

FBP: Filtered BackProjection;

FIFO: First In, First Out;

FFT: Fast Fourier Transform;

FPGA: Field-Programmable Gate Array;

FPS: Frames Per Second;

FMCW: Frequency Modulated Continuous Wave;

FWHM: Full width at half maximum;

G

GHz: Gigahertz;

GIF: Graphics Interchange Format;

GigE: Gigabit Ethernet;

GPIO: General-Purpose IO;

H

HBT: Heterojunction Bipolar Transistor;

HDPE: High Density Poly Ethylene;

HDR: High Dynamic Range;

HEMT: High-Electron-Mobility Transistor;

HF: High Frequency;

HIPS: High Impact PolyStyrene;

HM: Harmonic Mixer;

HPIO: High Performance IO;

HRFZ-Si: High Resistivity Float Zone Silicon;

I

IEP: Inverse Electromagnetic Problem;

IF: Intermediate Frequency;

IFFT: Inverse Fast Fourier Transform;

ILA: Integrated Logic Analyzer;

IMPATT: Impact Avalanche and Transit Time Diode;

IO: Input/Output ;

IR: Infrared;

IRT: InfraRed Thermography;

ISM: Industrial, Scientific and Medical;

IWEX: Inverse Wavefield EXtrapolation;

K

KHz: Kilohertz;

L

LED: Light-Emitting Diode;

LIA: Lock-In Amplifier;

LNA: Low Noise Amplifier;

LO: Local Oscillator;

LUT: Look-Up Table;

lwIP: lightweight IP;

LWIR: Long-Wavelength Infrared;

M

MHz: Megahertz;

MMIC: Monolithic microwave integrated circuit;

MRI: Magnetic Resonance Imaging;

MTF: Modulation Transfer Function;

MWIR: Middle-Wavelength Infrared;

N

NA: Numerical Aperture;

NDT: Non-Destructive Testing;

NEP: Noise Equivalent Power;

O

OAPM: Off-Axis Parabolic Mirror;

P

PCA: PhotoConductive Antenna;

PCB: Printed Circuit Board;

PFL: Parent Focal Length;

PHY: Physical Layer,

PL: FPGA Programmable Logic;

PLL: Phase Locked Loop;

POMc: PolyOxyMethylene copolymer;

PP: Polypropylene;

PS: FPGA Processing Subsystem;

PSF: Point Spread Function ;

PTFE: PolyTetraFluoroEthylene;

Q

QCL: Quantum Cascade Laser;

QCW: Quasi Continuous Wave;

R

ROI: Region Of Interest;

RAM: Random Access Memory;

RF: Radio-Frequency;

RFID: Radio-Frequency Identification;

RMS: Root Mean Square;

RT: Radiographic Testing;

RTD: Resonant-Tunneling Diode;

RX: Receiver;

S

SAR: Synthetic Aperture Radar;

SBMIR: Single Beam Multiple Intensity Reconstruction;

SD: Schottky Diodes;

SD: Standard Deviation;

SDK: Software Development Kit;

SHM: Sub-Harmonic Mixer;

SMA: Sub-Miniature Version A;

SNR: Signal to Noise Ratio;

SPI: Serial Peripheral Interface;

SWIR: Small-Wavelength Infrared;

T

TCP: Transmission Control Protocol;

TDS: Time-Domain Spectroscopy;

THz: Terahertz;

TUNNETT: Tunnel injection transit time negative resistance diode;

TX: Transmit;

U

UDP: User Datagram Protocol;

USAF-1951: United-States Air Force - 1951;

UT: Ultrasonic Testing;

UV: UltraViolet;

V

VCO: Voltage Controlled Oscillator;

VHDL: VHSIC Hardware Description Language;

W

WD: Working Distance;

WR: Rectangular Waveguide;

Symbols

Chapter I.

f: Radiation frequency;

h: Planck constant;

c_o: Speed of light in vacuum;

ϵ: Black-body emissivity;

E: Photon energy;

I_f: Radiant flux spectral density;

T: Temperature;

k_B: Boltzmann constant;

$\mathbf{E}_H$,$\mathbf{E}_L$: Energy Levels;

τ_K,τ_L: Lifetimes of energy levels;

n: Real refractive index;

λ_0: Wavelength in vacuum;

e: Coating thickness;

f_{min}: Lowest sweep frequency;

BW: Bandwidth;

T_s: Sweep time span;

t: Time;

V: Electric potential difference;

S_{probe}: Emitted radar signal;

$\widetilde{S}_{probe}$: Analytical emitted radar signal;

Φ_0: Static phase;

S_{echo}: Collected radar signal;

$\widetilde{S}_{echo}$: Analytical collected radar signal;

i: Considered target or echo;

τ_i: Propagation delay;

p: Maximal target number;

r_i: Target reflection coefficients;

S_{IF}: Beating signal;

$\widetilde{S}_{IF}$: Analytical Beating signal;

$\widehat{f}_{IF_i}$: Beating frequency;

d_i: Target distance;

δ_d: Range resolution;

Chapter II.

$\tilde{n}$: Complex refractive index;

n: Real refractive index;

κ: Complex part of the refractive index, Extinction coefficient;

c_o: Speed of light in vacuum;

c: Speed of light in propagation media;

$\boldsymbol{\lambda_0}$: Wavelength in vacuum;

U: Complex wave-function;

U_0: Wavefront amplitude;

$\overrightarrow{r}$: Position vector;

$\overrightarrow{x}$, $\overrightarrow{y}$, $\overrightarrow{z}$: Three dimensional axes;

x, y, z: Three dimensional coordinates;

r: Range;

t: Time;

Φ: Phase;

∇^2: Laplacian operator;

$\overrightarrow{k_0}$: Wave vector;

k_0: Wave number;

$t_{i,j}$: Amplitude transmission coefficient;

l: Sample thickness;

ω: Angular frequency;

I: Intensity;

I_0: Initial intensity;

α: Absorption coefficient;

θ_i: Incidence Angle;

θ_j: Refracted Angle;

θ_{ri}: Reflected Angle;

$r_{i,j}$: Amplitude reflection coefficient;

s: Radial distance from the optical axis;

ω_0: Gaussian beam waist;

ω: Gaussian beam radius;

$\omega_{-3d\mathrm{B}}$: Gaussian beam FWHM;

z: Distance;

R: Radius of curvature ;

ψ: Gaussian beam Gouy phase;

θ: Gaussian beam Divergence;

z_r: Rayleigh range;

f': Focal length;

D: Lens Diameter;

NA: Numerical Aperture;

N: Aperture f-number;

P: Collected power;

x_d: Blade position;

C_r: Contrast ratio;

Grp: Group number;

Res: Element resolution on a USAF test chart;

El: Element number;

ρ, Θ: Angular and radial coordinates;

$f(x,y)$: Absorption profile;

R_Θ: Projection profile;

δ: Dirac distribution ;

$\mathscr{F}$: Fourier transform operator;

δ_{Airy}: Radius of the Airy disk;

z: Sagitta, surface profile;

K: Conic constant;

α_i: i^{th} order polynomial asphérisation coefficient;

F_x,F_y: Galvanometeric oscillation frequencies;

τ: Pixel integration time;

$\alpha(t)$,$\beta(t)$: Galvanometric angular deviations;

A, B: Galvanometric amplitudes;

α_0, β_0: Galvanometric angular offset;

ϕ: Relative phase;

θ_p: Paraboloid off-axis angle;

$X(t), Y(t)$: Illumination beam parametric position;

γ: Galvanometric frequencies ratio;

c_v: Coefiscient of variation;

μ: Mean-value over the illuminated area;

σ: Standard deviation over the illuminated area;

Abs: Absorbance;

Φ_{back}: Optical flux from a background illumination;

Φ_{samp}: Optical flux through sample;

N_{pix}: Incremental frame displacement;

M: Magnification;

δ_{pix}: Pixel pitch;

v_0: Object displacement velocity;

C_t: Resolution target contrast ration;

$C_{Grp,El}$: Element contrast ratio;

$\widehat{C}_{Grp,El}$: Relative element contrast ratio;

Chapter III.

ω_0: Gaussian beam waist;

T_s: Sweep time span;

BW: Bandwidth;

Γ: Frequency sweep rate;

f_r: PLL reference frequency;

N: Integer PLL divisor;

f_{VCO}: VCO emitted frequency;

V_{VCO}: VCO voltage command;

VCC: Voltage common collector;

r^2: Linearity coefficient;

f_{LO}: Local Oscillator frequency;

P1**,**P2**,**P3: Power level at each coupler port respectively;

Θ_h: Horizontal beam divergence;

Θ_v: Vertical beam divergence;

α: Absorption coefficient;

f': Focal length;

n: Real refractive index;

R_1**,**R_2: Lens radii of curvature;

d: Lens central thickness;

S_{echoe}: Echoed chirped radar signal;

S_{probe}: Emmited chirped radar signal;

clk: FPGA clock signal;

t_{valid}, t_{last}: FPGA timing flags;

F_s: Sampling frequency;

N_s: Recorded sample points;

S_{IF}: Beating signal;

j: Sample count;

$\widetilde{S}_{probe}$: Analytical emitted radar signal;

t: Time;

a_{probe}: Spectral profile;

f_{min}: Lowest sweep frequency;

Φ_0: Static phase;

$\widetilde{S}_{IF}$: Analytical beating signal;

i: Considered target or echo;

τ_i: Propagation delay;

p: Maximal target number;

r_i: Target reflection coefficients;

f_{IF}: Beating frequency;

$\mathscr{F}$: Fourier transform operator;

a_{LO}: LO Spectral profile;

A_{probe}: Amplitude spectral profile;

Φ_{probe}: Phase evolution;

$\mathscr{H}$: Hilbert transform operator;

f_L, f_H: Cut-off frequencies;

$\widehat{S}_{samp}(t)$: Normalized sample signal;

$\widetilde{S}_{IF_{samp}}$: Analytical sample beating signal;

$\widetilde{S}_{IF_{back}}$: Analytical background beating signal;

p': Considered target or echo exempted from background;

i': Maximal target number exempted from background;

$\widetilde{S}_{IF_{ref}}$: Analytical reference beating signal;

τ_{ref}: Reference propagation delay;

$f_{IF_{ref}}$: Reference beating frequency;

$\widehat{f}_{IF_{i'}}$: Relative beating frequency;

$\widehat{d_{i'}}$: Relative target distance;

$\widehat{S}_{samp}$: Normalized sample signal;

$\widehat{S}_{ref}$: Normalized reference signal;

c_o: Speed of light in vacuum;

N_{ZP}: Zero-padding factor;

δ_f: Frequency resolution;

$\overrightarrow{x}$, $\overrightarrow{y}$: Scanning axes;

x_0, y_0: Scanning position;

$\overrightarrow{z}$: Depth sensing axis;

z_i: Depth slice;

$\tilde{n}_s$: Sample complex refractive index;

C_t: Resolution target contrast ration;

$C_{Grp,El}$: Element contrast ratio;

$\widehat{C}_{Grp,El}$: Relative element contrast ratio;

δ_d: Numerical distance resolution;

k: Numerical index;

$\delta_{d_{eff}}$: Effective distance resolution;

$\delta_{f_{-3dB}}$: Main lobe width;

DR_{back}: Dynamic range on background;

DR_{peak}: Dynamic range on reference;

Chapter IV.

f_{c_m}: Cladding characteristic frequency;

m: Modal integer;

c_o: Speed of light in vacuum;

t_{cl}: Cladding thickness;

n_{cl}: Cladding refractive index;

η: Coupling efficiency;

P_{Guided}: Coupled power level;

$P_{Excitation}$: Initial excitation power level;

$\overrightarrow{x}, \overrightarrow{y}, \overrightarrow{z}$: Three dimensional axes;

x, y, z: Three dimensional coordinates;

$\mathscr{F}$: Fourier transform operator;

ω: Angular frequency;

H_s: Simulated sample transfer function;

H_m: Measurement transfer function;

p: Number of layers;

d_i: Thickness of a layer;

$\tilde{n}_i$: Layer complex refractive index;

ρ_k: Reflection contributions;

k: Contributions index;

$r_{i,i'}$: Reflection coefficient;

$t_{i,i'}$: Transmission coefficient;

ϕ_i: Layer one-way phase shift;

i: Layer index;

λ: Wavelength in vacuum;

χ_i: Geometric series constant ratio;

γ_i: Stack reflectivity up to the i^{th} layer;

μ_i: Stack transmission up to the i^{th} layer;

$\widehat{S}_{samp}$: Normalized sample signal;

$\widehat{S}_{ref}$: Normalized reference signal;

n: Real refractive index;

κ: Complex part of the refractive index, Extinction coefficient;

$\delta\rho$: Amplitude objective function;

$\delta\phi$: Phase objective function;

Δd: Numerical thickness resolution;

Δn: Numerical refractive index resolution;

$\Delta\kappa$: Numerical extinction coefficient resolution;

Λ: Error objective function;

ζ: Error regulation coefficient;

T_s: Sweep time span;

δT: Sweep time cropping factor;

σ_m: Mechanical standard deviation;

σ_{FMCW}: FMCW standard deviation;

d_m: Mechanical thickness;

d_{FMCW}: FMCW extracted thickness;

δ: Relative error;

Chapter V.

U: Complex wave-function;

$\vec{r}$: Position vector;

$\vec{x}$, $\vec{y}$, $\vec{z}$: Three dimensional axes;

x, y, z: Three dimensional coordinates;

d: Distance to the considered plane;

c_o: Speed of light in vacuum;

$\boldsymbol{\lambda_0}$: Wavelength in vacuum;

t: Time;

$\mathscr{F}$: Fourier transform operator;

$\tilde{n}$: Complex refractive index;

n: Real refractive index;

H_d: Free space propagation transfer function;

h_d: Free space propagation impulse response;

ν_{0x}, ν_{0y}: Spacial frequencies;

k_{0x}, k_{0y}: Wavevector component;

$\mathscr{U}$: Complex wave-function in Fourier domain;

$o(x, y)$: Object pupillar function;

$p(x, y, 0)$: Probe complex wavefront;

$O(x, y)$: Object wavefront;

A_O: Object wavefront amplitude;

Φ_O: Object wavefront phase;

$R(x, y)$: Reference wavefront;

A_R: Reference wavefront amplitude;

Φ_R: Reference wavefront phase;

Θ: Holography interfering angle;

f: Frequency;

$I(x, y)$: Intensity profile;

k: Recorded profile index;

m: Number of recording planes;

Δ_z: Longitudinal pitch;

Δ_x, Δ_y: Lateral pitch;

z_0: Initial plane distance;

S: Measurement signal;

S_1, S_2: Digitized signals;

$S_{max1}, S_{max2}, S_{min1}, S_{min2}$: ILA Thresholds;

ζ: HDR regulation factor;

β: Phase plane tilt angle;

h(x,y): Height map;

Λ: Interference fringes spatial period;

General Introduction

Non-Destructive Testing (NDT) relates to the issue of automated inspection and monitoring for a wide variety of end-users applicative fields. It then includes a plethora of specific topics ranging from the detection of inclusions, defects, cracks, impacts or delaminations, up to the inspection of soldering traces or the assessment of material densities and hydrometric levels, to name a few.

An increase in the automation of productions led, in the recent years, to an unavoidably expanding demand for flaws detection, as to ensure production reliability. Such a growing demand of industrialists, along with the development of advanced production processes, then brings forth a wide range of products and structures to be tested. In this constructive and blooming dynamic, the NDT market is prospected to evolve from 16.72 billion USD in 2020 up to 24.64 billion by the year 2026 according to a recent Mordor Intelligence report.

The main established solutions, regrouping radiographic testing, ultrasonic inspection, thermography, visual testing, or Eddy currents, underwent strong development and sophistication for several decades already. They led to the development of advanced NDT processes with improved fault detection over several fields.

As an upcoming technological domain, terahertz non-destructive evaluation offers several benefits with respect to the previous solutions, that can specifically be put to good use in the scope of niche testing problematics. Namely, its ability to provide an in-depth sensing capability in a variety of materials, to offer contactless volumetric testing, coupled to the achievable sub-millimetric resolution, as well as its non-ionizing, hence harmless character, are contributing to the current growing interest toward the sub-millimeter waves spectral range.

However, a lack of technological background, with respect to the competing well-established sensing schemes, contains terahertz systems development to complementary and specific tool. Indeed, it should either provide an improved sensing capability or target issues that remain beyond the scope of the current NDT state of the art technologies. Namely, one of the striking example of such a successful transposition and assimilation to the industrial field has been witnessed with the niche topic of contactless assessment of paint stratified structures for the aeronautic and automotive sectors, through terahertz pulsed time domain inspection.

Among the well-established control technologies, terahertz then aims to fulfill specific and peculiar needs in the NDT environment, through the consideration of the most recent advances in the development of sources and sensing schemes. This work then specifically fits within this scope with the intend to entrench and establish few capabilities of millimeter-waves and terahertz technologies to fulfill such targeted monitoring requirements. Namely, through the development of instrumentation solutions, implementing forefront technological bricks, various advanced imaging and sensing approaches have then been successfully investigated.

The first chapter then aims to provide a quantitative glimpse of the status of terahertz technologies among the inspection applicative field, incorporated as a core motivation for the work provided along this manuscript. It then initially focuses on a coarse depiction of the NDT industry through the main established and widespread systems. It will feature their respective benefits and drawbacks as to put in perspective the capabilities inherent to the terahertz and millimeter-waves spectral range technologies. Namely, the intrinsic material penetration potential, contactless inspection abilities and harmless character when it comes to interactions with human bodies represent the favored traits that built the interest toward terahertz in the latest decades. To illustrate such recent developments, a quantitative review of the available technologies, for

sources and sensing solutions, is subsequently deployed, along with details in their current application fields. It shall then help the reader to pin down the several technological choices motivates along this manuscript. Additionally, a more targeted review of the FMCW (Frequency Modulated Continuous Wave) radars mode of operation, current state of the art, and applicative scopes in the millimeter-wave spectral range is provided to support the central developments carried out among this work.

In the second chapter, continuous wave imaging approaches are investigated. Namely, the basic optical interactions and models at stake are recalled to provide a theoretical ground to further assess the reference and standard terahertz imaging approach. Based on raster scan recording, this single sensing point methodology is declined with two advanced imaging scheme, with a simultaneous transmission-reflection configuration, and a dual frequency concomitant sensing geometry. Thanks to the optimal resolution and homogeneity, it provides a prospective inspection tool, demonstrated in this work over a wide frequency range, from 2.5 THz down to 75 GHz. 3D numerical reconstruction capabilities are as well demonstrated through tomographic processing. Real time full-field imaging is then discussed and detailed as a solution to overcome the inherent imaging time limitations of single point sensing. Nevertheless, three main challenges are to be faced with power density limitations, illumination beam homogeneity and optical coherence of the source, that induces irreversible imaging capabilities reductions. The demonstrated galvanometric illumination mechanism, operating at 2.5 THz, coupled to the use of a dedicated bolometric array and the development of a full field imaging lens, then provides a versatile tool for the mitigation of those three critical characteristics. It indeed grants a full control over the illumination beam geometry with an averaging of the coherence artifacts. Real time imaging results are then showed, along with advanced illuminations and recording schemes for enhanced performances. With such a greatly improved acquisition rate, tomographic reconstructions are as well demonstrated.

As the central effort of this work, the third chapter will provide an in depth focus on the implementation of the FMCW homodyne detection scheme in the millimeter-waves spectral range. As an inspection tool, the prior technological choices are detailed as to support the III/V based mono-static transceiver geometry which features harmonic mixing among the 150 GHz operation frequency window. With several preliminary characteristics in mind, the whole FMCW architecture is specified and supported by characterizations performed for each system stage. Namely, for coherent sensing unit with longitudinal sensing capabilities, the frequency chirp generation Phase Locked Loop is extensively detailed as a solution to mitigate the devastating non-linearities of the ground level part of FMCW transceivers. The high frequency architecture is then as well quantitatively described along with the simple sensing optical setup. From there, the requirement for additional processing on the retrieved homodyne beating signals will be highlighted. A two points referencing normalization procedure will be detailed as to uncover the expected longitudinal sensing capabilities of the FMCW operation. In an effort toward the integration of the system and an optimization of its measurement rate for volumetric inspection purposes, the implementation of a FPGA-based data processing unit will be succinctly addressed as well. From this operating FMCW unit, the main performances will be featured through the effective measurement rate, lateral and longitudinal resolutions for 3D inspection, longitudinal precision and accuracy, as well as the achievable dynamic range, and stability.

With the capabilities of the developed transceiver in mind, the fourth chapter will assess demonstrative works performed through the use of FMCW radar units, in the millimeter-waves spectral range. Namely, as an initially targeted application field, enabled by their intrinsic longitudinal sensing capabilities, volumetric inspection will be featured on a selection of samples of interest, tied to several industrial problematics. Namely, polymer samples fault detection and soldering inspections, as well as the consideration of pharmaceutical samples will be detailed as proof of work for the previously developed FMCW transceiver. See-through imaging is also covered as an issue related to airplane health monitoring. A specific geometry will subsequently demonstrate the use and characterizations of a simplified optical setup for the implementation of a guided

sensing tool. The advantage of the longitudinal FMCW sensing in this configuration will be highlighted. Another promising and upcoming applicative field of such tools, featuring depth sensing, relates to the investigation of stratified samples for contactless thickness extraction. On this specific topic, an analogy with terahertz time domain technologies and algorithmic methodologies, as references for sub-millimeter thickness paint layers extractions, are then provided as ground works. The enforcement of Inverse Electromagnetic Problems adapted to the FMCW mode of operation, and related to a physical depiction of stratified sample geometries, will then be explored. With the previously developed FMCW unit, this approach is applied to thickness extraction and mapping on mono-layer samples bellow the intrinsic longitudinal resolution. The natural extension to multi-layered structures will be subsequently addressed in this work.

Beyond the coherent sensing provided by the homodyne detection of FMCW operations, the latest chapter then assesses a more prospective sensing and imaging approach, with the transposition of lensless coherent imaging in the terahertz domain. Based on the consideration of incoherent intensity mapping recordings, such methodologies provide the recovery of an additional wave front phase, valuable for numerous inspection problematics. Specifically, the principles behind diffractive imaging will be recalled with holography, ptychography and iterative phase retrieval, along with a review of the current developments. The implementation of a challenging reflection configuration in the 300 GHz frequency band for diffractive iterative phase retrieval initiates this work, and is followed by its transposition in a more straightforward transmission geometry. The investigation of off-axis holographic instrumentation and data processing will be subsequently considered for comparative purposes. In the continuity of the transition established in the previous chapters, toward measurement rates beyond the academic implementation standards, this work is concluded with the initiation of coherent real time diffractive imaging at 2.5 THz.

The results gathered in this manuscript are part of a collaborative work among a CIFRE convention between the firm Lytid, under the supervision of Dr. Pierre GELLIE, and the Université de Bordeaux, under the tutelage of Dr. Patrick MOUNAIX and Dr. Jean-Paul GUILLET.

Chapter I

Terahertz Towards Non-Destructive Testing

«The universe doesn't allow perfection.»

Stephen Hawking,
in «A Brief History of Time»

I.1 Introduction

In this first chapter, *Terahertz Towards Non-Destructive Testing*, several necessary tools for the proper understanding of terahertz capabilities in the field of non-destructive testing will be detailed.

A global depiction of the current advances on the terahertz technologies field will be drawn after a brief review of historical inspection approaches. An overall state of the art of the main sensing principles, emission sources or sensors, and more broadly imaging solutions, in the terahertz and millimeter-waves spectral range will be provided. An emphasis on their relative performances and respective usage suitability that led to recent implementations will be given.

As Frequency Modulated Continuous Wave (FMCW) radar technology remains at the center of this work, a specific focus will hence be brought on such sensing mechanism. A review of the available technological solutions and applications will be depicted as well.

I.2 Non-Destructive Testing and Inspection Methods

Ever since production cadences reached industrialized levels, the reliability and safety of a product represent major concerns for manufacturers. One of the driving goals of the inspection industry is thus to find ways to ensure the integrity of a good and avoid premature degradations or failures. A straightforward solution for testing mechanical and thermal properties of a material would be to inflict stress, strain or thermal shocks until a breakdown threshold is reached. Such approach would obviously lead to unusable components after testing. Non-Destructive Testing (NDT), on the other hand, aims to avoid this damaging process through the use of other sensing means.

Not only limited to the subsequent stages of the production process, it can also be applied to post-production quality inspection and maintenance phases. The importance of NDT, and in particular the need of defining global standards for NDT methods, led to the creation, in 1998, of the European Federation of Non-Destructive Test (EFNDT). One of their goals is to bring together resources from organizations and companies all over Europe to draw the road map of the NDT field in regard of the industrial needs and available technologies.

In a general context, materials degradation is a process that leads to the alteration of their physical proprieties (mechanical, optical, electrical, *etc.*), due to ageing or under the effect of their environment. From UV alterations, through corrosion, vibrations, temperature variations up to direct impacts, any kind of material can be subject to deteriorations. From plastic molding, construction industry, automotive parts inspection, to precision luxury watchmaking assembly, NDT reaches a large variety of production fields with extremely diverse expectations.

Nevertheless, some specific fields display enhanced demands in NDT matters, due to their use of pioneering high-end materials and unique advanced production methods. For instance, the critical role of NDT for inspection and maintenance in the aerospace industry led to the creation of a dedicated board in several countries, the National Aerospace NDT Board, with the intent to supervise the compliance of NDT related procedures to the requirements defined by the European Aerospace Safety Agency (EASA). Indeed, aeronautics production is a major actor when it comes to composite materials, honey comb structures, technical foams, ceramics, and new generation lightweight materials. They require extensive testing for safety reasons and, as a matter of fact, are especially suitable for terahertz (THz) radiation inspection in absence of metallic parts or conducting materials.

Among a slew of available techniques, ranging from the most common visual inspection and automated optical imaging control, down to the most specific and advances approaches such as neutron imaging, few technologies have been established as references. They reached this status either for their applicable universality, or on the contrary, thanks to their targeted effectiveness toward the resolution of a given problematic. Specifically, several technological perspectives can

be distinguished [1, 2]:

- Optical and photonics approaches range over most of the electromagnetic spectrum with Ultraviolet (UV) inspection, visible light imaging and profilometry, or Infrared (IR) visualization, with thermal testing and thermography. Multi-spectral imaging using SWIR (Short Wavelength Infrared), MWIR (Middle Wavelength Infrared) and LWIR (Long Wavelength Infrared) sensors can a well benefit from the various materials characteristics in each spectral band.
- Radiographic testing [3, 4], among the high energy domain of the electromagnetic spectrum, with the largely democratized use of film or digital radiography and Computed Tomography (CT) 3D reconstruction in the X-Ray or γ-Ray spectral range.
- Magnetic testing [5] with the use of induction for eddy currents probing, or magnetic particles inspections, by employing ferromagnetic powder for the detection of magnetic flux leaks, up to the use of Magnetic Resonance Imaging (MRI).
- Ultrasonic testing [6], a widely used inspection method that ensures the detection of flaws through the propagation of mechanical waves within the material. Typical probes make use of frequencies ranging from 0.1 MHz up to 200 MHz with different beam profiles or even beam steering implementations.

Beside the simple external surface inspection that can be performed through well-established profilometry or visualization techniques such as dye penetrant inspection, industrial interest for the characterization of the structure's integrity tends to draw up towards volumetric inspection, with the investigation of in-depth sensing methods. While eddy current testing, and magnetic particles testing are mostly or exclusively used on metallic parts, visual inspection, ultrasonic testing, thermography and radiography can be applied to non-metallic components. From these four techniques, only the latest three can provide in-depth information.

Radiography makes use of X-rays or γ-rays to penetrate object under inspection and can produce a 3D image using conventional 3D CT technique. It benefits from a high resolutions, reaching up to the µm-level, enabling the detection of small cracks, inclusions and discontinuities. However, radiography remains a slow approach and requires cumbersome and expensive equipments, with dedicated facilities and high maintenance cost. Safety precautions must also be considered when conducting radiographic testing since due to their ionizing power, X-rays and γ-rays remain harmful toward biological entities.

Ultrasonic testing on the other hand represents a harmless solution, based on the propagation and detection of ultrasonic waves through the material, that may be either ferrous or non-ferrous, and provides subcentimetric resolution. Using a time of flight approach, this technique allows to sense and locate discontinuities, and can be applicable to thick parts even when if only one side is accessible. However, beside sparse recent developments [7], it requires direct contact with the sample for a proper wave coupling and even bath immersion in some cases. As for radiography, ultrasound testing operation and results interpretations require some specifically qualified personnel.

Thirdly, IR thermography can be implemented either through passive thermal imaging, that uses the sample itself as an IR source, or active thermography, via the use of an external energy source. The latest can highlight artifacts thanks to the induced discontinuities in the thermal conductance of the material. It represents a versatile solution with low equipment and operation requirements for standard implementations, allowing vidao-rate inspection, but can generate heat damages for sensitive samples. Such systems span over wide price ranges, mainly impacted by the performances of the selected thermal imager. This technique offers contact-less inspection but retains a limited accessible depth range and suffers from this restriction when it comes to probe thick samples.

As a newly investigated alternative, terahertz non-destructive evaluation offers several benefits over the previous solutions. Namely, in absence of metallic parts, it can be integrated as a

contact-less far field sensing solution with penetration capabilities in dielectric materials and remains a harmless technique when used in standard power ranges [8]. Such features brought this technological approach as a complementary tool to solve issues that remain beyond the reach of the well-established sensing techniques. To introduce the advances in this field, section I.3 will review the available technological bricks as well as the currently investigated application cases.

I.3 Context on Terahertz Technologies

Historically, even though it has been known and investigated since the beginning of the XXth century, it was not until the latest decades that significant scientific and technological advances have been witnessed in the sub-millimeter wave spectral range. Several remarkable developments led to a growing interest in the fields of astronomy [9, 10] followed by biology, communications [11], sensing [12] or security and defense [13].

In the electromagnetic spectrum, the terahertz (THz) wave spectral range spans between the microwaves and infrared radiations, as depicted on Figure I.1. Although the boundaries remain somewhat arbitrary, a standard definition is considered from 100 GHz up to 10 THz, equivalent to wavelengths ranging from 3 mm down to 30 µm respectively.

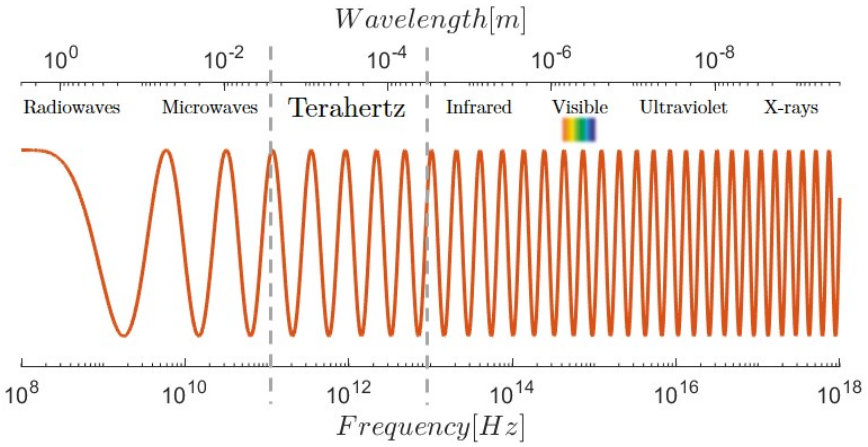

Figure I.1: Overview of the electromagnetic spectrum.

This proximity with the photonics corpuscular approach on the IR side and the wave consideration from microwave low frequency boundaries brings righteous physical features and abilities to such radiations.

Specifically, following the Planck–Einstein relation:

$$\mathrm{E} = hf, \tag{I.1}$$

with $h = 6.626 \times 10^{-34}\mathrm{J}.s$ the Planck's constant, and f the radiation frequency [Hz], a terahertz photon carries an energy that ranges from 0.41 to 41 meV. From a safety perspective, this energy range remains orders of magnitude below any ionization energy ($\sim 1e$V) and so, in contrast to high energy extreme UV or X-ray emissions, remains non-hazardous for biological entities. Additionally, terahertz light-matter interaction will be mostly bounded to low energy molecular vibration modes, or collective rotations of molecules and gaseous compounds. This will result in the significant transparency of dielectric materials and in contrast, induces absorption in polar compounds such as water. Hence, beside several absorption peaks induced by gaseous water vapor content in the atmosphere, free-space propagation remains achievable. Spectroscopic discrimination of gas or solid chemical compounds in the terahertz spectral range is also of interest and draws up strong attention in pharmacologic studies [14] or defense applications [15] for compounds identification.

In correlation with this enhanced transparency of non-conductive materials, with respect to infrared, the sub-millimetric wavelength implies an improved imaging resolution relatively to microwaves, making terahertz waves an especially compelling tool for inspection [16].

This section will be dedicated to the review of recent technological advances [17] that can be employed for the implementation of terahertz sensing systems. In such a system oriented approach, to justify the technological choices conducted in this work, a specific attention will be brought to existing terahertz sources and sensing units.

I.3.1 Terahertz sources

Despite those worthwhile light-matter interaction features, the terahertz spectral region underwent little development efforts since the beginning of the XX^{th} century. This limited growth is to be put in perspective with respects to the thriving decades of technological advances and maturation witnessed beyond the neighboring electromagnetic boundaries. As the root of this slow evolution, a lack of powerful sources and efficient detectors has to be incriminated. Such a shortage prevented the development of sensitive measurement schemes for spectroscopic and imaging problematics and consequently, their transposition toward industrial fields. This is the so called "terahertz gap", that emerges from the confluence between electronics and phonics technologies with reduced performances, well-illustrated around 1 THz in Figure I.2 [18, 19], with the lack of mW level sources.

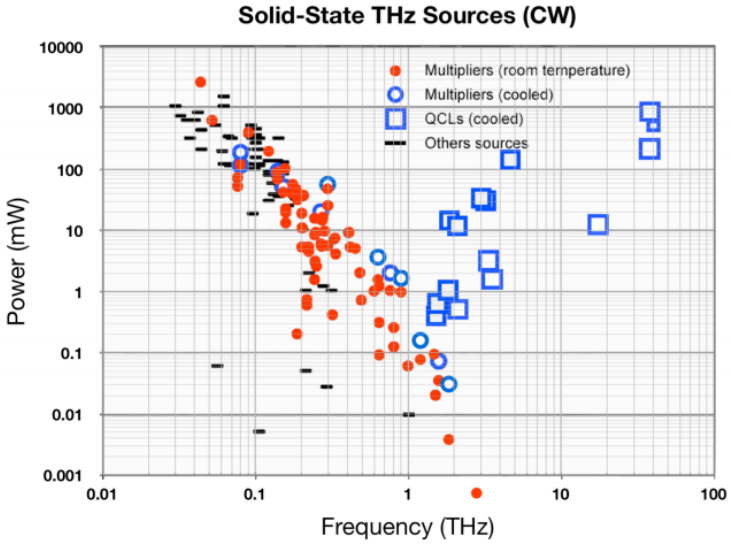

Figure I.2: Power distribution of currently available sources [18, 19].

A large variety of physical phenomena can nevertheless lead to emission or sensing capabilities in the terahertz range. An extended terahertz sources state of the art has been reviewed in [17, 20, 21] and a targeted depiction is drawn in this section with the selection of the most relevant technologies with respect to the issues covered in this manuscript.

- Vacuum electronic sources

On one extreme, with advanced emission processes, aiming for high power radiations, we could consider the vastly researched field of vacuum electronic sources. In this category, we can name carcinotrons and gyrotrons [22–24], that employ the cyclotron resonance of electrons in a strong magnetic field for the generation of millimeter waves, as well as free-electron lasers [25, 26] or even synchrotrons [27]. The synchrotron radiation is employed and ensures the generation of terahertz waves when the trajectory of a relativistic electron is bent in a strong magnetic field.

Due to their high operation costs and equipment requirements, they do not represent convenient sources for practical implementations by their end-users. In the following general depiction, we will therefore restrain this review to components and sources that are especially suitable to be scaled for NDT and sensing applications.

- Black-bodies

As the most intuitive and fundamental principle, the black-body radiation is tied to a continuous broadband emission spectrum of an object that, even for low temperature black-bodies (T < 20 K), will cover most of the terahertz band.

Defined by the Plank's law [28], which tends toward the Rayleigh-Jeans law at low frequencies and the Wien distribution law at high frequencies, I_f, the radiant flux spectral density (spectral power density per solid angle unit per unit of area [W.m^{-2}.sr^{-1}.Hz^{-1}]) of such a black-body depicts its spectral distribution at a given temperature as follows:

$$I_f(f,T) = \frac{2hf^3}{c_0^2\left(e^{\frac{hf}{k_bT}} - 1\right)}, \tag{I.2}$$

with f the radiation frequency [Hz], h the Planck's constant [J.s], k_B the Boltzmann constant [J.K^{-1}], c_o the speed of light in vacuum [$m.s^{-1}$], and T the temperature of the black-body [K].

In accordance with this distribution, the maximum emission frequency, f_{max}, is dictated by the Wein's displacement law [29] as follows ;

$$f_{max}(T) = T \times 5.879.10^{10} Hz.K^{-1}, \tag{I.3}$$

At room temperature, the maximum emission wavelength will be located in the IR range with a stretched emission tail in the terahertz region. While higher temperatures will shift this peak spectral radiance toward the visible range, reaching noticeable visible glow from T = 1000 K [30], at lower temperatures, most of the emission is contained in the terahertz range. With temperatures ranging from 1,7 K to 170 K, maximum radiance frequencies are respectively shifting from 100 GHz to 10 THz with a peak emission at 600 GHz for a black-body temperature of 10.2 K. Considering such low temperature ranges, millimeter-waves represent a predominant illumination source in astrophysics applications.

A depiction of $I_f(f,T)$ the radiant flux of black-body radiations at different temperature and $I_{f_{max}}(T)$, the peak spectral emission evolution with temperature are shown in Figure I.3.

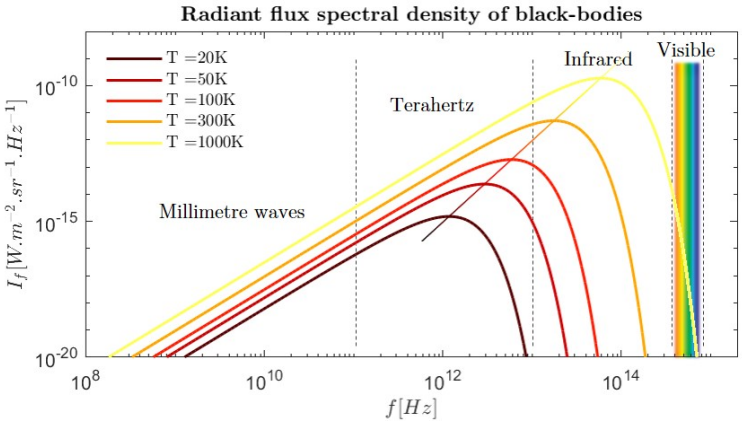

Figure I.3: Spectral distribution of black-bodies at various temperatures, following Plank's law and peak spectral radiant flux as a function of the temperature.

Nevertheless, for quantitative illumination considerations, the emissivity ϵ of a so called grey-body has to be accounted for. It can represent, just like in the IR spectral range, a usefully passive illumination process for sensing, imaging [31] or sensor calibration [32]. To do so, using either intrinsically emitting object, such as the human body for security screening applications [33–35], or a purposely heated black-body as a background source [36] can be considered. Using room temperature black-bodies, incoherent sub-mW level emissions [37] can be achieved in the terahertz band, even though most of the radiation will be generated in the Infrared spectral window with poor control over the beam profile quality.

- Femto-second laser based terahertz sources

Historically, one of the most widely adopted emission process for terahertz sensing remains based on short-pulse terahertz generation, and has been extensively democratized by Time-Domain Spectroscopy (TDS) systems [38]. This approach calls on the interaction of high power SWIR femtosecond laser pulses with non-linear materials, organic crystals, through optical rectification [39, 40] on Photo-Conductive Antennas (PCA) [41]. The later has been a standard approach for modern pulsed system. Through the absorption of high energy photons in the semi-conductor material, electron-hole pairs are generated. Those photocarriers are then accelerated by a static biasing of the PCA, hence the generation of a sub picosecond scale transient current that will lead to the emission of a broadband terahertz pulse. This process is depicted in Figure I.4 and has been firstly demonstrated in 1983 by Auston et al. [42, 43]. Since then, advances in this field have been tied to photoconductive materials [41], with the typical employement of III/V semiconductors such as GaAs, InGaAs or InGa(Al)As, antenna designs [44, 45] and beam shaping, mainly through High Resistivity Float Zone Silicon (HRFZ-Si) hemispherical and bullet lenses.

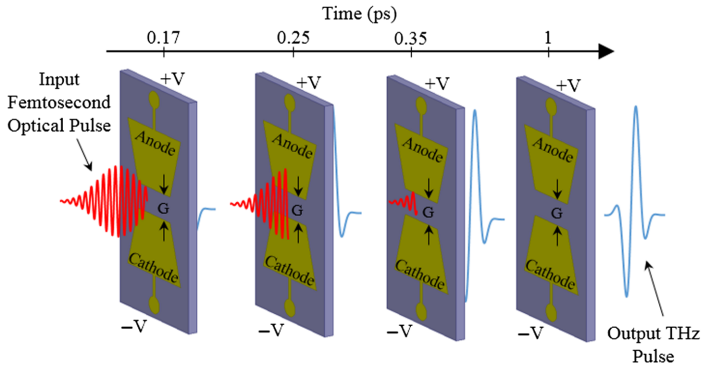

Figure I.4: Emission principle for photoconductive antennas [41].

This pulsed emission process remains too fast for any detection electronics and delivers a low average power. In order to overcome this limitation, PCAs have the ability to be employed as triggered sensors as well. In this configuration, the current, generated by the incoming terahertz pulse is detected upon femtosecond laser pulse absorption in the photo conductive material [46]. It therefore acts as an optically triggered sampler.

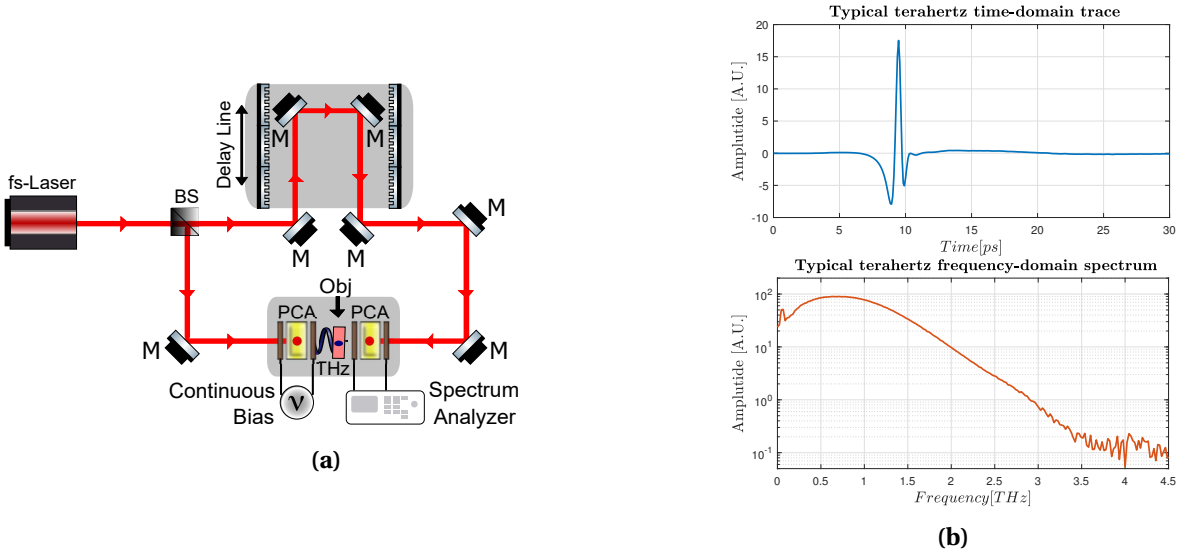

Figure I.5: (a) Standard terahertz time-domain sensing implementation schematic [47] and **(b)** the typical resulting picosecond pulsed waveform and relative spectral distribution.

Providing the high repetition rate of the laser source, hence a consistent terahertz pulse emission from a biased PCA, a full recording of a terahertz pulsed waveform can be performed through optical sampling by delaying a probing femtosecond pulse used to set off the sensing PCA [48]. This pump-probe scheme has become a standard implementation in TDS approaches and its typical implementation is depicted in Figure I.5a [47]. The resulting picosecond scale time trace and related spectral distributions are displayed in Figure I.5b.

Starting from complex technical implementations, the standardization of this sensing methodology drove significant developments and technical improvements from several manufacturers such as TeraView [49], MenloSystems [50] or Toptica [51], among others, to reach fully-packaged compact, table-top, and portable systems. Current systems reach up to 100 dB measurement dynamics, providing ~10 min integration time [52], and spectral span from 100 GHz up to over 6 THz, with full speed recording repetition rates ranging at 100 traces per seconds for conventional synchronous systems and up to multikilohertz scan-rate using asynchronous optical sampling systems [53].

- Laser based optical downconversion or photomixing

Beside those conventional sources, several emission processes have been inherited from the photonics technological advances in the IR toward the Long-Wavelength Infrared spectrum (LWIR) and beyond in the terahertz region.

Photomixing emerged as an efficient technique for continuous wave generation of a terahertz beating signal, from the mixing of 2 out of tune DFB lasers (distributed feedback lasers) when focused on a photoconductive switch [54]. The emission is then continuously tunable over a large portion of the spectrum from 100 GHz up to 3 THz by setting the detuning of the 2 lasers. Even though the low conversion efficiency does not allow for power generation that reaches mW-levels, up to 100 µW are demonstrated at 100 GHz for Toptica commercially available solutions [55] with up to 80 dB for integration times below 1s with a full integrated sensing system.

- Optically pumped gas lasers

Originating from photonics technologies, several gas lasers feature emission capabilities in the terahertz spectral region. Relying on the stimulated emission of photons by optical pumping, they can provide a high power monochromatic Continuous Wave (CW) emission by exploiting the molecular energy transitions of a gaseous gain medium.

Typically excited using the 10.6 μm CO_2 laser, with pump power in the order of 100 W, several specific gas lines are available throughout the terahertz range [56]. Namely, the CH_3OH methanol transition at 2.52 THz (118.8 μm) can provide a high conversion factor that enabled up to 1.25 W emission power [57]. Even though they can ensure high output power, beam quality and spectral purity, the operation of such sources does not allow much spectral tunability and remains a costly and demanding process featuring bulky systems. In order to tackle down that last limitations, progress toward tunable MIR Quantum Cascade Lasers pumping are enabling access to previously unreachable emission lines. Namely, among the IEMN laboratory, thanks so the precise tunability of such compact sources to reach resonant pumping, the 1.073 THz and 1.083 THz NH_3 ammonia lines are found to provide high optical gains under optimal pressure conditions [58, 59].

- Quantum Cascade Lasers

Originally scaled from optical technologies, demonstrated in 1994, in the IR domain [60], down to the high frequency terahertz spectrum in 2002 [61], Quantum Cascade Lasers (QCLs) are semiconductor lasers which exploit intersubband electronic transitions for terahertz emission. This point is the main distinction with respect to the common IR and visible semiconductor laser diodes that exploits the material related energy gap between conduction and valence band. The energy level differences at stake in the conduction intersubband transitions are finely tunable providing a proper engineering capability for the quantum well structure design. This gap engineering can ensure a controlled electron relaxation that will be paired with the emission of a photon and allows QCLs operations from 2 to 5 THz.

As depicted in Figure I.6, this radiation is obtained under a static biasing of the quantum well structure and given a proper population inversion, ensured by adequate life-times for each energy levels ($\tau_H >> \tau_L$ where τ_H [s] and τ_L [s] are the life time of the high and low energy levels respectively). This last point is guaranteed by the fast extraction of the relaxed electron that can be performed through several process such as an optical phonon interaction towards an intermediate band. Following this extraction, electrons can then be fed into a similar quantum well structure via quantum tunneling through an injection barrier. This process can be repeated a number of times that is equal to the number of stacked active heterostructures, giving rise to the denomination Quantum Cascade Laser. A single electron will then lead to the emission of N photons, for a quantum efficiency greater than unity, N being the number of periodic structures within the laser. This active heterostructure is then confined in a waveguide cavity, either in a metal-metal configuration or through a single plasmon waveguide, to ensure output beam shaping as well as laser resonance by reinjecting photons into the gain media.

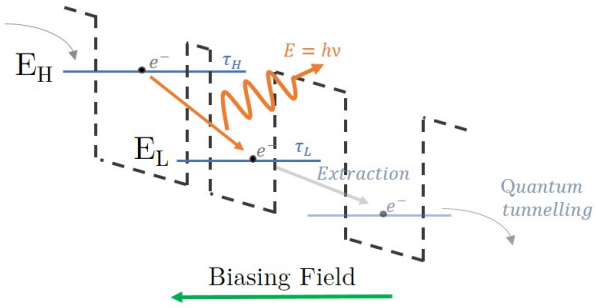

Figure I.6: Operating principle of QCLs.

Such devices nevertheless require cryogenic cooling (< 77 K) for efficient operation and high output power stabilization, therefore mostly restricting their use to cryogenic equipped structures. Several commercially available solutions have been developed over the last decade with Longwave photonics [63] and Lytid [62]. In order to overcome this complexified implementation, Lytid has been working towards turning this quantum technology into a suitable tool within reach of industry and academia. This solution, with the TeraCascade1000 product line, incorporates a Stirling engine based cooling unit and dedicated driving electronics to reach a high performance, ultra-compact, cryogenic-free cooling, QCL source with mW output power levels [62].

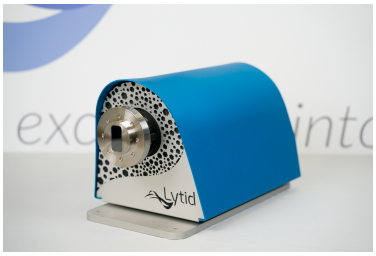

Figure I.7: TC2000 mW-level multi-frequencies QCL source developed by Lytid in a compact and criogenic free system [62].

- Solid-state electronic sources

In contrast with photonics inherited technologies, micro-waves electronic technologies, on the other side of the electromagnetic spectrum, pushed their technological advances towards higher frequencies up to the terahertz spectral range as well. Often referred as electronic sources, those solid state components are based on the use of various semiconductor diodes and transistors architectural behaviors. Those CW emission source technologies can be split in 2 main families [64] : power amplifiers or oscillators using negative differential resistance effect in transistors, and frequency multipliers through the non-linearity induced harmonics generation.

In the aforementioned first category, several physical behaviors have been deployed. Among those, IMPATT diodes (Impact Avalanche and Transit Time diode) exploit the avalanche outbreak in p-n junctions under high biasing conditions. They are recognized for their high power emission capabilities, with an emission power in the order of ten mW at 300 GHz and sub-mW levels above, with a $\sim f^{-2}$ power evolution [65–67]. With such attributes, this technology has been successfully adopted as an efficient high power sub-millimeter commercially available source [68]. Equally

interesting for high power emissions, Gunn diodes can be used as oscillators through the static biasing of the negative differential resistance region, with resulting emitted power levels around 100 mW at 100 GHz, varying with the employed semiconductor technology [69]. Other architectures, such as HEMTs (High-Electron-Mobility Transistor) and HBTs (Heterojunction Bipolar Transistor) can be integrated as oscillators, as their counterparts remain limited in term of noise figures and operation frequency. Targeting higher frequencies, TRDs (Resonant-Tunneling Diodes), and TUNNETT diodes (Tunnel Injection Transit Time Negative Resistance diodes) represent convincing candidates for high frequency operations even though, only µW-levels are achievable above 1 THz [70–72].

Contrary to the direct generation operated by the aforementioned technologies, frequency multiplication chains, are based on the sequential up-conversion of a signal derived from a low frequency synthesizer through frequency multiplier stages to reach the desired spectral band. Mainly implemented through planar Schottky diode designs [19, 73], this frequency conversion is guaranteed via the use of low order harmonics generations by the non-linearity of those non-symmetrical devices. To reach an optimized power transfer, a challenging harmonics handling is required to minimize unwanted frequencies generation and to enhance the desired one. As displayed in Figure I.8, this is performed through the integration of the active Schottky-based device among a rigorously designed waveguide block structure.

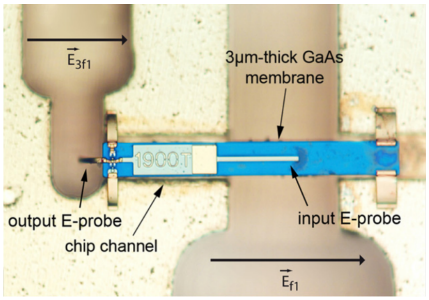

(a)

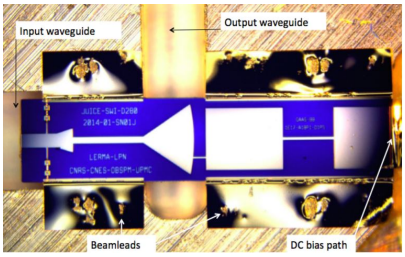

(b)

Figure I.8: Typical waveguide integration of a Schotty based frequency trippler at 1.9 THz [19], and a 600 GHz frequency doubler for the JUICE mission [74].

Supported by Space programs such as the Herschel HIFI [75] or the JUICE [74, 76] programs, a drastic improvement of GaAs Schottky diode capabilities have been witnessed in the past few years. Thanks to the simple geometry of those components and so, the simplified miniaturization of the frequency coupling membrane, it enabled emissions up to 1.9 THz [77–80]. Such a harmonic generation nevertheless induces ineluctable conversion losses in Schottky devices, leading to decreasing the achievable emission power with respect to the operation frequencies due to the increasing number of multiplication stages [81]. Essentially, power levels ranging from typically several hundreds of mW around 100 GHz, down to µW levels above 1.5 THz can be expected. Promising development using Gallium Nitride, GaN, technologies are targeting enhanced output powers to bridge the resilient "terahertz gap" [81–83].

A non-negligible aspect of those architecture remains the tunability of typically 15 to 20 % that can be achieved with respect to the central frequency. It then allow the coverage of most of the considered WR (Rectangular Waveguide) waveguide bands. This frequency multiplication chain architecture leads to a certain adaptability of the sources and, combined with the high achievable emission power, has led to the development of commercially available solutions. Nowadays, their are multiple providers, such as VDI [84], ACST [85] or Lytid [62]. The latest provides a fuly integrated TeraSchottky product line.

Figure I.9: Compact 600 GHz Teraschottky source, developed by Lytid featuring the cascaded multiplication chain [62] .

Similar integrated electronics components are available using Silicon-based or Monolithic Microwave Integrated Circuit (MMIC) based sources using CMOS (Complementary metal oxide semiconductor), or BiCMOS (Bipolar-CMOS) technologies when targeting frequencies over 300 GHz. Such solutions often provide extreme miniaturization capabilities and production scalability but still face substantial limitations. Namely, for high frequency transpositions, drastic limitations are witnessed in term of available emission power [86] with for example the -15 dBm emission provided by the developments of a 840 GHz source [87]. A 0 dBm, 530 GHz source has nevertheless been demonstrated [88], implemented as a combination of a multitude of pixel subsourses emitting -12 dBm each based on HBT geometries with a bandwidth caped to 3 GHz, hence less than 1%. Recent developments toward higher frequencies featured varactor frequency multipliers with a demonstrations up to 1.4 THz [89]. Beside their reduced achievable bandwidth and limited available emission power when considering high frequency transpositions in the sub-millimeter spectral range, they nevertheless provide unrivaled integration capabilities for the generation of array geometries or for compact detection solutions.

I.3.2 Terahertz detectors, sensing units and components

Similarly to the range of available physical principles that can lead to terahertz emissions, a variety of technological choices are reachable for the sensing of terahertz radiations [17, 90].

Already discussed in section I.3.1, broadband time-resolved pulsed sensing systems, implemented through the use of PCAs, will not be further detailed in this section.

- Empirical single-point detection approaches

At first glance, we can distinguish between incoherent and coherent, sensing. For the latest, an amplitude and phase information of the electric field is retrieved, while for the first, only the illumination field amplitude or power level is assessed.

In this first category, several physical processes can be highlighted. Notably, thermal-electrical conversion sensors represent an essential portion of the available solutions. Historically, introduced in 1947 [92], the Golay cell is based on the optical probing of a gas expansion under thermal effects [93]. A Quasi Continuous Wave (QCW) terahertz illumination is shined on an entrance facet of a gas filled container, covered by an absorbing coating. The generated heat will induce an expansion of this gas and will therefore bend the mirror coated probing face of the container, as displayed in Figure I.10. This bending is proportional to the input terahertz power. As the gas expands, an optical readout system probes the deflection of a beam reflected on this metallic face, through the use of a photo-diode for electrical signal conversion. The broadband spectral sensitivity is ensured by the broad absorption profile of the coating, and such detectors usually features sensitivity in the order of several kV/W with a Noise Equivalent Power (NEP) around $\sim 10^{-10}\mathrm{W}/\sqrt{\mathrm{Hz}}$. Be that as it may, due to the slow thermal process at stake, response times in the order tens of millisecond to several seconds are expected allowing modulation operation frequencies below 20 Hz. A high susceptibility to external perturbations such as IR illuminations, mechanical vibrations or air flows are also to be considered for practical implementations.

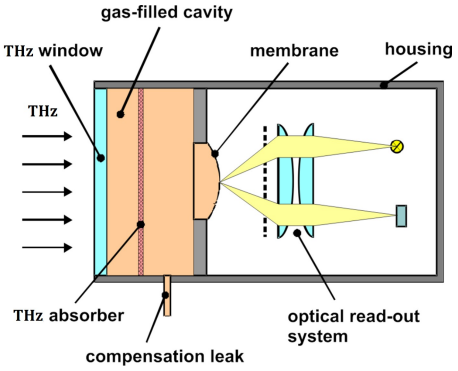

Figure I.10: Principle diagram of a Golay cell [91].

Similarly inherited from initial IR developments down to the terahertz and millimeter-wave spectrum, pyroelectric detectors are using the ability of certain crystalline materials to induce an electrical polarization when under changing temperature conditions. Coated in a terahertz absorbing material, typically carbon based absorber layers [94], in a similar way as the Golay cell,

and therefore procuring a broadband sensing capability, the absorption of an incoming QCW terahertz input power will induce a heat transfer to the pyroelectric crystal, resulting in the modification of its electrical response. With a limited parasitic capacitance and so the limited RC time response, such detectors feature operating frequencies up to several hundreds of Hz with a typical responsivity up to few kV/W with NEP levels below 10^{-9} W/$\sqrt{\text{Hz}}$. Another more recent geometry of pyroelectric detectors calls on the use of semi-metallic transparent sheets that features 50% power absorption and 25% power reflection and transmission [95, 96]. This semi-transparent sheet acts as intermediate component for heat absorption as well as a proper heat conduction channel towards the pyroelectric material. Such sensors, in addition to their large achievable active area, have the ability of showcasing an extremely flat response over a bandwidth spanning from 300 GHz to 30 THz. This allows for a simplified calibration of its sensitivity, typically in the order of 100 V/W with standard operating frequencies below 100 Hz for commercially available solutions from SLT [97].

More recently, and derived from IR sensors and focal plan array sensors, bolometric detectors have also been employed as thermal terahertz sensors. As an operation principle, a resistive thermometer is weakly coupled to a thermal ground. Coated with an absorber, this thermometer will see its temperature rise with respect to the heat sink under the absorption of an incoming illumination. A sensing of this temperature variation is then ensured by monitoring the resistance of the thermistor. The thermal conductivity of the weak thermal link, with respect to the thermal capacitance of the thermometer, will impact the response time of such detectors, that often feature operating frequencies around 100 Hz and NEP in the order of $\sim 10^{-10} - 10^{-11}$ W/$\sqrt{\text{Hz}}$ [98].

Figure I.11: Typical integration of a cryo-cooled bolometer [99].

Unlike its analogue thermal detectors, due to the non-transient nature of its response, it features the capability of working in Continuous Wave (CW) mode. Thanks to their eased array implementation, further details on such sensors are considered later in this work through their integration in focal plan array sensors for real-time full field imaging. Obviously, since they are based on thermal resistivity evolution, the thermal noise impact is of crucial importance. Cryo-cooled bolometers therefore feature orders of magnitude improvements in term of sensitivity and NEP, that can be reduced down to $\sim 10^{-12} - 10^{-13}$ W/$\sqrt{\text{Hz}}$. Nevertheless, these will require dedicated facilities with cryo-cooling as depicted in Figure I.11. Similarly, Hot Electron Bolometers (HEB), ensure similar NEP and sensitivity levels as cooled bolometers but allow much higher working frequencies [100] but will not be further detailed in this work.

Beside thermal based sensors that enable an extremely broadband detection over the whole THz range, electronic sensing solutions have been inherited from the frequency up-scaling of millimeter-wave technologies with HEMT (High-Electron-Mobility Transistor) sensors [101] or direct extrinsic semi-conductor sensors. In this work, we will mainly focus on Schottky-based solutions, that offer a spectrally universal sensing solution. Additionally, details on Field Effect Transistors (FET), that can successfully be transposed and integrated among array structures for full-field imaging, will be provided.

On a wide sub-millimeter wave spectral range, Schottky diodes offer a convenient incoherent sensing solution through the optical rectification process thanks to the high non-linearity response of those devices. Typically implemented as zero-bias sensors, operating frequencies in the order of several tens of gigahertz are achievable with sensitivities of several kV/W and NEP in the range of $\sim 10^{-9}$ W/$\sqrt{\text{Hz}}$ [102], when waveguide embedded. Quasi-optical sensing is also achievable and ensures a much larger spectral detection capabilities [103, 104] when removing the waveguide bandwidth limitations.

Considering transistor geometries, beside their marginal terahertz emission capabilities, FET transistors display efficient sensing potential [105] through the similar non-linear RF (Radio Fre-

quency) optical rectification of the current induced by an incoming illumination. Scaling the geometry of such a device to reach sub-micron transistor channel will enable detection up to the terahertz regime while remaining efficient at room temperature. Typical NEP in the order of $\sim 10^{-11}$ W/$\sqrt{\text{Hz}}$ are achievable [106, 107]. Used in such direct detection schemes, those electronic sensing solutions can ensure low power consumption up to power harvesting capabilities thanks to their static-biasing or zero-bias designs.

A special attention has been brought to those two specific components since beside their demonstrated array implementation, they can be integrated as coherent sensing devices for enhanced performances [73]. Initially derived from space sensing methods or astronomy [21] and now widely used for highly sensitive detection schemes, heterodyne and homodyne detection are executed by providing a Local Oscillator (LO) for detection through the down conversion towards a frequency window with direct sampling capability (typically 0.001-20 GHz). The non-linearity of the mixing unit is used for combining the probing LO and the sensed signal, equivalent to a multiplication operation. Such an operation can be performed with the LO within the same frequency range as the probed signal (for direct mixing), or considering harmonics or sub-harmonics LO for harmonic mixing operations. Once high frequency components (frequency sum) are filtered out, the down converted low frequency components (frequency difference) are retrieved and provide coherent sensing with a phase and amplitude information. Obviously, establishing such coherent detection scheme is much more demanding than direct zero-bias sensing mechanism, but will typically lead to enhanced sensing capabilities by at least several orders of magnitude. This performance improvement nevertheless especially relies on the stability of the provided LO. Commonly, the use of Schottky diodes, in anti-parallel paired placement (see Figure I.12), is the most widespread solution, that allows low conversion losses and room temperature operation. Of interest for this work, such a detection scheme represents the main sensing technological brick of FMCW radars via the implementation of a mixer unit as detailed in section I.4.

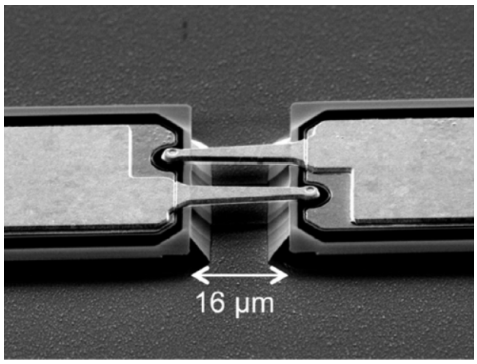

Figure I.12: SEM image of a pair of anti-parallel Schottky diodes for frequency mixing operation [73].

With the aim of overcoming, sensitivity, speed, operation temperature and spectral range limitations from existing terahertz sensors, additional current works are focusing on the development of advanced direct sensing scheme. Namely, a graphene sensor featured a NEP level of $\sim 80\ 10^{-12}$ W/$\sqrt{\text{Hz}}$ at room temperature with operational frequencies up to 30 MHz in the 1.8-4.25 THz spectral region with a responsivity level of 32 V/W [108]. Further innovations approaches are witnessed such as the THOR project [109] that aims to use molecular vibrational activity as an optomechanics sensing solution.

- Focal plane arrays

Nevertheless, when it comes to inspection problematics, the scanning rate represents a major criterion for industrial and inline integration. Hence, single point sensing remains limited to keep up and sustain large area inspections. With this in mind, addressing real-time sensing with imaging capabilities, latest developments lead to the integration of high end focal plane array sensors through different technologies. Valuable in this work concerning imaging thematic, this sub-

section will detail several available solutions. A review of some available focal plane arrays and camera sensors is provided in [110].

As a first approach, the reminiscent sensitivity of several LWIR cameras can be easily exploited and allows for low cost and compact solutions to emerge [111]. Providing minor optimizations such as the replacement of the protection window material, a direct transposition of those technologies can be considered. This would lead to a limited sensor size and sensitivity levels, adequate for beam profiling and optical alignment purposes. Nevertheless, the reduced average illumination power, coupled to the non-optimized sensitivity in this spectral window limits their capabilities when it comes to full-field imaging. One could as well question the usually small pixel pitch for spatial sampling with respect to the achievable resolutions in the terahertz range. A variety of solutions are available on the market with SwissTHz Rigi camera [112] or Xenics Gobi camera [113], amongst others. Similarly, pyroelectric-based sensor arrays, remain applicable in this spectral range.

On the other hand, resulting from specific development in the terahertz spectral range and targeting the upper part of the frequency spectrum, uncooled microbolometer cameras have emerged about 10 years ago with INO [114] [115, 116]. Based on a Vanadium oxide microbolometers, the INO IRXCAM provides pixel pitch of 35 µm with a 288×384 pixel matrix integration and allows camera frame rate up to 50 FPS (Frame Per Second). With their latest version, MICROXCAM-384I-THZ, (see Figure I.13b) higher sensitivity levels have been obtained.

Based on similar microbolometer technologies, using amorphous Silicon and coupling antennas, CEA Leti developed a sensor array [110, 117, 118] featuring a 320 × 240 pixels geometry with 50 µm pitch, working at 25 FPS and a minimum detectable power of 30 pW. This solution, extensively investigated in [37], is integrated and commercialized by I2S [119] (see Figure I.13a) with the TZCAM product-line. Thanks to the bow tie antenna design, and the two induced coupling mechanisms, two sensitivity peaks can be witnessed, with one typically centered around 2.5 THz and one at lower frequencies typically around 800 GHz.

Focusing on the lower part of the spectrum, electronic sensor arrays have also been developed and mainly implement through the aforementioned FET technology. Several commercially available solutions offer a variety of geometries, with for example the GaAs FET cameras and scanners offered by Terasense [68] (see Figure I.13c) (16×16 - 34×34 - 64×64 - 256×1 array with 1.5 mm pitch). It offers sensitivity up to 1 THz with a NEP of $\sim 10^{-9}$ W/$\sqrt{\text{Hz}}$. The TicMOS-1kpx camera from Ticwave [120] features its 32x32 array and NEP of $\sim 10^{-10}$ W/$\sqrt{\text{Hz}}$, or more recently with Ti-Hive Necter product line [121], with sensors operating around 300 and 840 GHz.

(a) **(b)** **(c)**

Figure I.13: Selection of commercially available imagers, with high frequencies solutions **(a)** I2S bolometric camera and **(b)** INO bolometric camera as well as a sub-millimetric solution with the **(c)** Terasens FET camera.

- Components and system oriented devices

Targeting system level investigations and developments, in addition of the available sources and detectors, those two elements have to be backed by several suitable components. The democratization and outburst of terahertz related projects lead to drastic improvements in term

of technological maturity for those intermediate parts. More precisely, optical (or quasi-optical for millimeter wave) elements, such as lenses, beam-splitters, polarizers, waveguides [122], and others, had to be adjusted to the wavelength range. As an example, polarizers are mainly implemented through unidirectional wire grid under tension or coated on transparent substrates. Several technologies of waveguides have also been investigated [123] with the goal of loss minimization mainly through air-core waveguides with different cladding structures (simple hollow-core waveguides [124, 125], metal-coated dielectric waveguides [126] or photonic crystal hollow-core waveguides10.1109/IRMMW-THz50926.2021.9566853[127]).

For beam shaping components, beside the spectral universality of mirrors, specific materials have to be considered for lenses. Namely, polymer lenses are used and offer low cost solutions with materials such as Topaz or Zeonex as well as PTFE (Polytetrafluoroethylene) or HDPE (High-density polyethylene), the last two being especially suitable for low frequencies applications. As a high-end solution, HRFZ-Si (>10 KOhm/cm) features a constant refractive index of $n = 3.42$ with anecdotal absorbance over the whole terahertz range, making it extremely suitable for high frequency or broadband systems.

Its large refractive index nevertheless induces non-negligible interface reflection losses that can be minimized by fine tuning an anti-reflective coating. To mitigate those reflection power losses, its thickness and respective optimum refractive index should be consistent with the following relations to generate a destructive reflection interference in the case of a normal incidence angle (See Figure I.14) :

$$n_1 = \sqrt{n_0 n_s}\ and,\ e = \frac{\lambda_0}{4n_1}, \tag{I.4}$$

With e, the coating thickness $[m]$, λ, the wavelength of the incident beam $[m]$, n_0, n_1, n_s, the refractive indices of the propagation media, the coating material and the substrate respectively.

In the case of HRFZ-Si, Parylene represents one of the best candidate to generate sustainable coated thicknesses up to several hundreds of µm with a well suited refractive index. An example of custom dedicated optics will be further covered in section II.3 with details on the design of a high aperture camera lens, for real-time imaging purposes using micro-bolometers arrays.

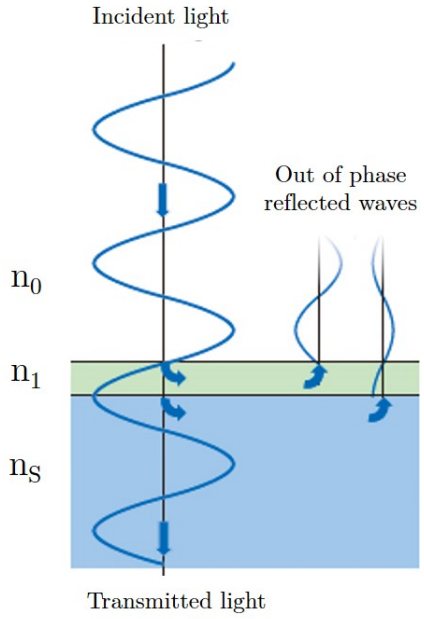

Figure I.14: Anti-reflective coating mode of operation.

I.3.3 Application fields

The latest developments of the aforementioned technologies have been driven by an increasing number of terahertz related research projects over the last 30 years.

Due to the non-negligible delay witnessed in this field, in comparison with the adjacent portions of the electromagnetic spectrum, its use remains limited to high-end targeted, applications because of the consequent developments required to reach mature solutions. Even-though feasibility is demonstrated, and achievable performances are in adequacy with the current requirements, the absence of an open market, that would enable large scale production, limits the available solutions to high-price systems. Hence, this allows marginal competitiveness with the well-established techniques for classical issues. Nonetheless, with the current growing interest in terahertz technologies, a non-exhaustive review of applicative implementations can be drawn in various fields when targeting niche challenges [21].

Specifically, in the pharmaceutical, biomedical and healthcare fields, a variety of problematic are currently assessed from chemical spectroscopic discrimination [128], gas spectroscopy [129]

(thanks to the predictable absorbance lines of certain chemical compounds) to biological studies [130, 131] and cancer sensing [47, 132] (through the high interaction of terahertz radiations with water), among many others. More broadly, terahertz brings forward several alternatives to the well-established sensing techniques, in the agrifood industry [133], up to artwork and cultural heritage inspection with pigment identification through spectral analysis [134], or 2D imaging for artifact detection, inspection and authentication [135–137].

With security topics [138] and advanced wireless communications [139], NDT represents as well a major participant in the development of terahertz technologies due to the numerous unresolved issues endured by the actors of these fast growing industries [140, 141]. Several topics are actively under investigation. Among those, multi-layer thickness sensing in stacked paint coatings [142, 143] is the perfect example of a niche application in automotive and aerospace industries, where only broadband TDS technology provides the ability to deliver individual layers parameters through contactless sensing, with precision down to the micron level. To another extend, lower frequency systems provide thickness measurements abilities using FMCW radars [144] for dimensions below their longitudinal resolutions and will be extensively explored in section IV.4. Terahertz inspection in aerospace and automotive industries fulfills the growing demand in penetrating inspection and imaging for fault detections or material degradations. The latest mainly calls on the use of FMCW radars and will therefore be further detailed in section I.4.4.

I.4 FMCW Radar

The high potential of millimeter-wave Frequency Modulated Continuous Wave (FMCW) Radar technology towards NDT problematics has been one of the driving forces for this work. A deepened study of this concept is done in this section, with a global depiction of the working principle and typical architectures for those systems. A review of the existing available technologies is performed and complemented with the current state of ensued applications.

I.4.1 FMCW basic principle

Although those implementations remain quite recent in the sub-terahertz range, FMCW emissions have been extensively exploited in the lower frequency ranges for decades for low resolution, long range detection purposes. Such technologies are based on coherent detection through signal mixing in a homodyne configuration [145]. Unlike static homodyne detection scheme that enables extremely sensitive detection with the use of a fixed frequency LO, both for probing and down-conversion purposes, FMCW mode of operation exhibits additional detection features through the use of a frequency sweep as a sensing signal. This continuously emitted cyclic frequency modulation, depicted as a simplified temporal signal in Figure I.15a, usually follows a linear saw-tooth or triangular profile as showed with the plain line frequency profile S_{probe} in Figure I.15b. Where S_{probe} represents the emitted frequency as a function of time, to allow range sensing through its coherent detection scheme.

As a first stage, the generation of this sweep is, in most cases, ensured by the use of a Voltage-Controlled Oscillator (VCO) from which a varying voltage command, $V(t)$ [V], results in the generation of the related frequency modulation. An eventual frequency up-conversion to the desired frequency band can be performed through frequency multiplication chains as depicted in Figure I.18, in the diagram of a simplified typical architecture. The frequency profile then follows $f(t)$ as:

$$f(t) = f_{min} + \frac{\mathrm{BW}}{\mathrm{T}_s} t, \tag{I.5}$$

with f_{min} [Hz] the lowest limit of the frequency sweep, BW the accessible frequency bandwidth [Hz] and T_s the sweep time span [s].

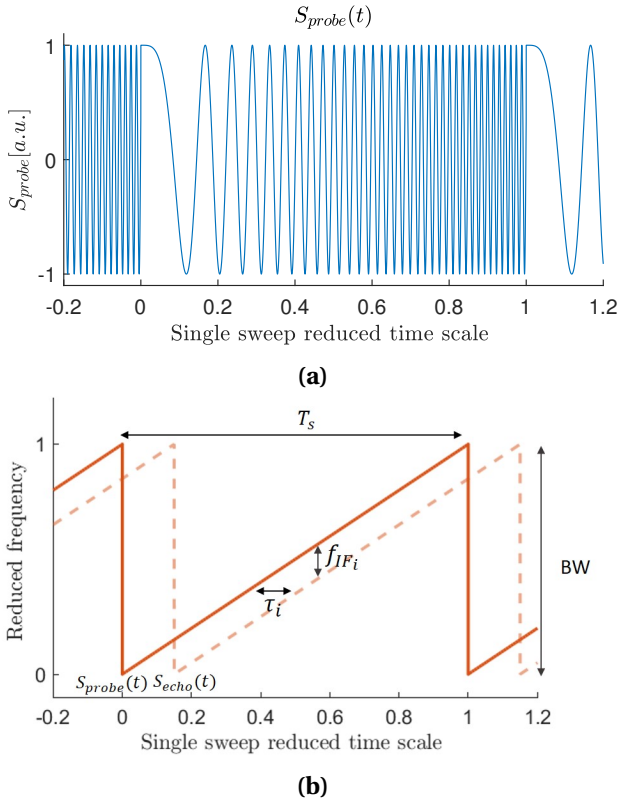

Figure I.15: (a) Simplified temporal representation of an emitted probing frequency chirp and **(b)**, relative frequency temporal profile for the emitted signal S_{probe} (plain line) and delayed collected return signal in the case of a single target S_{echo} (dashed line).

This time dependent modulation then leads, through the integration of the standing phase, to the following simplified analytical emitted electromagnetic chirped signal with unitary amplitude [145]:

$$\widetilde{S}_{probe}(t) = e^{i2\pi f_{min} t + i\pi \frac{BW}{T_s} t^2 + i2\pi\phi_0}, \tag{I.6}$$

with ϕ_0 the static phase of the emitted electromagnetic signal $[rad]$. The tilde denotes the consideration of analytical signals for the FMCW principle model, with respect to the experimental signals, devoided of such tilde notation.

This signal will then undergo free-space propagation towards a still target where a portion of it will be reflected towards the transceiver. This back and forth propagation will induce a delay $\tau_i = \frac{2nd_i}{c_o}$ $[s]$, with n the refractive index of the propagation media, d_i the path distance towards the considered target $[m]$ and c_o the speed of light in vacuum $[m.s^{-1}]$.

With this propagation induced time delay, the collected echoed analytical signal, can then be expressed as follows:

$$\widetilde{S}_{echo}(t) = \sum_{i=1}^{p} r_i \widetilde{S}_{probe}(t-\tau_i) = \sum_{i=1}^{p} r_i e^{i2\pi f_{min}(t-\tau_i) + i\pi \frac{BW}{T_s}(t-\tau_i)^2 + i2\pi\phi_0}, \tag{I.7}$$

with p the total number of targets, and i considered target, r_i [a.u.] the relative amplitude of each collected reflected contribution.

This signal reception can classically be performed through two geometries with either a bi-static or a mono-static transceiver configuration. They respectively either make use of distinct transmission (TX) and collection (RX) related antennas, hence requiring a partition between the emitting chain and receiving unit, or through a single antenna, purposed for both TX/RX tasks. The later requires the use of an additional unidirectional coupler to retrieve the echoed signal.

Considering high frequencies applications, a direct sampling detection remains impracticable. As an indirect detection mechanism, FMCW radar applies homodyne mixing down-conversion

through the use of a mixer unit. This principle, that offers high dynamic range sensing, is depicted in Figure I.16 in the case of a bi-static and mono-static transceivers. To do so, the S_{probe} reference emission chirp is fed as the LO to the mixing unit where a multiplication with the echoed return signal S_{echo} can be performed as follows: $\widetilde{S}_{IF}(t) = \widetilde{S}_{probe}(t)\widetilde{S}^{*}_{echo}(t)$ [146].

This homodyne down conversion is performed thanks to the use of highly non-linear devices, based in most cases, on a balanced Schottky diode mixer. Several mixing scheme are available with fundamental mixers, where the RF and LO components are in the same frequency band, and harmonic mixers, (HM) or sub-harmonic mixers, (SHM), where the LO is provided at a sub-multiple frequency band with respect to the RF probed signal. In order to extract only the low frequency, down-converted, components $S_{IF}(t)$, a passive filtering of the LO and RF input signals is performed, then considering the operation as double balanced mixing.

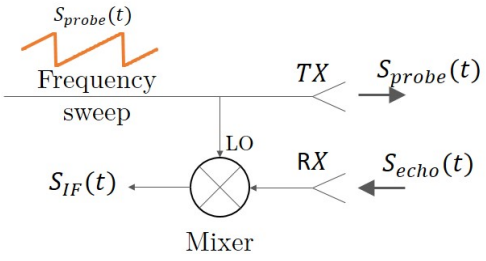

(a)

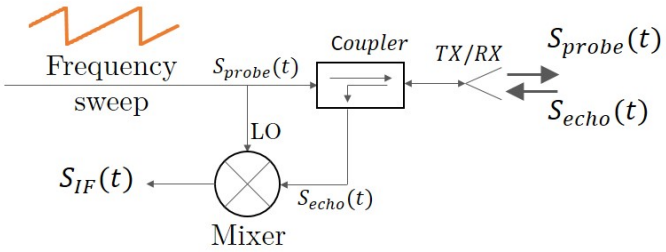

(b)

Figure I.16: Schematic of the homodyne down-conversion, through frequency mixing in the case of : **(a)** a bi-static transceiver, **(b)** a mono-static transceiver with the additional integration of an unidirectional coupler.

The resulting beating analytical signal, $\widetilde{S}_{IF}(t)$, can therefore be expressed as:

$$\widetilde{S}_{IF}(t) = \sum_{i=1}^{p} r_i e^{i2\pi f_{min}\tau_i + i\pi\frac{BW}{T_s}(2t\tau_i - \tau_i^2)} \approx \sum_{i=1}^{p} r_i e^{i2\pi(f_{min}\tau_i + \frac{BW}{T_s}\tau_i t)}. \tag{I.8}$$

The latest approximation can be performed since the high order term τ_i^2 remains negligible with respect to the other terms.

In-fine, this signal presents a static phase $f_{min}\tau_i$ when considering a motionless target, and more importantly, a beating signal at the intermediate frequency f_{IF_i} [Hz], directly linked to the propagation delay, and so to the distance to the target :

$$f_{IF_i} = \frac{BW}{T_s}\tau_i. \tag{I.9}$$

This relation is as well graphically depicted on Figure I.15b when considering the frequency sweep rate.

In the case where multiple targets are involved, modeled through the $\sum_{i=1}^{p}$ within the aforementioned Equation sets I.7 and I.8, each object contributes as a given distance-related beating frequency f_{IF_i}. This will allow for the differentiation and remoteness sensing through accessible

data processing steps in the frequency domain. In the case of a moving target, a Doppler effect frequency shift has to be considered in addition to the propagation induced frequency difference.

This prime FMCW sensing feature is illustrated in Figure I.17, where a simplified temporal down-converted signal $S_{IF}(t)$ is represented in Figure I.17a and contains contributions equivalent to 3 targets. An amplitude visualization in the frequency domain, in Figure I.17b, obtained through the use of the Fourier transform operation $\mathscr{F}$, then results in a typical sensed scene visualization with three distinct spectral components in the beating signal, related to each of the three targets.

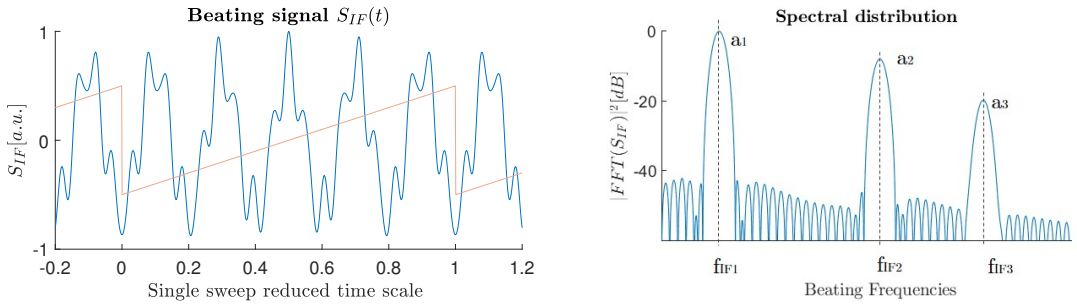

(a) **(b)**

Figure I.17: **(a)** Simplified FMCW radar beating signal representation (blue) and frequency sweep signal (red) **(b)**, relative spectral distribution featuring 3 targets.

Finally, accounting for the relation between the propagation delay and the distance to the target, the following relation can be established between the considered target position d_i $[m]$, and the beating frequency f_{IF_i} $[\mathrm{H}z]$:

$$d_i = \frac{c_o}{2n}\tau_i = \frac{c_o f_{\mathrm{IF}_i}}{2n}\frac{\mathrm{T}_s}{\mathrm{BW}}. \tag{I.10}$$

Then, considering the achievable frequency resolution of the beating signal, the range resolution can be deducted as follows:

$$\delta_d = \frac{c_o}{2n\mathrm{BW}}. \tag{I.11}$$

It is of importance to notice that this distance resolution, $\delta_d[m]$, is inversely proportional to the achievable frequency bandwidth, BW. Hence, it remains independent to the operation frequency of the radar transceiver.

Considering this operation principle with a mixing unit as the central detection stage, a classical architecture can be drawn. Figure I.18 presents a typical architecture in the case of a mono-static FMCW radar unit, therefore operating in reflection configuration. Driven by a cyclic command signal, a linear FMCW reference signal is generated at low frequency by a Voltage Control Oscillator, which is then fed into the frequency multiplication chain, for signal up-conversion, to reach the desired operating frequency band. A 3-ports coupler leads this probing signal towards the emission antenna while redirecting the reflected signal towards the mixing unit for down-conversion and sampling with the Data Acquisition (DAQ) unit.

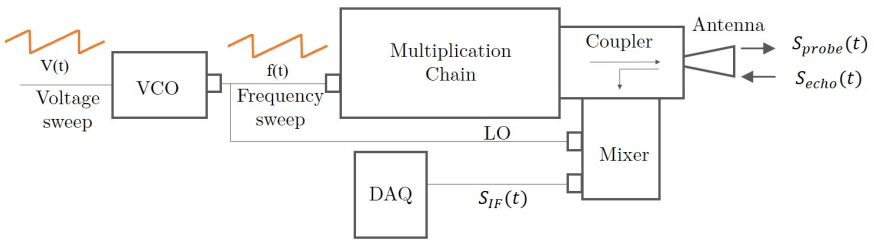

Figure I.18: Diagram of a typical mono-static radar architecture operating in reflection mode.

At last, FMCW radar mode of operation can natively provide additional phase information related to range sensing for simplified 3D reconstructions and further scene analysis. Nevertheless, as a single point sensing detector, such transceivers do not offer inherent imaging capabilities. Several mechanisms can nonetheless be implemented to reach imaging, such as with phase arrays beam steering [147], Image reconstruction through wide beam SAR [148–152] or through the use of parabolic reflectors [153, 154], and more classically through quasi-optical configurations single point sensing. Such implementation, combined with scanning approaches for full images recording, will be more precisely detailed in section III.2 and remains similar to low frequencies raster-scan CW systems addressed in section II.2.

I.4.2 Available technological implementations

Such FMCW radar mode of operations have emerged from the low frequency range of the electromagnetic spectrum [155] with their first demonstration for marine and defense threat sensing applications in the radio-frequency ranges. Ever since, technological advances brought those to the gate of the millimeter-wave domain, with two main implementations available. Si-based components will display high integration capabilities while the high performance III/V technologies will reach higher emission powers and noise figures. Both solutions are described in this section to provide a proper state of the art establishment.

Silicon based integrated radars

On one hand, Silicon-based radar transceivers are already quite popular and widespread solutions amongst some applicative industrial fields. They found usefulness for object-sensing ,such as in the automotive industry, for tank level monitoring, or in automation and precision position monitoring for micro-mechanic industrial applications, as well as for imaging or gesture recognition purposes. Those user cases have been enabled thanks to the reliability of those components in harsh environmental conditions. Their implementation simplicity as well as their versatility, hence make them highly adaptable tools.

The main benefits of those technologies come from their implementation convenience, with the compactness and very low power consumption of those miniaturized devices. Indeed, in most cases, a fully integrated Silicon based radar architecture is designed as an MMIC and processed on a few mm^2 chip to be integrated afterward on a small size processing PCB (Printed Circuit Board). This will then enable a simplified handling for its end-users. Low-cost devices derived from mass production can then be considered for standard architecture, such as the ones that typically exists in the 24 GHz and 77 GHz bands in the automotive industry [156] and for object detection problematics. They typically feature a bandwidth of 1 to few GHz (typ. 1 to 4 GHz up to 10 GHz) and a bi-static geometry (from the integration point of view) with two distinct antennas. Those are respectively coupled to a transmitter and receiving circuit unit.

Centered around 77 GHz [156], few references of those systems have already reached mass market production scale, thanks to automotive implementations such as the radars units Bosch LRR3, Conti ARS 300 or Denso DNMWR004. They offer a variety of performances, in term of maximum detection range that varies from 150 to 250 m, in term of field of view, from 30° to 60° and different beam steering techniques for similar compactness levels.

Thanks to their significantly lower development costs and design requirements, lower frequencies radars, such as in the 24 GHz band [157], have also been found suitable for automotive applications for about 10 years. They nevertheless remain less convenient when it comes to their integration due to the combination of the necessarily higher antennas dimensions, and so the related reduced compactness, as well as the lower resolution achieved amongst this wavelength range.

In order to target smaller antennas and components miniaturization, for simpler integration, and larger bandwidths, for better resolutions, higher frequency bands FMCW radars are being developed. This evolution has been allowed by the quite recent down-scale of SiGe transistors, enabling to reach operation frequencies around 300 GHz, for challenging designs at frequencies

up to 250 GHz. As an example of this market evolution, the fully integrated millimeter-wave SiGe based radar, sweeping in-between 121 and 127 GHz, marketed by Silicon radar GmbH, is one of the only commercially available component above 100 GHz with such a high level of integration (see Figure I.19). Its architecture have been developed within the European SUCCESS project (Silicon-based Ultra Compact Cost-Efficient System Design for millimeter-wave Sensors SUCCESS). The full structure of this design is developed in [158–160] where its different stages are introduced as follow: on the transmitter side, the VCO delivers a 60 GHz signal (also used as the LO signal for the sub-harmonic mixer), followed by a frequency doubler as well as an amplifier in order to deliver at least 0 dBm output signal in the 120 GHz band. On the receiver side, a Low Noise Amplifier (LNA) is cascaded with the sub-harmonic mixer, a polyphase filter and the VCO LO. On similar bases when it comes to technical criterion, 2π-LABS GmbH is working towards the distribution of a compact integrated unit in a slightly higher frequency range, featuring a broader frequency bandwidth (140 GHz - 170 GHz).

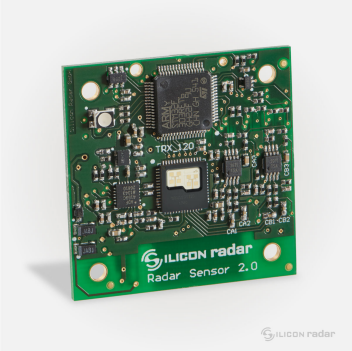

(a)

(b)

Figure I.19: (a) Silicon-radar transciever at 122 GHz on a 4 cm×4 cm PCB integration and **(b)** related radar-chip front-end featuring RX/TX patch antennas and a FMCW radar MMIC on a 7.5 mm×7.5 mm packaging [160].

Beyond those standard architectures, the highly integrated character of Silicon-based radar transceivers induces a strong development effort to reach a fully functional, optimized chip and leads to very expensive components for small series at first. Indeed, those radar architectures require a very time consuming development for every stage (VCOs, frequency multipliers, harmonic and sub-harmonic mixers, LNAs or Antennas) in order for them to be considered for full integration on PCBs and reach the final implementation stages for industrial applications. For example, following the developments of the aforementioned 122 GHz Silicon Radar GmbH solution [158–160], 245 GHz band components such as LNA [161], sub-harmonic mixer [162] and more broadly a transmitter [163, 164] and the receiver [162] are under development. Nevertheless, those elements might still require resources to reach maturity for their implementation as a monolithic, compact FMCW radar unit or to be in adequacy with the industrial market.

A multitude of other, less common radars, are being developed but have not reached the industrial market yet, such as the one introduced in [165], working around 140 GHz. Using the same typical architecture and SiGe BiCMOS technological advances allowing applications above 100 GHz, this 0.9 mm x 1.6 mm chip enables a bandwidth of 6 GHz for an emitted power of -8 dBm. Alternatively, the 80 GHz FMCW radar described in [166], used for implementation as a positioning tool for micro-machining [167], offers a 10 GHz bandwidth, for a 0.5 µm positioning accuracy. A bi-static imaging radar chip, working around 170 GHz with a 28 GHz bandwidth, described in [168], is another example in the multitude of such devices that could suit imaging and sensing applications, depending on the requirements and constraints.

High performances III/V radars

On the other hand, GaAs, GaN and InP technologies are quite often preferred for signal generation and noise figures in comparison with Si-based solutions. Adressing the same application fields, III/V-based MMIC radar transceivers have been developed [169] and enable a compact, low cost implementation. They represent a miniaturization solution for III/V radars use, in a certain operating range, with frequencies up to 200 GHz and limited emission powers. As an example, the Fraunhofer Institute for Applied Solid-State Physics of Frieburg processed a InAlGaAs 220 GHz (212-226 GHz) FMCW radar monolithic transceiver architecture [169, 170]. This bi-static full integration contains the whole transceiver chain, from the frequency multiplying chains, LNAs, the sub-harmonic mixers, as well as the antennas on the emitter and receiver unit in order to minimize coupling losses and to reach -6 dBm emission power. It is as well mounted on a hemispherical HRFZ-Si lens in order to improve the beam directivity. A lower frequency solution [171] was also demonstrated with an InAlAs/InGaAs HEMT Technology based receiver working around 140 GHz and allowing up to 25 GHz band. Divided in two MMIC components (the VCO on one chip and the homodyne receiver on another one) this radar solution remains a suitable candidate for miniaturization and tight space implementations but only allows performances comparable to Si-based technologies.

To reach higher frequency bands (>200 GHz), larger bandwidth and higher output powers, for high-end applications targeting, III/V based radar hybrid integration is required and is performed through the implementation and fine tuning of a succession of specific separated chips, either in discrete waveguide blocks [154, 172, 173], or packaged in a single block unit [174]. These architecture solutions enable the user to choose the adequate technology for each component, from the LNA or the frequency multipliers, up to the mixer's mode of operation (fundamental, sub-harmonic or harmonic) in order to optimize its transceiver. In the currently developed solutions, thanks to the eased Schottky diodes implementation in waveguide blocks discreet design (as frequency multipliers and mixing units), frequency multipliers can generate signals at frequencies close to or higher than 1 THz [77, 78] up to 2 THz [79]. Nevertheless, in order to reach a fully functional radar transceiver, all the system's bricks need to be available and developed for this given frequency range, hence, increasing the system's cost when aiming for high frequency bands due to the more technologically demanding chip designs and developments, as well as the more demanding requirements (block mechanical machining precision, electrical supplying, *etc.*).

For high frequency radars, typical solutions have been demonstrated around 600 GHz such as the one developed amongst the Jet Propulsion Laboratory. Based on various applicative motivations, mostly from personal screening and security purposes [154, 176]. The 580 GHz band FMCW radar unit, allowing nearly 30 GHz bandwidth for almost 0.5 mW emission power [175] enabled high speed standoff screening for concealed object detection at 4 m and 25 m distance with a longitudinal resolution of approximately 5 mm. The related components working in the 520-590 GHz frequency window, also developed amongst JPL lab facilities, are described in [177] for the sub-harmonic mixer, [178] for the fundamental mixer and [179] for the frequency tripler. Another variant of this imaging radar, have been developed amongst the same group around the operation frequency of 670 GHz (662-688 GHz) [172, 180].

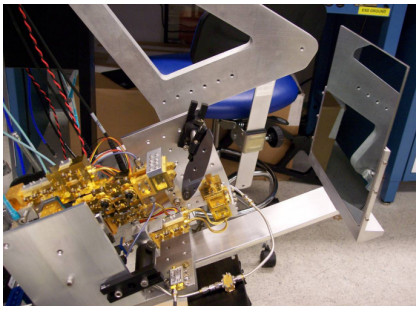

Figure I.20: 600 GHz Transmission/Reflection FMCW radar transceiver developed for concealed object detection and security screening, mounted on a scanning system [175].

A multitude of similar systems have been developed in the pursuit of the same applicative security goals in various frequency bands such as in [138, 153], where a 350 GHz transceiver emitting approximately 4 mW is used. Alternatively, compact and modular 220 GHz transceiver is described in [174, 181]. It features a 3-5 dBm output power over a 30 GHz bandwidth and a highly compact 21 mm×21 mm×33 mm design which enables multiple modules stacking and assembling to form

radar matrices.

Another system, much less documented, commercialized by Synview GmbH, and developed among the Fraunhoffer Insitute for Industrial Mathematics ITWM, was commercialized as a fully automated multi-frequency band radar scanner which allowed the user to simultaneously install up to 3 FMCW radar transceivers for reflection measurements with their paired transmission receiving head. The assessed frequency bands were centered around 100 GHz, 150 GHz, 300 GHz, 600 GHz and 850 GHz, suitable for a large variety of NDT applications. It could then suit large, absorbing samples with the lower frequency transcievers, up to fine artifacts detection and object mapping in transparent materials for higher frequencies. This system found a variety of applicative purposes and lead to significant results in the field of NDT for composite materials, especially for sensitive aeronautic parts [140, 148].

I.4.3 Millimeter-wave regulations

One of the main advantages of millimeter-wave and terahertz technologies when it comes to non-destructive testing topics, is the non-hazardous character of those radiations induced by their non-ionizing low energy levels, making them perfectly safe sensing tools. Be that as it may, this definition remains valid to some extends and tends to be challenged with the appearance of powerful sources as well as the democratization of terahertz and millimeter-wave systems. Hence, it led to a steady increase in human exposures to those electro-magnetic fields. Consequently, human safety topics are starting to emerge in synergy with the growing concerns that arise from to the democratization of such technologies which targets large publics. One can consider applications such as security screening, or with the use of high frequency telecommunication channels, with 5G deployments.

Unlike high energy radiations, considered as ionization sources, that can lead to the impairment of the intrinsic function of organs or human tissues, or low frequencies (< 10 MHz) RF fields that can induce nervous stimulations, millimeter-wave interaction with human tissue would be limited to thermal effects when high power densities are at stake [182].

Even-though infrequent, a growing number of work has been conducted when it comes to the assessment of such health risks and several studies still lack the deepening of specific body interaction phenomenon, clear experimental guidelines or did not show reproducibility yet. Among those research efforts, as part of an European initiative, the BRIDGE project initiated such technical studies [182] in 2004, while a general review study "Potential health effects of exposure to electromagnetic fields (EMF)" has been implemented by the Scientific Committee on Emerging and Newly Identified Health Risks (SCENIHR) in 2015 [183]. A recent extensively detailed survey of other existing works related to the biological effect of millimeter-waves has been conducted in [8].

Resulting as an additional difficulty, and owing to the complex nature of biological samples, terahertz and millimeter-wave expositions could give rise to a wide amount of interactions and so potential harmful processes. In addition, the physiological impact, as well as the challenging reproducibility of those surveys, are impacted by the variety of exposure parameters (frequency, peak and average power, polarization, exposure duration, *etc.*), which adds in to the complexity of the molecular composition of the targeted organisms. However, since millimeter-waves are strongly absorbed by water, a penetration depth of the order of 200 µm limits the related exposure risks to superficial skin and cornea layers. Nonetheless, through this strong absorption, an energy transfer will take place, mainly under the form of a heating effect on the exposed tissues [184].

In most cases, an accommodation of the human body to a slight temperature increase remains harmless thanks to our intrinsic heat dissipation capabilities. However, 2 mechanisms could lead to tissue damages and burns, either through pulsed high peak power exposition, where no-transient heat dissipation is possible, or when exposed to prolonged continuous radiation above a power density threshold, inducing a gradual temperature rise, and so irreversible damages. However, even with such still very active study fields, little demonstration has been made to date, that terahertz could induce toxicity, carcinogenesis or harmful effects on main biological

components.

With those estimated risks in mind, in regard to smaller wavelength illuminations, minimal regulation efforts have been pushed forth, beside extrapolated estimations from neighboring spectral regions. In the case of millimeter-wave CW sources, mainly of interest in this section, threshold levels have been set through the International Commission for Non-Ionizing Radiation Protection (ICNIRP) guidelines [185], updated in 2020 to the values displayed in Table I.1. Such guidelines have been mainly adopted by global [186, 187] and local [188, 189] standards.

Table I.1: Maximum power density guidelines for the exposition to CW millimeter-wave sources from 10 to 300 GHz as advocated by the ICNIRP **[185]**.

	Exposure Scenario	Incident power density [W.m^{-2}]
Occupational Exposure		
	Whole body, averaged over 30 min	50
	Local exposure, averaged over 6 min	100 @ 300 GHz
General Public Exposure		
	Whole body, averaged over 30 min	10
	Local exposure, averaged over 6 min	20 @ 300 GHz

Beside those power related concerns, a spectral regulation of those emission is also at stake with the delimitation of dedicated frequency bands. Such regulations apply mainly to nation-wide scale with for example the Agence Nationale des Fréquences (ANFR) for France of the Federal Communication Commission FCC in the United State. A precise band restriction below 30 GHz have been performed over the last decades but higher frequencies spectral regions regulation came more recently. Especially, industrial, scientific and medical applications are restricted to well limited ISM (Industrial, Scientific and Medical) radio bands. However, to avoid interferences with external systems those limitations can be bypassed when it comes to indoor uses, using mild-power sources, or applications that do not require broadcasting.

I.4.4 Current applications

The unique combination of longitudinal ranging sensing capabilities, material penetration, and high sensing dynamic range, granted by the use of millimeter-waves FMCW radars open access to a wide pallet of application fields.

From the historical micro-wave spectral boundary, low resolution, highly penetrating sensing have witnessed the development of several application cases, ranging from imaging problematics such as with ground penetrating sensing (typ. working frequency in the order of 1 GHz [146, 190]), through-wall inspection [191], up to long range sensing for military applications, navigation sensors, altimeters [192], weather radars [193], *etc.*

When evolving towards higher frequency bands, or equivalently, scaling down in term of wavelength, better resolution levels can be reached, larger achievable bandwidth and so better precision levels are also practicable. This will allow access to more demanding application domains with compact solutions. Especially, for precision positioning for robotics applications operating in harsh environments [167] (*e.g.* air suspended dust), millimeter-waves FMCW radars stand as suitable tools with µm range precision, where standard optical technologies would suffer from high performance degradations. With similar harsh environment preoccupations, in the aeronautic field, developments for precision short-range altimeter, as low-altitude sensor used under low visibility conditions in landing phases [194], have been witnessed for vision support.

Based on range sensing availability with increasing resolution and its capability to operation in harsh environments, another established application of higher frequencies millimeter-wave radar is found in the automobile industry, where such devices are under use for parking assistance, active cruise control, occupancy sensors, life-sign sensors and embedded target detection

sensors for autonomous vehicles. As detailed in the previous section, an evolution from the historical 24 GHz and 77 GHz sensors to higher frequencies transceivers will ensure miniaturization, higher integration and better performances in the perception of close range vehicle surroundings. Millimeter-waves SiGe radars are indeed intended to be integrated among the growing bundle of vehicle embedded sensors, especially for autonomous cars environment perception problematics, amongst video cameras, ultra-sonic transducers or LIDAR sensors. In this work, the adopted technological choices of III/V based radar, will not address this market, as cheaper and more integrated SiGe-based technologies have emerged from established foundries and actors such as NXP, Infineon, STMicroelectronics or Silicon Radar GmbH.

Beside simple range sensing, dielectric material penetrability remains a significant asset for FMCW sensing. In particular, with the high contrast that is obtained in presence of metallic components, defense and security screening applications have been successfully demonstrated using far field imaging systems with transceivers working at different frequencies [154, 181]. They have mainly been implemented for personal screening with clothe penetrating imaging and metallic object sensing. Commercially available solutions, based on such technologies are emerging, with for example the Rohde & Schwartz security body scanner, operating between 70 and 80 GHz, depicted in Figure I.21. Additionally, the high achievable measurement dynamic range makes FMCW sensors quite adequate for subtle material propriety variations and showed particular use for artwork inspection and heritage preservation [136, 137, 196].

Figure I.21: Rohde & Schwartz security screening solution [195].

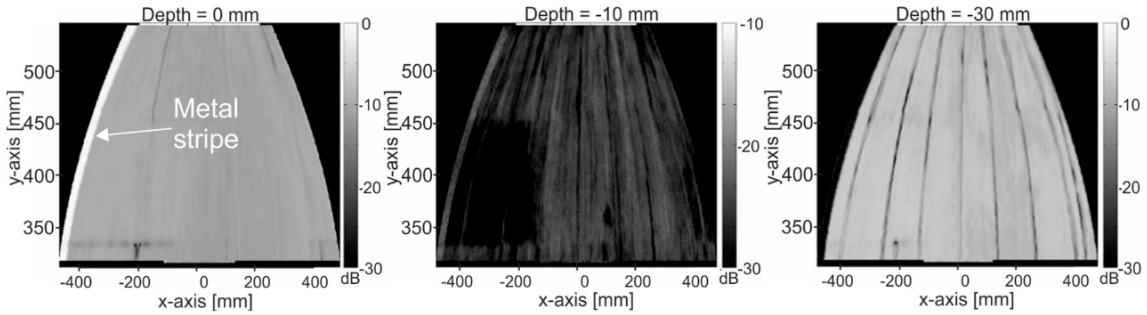

Figure I.22: 100 GHz terahertz images of a radome under inspection, featuring the internal structure on its different layers [173].

With a combination of those assets, volumetric inspection represents one of the main targets for FMCW sensors [140, 148, 197, 198], with extremely wide application fields. It then ranges from high volumes plastic molding and extrusion chains for quality control with artefacts detection and localization, joints inspection or thickness monitoring, up to the highly demanding automotive and aerospace high-added value materials inspection [173]. The latest is depicted in Figure I.22 with the inspection of a plane radome. It can indeed be intended as a defect detection sensor during production phases or as a maintenance tool for airplane on ground time reduction, by lowering the dismantling requirement in maintenance phases [199], or again for specific parts reuse on rockets launcher stages. Indeed, several optically opaque materials are especially suitable for millimeter-waves inspection thanks to their adequate transparency in this spectral region. Namely, one can consider fiber glass doped composite and a large variety of polymer doped composite materials, honeycomb structures, foams and rubbers or ceramics, which allows for eased material health monitoring. The adequacy of those components have been demonstrated through

a FP7 project DOTNAC [200] that ended in 2013 and justified the relevance and added value of FMCW radar sensing to the NDT problematic of the aeronautics industry, as a first-grade choice to complete the panel of tools allowing contactless inspection.

Additionally to the volumetric inspection problematics, towards 3D imaging, and in-depth sensing for a large scope of applicative cases of failure avoidance, the embedded phase information provided by the FMCW sensing process is of extreme importance. For instance, the characterization of mono-layer samples and the inspection of multi-layered polymers, foams and dielectric structures for thickness monitoring [140, 144, 198, 202] represents a current challenge, already featuring maturing solutions as depicted in Figure I.23. This latest approach will be especially addressed in the applicative section IV.4 of this work as an extended proof of work with dedicated algorithmic extraction methods.

Figure I.23: Sikora tube inspection solution for wall thickness, diameter and ovality assessment [201].

I.5 Conclusion

The exponentially growing number of scientific publications over the last few years can be featured as a direct marker of the academic and applicative interest for terahertz technologies.

Indeed, an abundance of advances has been witnessed with numerous targeted application fields, ranging from spatial mission embedded hardware to biology studies or NDT related problematics. Among those, a vast majority is emerging from time domain spectroscopy approaches, which has been demonstrated as an overly versatile tool for academia, as a high dynamic (>70 dB) broadband (>5 THz) solution. It therefore remains a handy tool for exploratory studies but still displays limitations in term of achievable measurement cadences and more globally industrial integrability and adequacy.

The topics of interest in this works precisely lies on this capability for advanced terahertz technologies to transpose from purely academic implementations to applied industrial sectors, on specific NDT problematics. With the growing number of available solutions, that arose from the neighboring spectral bands, capitalizing on the emerging maturation levels of the most adequate solutions remains an unrivalled way to bridge between academia and an industrial transposition.

A necessary review of several technologically available blocks was performed in this section to provide the reader with an open understanding of the hardware environment, their related latest developments and provides a quantitative performances comparison. Notably, since they have been subject to repeated implementations in this work, and now represents standard solutions, a detailed depiction of several targeted components of interest has been made. In particular, QCLs, broadband pyro-electric sensors, as well as micro-bolometer-based arrays are considered as performant components in the high frequency side of the spectrum, and will be featured for the development of an advanced real-time imaging configuration. On the other hand, electronic solutions, with Schottky diode-based frequency multipliers, sensors or mixing units, are crucial for millimeter-waves applications and will be featured in this work, especially through their implementations as sub-terahertz sources and for the development of a FMCW radar unit.

Indeed, in this millimeter-wave spectral range, with demonstrated NDT capabilities and as a centerpiece of the instrumentation work in this project, a specific attention has been brought to such FMCW radar mode of operation. It led to the highlight of the applicative potential of

such a homodyne down-conversion sensing method, with its intrinsic coherent longitudinal sensing abilities and high achievable sensing dynamic range. Through the up-scaling of this sensing scheme, native from the low frequencies, it has been at the center of many developments over 100 GHz, with several implementations, either through the use of SiGe-based designs for high integration capabilities and the development of low cost solutions, or through high-performances III/V-based solutions, that covers large application fields from volumetric inspection for NDT, precision positioning and targets detection, up to security applications.

With this recent democratization context, little regulations have yet been enforced beside simple security guidelines, based on the limited knowledge and insight of millimeter-waves induced health hazard. As part of the technological maturation process, triggered by the expansion of terahertz related applications, significant efforts in understanding the eventual impact on biological samples is witnessed but still ensure a wide applicative potential to the use of terahertz technologies.

I.6 Bibliography

[1] JB Hull and Vernon John. *Non-destructive testing*. Macmillan International Higher Education, 2015. 19

[2] S Gholizadeh. A review of non-destructive testing methods of composite materials. *Procedia Structural Integrity*, 1:50–57, 2016. 19

[3] Tanvi Menaria and Manish Kumar. Review on radiographic imaging modalities for non-destructive testing and evaluation (ndt & e). In *Proceedings of International Conference on Sustainable Computing in Science, Technology and Management (SUSCOM), Amity University Rajasthan, Jaipur-India*, 2019. 19

[4] Colin D Lockard. *Anomaly detection in radiographic images of composite materials via crosshatch regression*. PhD thesis, Mills College, 2015. 19

[5] Ali Sophian, GY Tian, D Taylor, and J Rudlin. Electromagnetic and eddy current ndt: a review. *Insight*, 43(5):302–306, 2001. 19

[6] Joseph L Rose. Success and challenges for ultrasonic testing in ndt and shm. *Materials Evaluation*, 68(5):494–500, 2010. 19

[7] Anuj Bhardwaj, Kashyap Patel, Mahesh C Bhardwaj, and Konstantine A Fetfatsidis. Application of advanced non-contact ultrasound for composite material qualification. In *ASNT Annual Conference 2014*, pages 17–25, 2014. 19

[8] Sergii Romanenko, Ryan Begley, Alan R Harvey, Livia Hool, and Vincent P Wallace. The interaction between electromagnetic fields at megahertz, gigahertz and terahertz frequencies with cells, tissues and organisms: risks and potential. *Journal of The Royal Society Interface*, 14(137):20170585, 2017. 20, 39

[9] George H Rieke, MW Werner, Rodger I Thompson, EE Becklin, WF Hoffmann, JR Houck, FJ Low, WA Stein, and FC Witteborn. Infrared astronomy after iras. *Science*, 231(4740):807–814, 1986. 20

[10] Arno A Penzias and Robert Woodrow Wilson. A measurement of excess antenna temperature at 4080 mc/s. *The Astrophysical Journal*, 142:419–421, 1965. 20

[11] Guillaume Ducournau, Pascal Szriftgiser, Fabio Pavanello, Emilien Peytavit, Mohammed Zaknoune, Denis Bacquet, Alexandre Beck, Tahsin Akalin, and Jean-François Lampin. Thz communications using photonics and electronic devices: the race to data-rate. *Journal of Infrared, Millimeter, and Terahertz Waves*, 36(2):198–220, 2015. 20

[12] G Mourou, CV Stancampiano, A Antonetti, and A Orszag. Picosecond microwave pulses generated with a subpicosecond laser-driven semiconductor switch. *Applied Physics Letters*, 39(4):295–296, 1981. 20

[13] Jean-Louis Coutaz. *Optoélectronique térahertz*. EDP Sciences, 2021. 20

[14] J Axel Zeitler, Philip F Taday, David A Newnham, Michael Pepper, Keith C Gordon, and Thomas Rades. Terahertz pulsed spectroscopy and imaging in the pharmaceutical setting-a review. *Journal of Pharmacy and Pharmacology*, 59(2):209–223, 2007. 20

[15] Meihong Lu, Jingling Shen, Ning Li, Yan Zhang, Cunlin Zhang, Laishun Liang, and Xiaoyu Xu. Detection and identification of illicit drugs using terahertz imaging. *Journal of Applied Physics*, 100(10):103104, 2006. 20

[16] Jean-Louis Coutaz, Frédéric Garet, and Lionel Duvillaret. Potentialité des ondes térahertz en imagerie. *La Revue de l'Electricité et de l'Electronique*, (9):29–38, 2007. 20

[17] Gintaras Valušis, Alvydas Lisauskas, Hui Yuan, Wojciech Knap, and Hartmut G Roskos. Roadmap of terahertz imaging 2021. *Sensors*, 21(12):4092, 2021. 21, 27

[18] A Maestrini. *Bridging the microwave-to-photonics gap with terahertz frequency multipliers*. PhD thesis, Thèse d'habiliation à diriger des recherches (HDR), Univ. Pierre et Marie . . . , 2009. vii, 21

[19] Alain Maestrini, Bertrand Thomas, Hui Wang, Cécile Jung, Jeanne Treuttel, Yong Jin, Goutam Chattopadhyay, Imran Mehdi, and Gérard Beaudin. Schottky diode-based terahertz frequency multipliers and mixers. *Comptes Rendus Physique*, 11(7-8):480–495, 2010. vii, 21, 26

[20] Roger A Lewis. A review of terahertz sources. *Journal of Physics D: Applied Physics*, 47(37):374001, 2014. 21

[21] SS Dhillon, MS Vitiello, EH Linfield, AG Davies, Matthias C Hoffmann, John Booske, Claudio Paoloni, M Gensch, Peter Weightman, GP Williams, et al. The 2017 terahertz science and technology roadmap. *Journal of Physics D: Applied Physics*, 50(4):043001, 2017. 21, 29, 31

[22] Nitin Kumar, Udaybir Singh, Anirban Bera, and AK Sinha. A review on the sub-thz/thz gyrotrons. *Infrared Physics & Technology*, 76:38–51, 2016. 21

[23] VL Bratman, Yu K Kalynov, and VN Manuilov. Large-orbit gyrotron operation in the terahertz frequency range. *Physical review letters*, 102(24):245101, 2009.

[24] Svilen Petrov Sabchevski and Toshitaka Idehara. Design of a compact sub-terahertz gyrotron for spectroscopic applications. *Journal of Infrared, Millimeter, and Terahertz Waves*, 31(8):934–948, 2010. 21

[25] BA Knyazev, GN Kulipanov, and NA Vinokurov. Novosibirsk terahertz free electron laser: instrumentation development and experimental achievements. *Measurement Science and Technology*, 21(5):054017, 2010. 21

[26] MA Dem'yanenko, DG Esaev, BA Knyazev, GN Kulipanov, and NA Vinokurov. Imaging with a 90 frames/ s microbolometer focal plane array and high-power terahertz free electron laser. *Applied physics letters*, 92(13):131116, 2008. 21

[27] Gwyn P Williams. High–power terahertz synchrotron sources. *Philosophical Transactions of the Royal Society of London. Series A: Mathematical, Physical and Engineering Sciences*, 362(1815):403–414, 2004. 21

[28] Max Planck. *The theory of heat radiation*. Courier Corporation, 2013. 22

[29] Seán M Stewart. Spectral peaks and wien's displacement law. *Journal of Thermophysics and Heat Transfer*, 26(4):689–692, 2012. 22

[30] John William Draper. Liv. on the production of light by heat. *The London, Edinburgh, and Dublin Philosophical Magazine and Journal of Science*, 30(202):345–360, 1847. 22

[31] Stefan Malz, Ritesh Jain, and Ullrich R Pfeiffer. Towards passive imaging with cmos thz cameras. In *2016 41st International Conference on Infrared, Millimeter, and Terahertz waves (IRMMW-THz)*, pages 1–2. IEEE, 2016. 22

[32] Berndt Gutschwager, Christian Monte, Hossein Delsim-Hashemi, Oliver Grimm, and Jörg Hollandt. Calculable blackbody radiation as a source for the determination of the spectral responsivity of thz detectors. *Metrologia*, 46(4):S165, 2009. 22

[33] Erich Grossman, Charles Dietlein, Juha Ala-Laurinaho, Mikko Leivo, Leif Gronberg, Markus Gronholm, Petteri Lappalainen, Anssi Rautiainen, Aleksi Tamminen, and Arttu Luukanen. Passive terahertz camera for standoff security screening. *Applied optics*, 49(19):E106–E120, 2010. 22

[34] Marcin Kowalski, Mariusz Kastek, Michal Walczakowski, Norbert Palka, and Mieczyslaw Szustakowski. Passive imaging of concealed objects in terahertz and long-wavelength infrared. *Applied Optics*, 54(13):3826–3833, 2015.

[35] E Heinz, T May, D Born, G Zieger, S Anders, V Zakosarenko, H-G Meyer, and C Schäffel. Passive 350 ghz video imaging systems for security applications. *Journal of Infrared, Millimeter, and Terahertz Waves*, 36(10):879–895, 2015. 22

[36] Alex Svetlitza, Michael Slavenko, Tatiana Blank, Igor Brouk, Sara Stolyarova, and Yael Nemirovsky. Thz measurements and calibration based on a blackbody source. *IEEE Transactions on Terahertz Science and Technology*, 4(3):347–359, 2014. 22

[37] Jean-Baptiste Perraud. *Reconstructions rapides d'images en régime térahertz 3D*. PhD thesis, Bordeaux, 2018. 22, 30

[38] Jean-Louis Coutaz, Frederic Garet, and Vincent P Wallace. *Principles of Terahertz time-domain spectroscopy*. CRC Press, 2018. 23

[39] G Kh Kitaeva. Terahertz generation by means of optical lasers. *Laser Physics Letters*, 5(8):559–576, 2008. 23

[40] Mojca Jazbinsek, Uros Puc, Andreja Abina, and Aleksander Zidansek. Organic crystals for thz photonics. *Applied Sciences*, 9(5):882, 2019. 23

[41] Nathan M Burford and Magda O El-Shenawee. Review of terahertz photoconductive antenna technology. *Optical Engineering*, 56(1):010901, 2017. vii, 23

[42] DH Auston. Subpicosecond electro-optic shock waves. *Applied Physics Letters*, 43(8):713–715, 1983. 23

[43] David H Auston, Kin P Cheung, and Peter R Smith. Picosecond photoconducting hertzian dipoles. *Applied physics letters*, 45(3):284–286, 1984. 23

[44] Ian S Gregory, Colin Baker, William R Tribe, Ian V Bradley, Michael J Evans, Edmund H Linfield, A Giles Davies, and Mohamed Missous. Optimization of photomixers and antennas for continuous-wave terahertz emission. *IEEE Journal of Quantum electronics*, 41(5):717–728, 2005. 23

[45] Guillermo P Acuna, Federico F Buersgens, Christian Lang, M Handloser, A Guggenmos, and R Kersting. Interdigitated terahertz emitters. *Electronics Letters*, 44(3):229–231, 2008. 23

[46] AG Davies, Edmund H Linfield, and Michael B Johnston. The development of terahertz sources and their applications. *Physics in Medicine & Biology*, 47(21):3679, 2002. 23

[47] Quentin Cassar. *Terahertz Radiations for Breast Tumour Recognition*. Theses, Université de Bordeaux, June 2020. vii, 23, 24, 32

[48] P Uhd Jepsen, Rune Hylsberg Jacobsen, and SR Keiding. Generation and detection of terahertz pulses from biased semiconductor antennas. *JOSA B*, 13(11):2424–2436, 1996. 24

[49] https://teraview.com/. 24

[50] https://www.menlosystems.com/. 24

[51] https://www.toptica.com/. 24

[52] https://www.menlosystems.com/assets/datasheets/thz-time-domain-solutions/menlo_era_k15-d-en_2021-07-21_3w.pdf. 24

[53] Albrecht Bartels, Roland Cerna, Caroline Kistner, Arne Thoma, Florian Hudert, Christof Janke, and Thomas Dekorsy. Ultrafast time-domain spectroscopy based on high-speed asynchronous optical sampling. *Review of Scientific Instruments*, 78(3):035107, 2007. 24

[54] Francis Hindle, Arnaud Cuisset, Robin Bocquet, and Gaël Mouret. Continuous-wave terahertz by photomixing: applications to gas phase pollutant detection and quantification. *Comptes Rendus Physique*, 9(2):262–275, 2008. 24

[55] https://www.toptica.com/products/terahertz-systems/frequency-domain/gaas-and-ingaas-photomixers/. 24

[56] M Inguscio, Giovanni Moruzzi, KM Evenson, and DA Jennings. A review of frequency measurements of optically pumped lasers from 0.1 to 8 thz. *Journal of applied physics*, 60(12):R161–R192, 1986. 24

[57] G Dodel. On the history of far-infrared (fir) gas lasers: Thirty-five years of research and application. *Infrared physics & technology*, 40(3):127–139, 1999. 24

[58] Martin Mičica, Sophie Eliet, Mathias Vanwolleghem, Roman Motiyenko, Anastasia Pienkina, Laurent Margulès, Kamil Postava, Jaromír Pištora, and Jean-François Lampin. High-resolution thz gain measurements in optically pumped ammonia. *Optics express*, 26(16):21242–21248, 2018. 24

[59] Antoine Pagies, Guillaume Ducournau, and J-F Lampin. Low-threshold terahertz molecular laser optically pumped by a quantum cascade laser. *Apl Photonics*, 1(3):031302, 2016. 24

[60] Jerome Faist, Federico Capasso, Deborah L Sivco, Carlo Sirtori, Albert L Hutchinson, and Alfred Y Cho. Quantum cascade laser. *Science*, 264(5158):553–556, 1994. 24

[61] Rüdeger Köhler, Alessandro Tredicucci, Fabio Beltram, Harvey E Beere, Edmund H Linfield, A Giles Davies, David A Ritchie, Rita C Iotti, and Fausto Rossi. Terahertz semiconductor-heterostructure laser. *Nature*, 417(6885):156–159, 2002. 24

[62] https://lytid.com/. vii, 25, 26

[63] https://longwavephotonics.com/index.html. 25

[64] H Eisele. State of the art and future of electronic sources at terahertz frequencies. *Electronics letters*, 46(26):8–11, 2010. 25

[65] Kai Chang, W Frank Thrower, and George M Hayashibara. Millimeter-wave silicon impatt sources and combiners for the 110-260-ghz range. *IEEE Transactions on Microwave Theory and Techniques*, 29(12):1278–1284, 1981. 25

[66] M Ino, T Ishibashi, and M Ohmori. Cw oscillation with p+-p-n+ silicon impatt diodes in 200 ghz and 300 ghz bands. *Electronics letters*, 12(6):148–149, 1976.

[67] Vesna Radisic, William R Deal, Kevin MKH Leong, XB Mei, Wayne Yoshida, Po-Hsin Liu, Jansen Uyeda, Andy Fung, Lorene Samoska, Todd Gaier, et al. A 10-mw submillimeter-wave solid-state power-amplifier module. *IEEE Transactions on Microwave Theory and Techniques*, 58(7):1903–1909, 2010. 25

[68] https://terasense.com/. 25, 30

[69] Gian Piero Gallerano, S Biedron, et al. Overview of terahertz radiation sources. In *Proceedings of the 2004 FEL Conference*, volume 1, pages 216–221, 2004. 26

[70] Jooseok Lee, Maengkyu Kim, and Kyounghoon Yang. A 1.52 thz rtd triple-push oscillator with a μw-level output power. *IEEE Transactions on Terahertz Science and Technology*, 6(2):336–340, 2015. 26

[71] Takeru Maekawa, Hidetoshi Kanaya, Safumi Suzuki, and Masahiro Asada. Oscillation up to 1.92 thz in resonant tunneling diode by reduced conduction loss. *Applied Physics Express*, 9(2):024101, 2016.

[72] Abdullah Al-Khalidi, Khalid Hamed Alharbi, Jue Wang, Razvan Morariu, Liquan Wang, Ata Khalid, José ML Figueiredo, and Edward Wasige. Resonant tunneling diode terahertz sources with up to 1 mw output power in the j-band. *IEEE Transactions on Terahertz Science and Technology*, 10(2):150–157, 2019. 26

[73] Imran Mehdi, Jose V Siles, Choonsup Lee, and Erich Schlecht. Thz diode technology: Status, prospects, and applications. *Proceedings of the IEEE*, 105(6):990–1007, 2017. vii, 26, 29

[74] A Feret, C Chaumont, and C Goldstein. A 520-620 ghz schottky receiver front-end for planetary science and remote sensing with 1070k-1500k dsb noise temperature at room temperature. vii, 26

[75] H Van de Stadt, G Beaudin, Th de Graauw, K Jacobs, and N Whyborn. Detectors for the heterodyne spectrometer of first. In *The Far Infrared and Submillimetre Universe.*, volume 401, page 457, 1997. 26

[76] A Maestrini, L Gatilova, J Treuttel, F Yang, Y Jin, A Cavanna, D Moro Melgar, F Tamazouzt, T Vacelet, A Féret, et al. 1200ghz and 600ghz schottky receivers for juice-swi. In *proceedings of the 27th International Symposium on Space Terahertz Technology*, volume 3, 2016. 26

[77] Alain Maestrini, John S Ward, John J Gill, Choonsup Lee, Bertrand Thomas, Robert H Lin, Goutam Chattopadhyay, and Imran Mehdi. A frequency-multiplied source with more than 1 mw of power across the 840–900-ghz band. *IEEE transactions on microwave theory and techniques*, 58(7):1925–1932, 2010. 26, 38

[78] Goutam Chattopadhyay, Erich Schlecht, John S Ward, John J Gill, Hamid HS Javadi, Frank Maiwald, and Imran Mehdi. An all-solid-state broad-band frequency multiplier chain at 1500 ghz. *IEEE Transactions on Microwave Theory and Techniques*, 52(5):1538–1547, 2004. 38

[79] Alain Maestrini, John Ward, John Gill, Hamid Javadi, Erich Schlecht, Goutam Chattopadhyay, Frank Maiwald, Neal R Erickson, and Imran Mehdi. A 1.7-1.9 thz local oscillator source. *IEEE Microwave and Wireless Components Letters*, 14(6):253–255, 2004. 38

[80] Frank Maiwald, Suzanne Martin, Jean Bruston, Alain Maestrini, Tim Crawford, and Peter H Siegel. *2.7 THz waveguide tripler using monolithic membrane diodes*, volume 3. IEEE, 2001. 26

[81] John S Ward, Goutam Chattopadhyay, John Gill, Hamid Javadi, Choonsup Lee, Robert Lin, Alain Maestrini, Frank Maiwald, Imran Mehdi, Erich Schlecht, et al. Tunable broadband frequency-multiplied terahertz sources. In *2008 33rd International Conference on Infrared, Millimeter and Terahertz Waves*, pages 1–3. IEEE, 2008. 26

[82] José V Siles and Jesús Grajal. Capabilities of gan schottky multipliers for lo power generation at millimeter-wave bands. In *19th International Symposium on Space Terahertz Technology*, pages 504–507, 2008.

[83] Chong Jin and Dimitris Pavlidis. Gan multipliers. *Fundamentals of Terahertz Devices and Applications*, pages 383–446, 2021. 26

[84] https://www.vadiodes.com/en/. 26

[85] https://acst.de/. 26

[86] Yaming Zhang, Ruonan Han, Youngwan Kim, Dae Yeon Kim, Hisashi Shichijo, Swaminathan Sankaran, Chuying Mao, Eunyoung Seok, Dongha Shim, and KO Kenneth. Schottky diodes in cmos for terahertz circuits and systems. In *2013 IEEE Radio and Wireless Symposium*, pages 43–45. IEEE, 2013. 27

[87] Erik Öjefors, Janus Grzyb, Yan Zhao, Bernd Heinemann, Bernd Tillack, and Ullrich R Pfeiffer. A 820ghz sige chipset for terahertz active imaging applications. In *2011 IEEE International Solid-State Circuits Conference*, pages 224–226. IEEE, 2011. 27

[88] Ullrich R Pfeiffer, Yan Zhao, Janusz Grzyb, Richard Al Hadi, Neelanjan Sarmah, Wolfgang Förster, Holger Rücker, and Bernd Heinemann. 14.5 a 0.53 thz reconfigurable source array with up to 1mw radiated power for terahertz imaging applications in 0.13 µm sige bicmos. In *2014 IEEE International Solid-State Circuits Conference Digest of Technical Papers (ISSCC)*, pages 256–257. IEEE, 2014. 27

[89] Zeshan Ahmad, Mark Lee, and KO Kenneth. 20.5 1.4 thz,- 13dbm-eirp frequency multiplier chain using symmetric-and asymmetric-cv varactors in 65nm cmos. In *2016 IEEE International Solid-State Circuits Conference (ISSCC)*, pages 350–351. IEEE, 2016. 27

[90] F Sizov and A Rogalski. Thz detectors. *Progress in quantum electronics*, 34(5):278–347, 2010. 27

[91] David Klocke, Anke Schmitz, Helmut Soltner, Herbert Bousack, and Helmut Schmitz. Infrared receptors in pyrophilous ("fire loving") insects as model for new un-cooled infrared sensors. *Beilstein journal of nanotechnology*, 2(1):186–197, 2011. vii, 27

[92] Marcel JE Golay. Theoretical consideration in heat and infra-red detection, with particular reference to the pneumatic detector. *Review of Scientific Instruments*, 18(5):347–356, 1947. 27

[93] EH Putley. The detection of sub-mm radiation. *Proceedings of the IEEE*, 51(11):1412–1423, 1963. 27

[94] Srisaran Venkatachalam, Klaudia Zeranska-Chudek, Mariusz Zdrojek, and Djamila Hourlier. Carbon-based terahertz absorbers: Materials, applications, and perspectives. *Nano Select*, 1(5):471–490, 2020. 27

[95] Ralf Müller, Berndt Gutschwager, Jörg Hollandt, Mathias Kehrt, Christian Monte, Ralph Müller, and Andreas Steiger. Characterization of a large-area pyroelectric detector from 300 ghz to 30 thz. *Journal of Infrared, Millimeter, and Terahertz Waves*, 36(7):654–661, 2015. 28

[96] Andreas Steiger, Werner Bohmeyer, Karsten Lange, and Ralf Müller. Novel pyroelectric detectors for accurate thz power measurements. *tm-Technisches Messen*, 83(6):386–389, 2016. 28

[97] https://www.pyrosensor.de/standard-924644.html. 28

[98] Alan WM Lee, Qi Qin, Sushil Kumar, Benjamin S Williams, Qing Hu, and John L Reno. Real-time terahertz imaging over a standoff distance (> 25 meters). *Applied Physics Letters*, 89(14):141125, 2006. 28

[99] https://www.irlabs.com/products/bolometers/bolometer-systems/. vii, 28

[100] V Dobrovolsky, F Sizov, Y Kamenev, and A Smirnov. Ambient temperature or moderately cooled semiconductor hot electron bolometer for mm and sub-mm regions. *Opto-Electronics Review*, 16(2):172–178, 2008. 28

[101] J Ajayan, D Nirmal, Ribu Mathew, Dheena Kurian, P Mohankumar, L Arivazhagan, and D Ajitha. A critical review of design and fabrication challenges in inp hemts for future terahertz frequency applications. *Materials Science in Semiconductor Processing*, 128:105753, 2021. 28

[102] Jeffrey L Hesler and Thomas W Crowe. Responsivity and noise measurements of zero-bias schottky diode detectors. *Proc. ISSTT*, pages 89–92, 2007. 28

[103] N Sobornytskyy, A Lisauskas, C Weickhmann, R Jakobi, A Semenov, H Hübers, R Müller, A Hoehl, and O Cojocari. Quasi optical schottky diode detectors for fast ultra-wideband detection. In *2013 38th International Conference on Infrared, Millimeter, and Terahertz Waves (IRMMW-THz)*, pages 1–2. IEEE, 2013. 28

[104] Lei Liu, Jeffrey L Hesler, Haiyong Xu, Arthur W Lichtenberger, and Robert M Weikle. A broadband quasi-optical terahertz detector utilizing a zero bias schottky diode. *IEEE Microwave and Wireless Components Letters*, 20(9):504–506, 2010. 28

[105] Wojciech Knap, Salman Nadar, Hadley Videlier, Stephane Boubanga-Tombet, Dominique Coquillat, Nina Dyakonova, Frederic Teppe, Kristoph Karpierz, Jerzy Łusakowski, Maciej Sakowicz, et al. Field effect transistors for terahertz detection and emission. *Journal of Infrared, Millimeter, and Terahertz Waves*, 32(5):618–628, 2011. 28

[106] Franz Schuster, Dominique Coquillat, Hadley Videlier, Maciej Sakowicz, Frédéric Teppe, Laurent Dussopt, Benoît Giffard, Thomas Skotnicki, and Wojciech Knap. Broadband terahertz imaging with highly sensitive silicon cmos detectors. *Optics express*, 19(8):7827–7832, 2011. 29

[107] L Vicarelli, MS Vitiello, D Coquillat, Antonio Lombardo, Andrea Carlo Ferrari, W Knap, M Polini, V Pellegrini, and Alessandro Tredicucci. Graphene field-effect transistors as room-temperature terahertz detectors. *Nature materials*, 11(10):865–871, 2012. 29

[108] Sebastián Castilla, Bernat Terrés, Marta Autore, Leonardo Viti, Jian Li, Alexey Y Nikitin, Ioannis Vangelidis, Kenji Watanabe, Takashi Taniguchi, Elefterios Lidorikis, et al. Fast and sensitive terahertz detection using an antenna-integrated graphene pn junction. *Nano letters*, 19(5):2765–2773, 2019. 29

[109] https://h2020thor.eu/. 29

[110] François Simoens, Jérôme Meilhan, Laurent Dussopt, Jean-Alain Nicolas, Nicolas Monnier, Gilles Sicard, Alexandre Siligaris, and Bruno Hiberty. Uncooled terahertz real-time imaging 2d arrays developed at leti: present status and perspectives. In *Micro-and Nanotechnology Sensors, Systems, and Applications IX*, volume 10194, page 101942N. International Society for Optics and Photonics, 2017. 30

[111] Erwin Hack, Lorenzo Valzania, Gregory Gäumann, Mostafa Shalaby, Christoph P Hauri, and Peter Zolliker. Comparison of thermal detector arrays for off-axis thz holography and real-time thz imaging. *Sensors*, 16(2):221, 2016. 30

[112] https://www.swissterahertz.com/. 30

[113] https://www.xenics.com/long-wave-infrared-imagers/gobi-640-series/. 30

[114] https://www.ino.ca/en/solutions/thz/. 30

[115] M Bolduc, L Marchese, B Tremblay, M Doucet, M Terroux, H Oulachgar, L Le Noc, C Alain, H Jerominek, and A Bergeron. Video-rate thz imaging using a microbolometer-based camera. In *35th International Conference on Infrared, Millimeter, and Terahertz Waves*, pages 1–2. IEEE, 2010. 30

[116] Timothy Pope, Michel Doucet, Fabien Dupont, Linda Marchese, Bruno Tremblay, Georges Baldenberger, Sonia Verrault, and Frédéric Lamontagne. Uncooled detector, optics, and camera development for thz imaging. In *Terahertz Physics, Devices, and Systems III: Advanced Applications in Industry and Defense*, volume 7311, page 73110L. International Society for Optics and Photonics, 2009. 30

[117] F Simoens, J Meilhan, B Delplanque, S Gidon, G Lasfargues, J Lalanne Dera, DT Nguyen, JL Ouvrier-Buffet, S Pocas, T Maillou, et al. Real-time imaging with thz fully-customized uncooled amorphous-silicon microbolometer focal plane arrays. In *Terahertz Physics, Devices, and Systems Vi: Advanced Applications in Industry and Defense*, volume 8363, page 83630D. International Society for Optics and Photonics, 2012. 30

[118] François Simoens and Jérôme Meilhan. Terahertz real-time imaging uncooled array based on antenna-and cavity-coupled bolometers. *Philosophical Transactions of the Royal Society A: Mathematical, Physical and Engineering Sciences*, 372(2012):20130111, 2014. 30

[119] https://www.i2s.fr/fr. 30

[120] https://ticwave.com/index.php/shop. 30

[121] https://www.tihive.com. 30

[122] Pan. *Terahertz wave-guided reflectometry system.* PhD thesis, Université de Bordeaux, 2020. 31

[123] Georges Humbert. *Optical Fibers in Terahertz Domain*, pages 1–49. Springer Singapore, Singapore, 2019. 31

[124] Chih-Hsien Lai, Borwen You, Ja-Yu Lu, Tze-An Liu, Jin-Long Peng, Chi-Kuang Sun, and Hung-Chun Chang. Modal characteristics of antiresonant reflecting pipe waveguides for terahertz waveguiding. *Optics express*, 18(1):309–322, 2010. 31

[125] Edwin Nguema, Denis Férachou, Georges Humbert, Jean-Louis Auguste, and Jean-Marc Blondy. Broadband terahertz transmission within the air channel of thin-wall pipe. *Optics letters*, 36(10):1782–1784, 2011. 31

[126] Bradley Bowden, James A Harrington, and Oleg Mitrofanov. Silver/polystyrene-coated hollow glass waveguides for the transmission of terahertz radiation. *Optics letters*, 32(20):2945–2947, 2007. 31

[127] YF Geng, XL Tan, P Wang, and JQ Yao. Transmission loss and dispersion in plastic terahertz photonic band-gap fibers. *Applied Physics B*, 91(2):333–336, 2008. 31

[128] Michael RC Williams, Daniel J Aschaffenburg, Benjamin K Ofori-Okai, and Charles A Schmuttenmaer. Intermolecular vibrations in hydrophobic amino acid crystals: experiments and calculations. *The Journal of Physical Chemistry B*, 117(36):10444–10461, 2013. 31

[129] Till Hagelschuer, Martin Wienold, Heiko Richter, L Schrottke, Klaus Biermann, Holger T Grahn, and H-W Hübers. Terahertz gas spectroscopy through self-mixing in a quantum-cascade laser. *Applied Physics Letters*, 109(19):191101, 2016. 31

[130] Alfonso Alessandro Tanga, Valeria Giliberti, Francesco Vitucci, Domenico Vitulano, Vittoria Bruni, Andrea Rossetti, Gabriele Carmine Messina, Maddalena Daniele, Giancarlo Ruocco, and Michele Ortolani. Terahertz scattering microscopy for dermatology diagnostics. *Journal of Physics: Photonics*, 2021. 32

[131] OA Smolyanskaya, NV Chernomyrdin, AA Konovko, KI Zaytsev, IA Ozheredov, OP Cherkasova, MM Nazarov, J-P Guillet, SA Kozlov, Yu V Kistenev, et al. Terahertz biophotonics as a tool for studies of dielectric and spectral properties of biological tissues and liquids. *Progress in Quantum Electronics*, 62:1–77, 2018. 32

[132] Quentin Cassar, Amel Al-Ibadi, Laven Mavarani, Philipp Hillger, Janusz Grzyb, Gaëtan MacGrogan, Thomas Zimmer, Ullrich R Pfeiffer, Jean-Paul Guillet, and Patrick Mounaix. Pilot study of freshly excised breast tissue response in the 300–600 ghz range. *Biomedical optics express*, 9(7):2930–2942, 2018. 32

[133] Gyeongsik Ok, Kisang Park, Hyun Jung Kim, Hyang Sook Chun, and Sung-Wook Choi. High-speed terahertz imaging toward food quality inspection. *Applied optics*, 53(7):1406–1412, 2014. 32

[134] AD Squires and RA Lewis. Terahertz analysis of phthalocyanine pigments. *Journal of Infrared, Millimeter, and Terahertz Waves*, 40(7):738–751, 2019. 32

[135] Kaori Fukunaga, Iwao Hosako, Michela Palazzo, Lorenza Dall'Aglio, Fabio Aramini, Costanza Cucci, Marcello Picollo, Tomofumi Ikari, and Irl N Duling. Terahertz time-domain imaging of "the last supper". In *2020 45th International Conference on Infrared, Millimeter, and Terahertz Waves (IRMMW-THz)*, pages 1–2. IEEE, 2020. 32

[136] Corinna L Koch Dandolo, Jean-Paul Guillet, Xue Ma, Frédéric Fauquet, Marie Roux, and Patrick Mounaix. Terahertz frequency modulated continuous wave imaging advanced data processing for art painting analysis. *Optics express*, 26(5):5358–5367, 2018. 41

[137] Jean-Paul Guillet, M Roux, K Wang, Xue Ma, F Fauquet, H Balacey, B Recur, F Darracq, and P Mounaix. Art painting diagnostic before restoration with terahertz and millimeter waves. *Journal of Infrared, Millimeter, and Terahertz Waves*, 38(4):369–379, 2017. 32, 41

[138] David M Sheen, Thomas E Hall, Ronald H Severtsen, Douglas L McMakin, Brian K Hatchell, and Patrick LJ Valdez. Standoff concealed weapon detection using a 350-ghz radar imaging system. In *Passive Millimeter-Wave Imaging Technology XIII*, volume 7670, page 767008. International Society for Optics and Photonics, 2010. 32, 38

[139] Jianjun Ma, Rabi Shrestha, Jacob Adelberg, Chia-Yi Yeh, Zahed Hossain, Edward Knightly, Josep Miquel Jornet, and Daniel M Mittleman. Security and eavesdropping in terahertz wireless links. *Nature*, 563(7729):89–93, 2018. 32

[140] F Ellrich, M Bauer, N Schreiner, A Keil, T Pfeiffer, J Klier, S Weber, J Jonuscheit, F Friederich, and D Molter. Terahertz quality inspection for automotive and aviation industries. *Journal of Infrared, Millimeter, and Terahertz Waves*, 41(4):470–489, 2020. 32, 39, 41, 42

[141] Dirk Nüßler and Joachim Jonuscheit. Terahertz based non-destructive testing (ndt): Making the invisible visible. *tm-Technisches Messen*, 1(ahead-of-print), 2020. 32

[142] Quentin Cassar, Adrien Chopard, Frederic Fauquet, Jean-Paul Guillet, Mingming Pan, Jean-Baptiste Perraud, and Patrick Mounaix. Iterative tree algorithm to evaluate terahertz signal contribution of specific optical paths within multilayered materials. *IEEE Transactions on Terahertz Science and Technology*, 9(6):684–694, 2019. 32

[143] Ian S Gregory, Robert K May, Philip F Taday, and Patrick Mounaix. Extending terahertz paint thickness measurements to advanced industry-standard automotive paint structures. In *2016 41st International Conference on Infrared, Millimeter, and Terahertz waves (IRMMW-THz)*, pages 1–2. IEEE, 2016. 32

[144] Nina S Schreiner, Wolfgang Sauer-Greff, Ralph Urbansky, Georg von Freymann, and Fabian Friederich. Multilayer thickness measurements below the rayleigh limit using fmcw millimeter and terahertz waves. *Sensors*, 19(18):3910, 2019. 32, 42

[145] Andrew G Stove. Linear fmcw radar techniques. In *IEE Proceedings F (Radar and Signal Processing)*, volume 139, pages 343–350. IET, 1992. 32, 33

[146] James D Taylor. *Ultra-wideband radar technology*. CRC press, 2018. 34, 40

[147] Alan J Fenn, Donald H Temme, William P Delaney, and William E Courtney. The development of phased-array radar technology. *Lincoln Laboratory Journal*, 12(2):321–340, 2000. 36

[148] Edison Cristofani, Fabian Friederich, Sabine Wohnsiedler, Carsten Matheis, Joachim Jonuscheit, Marijke Vandewal, and René Beigang. Nondestructive testing potential evaluation of a terahertz frequency-modulated continuous-wave imager for composite materials inspection. *Optical Engineering*, 53(3):031211, 2014. 36, 39, 41

[149] Edison Cristofani, Marijke Vandewal, Carsten Matheis, and Joachim Jonuscheit. In-depth high-resolution sar imaging using omega-k applied to fmcw systems. In *2012 IEEE Radar Conference*, pages 0725–0730. IEEE, 2012.

[150] Ian G Cumming and Frank H Wong. Digital processing of synthetic aperture radar data. *Artech house*, 1(3), 2005.

[151] Jinshan Ding, Matthias Kahl, Otmar Loffeld, and Peter Haring Bolívar. Thz 3-d image formation using sar techniques: simulation, processing and experimental results. *IEEE Transactions on Terahertz Science and Technology*, 3(5):606–616, 2013.

[152] R Hussung, A Keil, and F Friederich. Handheld millimeter wave imaging system based on a two-dimensional multistatic sparse array. In *2020 45th International Conference on Infrared, Millimeter, and Terahertz Waves (IRMMW-THz)*, pages 1–2. IEEE, 2020. 36

[153] David M Sheen, Thomas E Hall, Ronald H Severtsen, Douglas L McMakin, Brian K Hatchell, and Patrick LJ Valdez. Active wideband 350ghz imaging system for concealed-weapon detection. In *Passive Millimeter-Wave Imaging Technology XII*, volume 7309, page 73090I. International Society for Optics and Photonics, 2009. 36, 38

[154] Ken B Cooper, Robert J Dengler, Nuria Llombart, Tomas Bryllert, Goutam Chattopadhyay, Erich Schlecht, John Gill, Choonsup Lee, Anders Skalare, Imran Mehdi, et al. Penetrating 3-d imaging at 4-and 25-m range using a submillimeter-wave radar. *IEEE Transactions on Microwave Theory and Techniques*, 56(12):2771–2778, 2008. 36, 38, 41

[155] David GC Luck. *Frequency modulated radar*. McGraw-Hill, 1962. 36

[156] Jürgen Hasch, Eray Topak, Raik Schnabel, Thomas Zwick, Robert Weigel, and Christian Waldschmidt. Millimeter-wave technology for automotive radar sensors in the 77 ghz frequency band. *IEEE Transactions on Microwave Theory and Techniques*, 60(3):845–860, 2012. 36

[157] Dave Saunders, Steve Bingham, Gaurav Menon, Don Crockett, Josh Tor, Ralph Mende, Marc Behrens, Nitin Jain, Angelos Alexanian, et al. A single-chip 24 ghz sige bicmos transceiver for low cost fmcw airborne radars. In *Proceedings of the IEEE 2009 National Aerospace & Electronics Conference (NAECON)*, pages 244–247. IEEE, 2009. 36

[158] K Schmalz, W Winkler, J Borngraber, W Debski, B Heinemann, and C Scheytt. A 122 ghz receiver in sige technology. In *2009 IEEE Bipolar/BiCMOS Circuits and Technology Meeting*, pages 182–185. IEEE, 2009. 37

[159] K Schmalz, W Winkler, J Borngräber, W Debski, B Heinemann, and JC Scheytt. 122 ghz ism-band transceiver concept and silicon ics for low-cost receiver in sige bicmos. In *2010 IEEE MTT-S International Microwave Symposium*, pages 1332–1335. IEEE, 2010.

[160] Mario Pauli, Benjamin Göttel, Steffen Scherr, Akanksha Bhutani, Serdal Ayhan, Wolfgang Winkler, and Thomas Zwick. Miniaturized millimeter-wave radar sensor for high-accuracy applications. *IEEE Transactions on Microwave Theory and Techniques*, 65(5):1707–1715, 2017. vii, 37

[161] Klaus Schmalz, Johannes Borngraber, Yanfei Mao, Holger Rucker, and Rainer Weber. A 245 ghz lna in sige technology. *IEEE microwave and wireless components letters*, 22(10):533–535, 2012. 37

[162] Yanfei Mao, Klaus Schmalz, Johannes Borngraber, and John Christoph Scheytt. 245-ghz lna, mixer, and subharmonic receiver in sige technology. *IEEE transactions on microwave theory and techniques*, 60(12):3823–3833, 2012. 37

[163] K Schmalz, J Borngräber, B Heinemann, H Rücker, and JC Scheytt. A 245 ghz transmitter in sige technology. In *2012 IEEE Radio Frequency Integrated Circuits Symposium*, pages 195–198. IEEE, 2012. 37

[164] Klaus Schmalz, Ruoyu Wang, Johannes Borngräber, Wojciech Debski, Wolfgang Winkler, and Chafik Meliani. 245 ghz sige transmitter with integrated antenna and external pll. In *2013 IEEE MTT-S International Microwave Symposium Digest (MTT)*, pages 1–3. IEEE, 2013. 37

[165] Ekaterina Laskin, Pascal Chevalier, Bernard Sautreuil, and Sorin P Voinigescu. A 140-ghz double-sideband transceiver with amplitude and frequency modulation operating over a few meters. In *2009 IEEE Bipolar/BiCMOS Circuits and Technology Meeting*, pages 178–181. IEEE, 2009. 37

[166] Nils Pohl, Timo Jaeschke, and Klaus Aufinger. An ultra-wideband 80 ghz fmcw radar system using a sige bipolar transceiver chip stabilized by a fractional-n pll synthesizer. *IEEE Transactions on Microwave Theory and Techniques*, 60(3):757–765, 2012. 37

[167] Serdal Ayhan, Sven Thomas, Nanxi Kong, Steffen Scherr, Mario Pauli, Timo Jaeschke, Jens Wulfsberg, Nils Pohl, and Thomas Zwick. Millimeter-wave radar distance measurements in micro machining. In *2015 IEEE Topical Conference on Wireless Sensors and Sensor Networks (WiSNet)*, pages 65–68. IEEE, 2015. 37, 40

[168] Ali Mostajeran, Andreia Cathelin, and Ehsan Afshari. A 170-ghz fully integrated single-chip fmcw imaging radar with 3-d imaging capability. *IEEE Journal of Solid-State Circuits*, 52(10):2721–2734, 2017. 37

[169] Morteza Abbasi, Sten E Gunnarsson, Niklas Wadefalk, Rumen Kozhuharov, Jan Svedin, Sergey Cherednichenko, Iltcho Angelov, Ingmar Kallfass, Arnulf Leuther, and Herbert Zirath. Single-chip 220-ghz active heterodyne receiver and transmitter mmics with on-chip integrated antenna. *IEEE transactions on microwave theory and techniques*, 59(2):466–478, 2010. 38

[170] Sten E Gunnarsson, Niklas Wadefalk, Jan Svedin, Sergey Cherednichenko, Iltcho Angelov, Herbert Zirath, Ingmar Kallfass, and Arnulf Leuther. A 220 ghz single-chip receiver mmic with integrated antenna. *IEEE microwave and wireless components letters*, 18(4):284–286, 2008. 38

[171] S Koch, M Guthoerl, I Kallfass, A Leuther, and S Saito. A 140 ghz heterodyne receiver chipset for passive millimeter wave imaging applications. In *2009 Annual IEEE Compound Semiconductor Integrated Circuit Symposium*, pages 1–4. IEEE, 2009. 38

[172] Ken B Cooper, Robert J Dengler, Nuria Llombart, Bertrand Thomas, Goutam Chattopadhyay, and Peter H Siegel. Thz imaging radar for standoff personnel screening. *IEEE Transactions on Terahertz Science and Technology*, 1(1):169–182, 2011. 38

[173] Fabian Friederich, Karl Henrik May, Bessem Baccouche, Carsten Matheis, Maris Bauer, Joachim Jonuscheit, Michael Moor, David Denman, Jamie Bramble, and Nick Savage. Terahertz radome inspection. In *Photonics*, volume 5, page 1. Multidisciplinary Digital Publishing Institute, 2018. vii, 38, 41

[174] Tomas Bryllert, Vladimir Drakinskiy, Ken B Cooper, and Jan Stake. Integrated 200–240-ghz fmcw radar transceiver module. *IEEE transactions on microwave theory and techniques*, 61(10):3808–3815, 2013. 38

[175] Tomas Bryllert, Ken B Cooper, Robert J Dengler, Nuria Llombart, Goutam Chattopadhyay, Erich Schlecht, John Gill, Choonsup Lee, Anders Skalare, Imran Mehdi, et al. A 600 ghz imaging radar for concealed objects detection. In *2009 IEEE Radar Conference*, pages 1–3. IEEE, 2009. vii, 38

[176] KB Cooper, RJ Dengler, G Chattopadhyay, E Schlecht, J Gill, A Skalare, I Mehdi, and PH Siegel. A high-resolution imaging radar at 580 ghz. *IEEE Microwave and wireless components letters*, 18(1):64–66, 2008. 38

[177] Erich Schlecht, John Gill, Robert Dengler, Robert Lin, Ray Tsang, and Imran Mehdi. A unique 520–590 ghz biased subharmonically-pumped schottky mixer. *IEEE Microwave and Wireless Components Letters*, 17(12):879–881, 2007. 38

[178] Erich Schlecht, John Gill, Robert Dengler, Robert Lin, Ray Tsang, and Imran Mehdi. First wideband 520-590 ghz balanced fundamental schottky mixer. In *18th International Symposium Space Terahertz Technology, Pasadena, CA*, 2007. 38

[179] Alain Maestrini, John S Ward, John J Gill, Hamid S Javadi, Erich Schlecht, Charlotte Tripon-Canseliet, Goutam Chattopadhyay, and Imran Mehdi. A 540-640-ghz high-efficiency four-anode frequency tripler. *IEEE Transactions on Microwave Theory and Techniques*, 53(9):2835–2843, 2005. 38

[180] Ken B Cooper, Robert J Dengler, Nuria Llombart, Ashit Talukder, Anand V Panangadan, Chris S Peay, Imran Mehdi, and Peter H Siegel. Fast high-resolution terahertz radar imaging at 25 meters. In *Terahertz Physics, Devices, and Systems IV: Advanced Applications in Industry and Defense*, volume 7671, page 76710Y. International Society for Optics and Photonics, 2010. 38

[181] Duncan A Robertson, David G Macfarlane, and Tomas Bryllert. 220ghz wideband 3d imaging radar for concealed object detection technology development and phenomenology studies. In *Passive and Active Millimeter-Wave Imaging XIX*, volume 9830, page 983009. International Society for Optics and Photonics, 2016. 38, 41

[182] GP Gallerano, E Grosse, R Korenstein, M Dressel, W Mantele, MR Scarfi, AC Cefalas, P Taday, RH Clothier, and P Jepsen. Thz-bridge: an european project for the study of the interaction of terahertz radiation with biological systems. In *Infrared and Millimeter Waves, Conference Digest of the 2004 Joint 29th International Conference on 2004 and 12th International Conference on Terahertz Electronics, 2004.*, pages 817–818. IEEE, 2004. 39

[183] Scientific Committee on Emerging and Newly Identified Health Risks. Potential health effects of exposure to electromagnetic fields (emf). 2015. 39

[184] Kensuke Sasaki, Maya Mizuno, Kanako Wake, and Soichi Watanabe. Monte carlo simulations of skin exposure to electromagnetic field from 10 ghz to 1 thz. *Physics in Medicine & Biology*, 62(17):6993, 2017. 39

[185] International Commission on Non-Ionizing Radiation Protection et al. Guidelines for limiting exposure to electromagnetic fields (100 khz to 300 ghz). *Health physics*, 118(5):483–524, 2020. xv, 40

[186] Haim Mazar Madjar. Human radio frequency exposure limits: An update of reference levels in europe, usa, canada, china, japan and korea. In *2016 International Symposium on Electromagnetic Compatibility-EMC EUROPE*, pages 467–473. IEEE, 2016. 40

[187] William H Bailey, Ralf Bodemann, Jerrold Bushberg, Chung-Kwang Chou, Robert Cleveland, Antonio Faraone, Kenneth R Foster, Kenneth E Gettman, Kevin Graf, Tim Harrington, et al. Synopsis of ieee std c95. 1™-2019 "ieee standard for safety levels with respect to human exposure to electric, magnetic, and electromagnetic fields, 0 hz to 300 ghz". *IEEE Access*, 7:171346–171356, 2019. 40

[188] Patrick Staebler. *Exposition humaine aux champs électromagnétiques: De 0 Hz à 300 GHz*. ISTE Group, 2016. 40

[189] https://www.sfrp.asso.fr/. 40

[190] Gary Koh, James H Lever, Steven A Arcone, Hans-Peter Marshall, and Laura E Ray. Autonomous fmcw radar survey of antarctic shear zone. In *Proceedings of the XIII Internarional Conference on Ground Penetrating Radar*, pages 1–5. IEEE, 2010. 40

[191] Byungjoon Kim, Duksoo Kim, Youngjoon Lim, Sangwook Nam, Eun-Hyuk Kwak, Boo-Gyoun Kim, Hwanseok Yeo, and Jaeha Kim. A dual-band fmcw radar for through-wall detection. In *2015 IEEE 5th Asia-Pacific Conference on Synthetic Aperture Radar (APSAR)*, pages 54–57. IEEE, 2015. 40

[192] Jae-Hyun Choi, Jong-Hun Jang, and Jin-Eep Roh. Design of an fmcw radar altimeter for wide-range and low measurement error. *IEEE Transactions on Instrumentation and Measurement*, 64(12):3517–3525, 2015. 40

[193] Julien Delanoë, Alain Protat, Jean-Paul Vinson, Williams Brett, Christophe Caudoux, Fabrice Bertrand, Jacques Parent du Chatelet, Ruben Hallali, Laurent Barthes, Martial Haeffelin, et al. Basta: A 95-ghz fmcw doppler radar for cloud and fog studies. *Journal of Atmospheric and Oceanic Technology*, 33(5):1023–1038, 2016. 40

[194] LQ Bui, Y Alon, and T Morton. 94 ghz fmcw radar for low visibility aircraft landing system. In *1991 IEEE MTT-S International Microwave Symposium Digest*, pages 1147–1150. IEEE, 1991. 40

[195] https://www.rohde-schwarz.com/fr/produits/test-et-mesure/microwave-imaging/microwave-imaging-theme_230800.html. vii, 41

[196] M Bauer, A Keil, C Matheis, K Fukunaga, F Aramini, M Palazzo, L Dall'Aglio, and F Friederich. Terahertz fmcw measurements of leonardo da vinci's "the last supper" and other investigations in the field of cultural heritage. In *2020 45th International Conference on Infrared, Millimeter, and Terahertz Waves (IRMMW-THz)*, pages 01–02. IEEE, 2020. 41

[197] A. Chopard, J. Bou Sleiman, Q. Cassar, J.P. Guillet, M. Pan, J.B. Perraud, A. Susset, and P. Mounaix. Terahertz waves for contactless control and imaging in aeronautics industry. *NDT E International*, page 102473, 2021. 41

[198] Dirk Nüßler and Joachim Jonuscheit. Terahertz based non-destructive testing (ndt). *tm-Technisches Messen*, 88(4):199–210, 2021. 41, 42

[199] Adrien Chopard, Joyce Sleiman, Q Cassar, P Fauché, J Guillet, Patrick Mounaix, Perraud Jean-Baptiste, and A Susset. Millimeter waves radar: A way to see through the airplane covering? In *11 symposium international: NDT in Aerospace*, 2019. 41

[200] Marijke Vandewal. Dotnac–development and optimization of thz ndt on aeronautics composite multi-layered structures. *Innovation for Sustainable Aviation in a Global Environment: Proceedings of the Sixth European Aeronautics Days, Madrid, 30 March-1 April, 2011*, page 327, 2012. 42

[201] https://sikora.net/en/products/centerwave6000/. vii, 42

[202] Nina S Schreiner, Wolfgang Sauer-Greff, Ralph Urbansky, and Fabian Friedcrich. All-electronic high-resolution terahertz thickness measurements. In *2018 43rd International Conference on Infrared, Millimeter, and Terahertz Waves (IRMMW-THz)*, pages 1–2. IEEE, 2018. 42

Chapter II

Terahertz Imaging

«*If you're walking down the right path and you're willing to keep walking, eventually you'll make progress.*»

Barack Obama

II.1 Introduction

Following the state of the art study given in chapter I, this chapter will first pick up on a conventional method for terahertz imaging and spatial sensing, raster-scan focused point imaging. A detailed depiction of the inherent optical principles at stake will be drawn, relative to the macroscopic light-matter interaction as well as beam shaping, and will be followed by typical integrations that allow for enhanced imaging capabilities. More specifically, simultaneous transmission/reflection sensing, as well as a dual frequencies concomitant imaging approaches will be assessed. Further developments will lead to the capabilities of terahertz in the matter of 3D inspection through computed tomography reconstruction methods.

Nevertheless, the inherent limitations of such approaches, even though robust and optimized, remains an exceedingly slow recording process, that will lead to the consideration of full-field imaging techniques in a second section.

A depiction of the physical fundamental challenges, when considering such real time imagers in the terahertz region, will be addressed. In this second section, with the aim to overcome most of such limitations, an exhaustive report on an advanced illumination system, featuring galvanometric beam homogenization, will be detailed. Along with its working principle, that relies on Lissajous beam steering, the versatile and enhanced illumination schemes will be addressed with their relative imaging results. Those advances will then demonstrate their usefulness when it comes to the implementation of real-time tomographic volumetric inspection in the terahertz spectral range.

II.2 Raster Scan CW Imaging

With a limited choice in term of existing imaging system in the terahertz region, but a growing number of available sources and sensors, the implementation of the empirical approach of raster scanning single point imaging remains a widely used suitable choice for initial developments and performances assessments for terahertz applications [1–3].

When considering a given electromagnetic sensing mechanisms, the outcome originates from the interaction between a probing wave and a given sample. In the specific case of contactless terahertz testing, preliminary considerations and reminders on light-matter interactions on a macroscale are therefore of interest for the understanding of imaging, and more widely, sensing results.

II.2.1 Optical considerations

Located in between electronics and optics realms, terahertz interactions can still be primarily defined through the refractive index of the medium, which, in its complex form can be broken down as:

$$\tilde{n} = n - i\kappa, \tag{II.1}$$

with $n = \frac{c_0}{c}$ the relative propagation speed of light between vacuum, c_0 $[m.s^{-1}]$, and the medium, c $[m.s^{-1}]$, while κ depicts its extinction coefficient.

In this work, unless specified otherwise, materials will be considered as non-dispersive, therefore featuring a wavelength-invariant refractive index, $\tilde{n}(\lambda_0) = \tilde{n}$. Indeed, unlike when considering broadband systems such as pulsed TDS systems, this assumption can be made when integrating monochromatic or band-limited electric fields [4].

In a simplistic macro-scale approach, several interactions[5] can already be drawn and are depicted in Figure II.1. Namely, attenuated propagation through a homogeneous medium with sub-figures II.1a and II.1b respectively depicting an induced phase shift, ϕ and absorption, as well as geometric refraction considerations, in sub-figures II.1c and II.1d, that can be depicted through Snell-Descartes law. Diffraction at the encounter of an inhomogeneous discontinuity is

simplistically detailed in sub-figure II.1e, and scattering, depicted in sub-figure II.1f. can be linked to more microscopic depiction, described through various scattering models such as Rayleigh or Mie scattering [6–8].

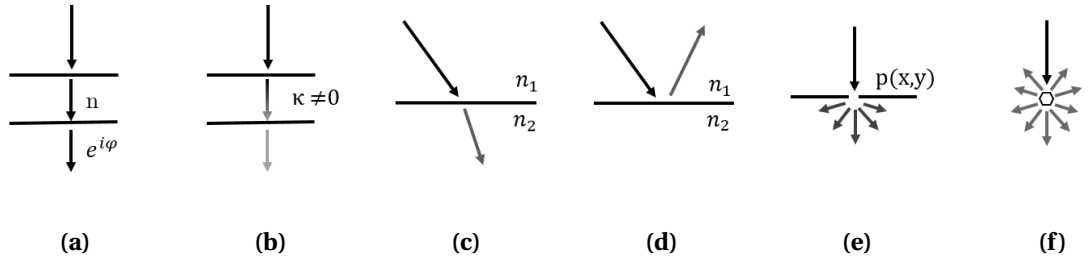

Figure II.1: Simplified diagram representing macro-scale light-matter interactions with **(a)** propagation, **(b)** attenuation, **(c)** refraction, **(d)** reflection, **(e)** diffraction and **(f)** scattering.

Wave propagation

A general depiction of a monochromatic wave can be found thought the following generic complex wave-function, $U(\vec{r},t)$ (not to be confused with the quantum mechanics wave-function):

$$U(\vec{r},t) = U_0(\vec{r})e^{i\phi(\vec{r})}e^{i\frac{2\pi c_o}{\lambda_o}t}, \tag{II.2}$$

with $\vec{r}$ = (x, y, z) the position vector $[m]$, c_o the speed of light in vacuum $[m.s^{-1}]$, λ_o the wavelength in vacuum $[m]$, and $\phi(\vec{r})$ the position dependant phase of the wave $[rad]$.

The physical validity of this wave-function is ensured when satisfying the following wave equation [9], derived from Maxwell's equations, that governs the general description of waves in their propagation medium:

$$\nabla^2 U - \frac{\tilde{n}^2}{c_0^2}\frac{\partial^2 U}{\partial t^2} = 0, \tag{II.3}$$

with ∇^2 the Laplacian operator as a double spatial derivative.

The complex notation then ensures a convenient dissociation between temporal and spatial contributions with $U(\vec{r}) = U_0(\vec{r})e^{i\phi(\vec{r})}$, denoted as the complex amplitude wave front. From this variable separation, and the ensued time-independent Helmholtz equation, $(\nabla^2 + \tilde{n}^2 k_0^2)U(\vec{r}) = 0$, usual wave-function for spherical wave fronts (see Equation II.4) and plane waves (see Equation II.5) in homogeneous materials can be derived :

$$U(r,t) = \frac{U_0}{r}e^{i\frac{2\pi c_o}{\lambda_o}t - i\tilde{n}k_o r}, \tag{II.4}$$

$$U(\vec{r},t) = U_0 e^{i\frac{2\pi c_o}{\lambda_o}t - i\tilde{n}\vec{k_o}.\vec{r}}, \tag{II.5}$$

with $\vec{k_0}$ the wave-number vector in vacuum, $k_0 = |\vec{k_0}| = \frac{2\pi}{\lambda_0}$ $[m^{-1}]$, and $r = |\vec{r}| = \sqrt{x^2+y^2+z^2}$ $[m]$.

Considering the later, quite simplistic, plane-wave model, the transmission through a given parallel slab propagation medium of thickness l [m] and refractive index $\tilde{n}$ would lead to the following transmission transfer function:

$$t_l = \frac{U(0,t)}{U(l,t)} = e^{-i2\pi\frac{\tilde{n}l}{\lambda_0}}. \tag{II.6}$$

Accounting for the real part of the refractive index, n, such a propagation will induce a proportional phase shift (see Figure II.1a) :

$$\Phi_l = n\frac{2\pi l}{\lambda_0} = n\frac{\omega l}{c_0}, \tag{II.7}$$

with $\omega = 2\pi\frac{c_0}{\lambda}$ the angular frequency, $[rad.s^{-1}]$.

Considering then the complex part of the refractive index will lead to an amplitude decrease related the absorption of a material (see Figure II.1b). This evolution of the intensity of the beam will then be dictated by the Beer-Lambert law as follows, in the case of a uniformly absorbing sample (κ = cte):

$$I(l) = I_o e^{-\alpha l}, \tag{II.8}$$

With $I = |U(\vec{r}, t)|^2$ the intensity of the monochromatic wave and I_o the input intensity, l the optical path length in the sample and α the absorption coefficient $[m^{-1}]$, with $\alpha = \frac{2\pi}{\lambda_0}\kappa$ in the case of pure material induced absorption. In a wider scope, this attenuation is usually imputed as an addition of the absorption and scattering contributions for macroscopic considerations.

Those equations are easily analytically implementable in the case of plane-waves of spherical-waves considerations. Nevertheless, when it comes to complex wave fronts, advanced propagation models, and more globally diffraction problematic (see Figure II.1e), have to be accounted for and will be fully detailed in Section II.2.1. Such assessment will be detailed through the Fourier optics principles [10], and numerically assessed for diffracting coherent imaging purposes.

Dielectric interface interaction

Up to this point, those mathematical considerations accounted for propagation into a homogeneous medium. Nevertheless, at the encounter with a discontinuity, several physical principles will come into play. Namely, refraction, at the partition between two homogeneous media of respective indices $\tilde{n_i}$ and $\tilde{n_j}$, is depicted in Figure II.1c. On purely geometrical considerations, the Snell-Descartes law dictates the beam path as :

$$n_i sin(\theta_i) = n_j sin(\theta_j) \quad and \quad \theta_{ri} = -\theta_i, \tag{II.9}$$

with n_i and n_j the real refractive indices relative to the two propagation media and θ_i, θ_j and θ_{ri} the incidence, refracted and reflected angles respectively $[rad]$.

Ensuring power conservation for such geometrical concern (${r_{i,j}}^2 + {t_{i,j}}^2 = 1$), amplitudes variations will ensue with partial power reflection and transmission at this interface. They are governed by the following coefficients for the reflected wave and, in the subsequent media, the transmitted wave, in the case of a TE wave front:

$$r_{i,j} = \frac{\tilde{n_i}cos(\theta_i) - \tilde{n_j}cos(\theta_j)}{\tilde{n_i}cos(\theta_i) + \tilde{n_j}cos(\theta_j)}, \quad and \quad t_{i,j} = \frac{2\tilde{n_i}cos(\theta_j)}{\tilde{n_i}cos(\theta_i) + \tilde{n_j}cos(\theta_j)}, \tag{II.10}$$

When describing a whole sample, such considerations for a single interface, remains quite simplistic and limited. Accounting for propagation, absorption, and successive interface reflections and transmissions, complex sample geometries can be investigated and physically depicted through the Rourad model [11, 12]. This approach will be extensively described in section IV.4 as a way to physically describe stacked multi-layered materials.

Beam shaping and achievable resolutions

Beside such propagation and interface encounter concerns, beam shaping challenges, to reach optimum resolutions and sensing capabilities, are also inherent to far field single point sensing. In this matter, emerging from the optical domain through a wavelength scaling towards the millimeter wave and terahertz regions, the Gaussian beam propagation model [13] offers a representative tool for beam shaping and upstream optical system design.

In its fundamental stable mode, the following equation can be used for the full spatio-temporal description of its electric field:

$$U(s,z) = U_0 \frac{\omega_0}{\omega(z)} e^{\frac{-s^2}{\omega(z)^2}} e^{-i(\frac{2\pi\tilde{n}}{\lambda_0}z + \frac{\pi\tilde{n}s^2}{\lambda_0 R(z)} - \psi(z))} e^{i\frac{2\pi c_o}{\lambda_o}t}, \tag{II.11}$$

with s the radial distance to the optical axis [m], R(z) the radius of curvature of the wave front [m], $\omega(z)$ the beam radius [m] at a given distance z [m], ω_0 the beam waist [m] and ψ the Gouy phase. While the first real exponential is relative to the Gaussian amplitude distribution, the second complex exponential is relative to the phase wave front, and features a linear term, related to propagation, and a second term, dictating the curvature of the wave front, completed by the time dependency in the last complex exponential.

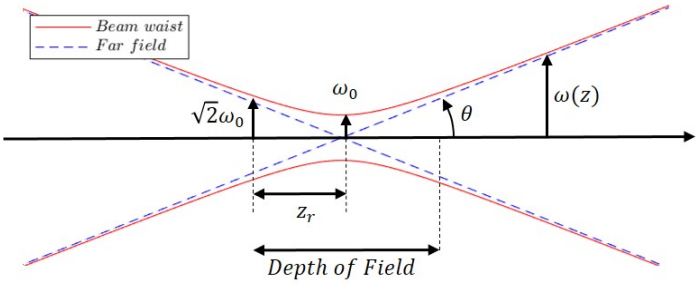

Figure II.2: $\omega(z)$, Gaussian beam width evolution with the propagation distance.

Considering this amplitude evolution, the beam radius at a position z will feature a hyperbolic evolution of parameter z_R, as follows:

$$\omega(z) = \omega_0 \sqrt{1 + \left(\frac{z}{z_R}\right)^2}, \tag{II.12}$$

with $z_R = \frac{\pi n {\omega_0}^2}{\lambda_o}$, the Rayleigh range [$m$], which will be relative to the system's sensing depth of field, as depicted on Figure II.2. In this definition, the beam spot size is defined as the radius at amplitude $\frac{1}{e}$, while the Full Width at Half Maximum (FWHM) would be defined as [14] :

$$\mathrm{FWHM}(z) = 2\omega_{-3dB}(z) = \omega(z)\sqrt{2ln2}, \tag{II.13}$$

From this model, further qualitative observations can be articulated, especially when considering objects that are not in the Rayleigh range. In such an imperfect setup or considering large targets, beyond the sensing depth of field, resolution loss will obviously be experienced according to Equation II.12, and a reduction of the back coupled power towards the sensor is expected in a normal reflection configuration.

Now considering the far field asymptotic evolution, where $\theta = \frac{\lambda_0}{\pi n \omega_0}$ [rad], and a classical infinite-focal focusing scheme, a relation between the effective Numerical Aperture (NA) and the waist diameter, and so the achievable resolution, can be drawn as follows [9]:

$$2\omega_0 = \frac{4\lambda_0 f'}{\pi n \mathrm{D}} = \frac{4\lambda_0 \mathrm{N}}{\pi n} \simeq \frac{2\lambda_0}{\pi \mathrm{NA}}, \tag{II.14}$$

with $\mathrm{N} = \frac{f'}{\mathrm{D}} \simeq \frac{n}{2\mathrm{NA}}$ the f-number relative to the beam's aperture with D the lens diameter [m], f' the focal length [m] and $\mathrm{NA} = nsin(\theta)$, the numerical aperture. This inherent beam sensing point physical limitation, relative to the Gaussian waist, provides quantitative information when it comes resolution expectations in a focal imaging plane of for optical setup design and dimensioning. Further resolution concerns will be detailed in section II.3 for the design of diffraction limited imagers.

Spatial resolution assessment

From those theoretical concerns, several technical approaches are employable to experimentally assess the resolution of a focused point imaging system.

As a first and most advanced solution, the use of a sensor array would allow for an instantaneous recording of the intensity profile of a beam, in any given plane. In the terahertz spectral

range, unfortunately, this technique remains quite seldom used due to the high prices of such newly introduced devices, their technological availability as well as their sensitivity levels with respect to specific low power sources such as photo-mixing emitters. Their limited universality in term of broadband sensitivity, pixel pitch and array size only makes them suitable for either millimeter wave applications (with transistor based arrays), or high frequencies sensing (with bolometer arrays). Such tools yet ensure an extremely simplified setup alignment procedure and allow for a direct beam profile assessment.

A raster scan sampling of the plane of interest is also experimentally valid, but much more time consuming, and requires the use of a highly limited aperture detector. As a rationalization of this full 2D beam profile scan, the knife edge method [15, 16] makes use of the progressive obstruction of the beam, through the gradual insertion of a straight blade in the beam profile. Extensively integrated for the characterization of laser beam profiles and diameter extractions, for its characterization, it demonstrated a proper adequacy for terahertz systems as well [17]. The transmitted power as a function of the position of the blade through the beam path, will therefore be represented as the primitive function of the local intensity profile of the beam. In the case of a Gaussian beam, this power profile will follow an complementary error function evolution with $P(x_d) = \int_{-\infty}^{+\infty}\int_{x_d}^{+\infty} I(x,y)\,dxdy = K \times erfc\left(\frac{\sqrt{2}x_d}{\omega(z)}\right)$, from which $\omega(z)$ can be extracted.

In imaging oriented approaches, the use of test charts, or resolution charts, represents a wide spread solution. It allows for a quantitative assessment of the effective spatial resolution of a system, by quantifying the contrast ratio, generally defined through Equation II.15 wit I_{max} and I_{min} the respective maximal and minimal recorded intensity levels, obtained on elements of different sizes. Considering an unitary contrasted samples (contrast of 1 for the reflection or transmission of the chart itself), a threshold of typically 0.5 on the measured contrast ratio, through the sensing system, is considered for the resolution of a given element [17]. Such a target is depicted in Figure II.3 with the bidirectional USAF-1915 (U.S. Air Force - 1951) resolution chart. The resolution of each element, in line pairs per millimeter, $Res[lp.mm^{-1}]$, is described by Equation II.16, with Grp and El, the considered group and element number respectively. Table A.1 in Appendix A depicts the spatial resolution and relative line width of each element in such a chart, according to Equation II.16.

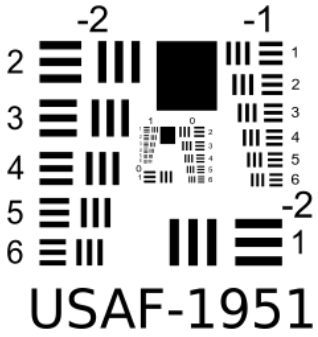

Figure II.3: USAF-1951 Test Chart.

$$C_r = \frac{I_{max} - I_{min}}{I_{max} + I_{min}} \tag{II.15}$$

$$Res[lp.mm^{-1}] = 2^{Grp + \frac{El-1}{6}} \tag{II.16}$$

II.2.2 Enhanced far-field sensing approaches

Related to those physical considerations, raster-scan imaging remains a conventional approach based on a focused beam single point sensing optical system, coupled to a relative sample displacement, for progressive pixel-by-pixel construction of its image. This well documented technique [1, 18] still remains an extensively used reconstruction process in the whole terahertz range, when using CW, FMCW as well as TDS systems. Since this approach represents a standard implementation, no attempt to get in the details of it have been pursued. Technical optimizations have still been elaborated and carried out for academic demonstration purposes. They have been

guided by specific problematics, and based on a wide sources and detectors availability, as a way to apprehend terahertz imaging related issues, more than for the pursue of their applicability.

Namely, two specific advanced setups are addressed in this work with a simultaneous transmission/reflection configuration, and a hybrid imaging setup allowing dual frequencies simultaneous and concomitant sensing, for which the optical geometries are depicted in Figure II.4.

As a recording mechanism, a simple homodyne detection scheme is often recommended through the use of a lock-in amplifier (LIA) [19, 20] paired with the selected sensor. A synchronized QCW emission, instead of direct CW, applied via an power chopping in order to perform signal denoising and achieve high measurement dynamic range, typically ranging from 40 dB up to 60 dB. An improvement to this detection scheme will be further addressed in section V.4, applied to high dynamics diffraction measurements, with the High Dynamic Range (HDR) scheme, applied to extend beyond the capabilities of a single lock-in detection.

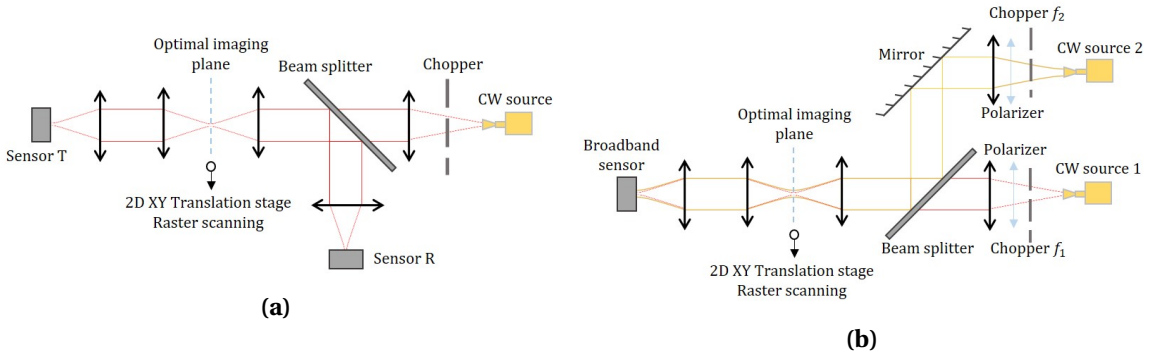

Figure II.4: Optical implementations for **(a)** a simultaneous transmission/reflection imaging setup and **(b)** a hybrid dual frequencies imaging setup in transmission configuration.

Transmission/reflection

The simultaneous transmission-reflection configuration, described in Figure II.4a, aims to broaden the suitability of CW terahertz imaging systems to a wider range of samples at a given imaging frequency. Indeed, as a rule of thumb, transparent materials remain more suitable for transmission sensing, while opaque samples or samples containing highly reflective or metallic parts would be restricted to reflection geometries.

In order to exploit this enhanced versatility to reach a didactic system, for primary tests, or high precision sensing and imaging, an integrated setup have been developed using a 2.5 THz mW-level Teracascade 1000 QCL source. It has been coupled with two identical pyroelectric sensors, completed by 2.5 THz coated HRFZ-SI lenses and a HRFZ-SI Beam Splitter (BS) in a compact system. An implementation in lower frequency bands have also been carried out to take advantage of better material transparencies. It features a tunable 75 GHz band, source, emitting 450 mW output power at 72 GHz, the TeraSchottky base unit, coupled with a broadband pyroelectric sensor in transmission, and a hemispherical Topas lens integrated HEMT sensor in reflection. On this optical configuration, simple PTFE lenses have been used with a sapphire wafer BS.

In each of those implementations, this measurement duality, between transmission and normal reflection sensing, is highlighted at the expense of a power loss in the probing arm, that is obviously induced by the introduction of a BS on the beam pathway. The availability of high power sources and sensitive detectors nevertheless ensure proper intensity measurements dynamic ranges approaching 50 dB.

The preponderance of this transmission/reflection duality is well depicted in Figure II.5a, with the 2.5 THz raster scan image of a Paris Navigo Transport pass. As it features a polymer side, it allows for the visualization of the internal RFID (Radio-frequency identification) tag and the backside inscriptions in transmission, and, in reflection, only features the engraved serial number due to the preponderance of the front-side reflected power. The metallic doped polymer side, on the

other hand, remains only exploitable on the reflection configuration with the visualization of several sample features, with the electronic card chip and imprinted logos.

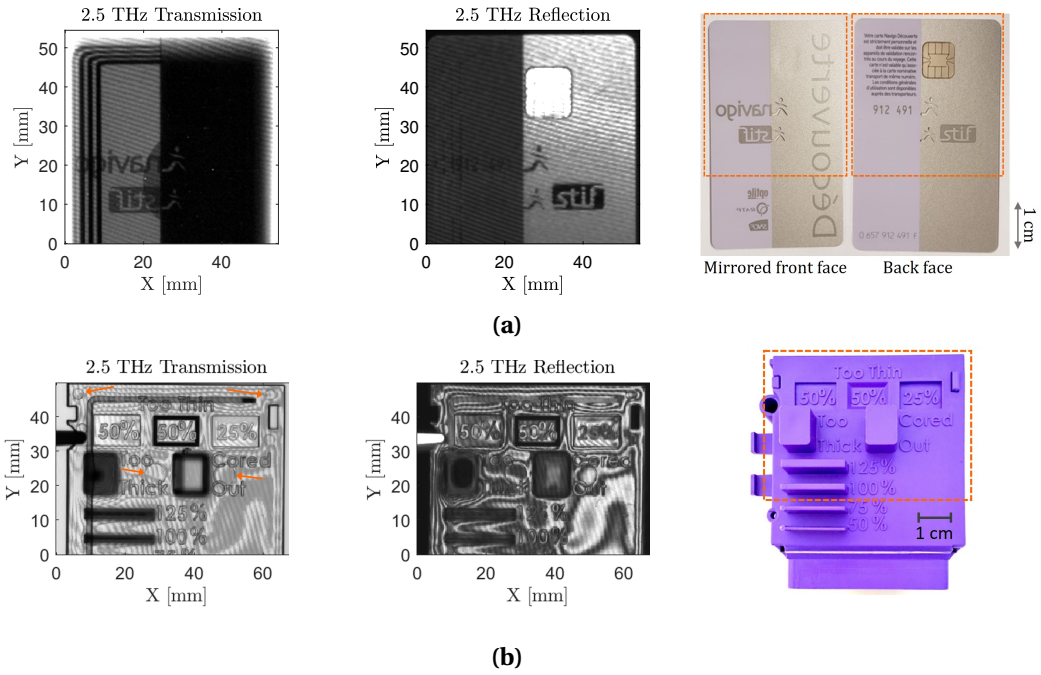

Figure II.5: Transmission and reflection images at 2.5 THz and visible depiction of **(a)** a Navigo transportation card and **(b)** a polymer injected sample.

The case of a transparent sample is depicted in Figure II.5b, with a representative inspection at 2.5 THz of the sample in transmission following a raster-scan reconstruction. It allows for the detection of features of interest, such as injection marks, pointed out through the orange arrows, and a proper depiction of structural elements. Even though the sensor sensitivity remains adequate, lower achievable SNR (Signal to Noise Ratio) are to be expected in the reflection configuration due to the relatively low refractive index and so, limited reflected power.

As one could observe, interference fringes are also noticeable in both images, due to the high coherence of the emission source, and the Michelson-like configuration of the optical setup. Such artifacts are not to be considered as alterations to those images, since coherent imaging mechanisms can lead to highly sensitive measurements [21]. Those interferences can account for several features, with first the angular miss-alignment of the sample with respect to the imaging system. This imperfection is related to the unidirectional fringes noticeable on the Navigo sample and polymer sample. From air-corner interference principle in Michelson configurations, an inter-fringe space of 1 mm would be equivalent to a 1.72° sample misalignment pitch when operating at 2.5 Thz. And secondly, topographic insights, perfectly depicted on Figure II.5b in reflection, are retrieved from thickness or refractive index inhomogeneities, in a similar fashion as cartographic topographic level lines mapping. The latest emerge from interferences between the reflected signals at each sample interface, acting as a Fabry-Perot cavity.

Simultaneous dual-frequencies sensing

Capitalizing on the trade-off between longitudinal resolution for focused single point sensing (see Equation II.14), and penetrability within materials, the development of a simultaneous concomitant dual frequency-setup prevents the need for multiple individual monochromatic scans to converge towards the most adequate frequency range for a given sample. It requires the implementation of a frequency source couple. Following the depiction of the optical setup given in II.4b, this particular integration features the aforementioned high power low frequency tunable source in the 75 GHz band, used at 72 GHz with the optimum emitting power of 450 mW, the Teraschot-

tky base unit. It is coupled to a 287 GHz, Gunn-based schottky multiplier source, emitting 14 mW. Once again at the expense of a reduction of the probing power, the introduction of a BS ensures a concomitant Gaussian waist sensing point for both frequencies. This point contrasts with most previous dual energy implementations [22, 23], where longer scan times were required along with additional image processing.

On the detection side, the use of a broadband detector is therefore necessary since the integration of multiple frequency specific waveguide integrated diodes would induce an additional optical complexification of the setup. The previously featured semi-metallic coupled pyroelectric power-meter, with a large detection area, traceable calibration, devellopped by SLT [24], has been implemented for its flat spectral sensitivity. Nevertheless, a partition between the two spectral contributions still has to be performed to properly retrieve the distinct images. This specific task was achieved in an indirect way thanks to the use of LIAs with chopped CW sources. The use of two specific modulation frequencies (f_1 and f_2) related to each optical source, allowed the sensor to be coupled to two distinct LIA channels, triggered on each of those modulation frequencies. In this particular case 240 Hz and 170 Hz respectively for the 287 GHz and 72 GHz sources. Specific precautions are nevertheless considered in order to avoid QCW cross-modulations of the spectral components, especially when using mechanical choppers. The use of cross-polarized sources allows for the insertion of additional polarizers in front of the eventual mechanical choppers to prevent an over-modulation emerging from the alternate source. In our case, a single polarizer was necessary in front of the 287 GHz mechanical chopper thanks to the electronic chopping of the 72 GHz source.

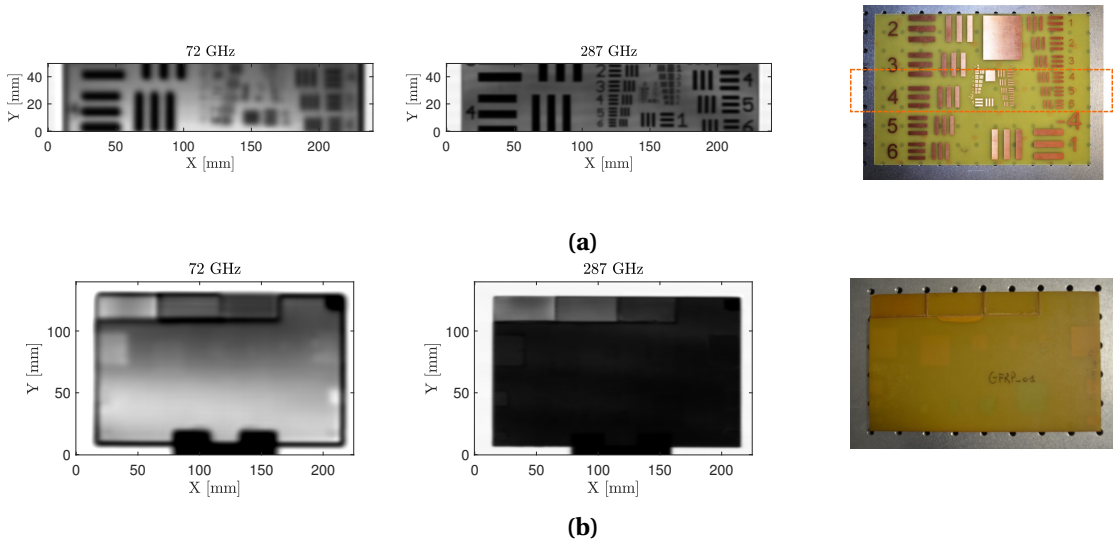

Figure II.6: 72 GHz, 287 GHz transmission images and Visible depiction of **(a)** a portion of an USAF 1951 Test-chart and **(b)** a fiber-glass composite material from DOTNAC project [25].

In order to highlight the capabilities of this dual-frequencies configuration, Figure II.6 depicts representative results on specific samples. With the central portion of the USAF 1951 test chart, realized from a metallic coated PCB, given in Figure II.6a, the frequency related spatial resolution impact is highlighted; with an achieved resolution of 3.5 mm, with the resolution of group -3 element 2 (outside of this specific scan), at 72 GHz, and a spatial resolution of 1 mm at 287 GHz, with the resolution of group -1 element 1 with an optical configuration featuring NA=0.5.

The impact of the PCB material transparency is also visible with a lower transmitted power at 287 GHz in comparison with the 72 GHz data, due to higher material absorption. This limited penetration depth at higher frequency is as well stressed out on Figure II.6b where a 5 mm thick fiber glass sample is under inspection. As one can notice on the full linear color scale images, the 72 GHz inspection, allows for the detection of hidden subtle materials inclusions while providing an adequate penetrability. On the other hand, the 287 GHz transmission image features a larger power loss across the whole sample. Only partially improved transmission levels are witnesses on

the thinner steps on top of the sample. A subtle identification of the main side inclusions remains achievable while the absorption level prevents an adequate measurement SNR in transmission for the observation of the central inclusions. This sample has been issued from the DOTNAC project [25], addressing the suitability of terahertz technologies in the field of non-destructive testing and inspection for high-end aeronautic materials.

Raster-scan imaging as a versatile prospection tool

More globally, beyond those somewhat innovative approaches, but still quite typical implementation schemes, several results emerged from the application of this standard method. Especially, during preliminary studies, they can be used extensively to provide proof of work when it comes to the suitability of terahertz and millimeter waves inspection towards specific samples and materials. Indeed they offer a high achievable spatial resolutions and high sensing dynamic range (typ. 50-60 dB for sub-second integration time using Lock-in Amplifiers), mainly limited by the source power stability over the measurement time and the detector noise. Additionally, the quite simplistic design of a raster-scan sensing and imaging setup ensures a large adaptability of the setup to the samples geometries.

Capitalizing on the wide availability of sources and sensors provided among the IMS lab and Lytid facilities, several of those simplistic integration have been carried out for a multitude of targeted materials and resolution adequacy tests. The resulting scans of the same opaque polymer injected sample in a variety of frequency bands, namely centered around, 75 GHz, 150 GHz, 300 GHz, 600 GHz and at 2.5 THz, in transmission configurations, are displayed in Figure II.7.

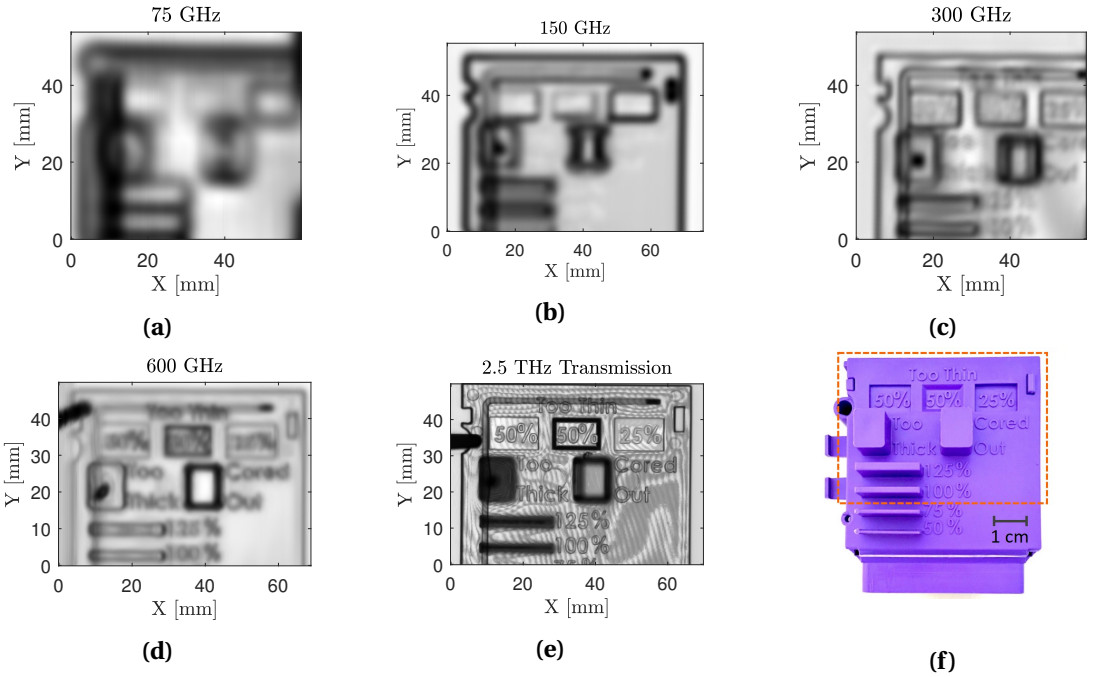

Figure II.7: Raster-scan transmission images of a polymer injected sample featuring a numerical aperture of NA=0.5, in the following frequency bands :**(a)** 75 GHz, **(b)** 150 GHz, **(c)** 300 GHz, **(d)** 600 GHz, **(e)** 2.5 THz, and **(f)** visible visualisation of the sample.

As resolution oriented systems, implemented with a NA=0.5 probing beam, spatial resolution levels ranging from approximately 3.5 mm in the 75 GHz band down to 125 µm at 2.5 THz have been witnessed in accordance with the Gaussian beam model, given in Equation II.14. To overcome such an optical intrinsic spatial resolution limitation, directly linked to the relatively large wavelengths in the sub-millimeter waves domain, several approaches of lateral resolution enhancement have already been published [26–28], mainly for FMCW sensors but offer additional optimization opportunities for further developments.

Pushing further towards volumetric inspection, the use of the limited sensing depth of field ensured by the focused sensing, allows for longitudinal selective imaging. Indeed, the sharpness of a given image can be used as a vector for 3D sensing through the implementation of algorithms such as Shape From Focus [29, 30], especially suitable for the reconstruction of bended 2D samples.

II.2.3 Towards 3D inspection with computed tomography

The very representative depiction of an object that can ensue from the raster scan sensing technique, through an optimized beam profile and sensing power stability, gives access to a 2D projection of a 3D object. From such projections, recorded under different angles, the tomographic reconstruction technique allows for a 3D depiction of the given sample. Extensively applied with CT using X-Rays, for radiographic medical imaging, such techniques rely on the use of the inverse Radon transform and can naturally be transposed to the Terahertz spectral range [31–35]. A projection itself can be formulated through the direct Radon transform, which in the case of a collimated sensing wave front, can be expressed as [36]:

$$\mathrm{R}_\Theta(\rho) = \int_{-\infty}^{+\infty}\int_{-\infty}^{+\infty} f(x,y)\delta\big(\rho - xcos(\Theta) - ysin(\Theta)\big)\,dxdy, \tag{II.17}$$

With Θ and ρ the angular and radial coordinates respectively $[rad]$, $\delta(\rho)$ the Dirac distribution, x and y, the spatial coordinate in the projection plane $[m]$, f the absorption profile of the sample $[m^{-1}]$ and R_Θ, the projection at a given angle, as represented in Figure II.8a.

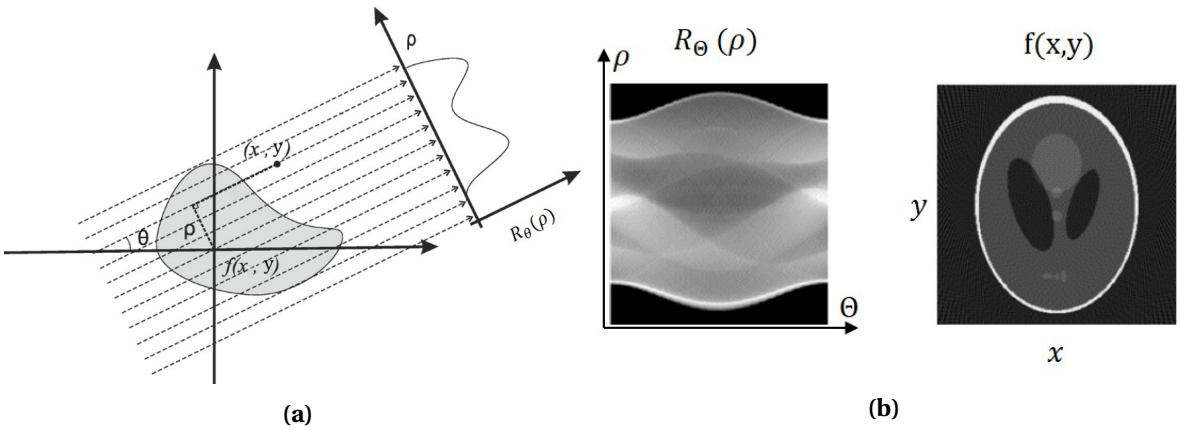

Figure II.8: **(a)** Projection principle for the Radon transform and **(b)** example of a sinogram and related reconstruction through the Filtered BackProjection, implementing an inverse Radon transform [37].

On a given rotation plane, a succession of these projections, R_θ, at each angle will give rise to a sinogram pattern (see Figure II.8b), which, in the Filtered BackProjection (FBP) approach, can be exploited, through the use of the inverse Radon transform, for the reconstruction of the absorption profile of the sample on this 2D plane as follows :

$$f(x,y) = \int_0^{\pi}\int_{-\infty}^{+\infty} \mathscr{F}(|\rho|)\mathrm{R}_\Theta(\rho)\delta\big(\rho - xcos(\Theta) - ysin(\Theta)\big)\,d_\rho d_\Theta, \tag{II.18}$$

with $\mathscr{F}$ the Fourier transform operator.

Such a direct reconstruction nevertheless induces non-negligible artifacts, especially when considering a limited number of projections, which is often the case for focused-point terahertz based approach, due to the time-consuming acquisition method. Iterative algorithms, such as THz-SART, THz-MLTR or OSC (Ordered Subsets Convex), on the other hand, have proven to produce reliable reconstructions for limited raster scan-based data-sets [22, 33, 38, 39]. Unlike for radiographic scans, additional phenomena have to be accounted for to reach reliable 3D reconstructions. Namely, the Gaussian beam profile limited depth of field, perfectly depicted in some

projections in Figure II.9a, can skew the reconstruction in offset parts of the sample, but can nevertheless be mitigated, as detailed in [40, 41]. Additionally, instead of only considering the Beer-Lambert law of absorption, interference patterns, diffraction or refraction induced power losses [42] can lead to strong impacts on the 3D numerical reconstruction capabilities of such processes.

The algorithm used in this work, implemented in the Noctylio software [43], took into account this limitation on the depth of field by considering the Gaussian beam expansion. No further attempt in considering refraction effects have been conducted due to the induced algorithmic complexification [44]. An example of such impact will be depicted on section II.3.6. Figure II.9, displays the application of this methodology on a PVC pipe, imaged at 287 GHz with NA=0.25 for the sensing optical configuration. Figure II.9a highlight a selection of recorded projections and Figure II.9b exhibits a clipped representation of the reconstructed 3D profile of the sample through the OSC algorithm [38]. A total of 60 projections over the π rotation motion have been recorded for this measurement.

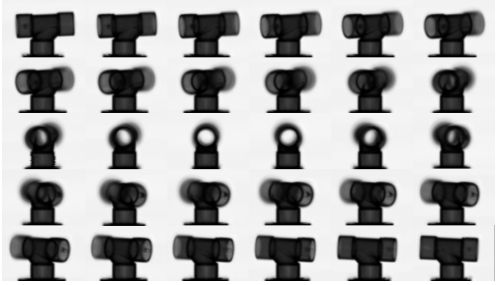

(a)

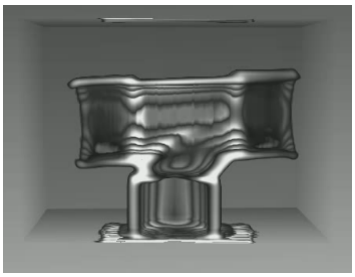

(b)

(c)

Figure II.9: (a) Selection of 2D projections of a PVC pipe junction sample, recorded through raster scanning at 287 GHz (NA = 0.25), **(b)** related 3D tomographic reconstruction and **(c)** visible range visualisation of the sample under inspection.

The consequent amount of data, required for the collection of such a projection-set, represents exactly the main limitation of such a standard raster scan approach: its extremely limited acquisition speed. Indeed, even though the final result is the most physically relevant depiction of the sample in the terahertz range, the use of LIAs homodyne detection remains an exceedingly slow process due to the required integration time for each measurement point, usuallly around 300 ms depending on the sensor. The recording of a typical 2D image, 128×128 pixels, would then require up to 1.5 hours and up to 4 days for a whole $[0; \pi]$ sinogram with a 3° angular pitch.

Pushed forward by the strong interest from high-end industrial fields, one of the key factor to reach the democratization of terahertz imaging would then be to overcome the acquisition speed limitation of this slow and teadious pixel-by-pixel raster scanning. Indeed, this process remains far from matching the required frame-rates targeted for quality control or non-destructive testing applications in an industrial context. To get closer from this goal, specific approaches have been perfected over the years [45]. As a classical integration using single pixel detectors [46, 47], compressed sensing encryption imaging can be performed with a monochromatic full field illumination, spatially modulated by random on/off amplitude masks. Such an obstructions through subsequent varying masks will allow a full image reconstruction using a single point detector. It can lead to an improved acquisition rate, while calling on a relatively simple optical configuration.

Nevertheless, direct full-field imaging remains the most adequate, when granted access to a suitable illumination power and sensitive array sensor. But even at this point, beside its relative high implementation cost, the simplest setup would still suffer strong limitations, related to the available power densities, the beam homogeneity as well as the interference artifacts induced by the source coherence. Such problematics will be extensively addressed in the next section, along with the depiction of the developed versatile illumination solution based on galvanometeric beam steering, that ensure the mitigation of those issues, to enable high performances real time full-field imaging.

II.3 Real Time Imaging

When it comes to full-field imaging, instead of focusing the probing optical power on a single sensing point, the illumination is spread over the whole imaging field, to get a full illumination of the scene. The selected optical source therefore plays a major role in the performances of the system, and has been facilitated by the wider availability of high power sources in the latest years. This criterion obviously goes hand in hand with the sensitivity or NEP of the sensor array, on the imaging side, to provide adequate measurement dynamics.

With once again the partition between the two extrema of the terahertz spectral range, as extensively addressed in I.3, a first solution can be oriented towards the low frequency spectral range, with electronic sources and transistor-based camera sensors, that would offer low resolution but high materials penetration. Towards higher frequency ranges, with bolometric cameras and power sources such as QCLs or gas lasers, much higher resolution standards would be ensured. This section will focus on the later, by capitalizing on the availability of a bolometric sensor array for the development of an imaging unit, therefore naturally coupled with the mW-power QCL sources provided by Lytid. Namely, most implemented elements have been optimized (AR coating, array sensitivity, QCL emission frequency, etc.) to work at 2.5 THz, unless specified otherwise.

Nevertheless, in complement with the implementation of the optical source and sensor array, the mounting of a lens is obviously necessary for far-field imaging purposes. It should ensure a recording of the whole scene by the sensor array, in an analogue fashion as for visible photography or microscopy. In this matter, no broadband or universal solution is yet available, and more globally, only limited on-shelf existing systems have been developed and require frequency-specific optimizations. Hence, as one of the cornerstone of an imaging solution, a versatile variable focal lens design has been initiated and manufactured.

II.3.1 Optical design

In the case of a diffraction limited optical design, the Airy disk Point Spread function (PSF) (see Figure II.10) [48] represents, its physical resolution limitation in far field, hence, its optimum response. Indeed, recorded images will result from the convolution of the object profile with this PSF when passing through an optical system. A minimization of the size of this PSF is therefore required. The radius of this Airy pattern, δ_{Airy} $[m]$, (delineated as the radius of the central peak, to the first zero) defines the best achievable resolution and is given by Equation II.19 with NA_{img}, the image-space numerical aperture.

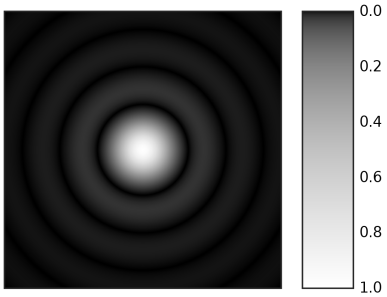

$$\delta_{Airy} = \frac{1.22\lambda_0}{2NA_{img}}, \tag{II.19}$$

Figure II.10: Simulated scaled Airy disk intensity profile.

If no care is procured to the design of a lens, for instance when using high curvature spherical interfaces, the PSF is altered by optical aberrations, such as spherical aberrations, field curvature or coma, resulting in the degradation of the achievable resolution. To minimize such tampering, the aspherisation of the lens surfaces represents a powerful tool for the mitigation of optical aberrations and can be performed through specific design software such as Zemax, OSLO or CodeV.

It allows for the generation of optimized exotic surface profiles, as depicted on Figure II.11, in accordance with Equation II.20 :

$$z(r) = \frac{s^2}{\mathrm{R}\left(1+\sqrt{1-(1+\mathrm{K})\frac{s^2}{\mathrm{R}^2}}\right)} + \alpha_4 s^4 + \alpha_6 s^6 + ..., \qquad \text{(II.20)}$$

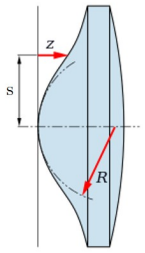

Figure II.11: Typical aspheric lens profile.

with s, the radial distance to the optical axis $[m]$, z the surface profile or sagitta $[m]$, R the first order spherical curvature radius of the surface $[m]$, K the conic constant and α_i the even polynomial correction coefficients.

The low-dispersion of HRFZ-Si, for the aspheric design performed on the Teralens (Figure II.12), ensures a broadband performance of the lens with on-axis diffraction limited use, as depicted on Figure II.12b through the spots diagram representations, where the surrounding circle represents the Airy diffraction limit. On-axis diffraction limited imaging is expected up to for 4 THz from wavelength scaling extrapolations. Additionally, in Figure II.12b, the related simulated 2.5 THz Modulation Transfer Function (MTF) is depicted. It details the achieved contrast ratio as a function of the objects spatial frequencies and relates to the amplitude of the Fourier transform of the spatial PSF [49].

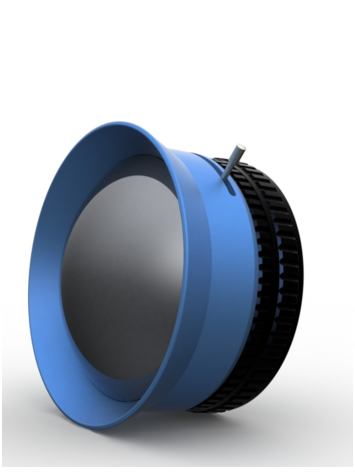

(a)

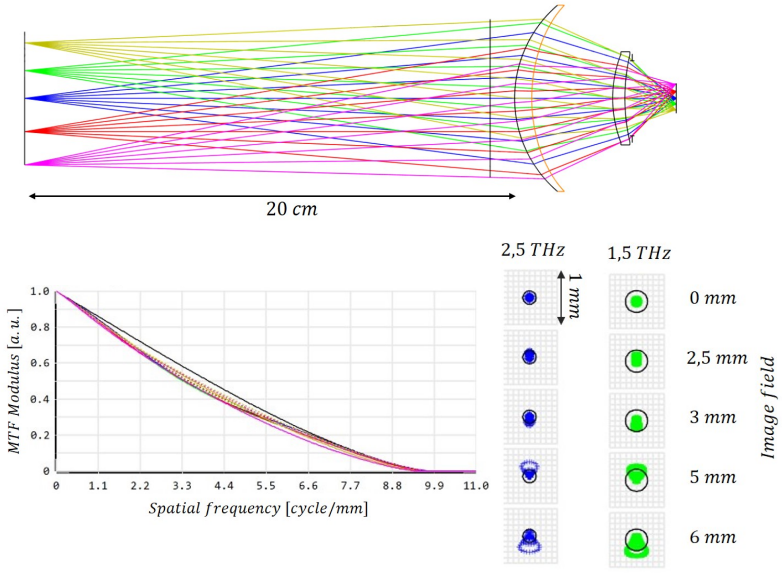

(b)

Figure II.12: (a) Rendering of the Teralens imaging lens with **(b)** technical specifications for the lens design, at the 20 cm optimized working distance, with the layout and ray tracing, the 2.5 THz Modulation Transfer Function over a 0-6 mm object field, and the related spot diagrams at 2.5 and 1.5 THz.

A selective single-layer Parylene coating, applied on each of the two lens interfaces, also ensures proper power transmission (> 90%), avoiding multiple 30% interface power losses induced by the high refractive index of this material ($n_{\mathrm{HRFZ-Si}} = 3.42$ [50]) (see Equation II.10). By preventing large reflections, it is minimizing unwanted coherent Fabry-Perot cavity interference patterns as well.

Additionally, as detailed in Equation II.19, the Numerical Apperture in the image space im-

pacts the achievable resolution, but should nevertheless allow practical back working distance for mechanical mounting concerns. On another note, as we can intuit from Figure II.12b, the NA in the object space will play an important role in term of collected optical flux, a characteristic of interest in the case of low illumination power applications. This specific implementation features NA_{obj} = 0.12 and NA_{img} = 0.50, for a working f-number of N=0.83. The additional integration of an adjustable mechanical iris allows for an artificial reduction of the NA. This feature is specifically integrated for Depth Of Field (DOF) improvement, obviously at the expense of the lateral resolution and collected flux eventually required for targeted applications.

This specific design has been optimized to be implemented with a front Working Distance (WD) of 20 cm. The additional focusing ring nevertheless ensures an adjustable working distance by fine-tuning the imaging array plane position with respect to the objective lens. A front working distance ranging from 10 to 35-40 cm is attainable, depending on the camera sensor array mechanical constraints. In its optimal configuration, it features an effective focal length of 40.8 mm for a magnification of ×0.22. Vignetting and distortion levels remains below 10% and 1.3% respectively over a 6 mm image field. Over the whole working distance span, several characterizations displayed magnification ranging from ×0,46, for a macro implementation at 10 cm WD, to ×0.115 at 35 cm WD for broad field imaging configurations. Further effective resolution performances will be detailed in section II.3.5. On this matter, the diffraction limited spot size does not represent the only limitation to the resolution since, unlike for single point raster scan imaging, the numerical resolution is fixed by the pixel pitch of the focal plane array.

II.3.2 Global full-field imaging problematics

Additionally to the required imaging optics, illumination source and adequate array sensor, several issues have to be accounted for as well when moving towards real time imaging.

First, scaling up from a single diffraction-limited illumination spot for raster scanning, up to the full image field to be illuminated, such a surface increase leads to a drastically lowered average power density. Along with the limited power of compact sources in the terahertz domain, this SNR loss may lead to extremely noisy or irrelevant images if no care is taken. Secondly, induced by a Gaussian-like beam profile, the object field could be exposed to a non-uniform radiation power, and the potential SNR in the vicinity of the optical axis generally reaches higher values than for off-axis contributions. And last but not least, due to most of terahertz sources high coherence [51], above several meters coherence length for single frequency QCLs [52, 53], and the complexity of optical paths through the sample and lenses, strong interference artifacts can appear [17, 54]. Highly contrasted interference patterns will therefore emerge in the sensor plane, which have for direct effect to irrevocably degrade the image quality, undoubtedly revoking the usefulness of such sample depictions.

Demonstrating this last problematic aspect of the light source's coherence when it comes to imaging capabilities, Figure II.13 displays a typical transmission acquisition at 2.5 THz, when no specific precautions are considered for the illumination system. The interference patterns from the illumination source are clearly observable, and eradicate the imaging and tomographic reconstruction capabilities with such a simplified system. They induce strong interference artifacts when interacting with the illuminated object, a parallelepiped of Teflon in this case. No corrective data processing seems practicable since the recorded inner interferogram is highly impacted by the geometry of the object itself.

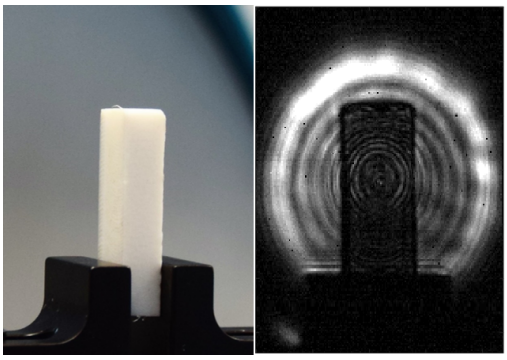

Figure II.13: Typical transmission image at 2.5 THz of a sample illuminated using a coherent QCL emitter [17].

In order to overcome this limiting factor, one solution consists in quickly modifying the co-

herent optical path, typically using wobbling mirrors [17]. Considering the relatively long time response of the sensors, a fast enough variation of the interference fringes on the image plane will lead to an averaging and smoothing of those coherent contributions on the recorded output signal. Such a time averaging, coupled to a random optical path variation by a reflecting or scattering optical scrambler, has been investigated for laser projection applications. It found suitability in averaging speckle patterns in the visible range, or interference patterns induced by the diffusion of wavelength-sized particles [55]. This solution has also been investigated in the terahertz range, demonstrating an improved illumination quality, but induces a significant radiation power loss due to the poor control over the scattered beam profile [17].

Another suited solution, to overcome these coherence issues, consists in fast assessing the position of a small size illumination beam, using galvanometric beam steering, to lead to the expected averaging mechanism over an imaging frame. This solution has already been investigated for sensors array characterizations [56], and has shown an improved beam homogenization. The full investigation of this solution, as a flexible illumination system in the terahertz range [57], will be fully addressed in this section. Not only to limit the impact of the interference fringes on the image, but also to ensure an enhanced control over the illuminated area, better suiting the size and the opacity of samples under inspection, it will provide an improved versatility and adaptability toward real-time imaging applications.

II.3.3 Technical implementation and available technologies

Such an implementation endured several iteration, that lead to the refining of the setup capabilities for optimized illumination and imaging performances. As a main component, the light source, it featured Lytid's multi-frequencies QCL source emitting up to 5 mW at 2.5 THz and 4.7 THz in its latest implemented version, combined with its automated laser selection auto-alignment unit. On the imaging side, coupled to the above mentioned aspherical f/0.8 and ×0.22 magnification silicon lens with 20 cm working distance, two distinct uncooled microbolometer sensor array focal planes have been implemented. The first generation INO IRXCAM (288 × 384 pixels matrix with 35 µm pitch), has been featured as the limited sensitivity development tool, and the I2S TZCAM microbolometer array (240 × 320 pixels matrix with 50 µm pitch), available in the final implementation, ensured better sensitivity performances and thermal stability.

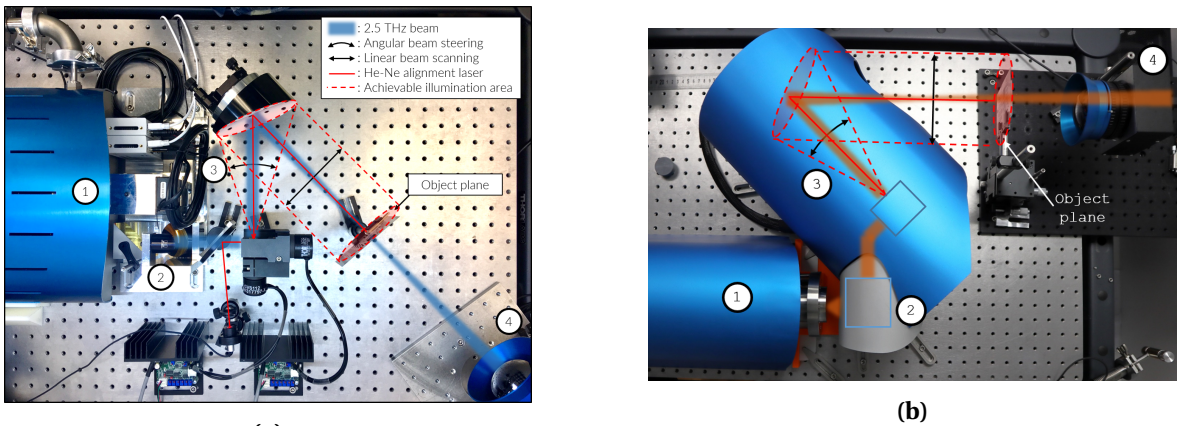

(a) **(b)**

Figure II.14: **(a)** Experimental imaging setup, and **(b)** fully integrated imaging system implementing (1) a Teracascade QCL source, (2) an auto-alignment unit for multi-spectral imaging, (3) the galvanometeric homogeneizer and (4) the imaging unit with either the first generation INO 288 × 384 microbolometer array or the 240 × 320 I2S TZCAM mounted with the aspherical f/0.8 ×0.22 coated silicon lens, Teralens.

In order to overcome the limiting artifacts induced by the high coherence of such THz QCL sources, and ensure the versatility of the imaging system, the homogeneous illumination in the object plane is performed via a combination of fast beam steering and adequate imaging exposure. This is achieved thanks to the implementation of a commercially available double mirror

galvanometer, allowing a controllable angular beam steering up to ±20° along both $\vec{x}$ and $\vec{y}$ axes, with a maximum oscillating frequency of 130 Hz. Each mirror is mounted on a voltage regulated motor, fed by a dedicated controller. A variety of voltage waveforms with adjustable offsets and amplitudes are thus achievable, in favor of the flexibility of the system. The second mirror of the galvanometer is located at the focal point of a 45° off-axis parabolic mirror (OAPM) with 4" diameter and 152.4 mm parent focal length (PFL), converting the unsuited angular beam steering in an appropriate linear lateral beam scanning towards the object plane and camera. For alignment and centering purposes, as well as illumination pattern visualization, the two experimental imaging systems feature a He–Ne alignment laser diode coinscident with the THz beam thanks to a 2 µm thick THz-transparent membrane.

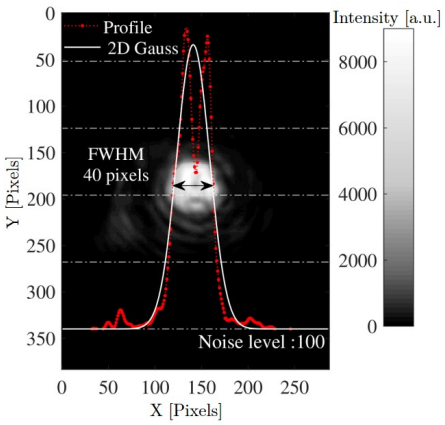

Figure II.15: Still beam profile in with related 1D profile and Gaussian fit.

In this illumination system, without galvanometric movement, the beam itself is still strongly impacted by the light source coherence, as depicted in Figure II.15, with a typical irregular beam shape. Its profile cut and related 2D Gaussian fit profile are plotted, and feature an estimated FWHM of 40 pixels on the INO 35 µm pitch array, equivalent to 1.40 mm in the imaging plane, or 6.4 mm in this given object plane.

Yet, to overcome those profile irregularities and reach a larger homogenized illumination area, a fast enough beam sweeping over the object plane averages the coherence artifacts. To properly fulfill this task, the galvanometer is set with high enough angular oscillation frequencies (F_x and F_y), as to ensure an averaged recording of the varying radiation pattern over a microbolometer array integration time. Intrinsically, the maximum camera frame rate, 50 FPS for INO IRXCAM (20 ms integration time) and 25 FPS for the TZCAM (40 ms integration time), is tightly linked to the minimal microbolometer temperature elevation and stabilization time response τ, evaluated to 10 ms for the CEA LETI-based TZCAM [58]. Considering a pixel exposure time much lower than τ would then result in an approximated linear averaging over the integration time of the given pixel. The maximum mirror's oscillating frequency of 130 Hz is then more than suitable for our averaging purposes in an unidirectional oscillation configuration, but remains necessary for the generation 2D complex patterns.

II.3.4 Illumination pattern principle

Based on optimized 2D Lissajous curves, extensively used for surface scanning [59, 60], the illumination pattern in the object plane is controlled by two sinusoidal voltage signals, fed into the galvanometer. Considering the linear voltage-to-angle conversion from each individual mirror of the galvanometer, the vertical and horizontal steering angles before the OAPM, with respect to its aperture center, $\alpha(t)$ and $\beta(t)$ respectively, are define as follow:

$$\begin{aligned} \alpha(t) &= A cos(2\pi F_x t + \phi) + \alpha_0, \\ \beta(t) &= B cos(2\pi F_y t) + \beta_0, \end{aligned} \tag{II.21}$$

with A and B, the angular amplitudes $[rad]$, F_x and F_y, the oscillation frequencies $[Hz]$, ϕ, the relative phase between the two channels introduced for pattern shaping improvement, and α_0 and β_0, additional offset angles from the OAPM optical axis $[rad]$. A proper optical alignment ensures that, the latest are null when the angular pattern is centered on the aperture axis of the OAPM, and so when the THz illumination pattern is generated along the imaging optical axis.

Now, considering the OAMP angular-displacement conversion, the beam off-axis distance, s, as a function of the paraboloid off-axis angle, θ_p $[rad]$, is given by:

$$s(\theta_p) = 2\mathrm{PFL}\left(\frac{1-cos(\theta_p)}{sin(\theta_p)}\right), \tag{II.22}$$

with PFL, the OAPM parent focal length $[m]$, equal to 152.4 mm in this setup. Taking into account the additional 45°off-axis angle, hence considering a relative horizontal displacement dictated by $s_x(\theta_p) = s(\theta_p) - s(45°)$, and a vertical displacement directly linked to Equation II.22, the illumination beam coordinate with respect to the OAPM axis is depicted by Equation II.23. Considering the maximum achievable galvanometer angle, a full coverage of the 4" OAPM aperture is achievable. For the sake of simplicity, those equations have been evaluated assuming a punctual angular beam steering at the OAPM focal point, thus neglecting the spacing between the two galvanometer's mirrors.

$$\begin{aligned} \mathrm{X}(t) &= s\Big(45° + \alpha(t)\Big) - s\Big(45°\Big) = s\Big(45° + \mathrm{A}cos(2\pi \mathrm{F}_x t + \phi) + \alpha_0\Big) - s\Big(45°\Big), \\ \mathrm{Y}(t) &= s\Big(\beta(t)\Big) = s\Big(\mathrm{B}\ cos(2\pi \mathrm{F}_y t) + \beta_0\Big). \end{aligned} \tag{II.23}$$

Equations II.23, then represents the time parametric equations related to the beam position at the object plan. The resulting beam trajectory is mapped out as a modified Lissajous pattern. Indeed, the OAPM projection, represented by $s(\theta_p)$, induces additional distortion on the illumination beam, with respect to the sinusoidal input Lissajous commands.

As a first observation, depicted in the examples of Figure II.16, the chosen scanning oscillation frequencies will obviously impact the scanning pattern. As a prerequisite, the horizontal and vertical frequency ratio, $\gamma = \frac{\mathrm{F}_y}{\mathrm{F}_x}$, is required to be rational to form a closed scanning pattern [61], in order to reach a repeatable background beam. Additionally, the repetition rate of the chosen pattern should fit the frame rate of the camera to avoid any rolling illumination artefacts and reach a stable background over the course of a measurement. In this matter, the implementation using the INO IRXCAM required a frame averaging factor of 8, to improve the SNR due to the lower sensitivity of the sensor, leading to a 6.25 FPS; while a full speed recording at 25 FPS gave exploitable SNRs using the TZCAM. Finally, the relative phase ϕ is a significant parameter to ensure the optimum homogeneity over the enlightened area on the sensor array. The least wanted configurations lead to degenerate paths in the case where $\phi = 0 mod(\frac{\pi}{\gamma})$, with the generation of a two-ways path that will manifestly maximize the lighting heterogeneity. Contrariwise, the optimum homogeneity is reached for the most favorable spatial distribution of the path way, achieved for $\phi = \frac{\pi}{2\gamma} mod(\frac{\pi}{\gamma})$ [62].

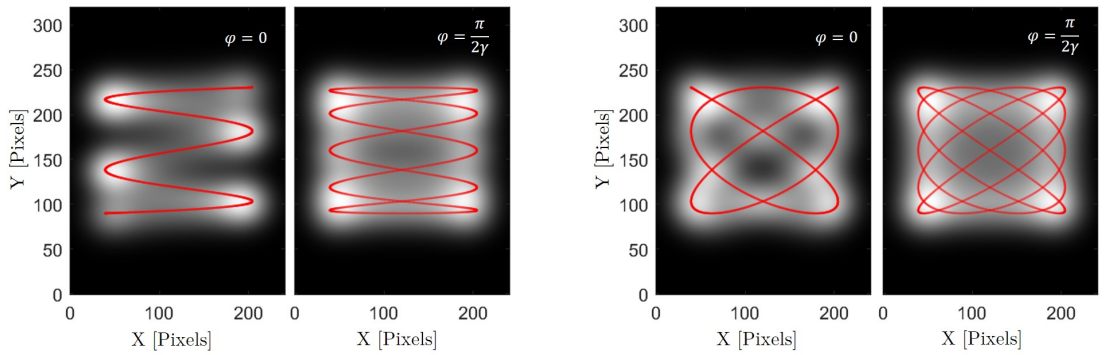

Figure II.16: Lissajous pattern and related simulated illumination pattern resulting from the beam Gaussian fit with parameters A = B = 6° for **(a)** $\gamma = 0.2$ with $\mathrm{F}_x = 125$ Hz, $\mathrm{F}_y = 25$ Hz with a 40 ms repetition rate (25 FPS cycle) and **(b)** $\gamma = 0.8$ with $\mathrm{F}_x = 125$ Hz, $\mathrm{F}_y = 100$ Hz with a 40 ms repetition rate. Both, degenerate ($\phi = 0$) and optimal coverage ($\phi = \frac{\pi}{2\gamma}$) patterns are depicted in their relative subfigure.

In order to illustrate those settings, Figure II.16 displays, for a square amplitude of A = B = 6°, two suitable beam steering patterns and related simulated illumination. Figure II.16a features $\gamma = 0.2$ when $F_x = 125$ Hz and $F_y = 25$ Hz, which mimics a smoothed sinusoidal raster-scanning illumination method, that leads to a 40 ms repetition rate, suitable with the full speed camera frame rate of 25 FPS. And similarly, Figure II.16b considers $\gamma = 0.8$ when $F_x = 125$ Hz and $F_y = 100$ Hz, a somewhat less intuitive pattern. One could easily intuit that changing the respective amplitudes, A and B, would affect the aspect ratio of the pattern, along the X and Y axis respectively, and affect in a similar way the effective illuminated area. The specific relative phase feature is depicted on Figure II.16 between similar patterns. Both relative phase values, $\phi = 0$ (degenerated pattern) and $\phi = \frac{\pi}{2\gamma}$ (optimum spatial coverage), are presented while only the latter is efficient when expecting a homogeneous illumination.

To simulate those equivalent terahertz illumination patterns on the sensors array, the 2D Gaussian fit from the still mode beam pattern (6.4 mm FWHM as depicted on Figure II.15) is averaged on every positions of the closed Lissajous path way in the image plane, considering the ×0.22 lens magnification factor and the OAPM projection. The simulation spatial resolution is set to be the 50 μm array pitch, while the integration time is set to 40 ms to ensure a complete closed loop Lissajous curve scan to fit the TZCAM parameters.

As depicted, the chosen frequencies F_x and F_y, and the relative phase ϕ are highly impacting the scanning pattern as well as the resulting homogeneity. The assessment of such heterogeneity represents an important criterion for imaging quality, and can be represented through a coefficient of variation, c_v, defined as the ratio of the standard deviation of the intensity σ by the mean value μ over the illuminated area, $c_v = \frac{\sigma}{\mu}$. This specific region of interest, at a given amplitude angle, can be considered as the image sections delimited by the extrema of the Lissajous beam path. In the ideal case of a perfectly homogeneous illumination, such as for single point raster-scanning, the coefficient of variation is equal to 0.

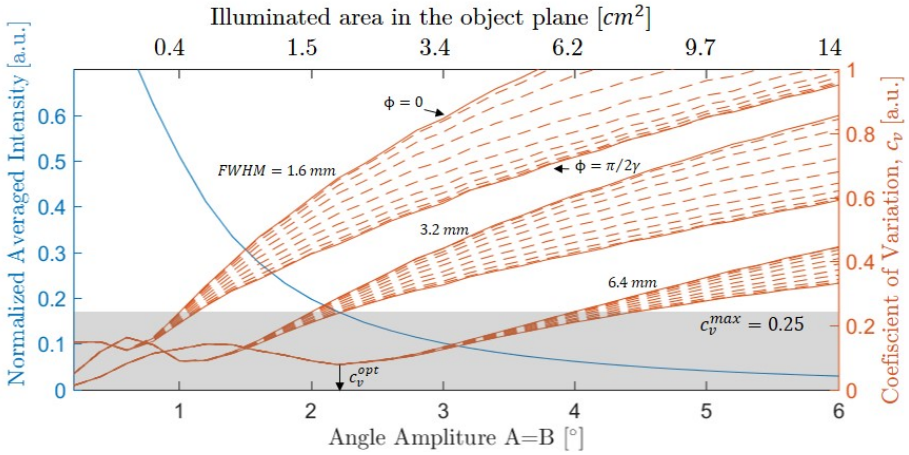

Figure II.17: Simulated pattern average intensity, illuminated area in the object plane and heterogeneity criteria, c_v, as a function of the oscillation amplitude angle, the beam diameter (FWHM) in the object plane and the relative phase ϕ at $\gamma = 0.8$.

Considering a square pattern command (A = B), the assessment of this heterogeneity is performed for angular amplitudes ranging from 0.2° to 6° in Figure II.17, for $\gamma = 0.8$, equivalent to the pattern of Figure II.16b. The simulated evolution of the average intensity with respect to the amplitude is displayed on the left axis and the heterogeneity criterion evolution, c_v is given on the right axis. On one hand, the higher the amplitude, the larger the illuminated area. As a consequence, due to the limited emission power, and so accounting for the quadratic drop of the power density, the average intensity naturally decreases with the amplitude. On the other hand, the heterogeneity criterion, c_v, calculated for various FWHM, exhibits a non-monotonous evolution, with an optimum located at oscillation amplitudes corresponding to pattern lobe size equal to the still

beam FWHM, ~ 2.3° in the case of the used 6.4 mm FWHM beam in the object plane. c_v then follows an expected monotonous increase, induced by the enlargement of the lobes of the Lissajous path way.

In addition, a consideration of several beam FWHM diameter have been processed to highlight its impact on the homogeneity of the illumination, and so the achievable imaging area. This point is as well depicted on Figure II.18. A pattern with $\gamma = 0.8$ with $F_x = 125$ Hz, $F_y = 100$ Hz and A = B = 6° is displayed for several beam diameters, 6.4 mm, 3.2 mm and 1.6 mm respectively, and denotes a visible and expected negative impact on the homogeneity when considering small beam diameters. From an integration perspective, it is then interesting to note that, in the given implementation, the beam size in the image plane can be easily adjusted by tuning the distance between the focusing 45° OAPM and the camera unit system. Indeed the OAPM induces a slightly converging steered beam profile, as depicted on both beam paths in Figure II.14. This characteristic represents another versatile aspect of the complete system that allows for small area high SNR illuminations or full-field, lowered power density imaging.

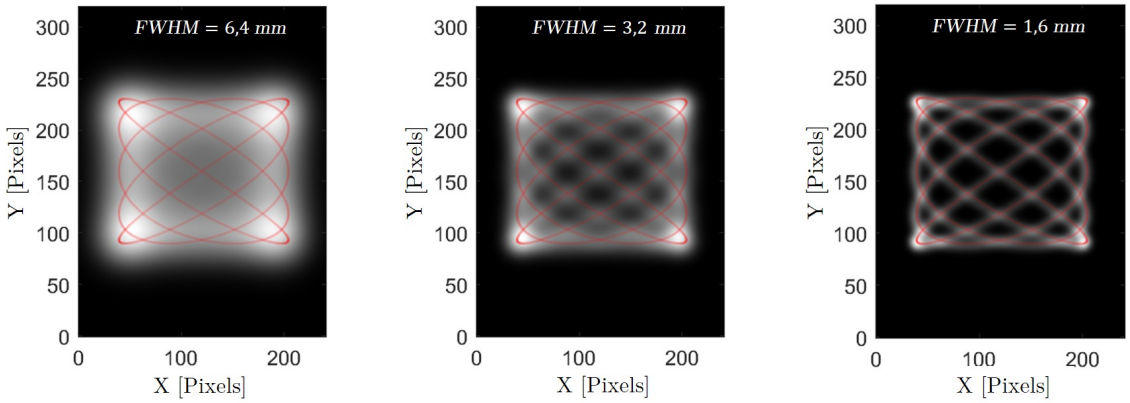

(a) **(b)** **(c)**

Figure II.18: Lissajous pattern and related simulated illumination resulting from the beam Gaussian fit with parameters A = B = 6°, $\gamma = 0.8$, $\phi = \frac{\pi}{2\gamma}$ with $F_x = 125$ Hz and $F_y = 100$ Hz, for a beam diameter in the imaging plan of **(a)** 6.4 mm, **(b)** 3.2 mm and **(c)** 1.6 mm.

Once more, the predominance concerning the impact of the relative phase, ϕ, is noticeable for small scanning beam diameters, or large amplitudes. Nevertheless, in a classic implementation, 6.4 mm FWHM beam diameter in the object plan, the impact of the relative phase and the Lissajous pattern factor γ on c_v remains limited. Considering an acceptable homogeneous illumination for $c_V < 0.25$ [63], an amplitude oscillation angle up to A = B = 4.5° is practicable.

II.3.5 Imaging capabilities

With an appropriate fast beam steering in regard to the camera response time, a homogeneous lighting is therefore achievable and allows for the generation of versatile illumination patterns, suitable for imaging without the appearance of critical interference patterns.

Full-field illumination for versatile real-time imaging

The previously depicted Lissajous patterns ensures a simplified optimization of the illumination to fit the area of interest of a sample, considering an adequate selection of the oscillation amplitudes A and B at a given γ and ϕ. From this proper illumination, optimized imaging capabilities, in particular the measurement dynamics, linked to the illumination power density, can be expected with respect to the sample dimension.

Capitalizing on the high sensitivity of the TZCAM, large object field imaging can easily be achieved as demonstrated in Figure II.19 where the previously encountered polymer sample is recorded with a 60 $mm \times 60\ mm = 36\ cm^2$ illuminated area, for A = B = 8° using adiameter beam configuration in the order of 6.4 mm . As a simple cadence comparison with the raster scan image of this same sample at 2.5 THz, highlighted in Figure II.7e, that required approximately 4 hours to record, the frame rate recording on the TZCAM ensures a full field single image retrieval every 40 ms.

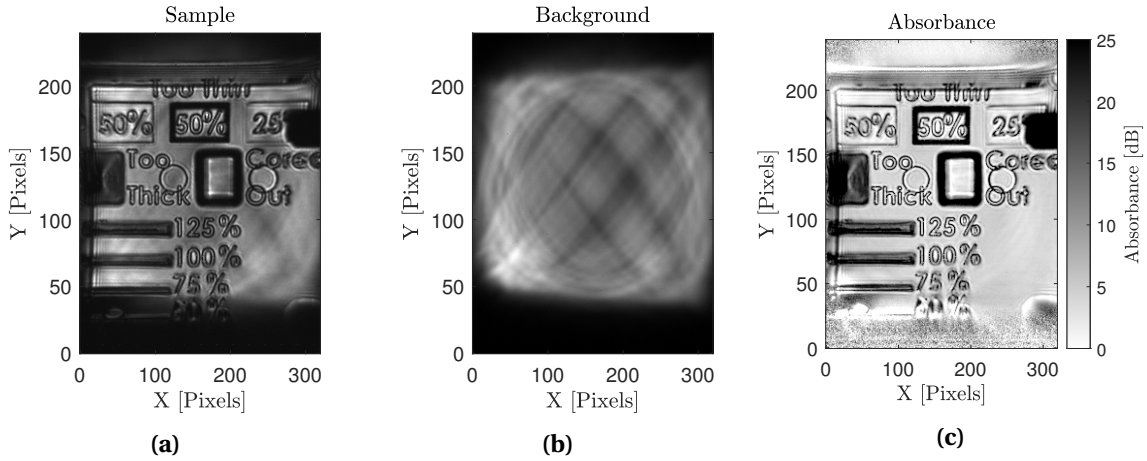

Figure II.19: **(a)** Full field transmission image of a polymer sample at 2.5 THz, **(b)** related background illumination pattern and **(c)** computed absorbance image.

Nevertheless, as one can notice in Figure II.19b, the background illumination is not perfectly homogeneous due to the large galvanometric amplitude. In transmission configuration, however, further image processing steps allow for improved visualization capabilities. Especially, in order to get rid of this illumination heterogeneity, a normalization with respect to the background image can then be performed and gives access to a relative transmission image of the sample. Furthermore, considering the exponential Beer-Lambert law, the application of a logarithmic scale to the transmission image leads to an absorbance image in decibels (see Equation II.24) and enables high dynamic range visualization, as depicted in Figure II.19c.

$$Abs = -10log_{10}\left(\frac{\Phi_{samp}}{\Phi_{back}}\right), \tag{II.24}$$

with Φ_{back}, the received optical flux from the background illumination without sample, and Φ_{obj}, the received optical flux in presence of the investigated object in the illumination path. It should once again be noted that the flux difference in presence of the sample can be induced by the material absorption, interfaces reflections, diffusion as well as beam refraction or diffraction.

Such a large field implementation nevertheless remains limited to weakly absorbing samples to keep an adequate SNR on the measurement. Yet, the intrinsic illumination field adjustment, through the amplitude parameters A and B, allows for an optimization of the illuminated surface area for power density management. Those parameters ensure to get a suitable SNR when considering either a higher absorbance sample, a lesser sensitive focal plane array or again a lower emission power. This approach is depicted in Figure II.20 on a bamboo leaf, where the illumination area has been unidirectionaly scaled to a biological slender sample that presents a water charged highly absorbing area and a mildly absorbing dry section. Such an optimization of the region of interest (A = 3° and B = 8° for an illuminated area of $22.5 \times 60\ mm^2$) establishes sensitive sensing (>40 dB at 25 FPS) on typically highly varying absorbance sample. The linear gray-scale depiction of a high dynamic range image remains unable to visually depict the sample in its entirety, due to a projection over a 256 shades scale. Indeed, it either compresses data in the region of interest (Figure II.20a) or saturates images section to spread out the region of interest over most of

the gray scale (Figure II.20b). On the other hand, global absorbance logarithmic depiction allows for high dynamic range visualization (Figure II.20b).

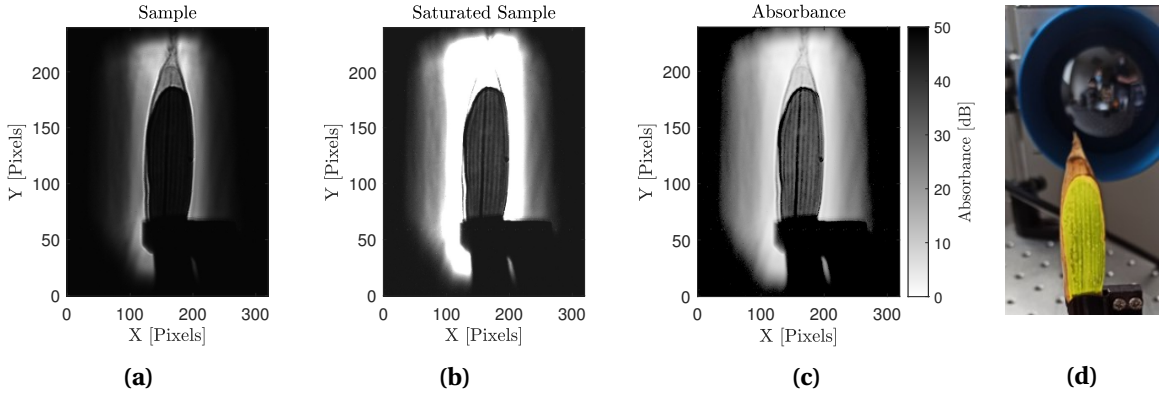

Figure II.20: **(a)** Optimized illumination full field transmission image of a drying bamboo leaf at 2.5 THz on full linear gray-scale, **(b)** on a saturated linear gray-scale, and **(c)** related logarithmic absorbance image with **(d)** a photograph of the sample.

Featuring an unoptimized system, with the use of the less sensitive INO IRXCAM first generation camera, operating with a frame rate of 6.25 FPS, and a lower QCL emission power of 1.3 mW, other examples of samples can be fond in Figure II.21. They depict an fitted smaller illumination areas to mitigate the loss of sensitivity and emission power while allowing for proper recording SNR levels. Figure II.21a displays the obtained raw image of a part of a 20 € bill holographic strip with galvanometer amplitude of A = B = 4° for a 30×30 mm^2 illuminated area, recorded at 6.25 Hz. Figure II.21b displays the processed absorbance image of a 3D printed alumina-based ceramic microfluidic chip, revealing internal 500 µm micro-fluidic channels, with optimized galvanometer amplitude of A = 4° and B = 2° for a 30×15 mm^2 illuminated area. This latest image made use of the adjustable working distance of the objective lens, allowing a larger magnification at lower working distance, 13 cm in this case, ensuring better resolution.

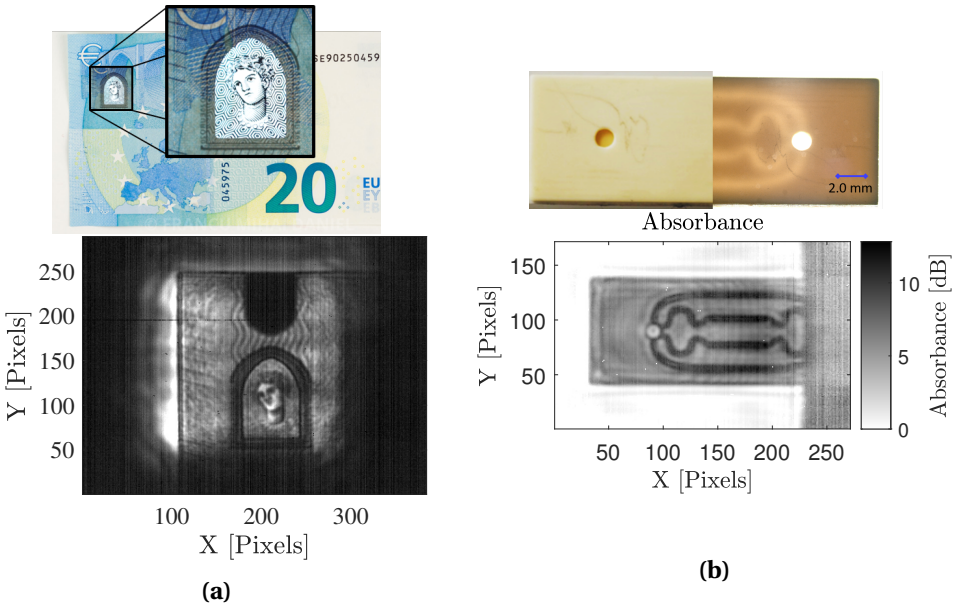

Figure II.21: **(a)** Photograph and transmission image of a 20 € bill holographic strip at 2.5 THz, **(b)** Photograph and 2.5 THz absorbance image of a 3D printed alumina-based ceramic micro-fluidic chip.

Thanks to the penetrability of THz waves in various dielectric materials, transmission imaging can offer a very interesting tool for non-destructive testing applications. The previously described setup (see Figure II.14b), initially implemented for transmission imaging, has been straightfor-

wardly converted to a reflection configuration by placing the camera next to the 45° OAPM, avoiding the additional insertion of a beam-splitter for this near normal integration. As the approach depicted above lies on the volumetric inspection capabilities of terahertz waves, no results recorded with this reflection configuration has been integrated to this work as they mainly assess surface sensing problematics.

Enhanced illumination approaches

Besides the improved versatility of the galvanometer implementation compared to other homogenization techniques, and thanks to the adaptable aspect of this approach, further improvements can be provided through different illumination schemes. They can be implemented to overcome the limited emission power of a source, the limited sensitivity of a sensor, or the high absorbance of a sample. The following tailored illumination processes have been implemented using the low sensitivity INO IRXCAM first generation focal plane array to depict the robustness of the galvanometer illumination system with respect to such limiting conditions. Similar implementations with the optimized TZCAM camera sensitivity can further improve the results and broaden the applicative spectrum of such a real-time illumination system. No attempt to duplicate those illumination scheme in this optimized setup have been pursued.

- Multi-exposure imaging

Firstly, to overcome the quadratic power density and SNR decrease in regard to the galvanometric amplitudes, A and B, a first solution, comparable to expanded raster scanning, consists in illuminating successively smaller areas of the sample. Along with the acquisition of such sub-images with adjacent limited illuminations areas, an improved power density leading to a better localized SNR is then achieved. This sequencing can indeed be performed by considering a smart combination of the oscillation amplitudes A and B, and a sequence of adequate offsets α_0 and β_0 to illuminate a different sample portion for each frame as depicted on Figure II.22. Combined with the background illumination measurement for the lighting pattern of each sub-figure, an adequate merging process is then practicable.

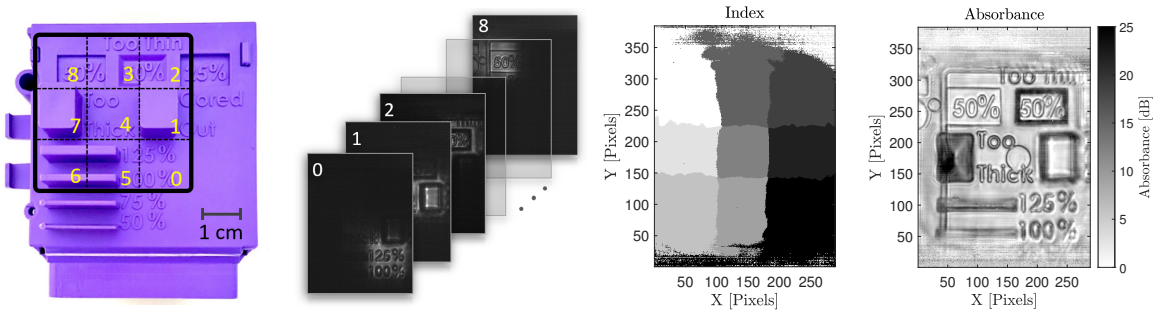

Figure II.22: **(a)** Photograph of the polymer injected sample under investigation [64],**(b)** stack of the unprocessed sequentially illuminated sub-images in transmission at 2.5 THz, **(c)** respective optimal sub-image index selection and **(d)** full-field absorbance reconstructed multi-exposure image.

A direct sum or averaging of the complete stack of images would grant a proper reconstruction of the image, but would result in the integration of the noise included in each non-illuminated area, remaining counterproductive and resulting in a similar SNR level as a single exposure full-field images. A more appropriate approach consists in carefully selecting the sub-image portion where its illumination is maximal. Such a selection process by considering the illumination background level of each sub-image, ensures an automated area selection on each sub-image in the final reconstruction, thus only considering the high SNR sections of each image. Figure II.22c depicts this automated selection level with the mapping of the most adequate sub-image index,

ranging from 1 to 9. On this reconstruction, further processing, for absorbance image generation, can then be performed, with, as a result an improved SNR image based on multiple smaller illumination area images (see Figure II.22d).

This implementation features a 3 × 3 illumination square subdivision with A = B = 2° amplitudes and α_0 and β_0 offsets combinations in { -4°; 0°; 4° }, in order to form the 9 adjacent sub-illumination areas. For such a 3 × 3 subdivision configuration, a 10 dB SNR improvement is achieved as the effective illumination area is divided by a factor of 9 in comparison with a single exposure full field illumination, requiring however a total image exposure under 2 seconds for a 6.25 FPS frame rate. Larger subdivision levels proved to further improve the SNR, being helpful for highly absorbent objects, larger illumination areas and for lower power sources or less sensitive detectors. Nevertheless, doing so will increase the required number of frames for a full acquisition, thus reducing the effective imaging frame rate. A frame rate/SNR trade-off can then be adequately selected, depending on the sample geometry and the desired recording rate.

With efforts towards industrial non-destructive testing, such sequential illumination technique can allow selective screening of several regions of interest in a sample. It then ensures optimum detection performances with high cadences while offering unrivaled flexibility.

- Linear illumination object scanning

Another similarly exotic implementation, especially suitable for inline inspection, or for sample with high form factors, consists in the generation of a linear illumination pattern, used for scanning through the orthogonal displacement of the object.

Such a continuous displacement of the object ensures the capability of simply concatenating part of the successive images to obtain a reconstruction of the sample. The width of this portion of image, to be considered in pixel count N_{pix}, is obviously linked to the object displacement speed, v_o $[m.s^{-1}]$, the camera frame rate, FPS $[s^{-1}]$, as well as the lens magnification, M, and the detector's pitch, δ_{pix} $[m]$ as follows:

$$N_{pix} = \frac{v_o M}{\delta_{pix} FPS} \tag{II.25}$$

A spatial sub-sampling of the image is nevertheless necessary to improve the reconstruction precision as N_{pix} might not be an integer, depending on the selected object displacement speed. A lateral concatenation of the N_{pix}-wide central portion of the illuminated area then leads to the recovery of the whole sample. Additionally, considering the width of the linear illumination pattern in comparison with this incremental frame displacementof the object, N_{pix}, a larger illuminated area can be considered for the concatenation through a laterally shifted averaging operation over a few frames. This operation will capitalize on the whole available illumination area in order to further improve the obtained SNR, and dampen any time related fluctuation.

However, due to the limitation of the imaging frame rate, capped by the oscillating frequency of the galvanometer in order to keep a repeatable and homogeneous illumination, the object displacement speed remains also limited to a few tens of millimeter per second in order to avoid any motion-induced blur.

Once again in this implementation, the same polymer sample has been investigated. A full height illumination of the sensor has been achieved for this 6.4 mm wide unidirectional lighting in the camera object plane, with B = 8° and A = 0° and a galvanometric frequency of F_y = 125 Hz. The unidirectional background illumination and a given frame of the object recording are shown in Figure II.23a and II.23b respectively, while the sample concatenated reconstruction is depicted in II.23c and featured an achieved 20 dB measurement dynamic range when implementing a five frame moving average.

Such an unidirectional oscillation setting of the galvanometer ensures a much faster pattern repetition rate, therefore providing a faster accessible frame rate, set to 25 FPS (averaging factor of 2 in the INO IRXCAM) for this measurement. It allows for an object displacement speed of 20 $mm.s^{-1}$ and so a measurement time under 4 seconds for the full sample scan. Reminiscent coherence artifacts remain noticeable on the vicinity of the illumination patterns due to the more

consistent nature of this steering scheme. Nevertheless, for the object reconstruction, only the homogenized part of the pattern is considered. A slight transverse amplitude, typ. A = 0.2 °, would as well ensure enhanced homogenization while maintaining the power density level.

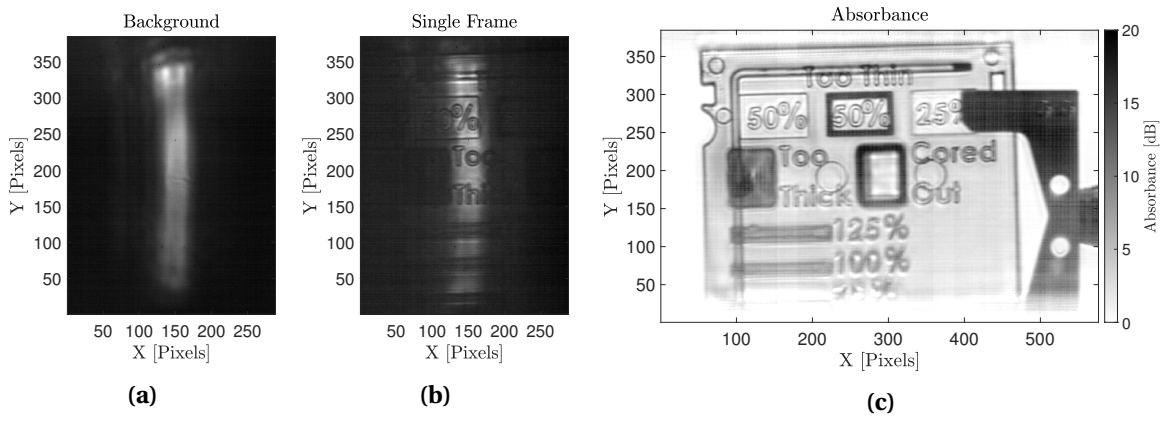

Figure II.23: **(a)**Background unidirectional illumination pattern, **(b)** single frame image corresponding to a narrow part of the polymer sample, **(c)** reconstructed absorbance image of the scanned object using a sub-sampling factor of 4, and shifted averaging over five frames for an object displacement of 20 mm^{-1}.

Lateral resolution assessement

The assessment of those illumination schemes demonstrated the versatility and adaptability of such an imaging system. Nevertheless, beside the achievable dynamics, which highly relies on the illumination area, focal array sensitivity and source emission power, the lateral resolution is also of interest as a crucial performance marker. Assuming a proper coherence artefact mitigation, this characteristic solely rely on the sensing unit, namely the objective lens and the focal plane array. The illumination scheme does not play any part in this assessment.

To evaluate this technical point, once again, the use of a resolution test-chart (see Figure II.3) is extremely suitable, even more when considering real time imaging, since it provides an immediate access to the lateral resolution information. Namely, for high frequency applications, such a test-chart has been printed on a transparency film projector sheet and, thanks to the opacity of the printer ink in the terahertz range, still offers a proper contrast ratio, even though not unitary.

Figure II.24 displays two measurements performed at 2.5 THz and 4.7 THz at 10 cm working distance, to take advantage of on the larger magnification factor of the objective lens, allowing for higher resolution levels. Those measurements have been performed using the high sensitivity TZCAM imaging unit, in correlation with a unique multi-chip Teracascade QCL source integrating both frequencies. In this context, no enhanced galvanometric illumination is required. A sole single frame illumination optimized on the area of interest was considered.

On both those measurements, a first pre-processing normalization step is performed, relative to the background illumination to get a normalized depiction of the sample. As one can notice, on the relative Intensities, the target contrast ratio, C_t, defined through Equation II.15, is quantified on a perfectly resolved item and remains non-unitary due to the power losses induced by the transparency sheet and the not full opacity of the printer ink. The normalization contrast ratio has then to be taken into account such that $\widehat{C}_{Grp,El} = \frac{C_{Grp,El}}{C_t}$ with indices Grp and El relative to the group number and element number respectively.

With such a normalization, at 10 cm WD, at 2.5 THz, contrast ratios of $\widehat{C}_{0,5} = 0.747$ and $\widehat{C}_{0,6} = 0.621$ are reached for elements 5 et 6 in the group 0 respectively while contrast ratio below 0.5 are measured for smaller elements. This leads to a resolution of 280 µm at 2.5 THz. In a similar procedure, a resolution of 222 µm is achieved at 4.7 THz with a contrast ratio of $\widehat{C}_{1,1} = 0.735$ and $\widehat{C}_{1,2} = 0.650$ for elements 1 ant 2 respectively in group 1.

Additional measurements have been performed at the optimized working distance of 20 cm

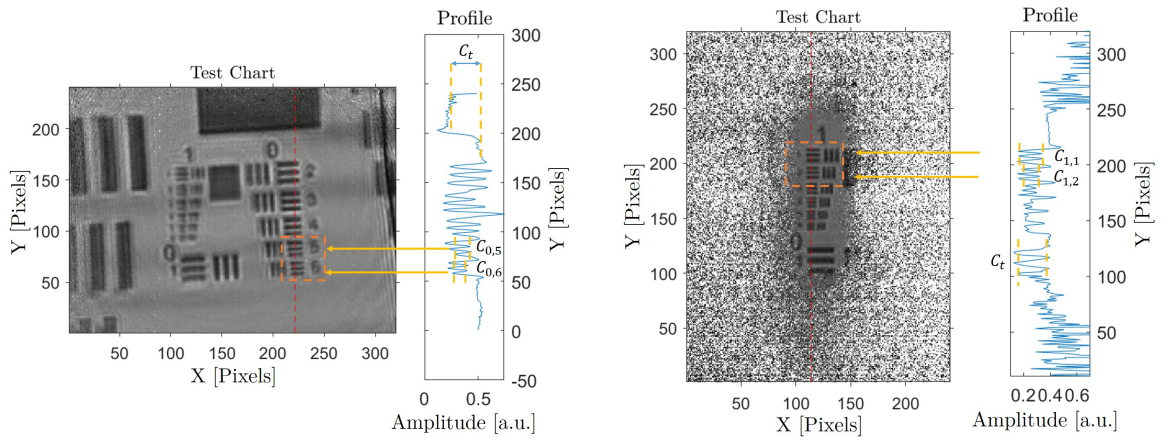

(a) **(b)**

Figure II.24: Normalized images at **(a)** 2.5 THz and **(b)** 4.7 THz at 10 cm working distance of a test chart portion, with respective amplitude profiles for contrast definition.

with achieved resolutions of 500 µm at 2.5 THz and 396 µm at 4.7 THz over a wider object frame due to the lowered magnification.

It is important to notice that, at this point, the resolution is not only limited by the optical configuration, and especially the imaging lens, but also restricted by by the numerical sampling dictated by the focal plane array pixel pitch. Indeed as a direct consequence of the spatial Nyquist sampling frequency, with respect to the MTF cut-off frequency of the objective lens, a subsampling of the image obviously impacts the achieved contrast ratio. The 50 µm array pitch in the object plane is then the main reason why the resolution obtained at 4.7 THz does not proportionally scale down from the 2.5 THz resolution.

Additionally, as one can notice, the 4.7 THz image features a much smaller illuminated area, for a similar optical configuration in regard with the 2.5 THz image. This limitation has been applied to ensure a viable power density and SNR, on the region of interest, despite the strong power losses endured by the 4.7 THz illumination beam. Indeed, in addition to the lower sensor array sensitivity at this frequency [65], the lens mono-layer anti-reflection coating does not fulfill properly its task, as it has been optimized for 2.5 THz radiation.

From similar dimensioning measurements, magnifications of ×0.46, ×0.22 and ×0.115 have been extracted at 10, 20 and 35 cm WD respectively, allowing for a wide range of imaging configurations.

II.3.6 Towards real-time 3D inspection

Thanks to the adequate achievable resolution and the steady illumination obtained with the galvanometric system, relevant sample depiction in the terahertz range can be achieved in real time. Similarly to the raster scan approach (see section II.2.3), those representative depiction of 2D sample projections can be implemented for 3D tomographic imaging, and recorded at much higher rates.

Indeed, an image, that would take several hours to be recorded using a raster scan approach, is instantaneously available through full-field imaging. More specifically, considering the 25 FPS frame rate and 240 × 320 array size, a recording rate of $1.92 \times 10^6 pixel.s^{-1}$ is achieved and is to be compared with the few recorded sample point per second for raster scan approaches. Through this real-time recording improvement, a full sinogram recording is easily obtained under 1 minute, to be placed in perspective with the several days, required for raster-scan tomographic inspections.

An example of this fast recording process is given in II.25 where a triple leaf has been investigated at 2.5 THz. A single-frame illumination, scaled to the leaf size was used as to take advantage of the full frame rate of the the TZCAM sensor while allowing for a proper power density.

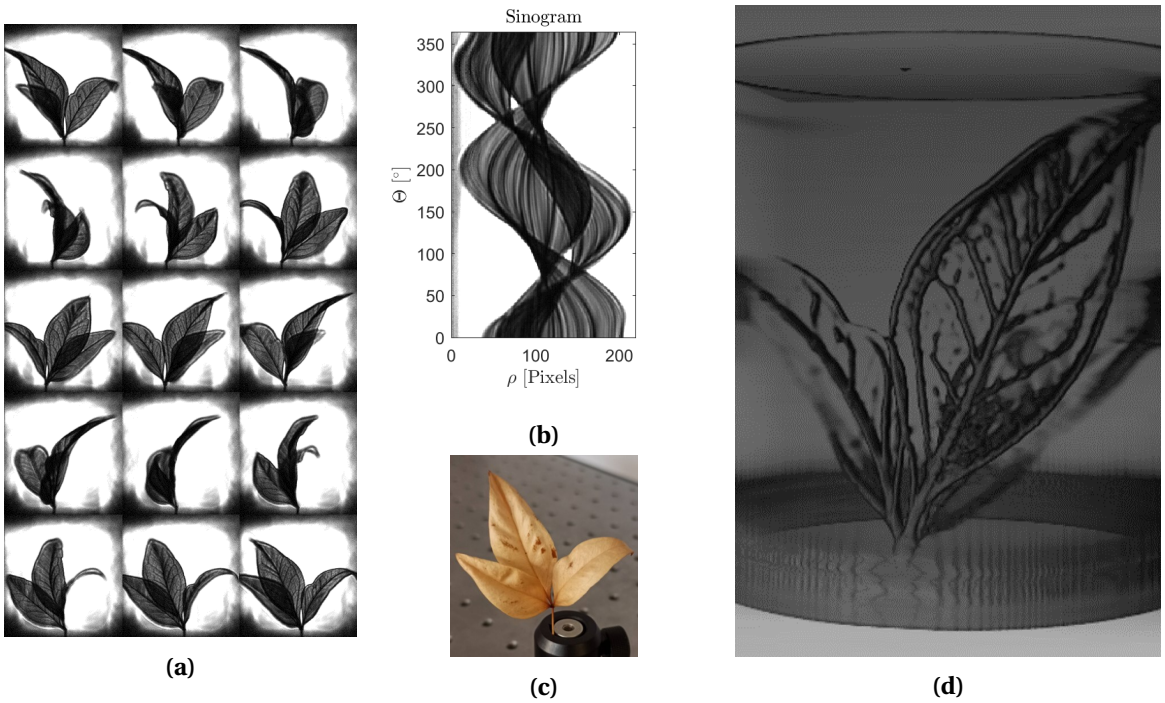

(a) **(b)** **(c)** **(d)**

Figure II.25: **(a)** Selection of 2D projections, recorded in real-time, **(b)** recorded sinogram relative to the central recording plane, **(c)** photograph of the sample, a triple tree leaf and **(c)** isometric view of the sample reconstructed by terahertz tomography.

A rotation speed of $25°.s^{-1}$ allowed for a total 360° sinogram recording in under 15 second with a projection every degree. With such an amount of projections, the classical FBP reconstruction algorithm can be implemented. The OSC [38], specifically designed for a convergence over few projections, necessary in the case of focused point tomography, is not required in this case. The final reconstruction is given in Figure II.25d while a central sinogram is given in Figure II.25b along with a selection of recorded projections in Figure II.25a.

In such an implementation, several artifacts are nevertheless noticeable in those reconstructions and remains inherent with the terahertz tomography technique. In particular, as one can notice on the 3D isometric sample visualization, a cylindrical surrounding of the reconstruction volume appears, and is induced by the reduced illumination levels on the side of the samples. Furthermore, a reduced contrast over the extremities of the leaves is noticeable and induced by the limited depth of field of the imaging system, decreasing the impact of such off-centered regions on the reconstruction. Several other inherent limitations are well depicted in Figure II.26a with the investigation of a pen cap at 2.5 THz with a similarly scaled single-frame illumination. Namely, the background brightness still suffers slight variations over the course of a full scan, impacting the exactitude of the reconstruction for low contrast samples and leading to the generation of a "cloudy" volume around the sample as one can see in II.26b. Additionally, the resolution power of 500 µm in the imaging plane also obviously impacts the smallest resolvable voxel in the reconstruction of the sample. Lastly, the impact of refraction can be noticeable on specific sample geometries, as depicted on several pen cap projections in the first line of Figure II.26a, with the lens-like shape of the pen cap handle. This behavior leads to particularly irrelevant tomographic reconstructions, as depicted on the back view of the pen cap holder in Figure II.26b.

Considering the same sample, a pen cap, a similar implementation, fully detailed in [57, 64], makes use of the versatility of the imaging system for tomographic reconstructions using a low power source. Namely, a 100 µW, 3.78 THz QCL source TC100 unit, developed by Lytid, allows for better lateral resolution. Nevertheless, because of this limited available power, a drastic reduction of the illuminated sample area is required. In order to provide a complete projections of the object under investigation, the multi-exposure imaging technique, presented in the Section II.3.5, is ex-

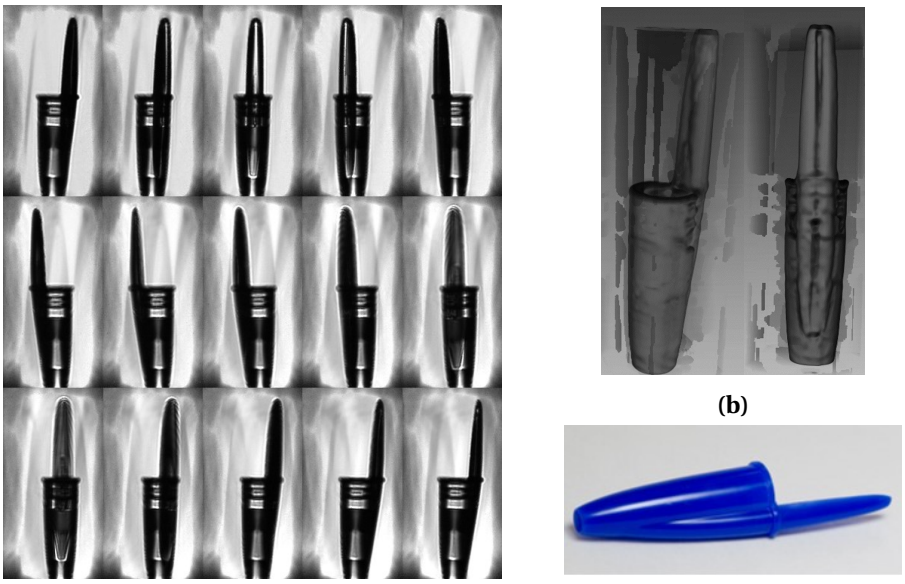

(a) **(b)** **(c)**

Figure II.26: **(a)** Selection of 2D projections, recorded in real-time, **(b)** isometric view of the sample reconstructed by terahertz tomography and **(c)**, photograph of the sample, a pen cap.

ploited using a 7×7 illumination subdivision of the field. It resulted in a 2 FPS video rate instead of the available 25 FPS, leading to a 25 s full frame acquisition time. A full sinogram recording under 15 minute was performed with a 5° angular step over $[0°, 180°]$.

II.4 Conclusion

The capabilities of a sensing system rely on the interaction of its given probing mean, in our case terahertz radiations, with its environment, or a given sample. In our macro-scale considerations, such light-matter interaction principles have been recalled with propagation and beam shaping concerns, refraction, power transmission and reflections, to enlight the results gathered in this work.

Namely, the standard raster scan imaging reconstruction scheme, through focused point sensing, is addressed with two enhancements that target the wider applicability of such a simplistic implementation. Simultaneous transmission/reflection sensing have been integrated in a first place to take advantages of the complementary information retrieved from each of those configurations. Concomitant multi-frequencies sensing at 72 and 287 GHz, has as well been covered, and rely on the compromise between material penetrability and achievable resolution at a given frequency.

More globally, a large portion of the spectrum has been explored with such imaging setups from lowest frequencies starting in the 75 GHz band, for low resolution, high penetrability capabilities, up to 2.5 THz by tampering with this trade-off when ranging to higher frequencies.

In fine, several hours recording for a single image allows this technique to remain a convenient, versatile, easily implementable and optimizible inspection tool, especially suitable for academia, but unambiguously prevents its expansion to larger application fields.

A solution to solve this recording time issue is to evolve towards real-time full field imaging. The naive use of an available, even though sparse, focal plane sensor array, coupled to a dedicated optical imaging lens and an adequate terahertz illumination source would, in such a simplistic configuration, still suffer major limitations.

Especially, in addition to the power density spreading when covering a large area, the inherent source coherence compels us to the integration of additional modules dedicated to the mitigation of interference artifacts in order to ensure representative real-time imaging. A specific solution has been developed, based on the principle of galvanometic fast beam steering for coherence induced

artifacts averaging. Additionally, thanks to the full control over the beam trajectory, such a development enables the use of this unit for power density management, through the assessement of the scanning area. It then ensures a large adaptability in term of accessible illumination scheme. Namely, the trade-off between available power density and effective imaging area can be swept from either wide field reduced power density for low absorption samples inspection, down to reduced investigation areas for better SNR and measurement dynamics. Even though the resulting illumination homogeneity remains far from the capabilities of raster-scanning techniques, thanks to the recording of the repeatable background illumination, the impact of the inhomogeneities is minimized through simplistic data processing steps. Hence, high quality transmission or absorbance images are achieved on a large variety of samples while ensuring video rate recording.

Specific advanced illumination approaches can as well be integrated for targeted applications such as the linear scanning, for 1D moving objects, or multi-exposure imaging for enhanced SNR performances at the expense of a lowered equivalent frame rate.

Such an integration of full-field array-based imaging could enable terahertz technologies to bridge with the standards of industrial inspection cadences, with the availability of video-rate visualizations in the terahertz domain. Especially when it comes to 3D imaging via tomographic reconstruction, orders of magnitude of improvements on this matter have been witnessed with the highly simplified recording setup. The real-time full frame collection then allows for a complete terahertz sinogram collection under a minute. Even so, at this point, the subsequent limitation is deported to the demanding additional data processing.

This need for computational power for 3D reconstruction assessment remains one limitation of CW measurement schemes when it comes to volumetric inspection. Contrariwise, the longitudinal sensing embedded in the FMCW procedure allows for simplified 3D sensing and will be extensively addressed in the coming chapter.

II.5 Bibliography

[1] Yumeng Cui, Wenjie Fu, Xiaotong Guan, Min Hu, Yang Yan, and Shenggang Liu. Experiment studies on two-dimension terahertz raster scan imaging. *Journal of Infrared, Millimeter, and Terahertz Waves*, 33(5):513–521, 2012. 58, 62

[2] Gyeongsik Ok, Hyun Jung Kim, Hyang Sook Chun, and Sung-Wook Choi. Foreign-body detection in dry food using continuous sub-terahertz wave imaging. *Food control*, 42:284–289, 2014.

[3] Cheng-Wu You, Chengchangfeng Lu, Tian-Yi Wang, Shun-Rong Qian, Zhen-Gang Yang, Ke-Jia Wang, Jin-Song Liu, and Sheng-Lie Wang. Method for defect contour extraction in terahertz non-destructive testing conducted with a raster-scan thz imaging system. *Applied optics*, 57(17):4884–4889, 2018. 58

[4] Timothy D Dorney, Richard G Baraniuk, and Daniel M Mittleman. Material parameter estimation with terahertz time-domain spectroscopy. *JOSA A*, 18(7):1562–1571, 2001. 58

[5] Frank L Pedrotti, Leno M Pedrotti, and Leno S Pedrotti. *Introduction to optics*. Cambridge University Press, 2017. 58

[6] Frédéric Garet, Maxence Hofman, Jérôme Meilhan, François Simoens, and Jean-Louis Coutaz. Evidence of mie scattering at terahertz frequencies in powder materials. *Applied Physics Letters*, 105(3):031106, 2014. 59

[7] Lord Rayleigh. Xxxiv. on the transmission of light through an atmosphere containing small particles in suspension, and on the origin of the blue of the sky. *The London, Edinburgh, and Dublin Philosophical Magazine and Journal of Science*, 47(287):375–384, 1899.

[8] Julius Adams Stratton. *Electromagnetic theory*, volume 33. John Wiley & Sons, 2007. 59

[9] Amnon Yariv and Pochi Yeh. *Photonics: optical electronics in modern communications*. Oxford University Press, 2007. 59, 61

[10] Okan K Ersoy. *Diffraction, Fourier optics and imaging*, volume 30. John Wiley & Sons, 2006. 60

[11] Doris L Caballero. A theoretical development of exact solution of reflectance of multiple layer coatings. In *Journal of the Optical Society of America*, volume 36, pages 710–711. AMER INST PHYSICS CIRCULATION FULFILLMENT DIV, 500 SUNNYSIDE BLVD, WOODBURY . . . , 1946. 60

[12] Antonin Vasicek. Sur la réflexion de la lumière sur des verres supportant des couches minces multiples. *Journal de Physique et le Radium*, 11(7):342–345, 1950. 60

[13] Leroy D Dickson. Characteristics of a propagating gaussian beam. *Applied Optics*, 9(8):1854–1861, 1970. 60

[14] Kiarash Ahi. Mathematical modeling of thz point spread function and simulation of thz imaging systems. *IEEE Transactions on Terahertz Science and Technology*, 7(6):747–754, 2017. 61

[15] Yi Chiu and Jiun-Hung Pan. Micro knife-edge optical measurement device in a silicon-on-insulator substrate. *Optics express*, 15(10):6367–6373, 2007. 62

[16] John M Khosrofian and Bruce A Garetz. Measurement of a gaussian laser beam diameter through the direct inversion of knife-edge data. *Applied optics*, 22(21):3406–3410, 1983. 62

[17] Jean-Baptiste Perraud. *Reconstructions rapides d'images en régime térahertz 3D*. PhD thesis, Bordeaux, 2018. viii, 62, 71, 72

[18] Daniel M Mittleman. Twenty years of terahertz imaging. *Optics express*, 26(8):9417–9431, 2018. 62

[19] John H Scofield. Frequency-domain description of a lock-in amplifier. *American journal of physics*, 62(2):129–133, 1994. 63

[20] RF User's Manual Model SR844. Lock-in amplifier standford research systems. *Inc., Sunnyvale, CA*, 1997. 63

[21] Jon L Johnson, Timothy D Dorney, and Daniel M Mittleman. Enhanced depth resolution in terahertz imaging using phase-shift interferometry. *Applied Physics Letters*, 78(6):835–837, 2001. 64

[22] Benoit Recur, Hugo Balacey, Jean-Baptiste Perraud, Jean-Paul Guillet, Bruno Bousquet, and Patrick Mounaix. Towards a 3d material characterization using dual-energy thz tomography. In *2014 39th International Conference on Infrared, Millimeter, and Terahertz waves (IRMMW-THz)*, pages 1–2. IEEE, 2014. 65, 67

[23] Hugo Balacey, Jean-Baptiste Perraud, J Bou Sleiman, Jean-Paul Guillet, Benoît Recur, and Patrick Mounaix. Processing sequence for non-destructive inspection based on 3d terahertz images. In *Infrared, Millimeter-Wave, and Terahertz Technologies III*, volume 9275, page 92750J. International Society for Optics and Photonics, 2014. 65

[24] https://www.pyrosensor.de/standard-924644.html. 65

[25] https://cordis.europa.eu/docs/results/266320/final1-final-report-dotnac.pdf. viii, 65, 66

[26] Tak Ming Wong, Matthias Kahl, Peter Haring Bolívar, and Andreas Kolb. Computational image enhancement for frequency modulated continuous wave (fmcw) thz image. *Journal of Infrared, Millimeter, and Terahertz Waves*, 40(7):775–800, 2019. 66

[27] Zhenyu Long, Tianyi Wang, ChengWu You, Zhengang Yang, Kejia Wang, and Jinsong Liu. Terahertz image super-resolution based on a deep convolutional neural network. *Applied optics*, 58(10):2731–2735, 2019.

[28] Yade Li, Weidong Hu, Xin Zhang, Zhihao Xu, Jiaqi Ni, and Leo P Ligthart. Adaptive terahertz image super-resolution with adjustable convolutional neural network. *Optics Express*, 28(15):22200–22217, 2020. 66

[29] J-B Perraud, J-P Guillet, O Redon, M Hamdi, F Simoens, and P Mounaix. Shape-from-focus for real-time terahertz 3d imaging. *Optics letters*, 44(3):483–486, 2019. 67

[30] Shree K Nayar and Yasuo Nakagawa. Shape from focus. *IEEE Transactions on Pattern analysis and machine intelligence*, 16(8):824–831, 1994. 67

[31] Jean Paul Guillet, Benoît Recur, Louis Frederique, Bruno Bousquet, Lionel Canioni, Inka Manek-Hönninger, Pascal Desbarats, and Patrick Mounaix. Review of terahertz tomography techniques. *Journal of Infrared, Millimeter, and Terahertz Waves*, 35(4):382–411, 2014. 67

[32] A Brahm, M Kunz, S Riehemann, G Notni, and A Tünnermann. Volumetric spectral analysis of materials using terahertz-tomography techniques. *Applied Physics B*, 100(1):151–158, 2010.

[33] A Brahm, A Wilms, M Tymoshchuk, C Grossmann, G Notni, and A Tünnermann. Optical effects at projection measurements for terahertz tomography. *Optics & Laser Technology*, 62:49–57, 2014. 67

[34] Alexandre Duhant, Meriam Triki, and Olivier Strauss. Terahertz differential computed tomography: a relevant nondestructive inspection application. *Journal of Infrared, Millimeter, and Terahertz Waves*, 40(2):178–199, 2019.

[35] Holger Quast and Torsten Loffler. 3d-terahertz-tomography for material inspection and security. In *2009 34th International Conference on Infrared, Millimeter, and Terahertz Waves*, pages 1–2. IEEE, 2009. 67

[36] Sigurdur Helgason and S Helgason. *The radon transform*, volume 2. Springer, 1980. 67

[37] Nicholas E Protonotarios, George A Kastis, and Athanassios S Fokas. A new approach for the inversion of the attenuated radon transform. In *Mathematical Analysis and Applications*, pages 433–457. Springer, 2019. viii, 67

[38] Benoît Recur, Hugo Balacey, J Bou Sleiman, Jean-Baptiste Perraud, J-P Guillet, Andrew Kingston, and Patrick Mounaix. Ordered subsets convex algorithm for 3d terahertz transmission tomography. *Optics express*, 22(19):23299–23309, 2014. 67, 68, 83

[39] Lawrence A Shepp and Yehuda Vardi. Maximum likelihood reconstruction for emission tomography. *IEEE transactions on medical imaging*, 1(2):113–122, 1982. 67

[40] Benoît Recur, Jean-Paul Guillet, Inka Manek-Hönninger, Jean-Christophe Delagnes, William Benharbone, Pascal Desbarats, Jean-Philippe Domenger, Lionel Canioni, and Patrick Mounaix. Propagation beam consideration for 3d thz computed tomography. *Optics express*, 20(6):5817–5829, 2012. 68

[41] Hugo Balacey, Benoit Recur, Jean-Baptiste Perraud, Joyce Bou Sleiman, Jean-Paul Guillet, and Patrick Mounaix. Advanced processing sequence for 3-d thz imaging. *IEEE Transactions on Terahertz Science and Technology*, 6(2):191–198, 2016. 68

[42] Emmanuel Abraham, Ayesha Younus, Cédric Aguerre, Pascal Desbarats, and Patrick Mounaix. Refraction losses in terahertz computed tomography. *Optics Communications*, 283(10):2050–2055, 2010. 68

[43] http://www.noctylio.com/. 68

[44] Jens Tepe, Thomas Schuster, and Benjamin Littau. A modified algebraic reconstruction technique taking refraction into account with an application in terahertz tomography. *Inverse Problems in Science and Engineering*, 25(10):1448–1473, 2017. 68

[45] Hichem Guerboukha, Kathirvel Nallappan, and Maksim Skorobogatiy. Toward real-time terahertz imaging. *Advances in Optics and Photonics*, 10(4):843–938, 2018. 68

[46] Claire M Watts, David Shrekenhamer, John Montoya, Guy Lipworth, John Hunt, Timothy Sleasman, Sanjay Krishna, David R Smith, and Willie J Padilla. Terahertz compressive imaging with metamaterial spatial light modulators. *Nature Photonics*, 8(8):605–609, 2014. 68

[47] Wai Lam Chan, Kriti Charan, Dharmpal Takhar, Kevin F Kelly, Richard G Baraniuk, and Daniel M Mittleman. A single-pixel terahertz imaging system based on compressed sensing. *Applied Physics Letters*, 93(12):121105, 2008. 68

[48] George Biddell Airy. On the diffraction of an object-glass with circular aperture. *Transactions of the Cambridge Philosophical Society*, 5:283, 1835. 69

[49] Glenn D Boreman. *Modulation transfer function in optical and electro-optical systems*, volume 4. SPIE press Bellingham, WA, 2001. 70

[50] http://www.tydexoptics.com/products/thz_optics/thz_materials/. 70

[51] Lorenzo Valzania, Yuchen Zhao, Lu Rong, Dayong Wang, Marc Georges, Erwin Hack, and Peter Zolliker. Thz coherent lensless imaging. *Applied optics*, 58(34):G256–G275, 2019. 71

[52] L Mahler, Alessandro Tredicucci, and MS Vitiello. Quantum cascade laser: a compact, low cost, solid-state source for plasma diagnostics. *Journal of Instrumentation*, 7(02):C02018, 2012. 71

[53] Andriy A Danylov, Thomas M Goyette, Jerry Waldman, Michael J Coulombe, Andrew J Gatesman, Robert H Giles, Xifeng Qian, Neelima Chandrayan, Shivashankar Vangala, Krongtip Termkoa, et al. Coherent imaging at 2.4 thz with a cw quantum cascade laser transmitter. In *Terahertz Technology and Applications III*, volume 7601, page 760105. International Society for Optics and Photonics, 2010. 71

[54] Barry N Behnken, Gamani Karunasiri, Danielle R Chamberlin, Peter R Robrish, and Jérôme Faist. Real-time imaging using a 2.8 thz quantum cascade laser and uncooled infrared microbolometer camera. *Optics letters*, 33(5):440–442, 2008. 71

[55] Xuyuan Chen, Øyvind Svensen, Muhammad Nadeem Akram, et al. Speckle reduction in laser projection using a dynamic deformable mirror. *Optics express*, 22(9):11152–11166, 2014. 72

[56] Naoki Oda, Iwao Hosako, Tsutomu Ishi, Hiroaki Minamide, Chiko Otani, and Norihiko Sekine. The need of terahertz cameras for standardizing sensitivity measurements. *Journal of Infrared, Millimeter, and Terahertz Waves*, 35(8):671–685, 2014. 72

[57] Jean-Baptiste Perraud, Adrien Chopard, Jean-Paul Guillet, Pierre Gellie, Antoine Vuillot, and Patrick Mounaix. A versatile illumination system for real-time terahertz imaging. *Sensors*, 20(14):3993, 2020. 72, 83

[58] François Simoens. Thz bolometer detectors. In *Physics and Applications of Terahertz Radiation*, pages 35–75. Springer, 2014. 73

[59] Shane Z Sullivan, Ryan D Muir, Justin A Newman, Mark S Carlsen, Suhas Sreehari, Chris Doerge, Nathan J Begue, R Michael Everly, Charles A Bouman, and Garth J Simpson. High frame-rate multichannel beam-scanning microscopy based on lissajous trajectories. *Optics express*, 22(20):24224–24234, 2014. 73

[60] J Wesley Anderson and Garrett M Clayton. Lissajous-like scan pattern for a gimballed lidar. In *2014 IEEE/ASME International Conference on Advanced Intelligent Mechatronics*, pages 1171–1176. IEEE, 2014. 73

[61] Thomas Boardman Greenslade. *Adventures with Lissajous Figures*. Morgan & Claypool Publishers, 2018. 74

[62] Francesco Marchetti. Spectral filtering for the resolution of the gibbs phenomenon in mpi applications by lissajous sampling. 2016. 74

[63] Roi Méndez, Enrique Castelló, José Ramón Ríos Viqueira, and Julián Flores. A new calibration process for a homogeneous cyclorama illumination in virtual tv sets. *Applied Sciences*, 9(10):2020, 2019. 76

[64] JB Perraud, A Chopard, Jean-Paul Guillet, P Gellie, F Fauquet, and P Mounaix. A fast and homogeneous illumination applied to full-field terahertz imaging. In *2020 45th International Conference on Infrared, Millimeter, and Terahertz Waves (IRMMW-THz)*, pages 1–2. IEEE, 2020. ix, 79, 83

[65] François Simoens, Jérôme Meilhan, Laurent Dussopt, Jean-Alain Nicolas, Nicolas Monnier, Gilles Sicard, Alexandre Siligaris, and Bruno Hiberty. Uncooled terahertz real-time imaging 2d arrays developed at leti: present status and perspectives. In *Micro-and Nanotechnology Sensors, Systems, and Applications IX*, volume 10194, page 101942N. International Society for Optics and Photonics, 2017. 82

Chapter III

FMCW Radar Developments

«All we have to decide is what to do with the time that is given us.»

J.R.R. Tolkien

III.1 Introduction

The development of CW imaging systems, detailed in Chapter II, brought up several improvements, especially when it comes to real-time short wavelength considerations. An initial approach of single point raster-scanning CW imaging displayed several inherent limitations. Namely, the caped measurement rate for QCW operation, dictated by the response time of the detector correlated to the use of lock-in synchronous detection, abolishes its relevance for industrial purposes. With respect to this approach, coherent sensing would grant non-negligible improvements with the acquisition of an additional phase information, often witnessed along with an enhancement of the measurement dynamic range and recording speed.

Beside single tone coherent sensing, the millimeter-waves frequency range can highly benefit from the FMCW mode of operation to unlock an additional longitudinal sensing capability. In this context, the central task, depicted in this work, relies on the transition from such tunable, CW operation, up to the FMCW radar sensing mode. More precisely, it follows the development and integration of III/V GaAs-based planar Schottky frequency multiplier for the integration of high power tunable sub-terahertz sources ranging up to 640 GHz, to evolve towards the design of fully integrated sub-terahertz FMCW unit.

This transition is driven by the well-established capabilities of millimeter-waves FMCW sensors toward NDT topics. Namely, the contactless in-depth inspection capabilities, relatively low implementation cost, compactness and high measurement rates represent net benefits for such technological candidates when it comes to inspection problematics. Such characteristics have been highlighted by the DOTNAC project [1], which additionally featured a net advantage of FMCW approaches for the inspection of a variety of composite materials with respect to other well established NDT techniques. Figure III.1 features the result of a comparative study with respect to Ultrasonic Inverse Wavefield EXtrapolation (IWEX), Infrared thermography (IRT), Radiographic Testing (RT), pulsed Time Domain TDS and Utrasonic Testing (UT) to display the unrivalled NDT capabilities of millimeter-waves FMCW testing on specific samples of interest.

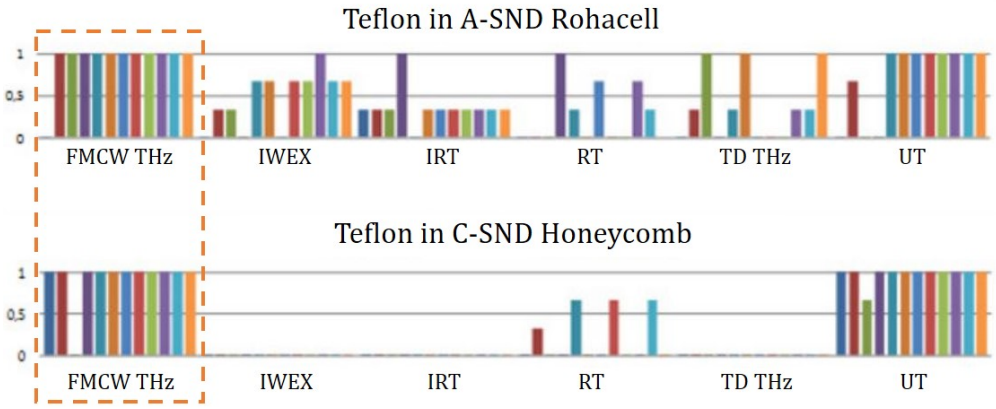

Figure III.1: Comparative defect detection capabilities in layered composite materials through different NDT approaches. Adapted from [1]

Backed by the capabilities features in this study, a full depiction of the architecture of the developed FMCW transceiver will be detailed along the first section of this chapter. An in-depth characterization of each major stage will be addressed. It will then lead to the required additional processing induced by the divergence with the perfect FMCW model. This corrective normalization will then be detailed alongside with its performances and integration architecture. Finally, the current transceiver specifications will be assessed through specific FMCW oriented characterizations.

III.2 Architecture and Developments

In this scope of transitioning from CW sources to FMCW sensors, this section will be describing all the technical choices made for the integration of the architecture of this FMCW unit. Those details will go along with the resulting performances of each stage.

III.2.1 Preliminary technological choices

Prior to the full FMCW unit integration, conception and design choices have to be highlighted. They will indeed advocate the adequacy of this solution with the demand witnessed in the related industrial fields, such as the one detailed in section I.4.4.

As the widest consideration, the technological choices when it comes to semiconductor technology, remains at the center of the design process. Indeed, even though Si-Ge technologies demonstrated an important development in the latest years [2–4], as detailed in section I.4.2, the lack of integrated components would induce that a tedious full MMIC design would be the only available path to follow, to reach modest performances in term of bandwidth, available power and noise figures. On the other hand, III/V Schottky diode based frequency multipliers and frequency mixing units capabilities has been widely demonstrated over the years [5–9], with high power handling capabilities, higher operation frequencies and enhanced noise figures. Therefore, targeting the development of a high-end performance system naturally settled the semi-conductor technologicl choice in favor of III/V block integrated components. Such an architecture would nevertheless suffer from higher production cost with respect to fully integrated Si-based compact solutions. However, the current niche aspect of the millimeter-wave FMCW radar market, with low production volumes, prevents this disparity.

Another important initial choice relies on the geometry of the radar unit with either a bi-static architecture where the transmitter and receiver chains integrate distinct TX and RX antennas. Oppositely, in a monostatic implementation, both chains share the same antenna and an additional decoupling element can be used to dissociate the emitted and received contributions. The later solution has been selected as it allows for much simplified quasi-optical integration with a single coupling focal point as the RX/TX antenna, which allows for an intrinsic normal reflection configuration. This additionally ensures a better compactness of the system while allowing for more versatility on the optical implementation for either focused point sensing or wide field SAR reconstruction.

This technical choice obviously restricts the use of this FMCW unit to a reflection sensing configuration. However, for a large variety of applications, this architecture remains the best suited approach for system integration, as the access to the sample under test only needs to be performed on a single side. It hence represents the usual industrial configuration for production chains. It also allows for the partial inspection of highly absorbing samples. Beyond this reflection mode of operation, a transposition to the transmission or bi-static configuration could remain quite accessible with an additional distinct receiver comprised of a mixing unit, fed with a coherent LO, for which the implementation would be simplified thanks to the chosen interchangeable block architecture.

Now that the global geometry of the transceiver is settled, the working frequency remains a major parameter of interest. Indeed, it will directly impacts the FMCW unit performances in term of achievable lateral resolution (see Equation II.14 for a focused Gaussian beam geometry), attainable bandwidth, hence longitudinal resolution, as well as available emission power. More broadly, beside those radar technicality considerations, the suitability of the targeted materials of interest should be accounted for as well. Especially the absorption coefficient in the frequency range of interest, which, if too high, would irrevocably alter the achievable inspection capabilities of the transceiver. As a rule of thumb, the higher the frequency, the higher the material absorption losses. Hence, a trade-off between good material penetrability and achievable lateral and longitudinal resolutions have to be considered.

Accounting for all those criteria, a 150 GHz central working frequency has been selected for

the design of the considered FMCW radar transceiver. Indeed, millimeter level resolutions can be achieved through high numerical aperture focusing. Typically, for NA = 0.5 focusing, ω_0 = 1.3 mm as the $\frac{1}{e^2}$ beam radius would be expected, equivalent to a FWHW beam diameter of 1.5 mm, (see Equation II.14). Additionally, accounting for a generic 12 % tunability of the source, granted by the integrated Schottky components that would lead to the desired 128-160 GHz frequency band, a 32 GHz bandwidth would ensure an adequate 4.6 mm longitudinal resolution (see Equation I.11). Subsequently, the adequacy of this frequency range to specific materials has been experienced, with the DOTNAC project for aeronautics oriented NDT problematics [10]. Of course, targeting higher frequency ranges could acknowledge improvements on the lateral and longitudinal resolutions. However, a large variety of materials turns too opaque, for a successful inspection as soon as the 300 GHz frequency window is considered. Additionally, as a counterpart for the lateral resolution gain, the achievable components performances (available emission power, mixer conversion losses, etc.) might lead to lower sensing dynamic range when targeting higher frequency bands, along with the significant system price increase.

From the initial integrated RF multiplication stage mode of operation, an input pumping signal ranging from 16 to 20 GHz with a pumping level of typ. +5 dBm would be expected, as it is composed of a quadrupler amplifier up-converting an input signal in the 75 GHz band, followed by a frequency doubler, generating the desired 150 GHz emission, .

As a matter of fact, when it comes to the homodyne detection scheme, required for the FMCW mode of operation, this low frequency signal can as well be used as LO if the detection is performed through harmonic mixing. Indeed, either direct mixing, that requires the provision of a 150 GHz LO frequency sweep, or subharmonic and harmonic mixing are suitable solutions. The latter option has been adopted as it drastically simplifies the HF (High Frequency) component requirements, at the expense of the conversion efficiency with respect to direct mixing. It will then only necessitate specific 20 GHz range equipment to be integrated for the LO handling and provision so that a 8^{th} harmonic mixing can be performed.

Beyond the homodyne detection scheme, the frequency chirp remains a central point for the FMCW radar mode of operation. Considering a saw-tooth frequency profile as displayed in section I.4.1, from Equation I.9 one can notice that the chirp rate, $\Gamma = \frac{BW}{T_s}$ $[s^{-2}]$, will impact the beating frequency when considering a target at a given distance. This IF (Intermediate Frequency) beating signal should be in an accessible frequency range as sampling under 100 MHz remains practicable while extremely low frequencies should be avoided due to low frequency noise issues. With the goal of targeting beating frequencies in the order of 1 MHz as a convenient frequency window to be recorded, considering a sample placed at 50 cm from the transceiver, a T_s = 100 µs full bandwidth chirp should be targeted, implying a chirp rate in the order of Γ = 320 $THz.s^{-1}$. A theoretical measurement acquisition rate of 10 kHz should then be achievable.

As detailed in Section I.4, the need for such sweep speeds often calls on the use of VCOs, controlled through adequately timed voltage commands. Nevertheless, those components can display a large input voltage/output frequency non-linearity, as technically demonstrated with the VCO characteristic displayed in Figure III.6a. This aspect can drastically alter the longitudinal sensing performances of a FMCW radar if not mitigated [11], leading to a impulse response broadening and a subsequent reduction the achievable measurement dynamic range. An adequate calibration would minimize this impact, as performed for commercially available III/V FMCW radar solutions. Nevertheless, such components remain extremely sensitive to external perturbations as well. For example, subtle temperature changes or electromagnetic disturbances could highly impact it characteristics. Hence, it would then lead to drastic performance losses of the radar itself, with non-repeatable measurement and limited time stability issues. To rectify such aspects, a stabilization through a feedback-loop can be found in the mode of operation of a PLL (Phase Locked Loop) [12] and will be implemented in this solution, as a major improvement for reliability purposes with respect to state of the art millimeter-waves FMCW radars. Additionally to this stabilization of the VCO, such a PLL integration will display drastic improvements when it comes to phase noise performances, of importance to such homodyne detection scheme.

III.2.2 Full architecture

As the central piece of the FMCW unit, a special attention should be brought to the characteristics of the signals provided to the homodyne detection harmonic mixing unit. Namely, on one side, the low frequency LO is supplied on the sweeped 16-20 GHz frequency range, and on the other side, the reflected HF signal is collected with a 128-160 GHz frequency chirp in order to perform the 8^{th} harmonic mixing. To do so, the radar transceiver can be spitted in several primary groups, with first, a low-frequency PLL-based circuit for the generation of this proper LO. It is then followed by the up-conversion HF chain that will enable the transceiver to reach the sub-millimeter domain of interest, i.e. the 150 GHz range. It is then completed, in reflection configuration, by the homodyne detection branch that will allow for FMCW sensing. Beyond the radar transceiver itself, additional beam shaping optics can be considered. The complete depiction of each of those stages will be performed in this section and will be supported by their relative performances assessment. To support those technical characterizations, a full architecture diagram depiction is provided in the overview Figure III.20 at the end of this section, and complemented with a photograph of the development integration in Figure III.19.

Low frequency stage

As the ground level of the radar transceiver, this first elementary brick is intended for the generation, settling and formatting of the input signals for the subsequent HF stages. Namely, for the provision of the LO frequency chirp for the homodyne detection on one side, and the generation of the up-converted frequency chirp in the millimeter-wave domain on the other side.

It is therefore of extreme importance for the performances of the FMCW radar transceiver that this stage delivers signals with proper emission power as well as proper spectral characteristics. Namely, it should be able to supply a linear frequency chirp ranging from 16 to 20 GHz in a sweep time neighbouring 100 µs with adequate power levels so that the up-conversion stage could range over the 128-160 GHz bandwidth.

To reach such an emission signal, the low frequency power handling circuit is divided in 3 main stages. It features first a PLL incorporated VCO to ensure the "perfect linearity" and stability of a chirp ranging from 8 to 10 GHz, followed by a frequency doubling stage to reach the desired 16 to 20 GHz range, and completed by a spectral filtering operation.

- PLL integrated VCO

In its simplest design, a classical PLL, remains a system designed to relate and stabilize the phase of an output signal with respect to an input command. Its elementary implementation is depicted in Figure III.2a, and features a VCO which generates a periodic signal subsequently compared to the input command, through a phase feedback loop. It then adjusts the oscillator command to keep their phases matched. Such a phase stabilization also implies a synchronization of the input and output frequencies but, in this simple integration, remains designed to work using a single tone input command, or limited to slow frequency deviations. The filter itself handles the dynamic response of the PLL when reacting to disturbances, hence relating to the PLL stability.

As a more modern architecture [12, 13], based on digital circuits, integer-N PLL and fractional PLL offers an output frequency tuning capability through the insertion of a frequency division block on the feedback loop as depicted on Figure III.2b. In this case, a reference frequency, f_{ref} [Hz], is provided to the phase comparator. When locked, this reference frequency should then be equal to $\frac{f_{\mathrm{VCO}}}{\mathrm{N}}$, with f_{VCO} [Hz], the output PLL frequency, and N the divisor feedback loop factor. A change of f_{VCO} can therefore be expected when tuning the frequency divider N. A spectral resolution of f_{ref} can then be achieved for such an Integer-N PLL.

In this configuration, targeting high spectral resolution, the use of high feedback-loop divisor N numbers is problematic for phase noise issues [13]. Nevertheless, by tuning dynamically the value of N in locked state, fractional frequency multiplications can be achieved. Such architectures allow for the use of higher reference frequency and better achievable PLL spectral resolution. Due

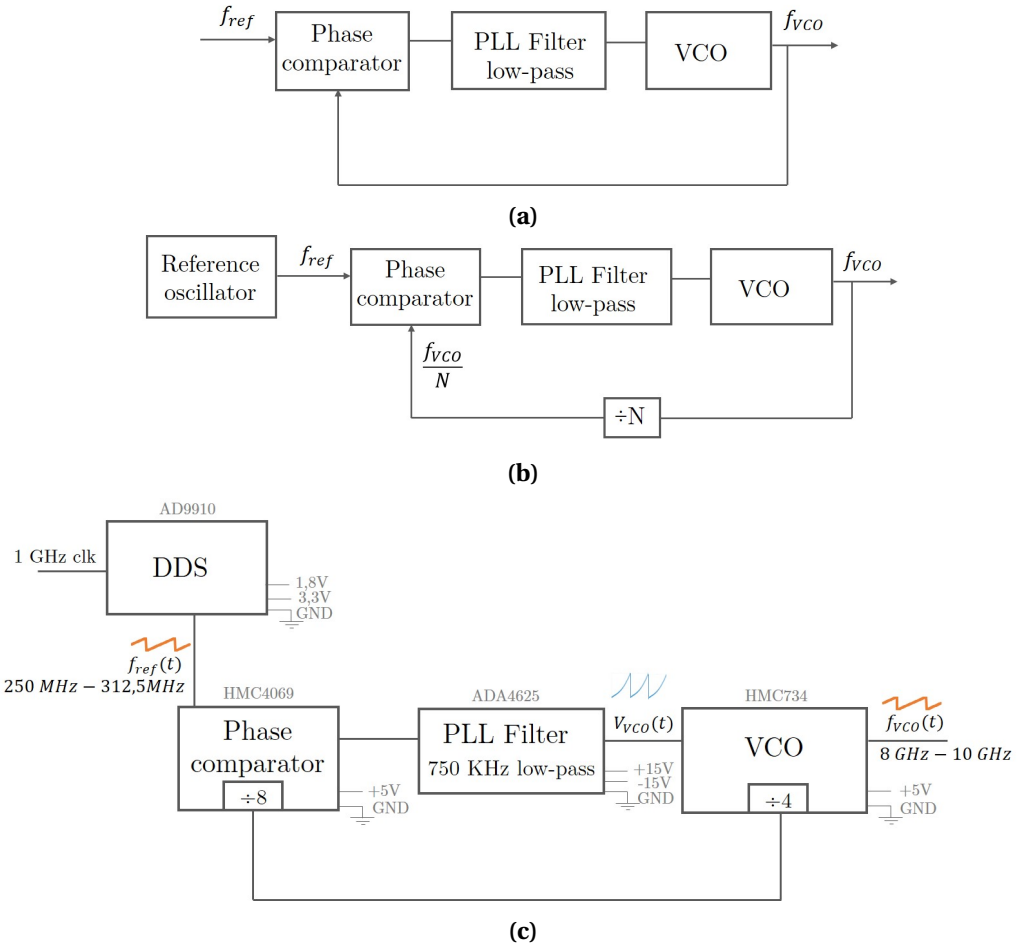

Figure III.2: **(a)** Simplest PLL architecture diagram, **(b)** typical advanced tunable fractional/Integer-N PLL diagram and **(c)** Hybrid digital/analog PLL integrated as the basic sweeping unit of the FMCW radar.

to the averaging of several digital cycles,they nevertheless lead to the appearance of spectral artifacts depending on the chosen fractional numbers. The filter then plays an important role, since, as its bandwidth decreases, the slower the PLL reaction time will be but the better its spurious filtering capabilities are. While, the larger the BW, the more unstable it can get, annihilating at some point the frequency locking capabilities of the PLL.

Such architectures could easily be implemented for frequency sweeping and are commercially available. Nevertheless, they either display limited bandwidth, or remain too slow for the generation of fast frequency chirps [14, 15], required for the radar mode of operation. Indeed, they rely on the addressing of internal divider registers, that can take up to hundreds of µs for a single frequency change. Ramps capabilities are as well integrated but remain far from matching the requirements of a 100 µs full 2 GHz BW sweep, hence at $\Gamma = 20\ \mathrm{THz.s^{-1}}$. Several designs demonstrates chirp rates up to few $\mathrm{THz.s^{-1}}$ (maximum at 2 $\mathrm{THz.s^{-1}}$ for [16]) limited by such analog register assessment.

A hybrid PLL, that allows for locked fast frequency sweeps, has then been developed in order to ensure a stable and consistent radar chirp as well as to eliminate the VCO non linearity and characteristics variations. To do so, a fixed divisor Integer-N PLL is integrated as depicted in Figure III.2c. With the combination of the two pre-integrated divisors among the VCO and phase comparator chips, 4 and 8 frequency divisors respectively, a factor of N=32 is introduced in our case as to reduce the VCO frequency to a range accessible by affordable phase comparators and Direct Digital Synthesizers (DDS). The fast chirp required for the FMCW operation is then achieved by sweeping rapidly the reference frequency, f_{ref} on which the PLL will lock and perform a frequency up-conversion to the 8-10 GHz band of operation of the VCO.

This fast input frequency chirp, $f_{ref}(t)$ is performed by a DDS, synchronysed by a 1 GHz input

clock. The VCO has been selected to operate with a 8 to 10 GHz output frequency, which, accounting for the division factor, then requires a reference frequency ranging from 250 to 312.5 MHz. The capability of the DDS to achieve ns scale frequency changes allows for full bandwidth frequency chirps under 100 µs with kHz resolution steps as to minimize digitization steps artifacts in the sweep. But, *in fine*, the global dynamics of the PLL remains governed by the PLL filter. After an iterative selection process on the filter cut-off frequency, a 750 kHz low-pass filter demonstrated a stable frequency tracking over the whole chirp bandwidth under 100 µs. Higher cut-off frequency led to an unlocked state unstable behavior over part of the frequency bandwidth. While lower cut-off frequencies ensured a stable locked state over the whole chirp bandwidth but tend to slow down the PLL. In order to avoid sudden frequency jumps, that could alter the stability of the PLL, a symmetrical triangular frequency chirp is used.

An in depth investigation of the characteristics of the PLL output frequency chirp is necessary in order to allow for the best performances in the FMCW radar operation. Namely, output power concerns as well as the spectral characteristics of the generated signal are of interest to properly drive or pump the subsequent stages. In sweep mode, a spectral investigation has been performed to ensure the proper coverage of the expected 8-10 GHz bandwidth on a typical 100 µs chirp time. As demonstrated in Figure III.3a a flat amplitude response is achieved, in accordance with the VCO specifications [17]. The full spectrum analyzer span scan, featured in Figure III.3b, displays the emission of higher harmonics in the 16-20 GHz band with non-negligible power levels. Such components emerge from the VCO non-linearity with 66 and 15 dBc amplitudes for the 1/2 sub-harmonic and the second harmonic respectively. A 30 dBc third harmonic should as well be expected according to the component specifications [17], beyond the spectrum analyzer window. Such measurements have been performed with a 3 MHz resolution bandwidth in max-hold configuration on the Agilent E4407B scalar analyzer. Slight power disturbances centered at 8, 8.5, 9, 9.5 and 10 GHz have been noticed and originate from spurious recombination.

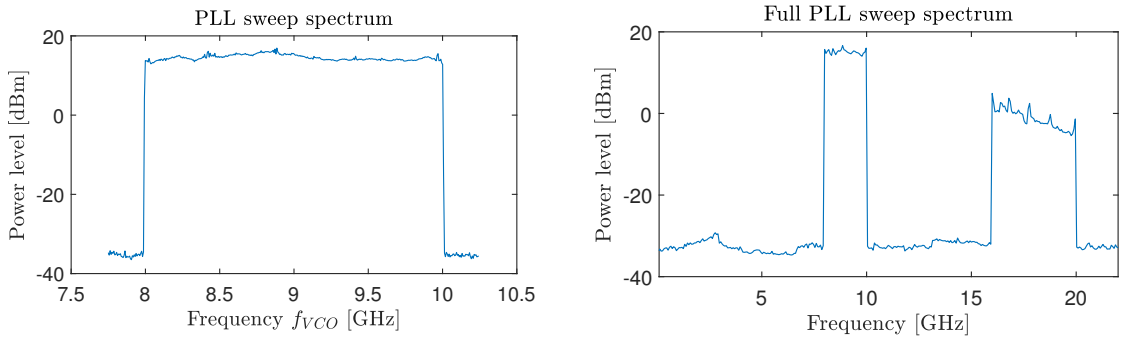

Figure III.3: Power spectra recorded in max hold configuration and 3 MHz resolution bandwidth, **(a)** on the spectral region of interest, the 8-10 GHz band, **(b)** on the full-span analyzer spectral window when operating the PLL with 100 µs sweep time.

Due to the spectrum analyzer mode of operation, with respect to the chirp time of 100 µs, no time resolution of the chirp can be achieved. Hence, such sweep spectrum results from a time averaging over several frequency chirps. A quantitative information on the emitted power at each frequency can then only be retrieved on single tone-commands, where the PLL is locked to be fixed on a stable frequency. Such characterizations are depicted in Figure III.4a at discrete frequencies, with a 100 MHz measurement step. From this assessment, a power level ranging from 16 to 18 dBm over the sweep band remains in adequacy with the VCO specifications. Figure III.4b displays a superposition of each recorded component, recentered relatively to its central frequency, following the color code of Figure III.4a. One can notice the appearance of spurious side peaks with amplitudes around -30 dBc that could be related to beating integer boundary spurs, inherent to integer-N PLL operations [18, 19]. No further investigations on the origin or the mitigation of those parasites have been conducted as it seems that they not drastically alter the PLL chirp

mode of operation capabilities or the final radar performances. Additionally, such low amplitudes should prevent their propagation though the subsequent multiplication stages as they often feature a threshold pumping power. Furthermore, from such a detailed spectral window, recorded with a resolution bandwidth of 10 kHz, the standard spectral shoulders profiles featured by locked PLL operation, can be highlighted [20], with a width linked to the PLL filter bandwidth, evolving from 2 MHz for the frequency of 8 GHz down to 700 kHz at 10 GHz. Further investigations demonstrated a spectral line-width ranging from 2 to 3 kHz on measurements performed at 8 and 10 GHz with resolution bandwidth down to 30 Hz on limited 5 kHz spectral spans.

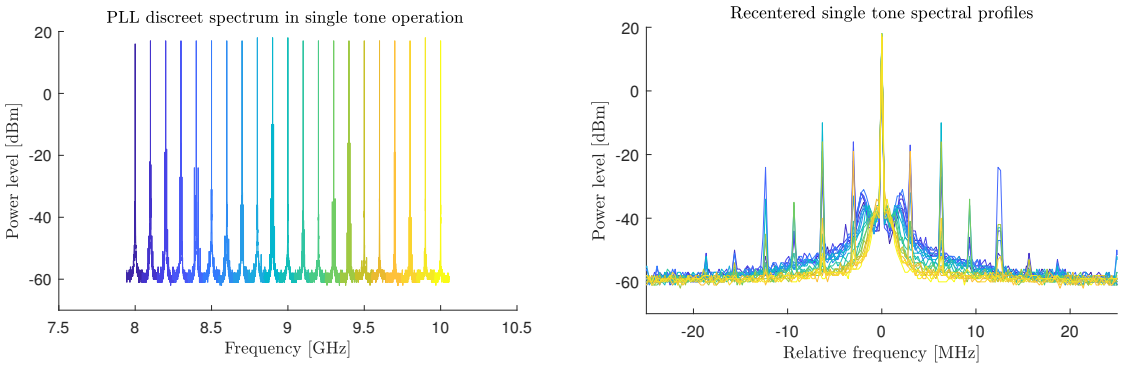

(a) **(b)**

Figure III.4: **(a)** Discreet spectral components when operating the PLL with a single tone command and **(b)** re-centered single tone spectral profiles with respect to their central frequencies, following the same color code as III.4a. Measurements have been performed with a 10 kHz resolution bandwidth at fixed frequencies instructions.

Nevertheless, the spectrum analyzer prevents direct time related investigations. Namely, such characterizations do not provide quantitative information on the chirp linearity. To address this problem, real time characterizations of the PLL signal in sweep mode have been performed using a 80 G$sample.s^{-1}$ 20 GHz BW, Teledyne LeCroySDA 820Zi-B oscilloscope. An attenuation of 10 dB was inserted to protect the oscilloscope input channels. The collection of a full triangular sweep pattern required the recording of $16e \times 10^6$ sampling points over 200 µs. Using time shifted Fast Fourier Transform (FFT) operations, over subsequent 40 ns time windows segmentation, the full spectral evolution over a symmetrical frequency chirp is recovered and displayed in Figure III.5. As one can see, the linearity of the chirp is unequivocal and depicted a linear correlation coefficient of $r^2 = 0.999$ with the expected slope of 20 TH$z.s^{-1}$.

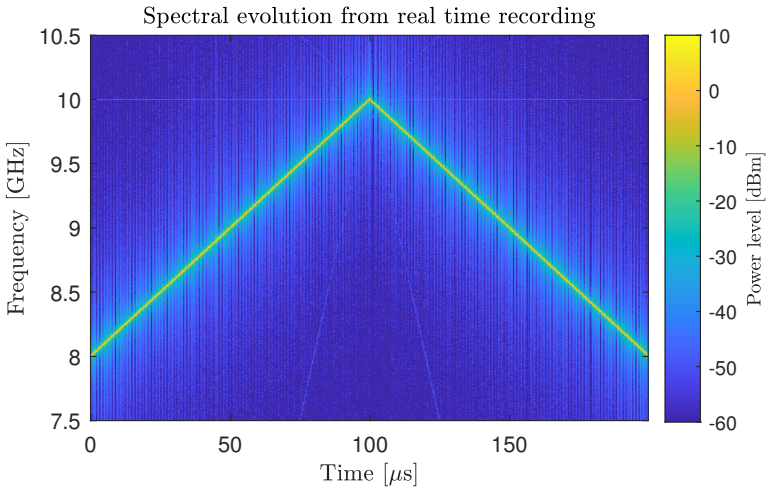

Figure III.5: Spectral evolution of the PLL output main spectral component over a symmetrical triangular chirp processed from real-time recorded data at 80 GS$ample.s$−1.

The low amplitude spreading featured in this representation emerges from the limited time window considered for each 40 ns time step. Additional subtle spectral features are noticeable, such as the fixed component at 10 GHz with amplitude around - 50dBc, and are induced by the limited sampling rate of the oscilloscope with respect to the oscillation frequency. The first harmonic chirp was as well recorded in the 16-20 GHz band.

The frequency linearity is ensured by the PLL capability to follow the incremental highly linear incremental digital ramp command sent by the DDS. Indeed, as displayed in Figure III.6a on its frequency-voltage specification curve, the VCO introduces a strong non-linearity, which could drastically reduce the capabilities of a FMCW radar if not accounted for (see section III.3.1). With the correction applied by the PLL, the tuning voltage, V_{VCO}, then follows the inverse function of the VCO characteristic, over the operation frequency band, as depicted in Figure III.6b. This measurement has been collected when probing the command channel of the VCO when operating with typical sweep characteristics. Those two curves display a linear correlation coefficient of $r^2 = 0.95248$, to be compared to the previously given correlation coefficient of the VCO output linear chirp, almost unitary.

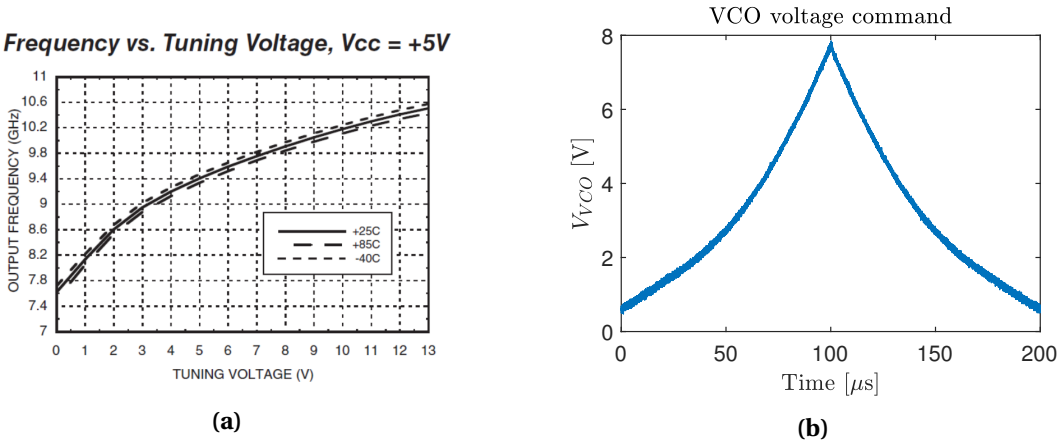

(a) **(b)**

Figure III.6: **(a)** VCO Voltage-Frequency characteristic curve [17] and **(b)** VCO tuning voltage command, V_{VCO}, over a symmetrical linear triangular chirp with 100 µs rise time.

The characteristics of the frequency chirp, generated by the PLL have been addressed and further demonstrated a perfect suitability as the ground stage for an FMCW radar chirp operation. Nevertheless, at this point, the chirp itself is not adequate for driving the HF stage or to be used as the LO for the homodyne detection. Indeed, as detailed in section III.2.1, a 16-20 GHz frequency chirp is expected to operate the first stage 64-80 GHz quadrupler, then followed by a 128-160 GHz doubler, and will as well be used for LO purposes in the harmonic mixing scheme. The up-convertion of the HF stage composed of a quadrupler chained with a doubler then leads to the use of the 8^{th} LO harmonic for mixing.

- Frequency doubling

A frequency doubler, operating in the 16-20 GHz range is then to be integrated at the output of the PLL as depicted in the full low frequency stage diagram of Figure III.9. To fulfill the input power requirements of this subsequent component, an additional 10 dB attenuation is integrated at the output of the PLL, prior to the frequency doubler. To assess the suitability of the signals for driving the FMCW mode of operation, similar characterizations as the ones performed at the direct 8-10G Hz output of the PLL have been conducted on this 16-20 GHz band. For instance Figure III.7a depicts the single tone spectral characterizations that gives a stable output power ranging from 16.5 dBm down to 13.5 dBm. In this same characteristic, the frequency spurious are still noticeable. Figure III.7b details once again, the spectral component evolution over a symmetrical triangular frequency chirp in the 16-20 GHz band. This specific measurements have been performed on the previously featured oscilloscope, displaying a 80 G$sample.s^{-1}$ sampling rate

for a 20 GHz bandwidth. Once again, a protective 6 dB attenuation is employed as to prevent any damage to the oscilloscope channels. Specific artifacts emerge in this measurement with the appearance of spectral aliasing above 20 GHz, depicted by the crossing continuity above 20 GHz, as well as harmonics aliasing components, which emerge as tiling artifacts.

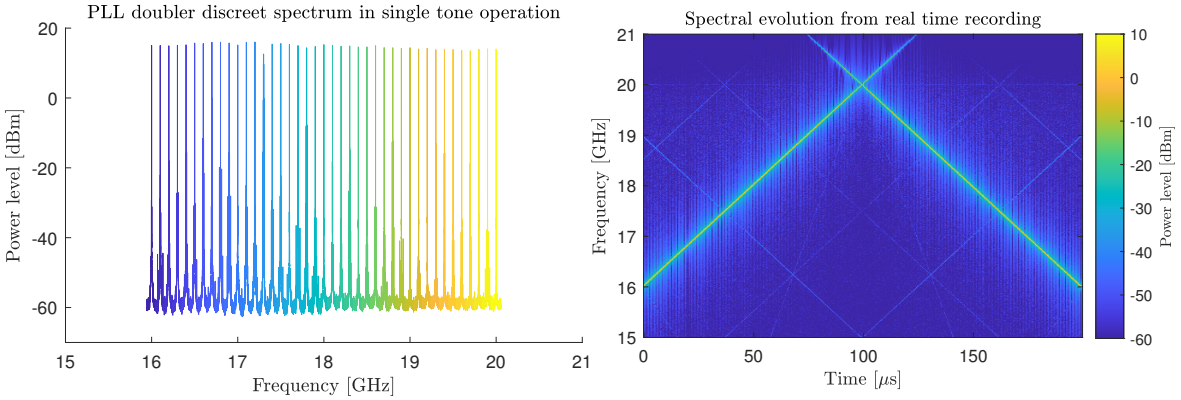

(a) **(b)**

Figure III.7: **(a)** Discreet spectral components at the output of the frequency doubler when operating the PLL with fixed frequency commands, recorded with a resolution bandwidth of 10 kHz and **(b)** related spectral component collected from a real time recording at 80 GS$ample.s^{-1}$, in typical chirp operations displaying a 100 µs frequency chirp over the 16 to 20 GHz frequency window.

In this spectral region of interest, 16-20 GHz, the driving frequency chirp then displays suitable characteristics with a stable linear chirp. Nevertheless, harmonics and sub-harmonics frequency components, generated through the limited 25 dBc isolation of frequency doubler, remains non negligible, with amplitudes around -25 dBc, as detailed in Figure III.8a.

- Spectral filtering

In order to provide a proper mono-frequency driving chirp, for the HF multiplication stages as well as the LO for the homodyne detection, an additional band-pass filter (BPF) is inserted. Due to the absence of BFP with suitable cut-off frequencies in this spectral range, it is composed of a low-pass filter cascaded with a high-pass filter, with cut off frequencies surrounding the spectral region of interest. A drastic suppression of the undesired frequency components is witnessed as showed in the spectral characterization of the sweep signal in Figure III.8b in comparison with Figure III.8a for the unfiltered chirp.

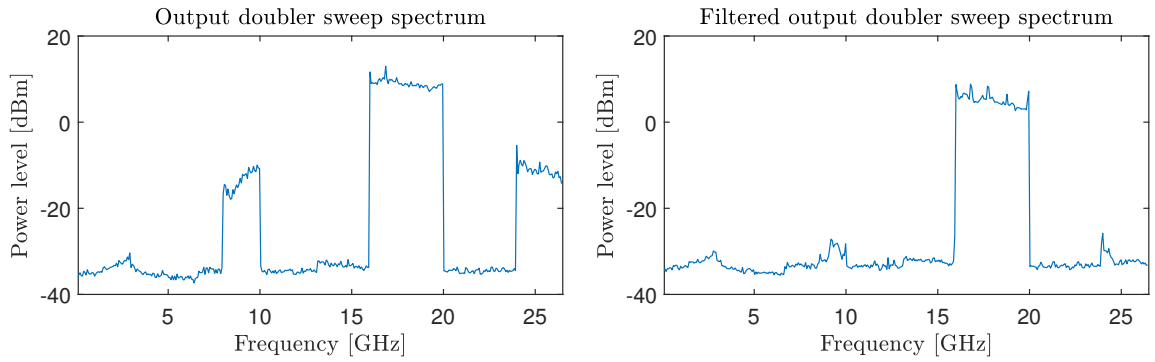

(a) **(b)**

Figure III.8: **(a)** Full-span power spectrum, measured with a 3 MHz resoution bandwidth after the frequency doubler when operating the PLL in typical 100 µs sweep mode and **(b)** similarly after the band-pass filtering stage for harmonics dampening.

In addition, due to the filters insertion losses, a slight impact on the amplitude is as well endured with power losses in the order of 4-5 dB. It led to single tone power levels ranging from

12 dBm down to 9 dBm, suitable after the insertion of a power splitter for driving the HF multiplication stage quadrupler.

- Power splitter

In order to achieve the homodyne detection, a LO should be provided to the mixer. In our case, implementing a harmonic mixing operation, a portion of this 16-20 GHz signal will be provided for a mixing through the 8^{th} harmonics. Hence, the addition of a power splitter ensures the creation of two identical chirp channels, either dedicated to the HF stage pumping for signal up-conversion or as the LO for the homodyne detection. A 3 dB power reduction on each branch is then expected as the signal is symmetrically distributed. A standard additional 0.7 dB typ. insertion loss has been measured on each branch.

A global depiction of the full previously detailed low frequency 16-20 GHz fast chirp generation circuit is given in Figure III.9.

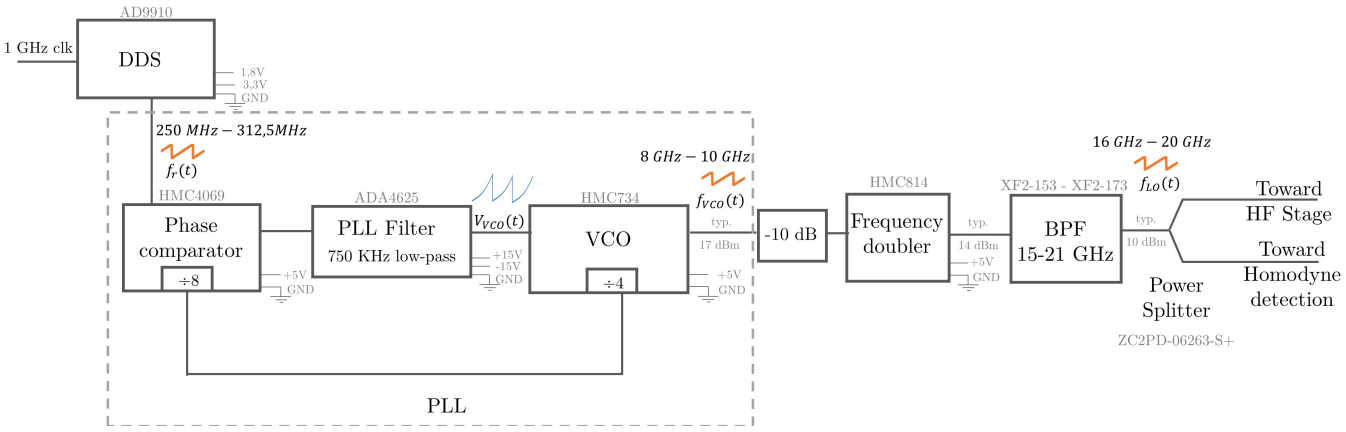

Figure III.9: Diagram of the low frequency sweep generation unit.

Direct emission HF stage

Downstream from this low frequency sweep generation unit, on one of the splitter's arm, the direct high frequency stage is implemented at first. It features the up-conversion frequency multiplication chain based on Schottky multipliers (see section I.3.1). As displayed on the global depiction of Figure III.20, an active amplifier frequency quadrupler is pumped through the previously generated $f_{LO}(t)$ signal, leading to the generation of a chirp in the 64-80 GHz frequency range with a peak emission power over 450 mW, or 26.5 dBm. This emission power is then used for the passive driving of the subsequent self-biased Sckottky frequency doubler to reach the 128-160 GHz frequency band of interest. An emission power of over 120 mW, or 20.5 dBm is retrieved.

In this mono-static architecture, in foresight of the need for collecting the back-coupled reflected signal, a three port directional coupler is inserted. This asymmetrical component, for which the integration diagram is given in Figure III.10a, ensures a proper signal transmission towards the horn antenna, from port 1 to port 2, providing a minimal insertion loss of approximately 1.4 dBm according to the provider. It then allows for a redirection of the back-reflected signal towards the third output port from port 2. An optimal coupling coefficient of 3 dB has been selected from the provider to ensure maximal reflected power retrieval with 1.2 dB insertion losses while a directivity level of at least 38 dB according to the manufacturer specifications ensures a proper signal dissociation. The power definitions of those characteristics are given in Equation III.1 with

P_i the relative power levels witnessed at each ports [W].

$$\begin{aligned} Insertion\,loss &= -10log\left(\frac{P_2}{P_1}\right), \\ Coupling &= -10log\left(\frac{P_3}{P_2}\right), \\ Directivity &= Coupling - 10log\left(\frac{P_3}{P_1}\right). \end{aligned} \tag{III.1}$$

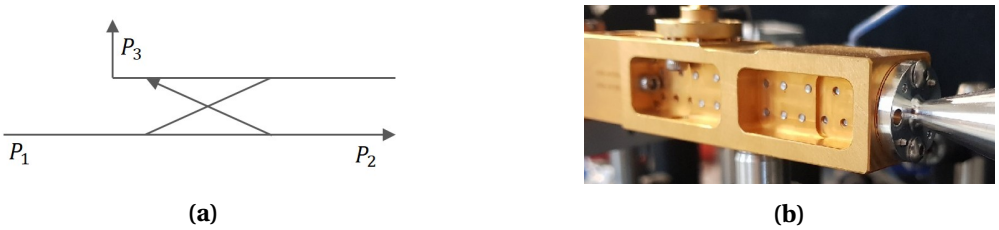

(a) **(b)**

Figure III.10: **(a)** Diagram of a directional coupler implemented for reflectometric measurements, along with **(b)** a picture of the implementation of such a coupler among the radar transceiver.

With this integration, a WR06 diagonal horn antenna is inserted at the output of the coupler for free space emission and features a 26 dBi directional gain, that should lead to 7.7° and 8.5° -3 dB beamwidth in the E and H plane respectively [21].

Accounting for the insertion loss from the directional coupler, the resulting emitted power reaches a peak value of 50 mW, or 17 dbm, with typical power variations induced by waveguide interference cavities that are displayed in the spectral characterization of Figure III.11. At the expense of supplementary insertion losses (typ. several dB), an additional passive Faraday isolator could reduce the amplitude impact of such resonant effect by introducing high return losses. Such power spectra have been measured at the direct output of the horn antenna using a calibrated wide aperture pyroelectric sensor. The impact of these power variations over the FMCW radar resulting beating signal will be further detailed in section III.3.1.

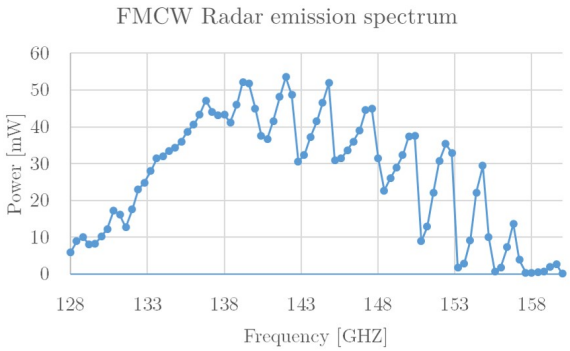

Figure III.11: Emission power spectrum of the FMCW unit over the bandwidth of interest.

Beside the spectral characterization of the emission, spatial profile is of importance as well for beam shaping problematics. Its intensity distribution has been assessed using a 3D raster-scan mapping of the emission field with a lateral 2 mm pitch and longitudinal measurements plane every 1 cm. A limited aperture calibrated pyro-electric detector has been considered for this characterization for which some results are displayed in Figure III.12. The evolution of the intensity beam diameter features a Θ_h=4.26° and Θ_v=4.16° half angle divergence in the horizontal and vertical direction respectively, in the expected order for the 26 dBi antenna gain. A longitudinal profile taken at 300 mm from the endpoint of the diagonal horn antenna is as well depicted with the appearance of diagonal side-lobes.

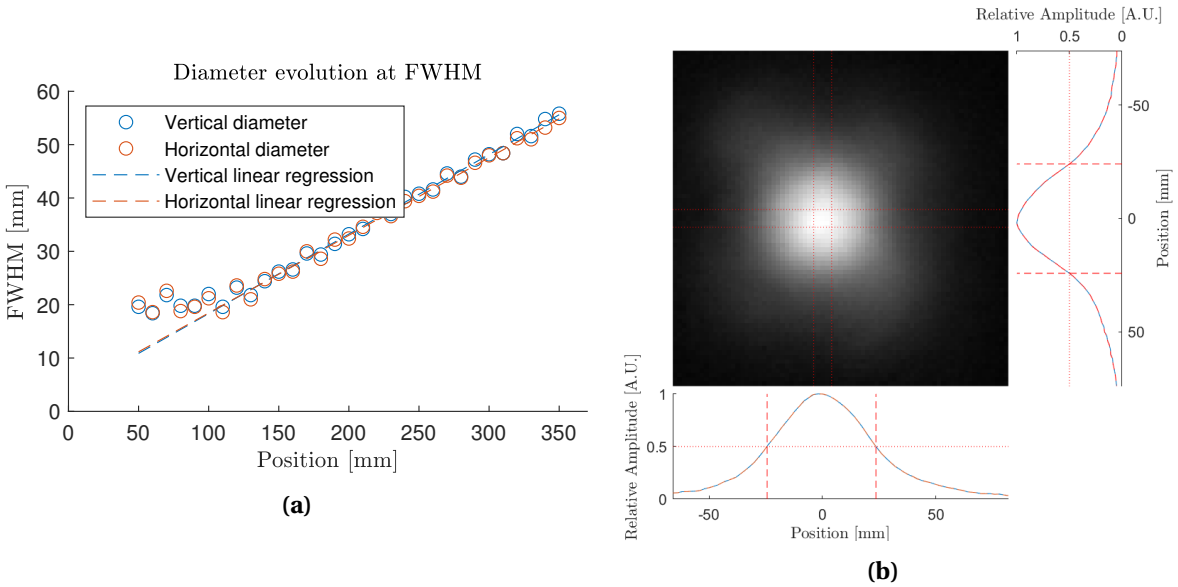

Figure III.12: **(a)** Beam diameter evolution at intensity FWHM for the 26 dBi implemented diagonal horn antenna and **(b)** typical profile measured at 300 mm from the horn antenna endpoint.

Optical configuration

Beside the radar architecture itself, that will offer specific performances, a non-negligible aspect of the FMCW radar implementation rely on quasi-optical considerations. Indeed, the emitted beam shaping is of importance for the obtention of optimum performances and can be specific for each targeted application.

With the simplest open diverging beam configuration, a wide field sensing can be achieved and highly depends on the antenna profile. From such a full field sensing, the conventional Synthetic aperture Radar (SAR) image focusing [22, 23] can be considered and has been extensively applied [24–27] to NDT problematics or scene reconstruction for object detection.

Nevertheless, for punctual sensing and scanned imaging purposes, fixed quasi-optical systems can be integrated as well for beam shaping. In such a focused point scheme, the use of simple HDPE or PTFE plano-convex lens doublet offers a proper adaptability to the radar integration. This focal-infinite-focal configuration will feature a primary collimation lens from which the characteristics should be linked to the emission beam profile. In this case, with a Θ=4.2° half angle divergence, a conventional 2" diameter 20 cm focal f/4 plano-convex lens is used to guarantee a proper beam coverage of the lens. The use of HDPE or PTFE as materials, thanks to their perfect transparency in the millimeter-wave domain (α <0.3 $cm.^{-1}$ @ 150 GHz) and relatively low refractive index of $n_{\mathrm{HDPE}} = 1.54$ and $n_{\mathrm{PTFE}} = 1.4$ respectively [28, 29], ensure low insertion losses.

On the focalization side, the lens selection rely as well on the expected performances. The chosen lens geometry will impact the resolution (see Equation II.14) as well as the expected depth of field related to the Rayleigh range, and obviously the optimum working distance. Due to the use of a diagonal horn antenna, the Gaussian beam model (see section II.2.1) provides proper performances estimations but cannot be rigorously applied. Those considerations have to be accounted for in adequacy with the sample geometry and the sample related obstruction. For instance, a thin flat sample would be especially suitable for high NA setups, typ. f'/1, to reach an enhanced lateral resolution. Thicker samples would require larger depth of field to allow for a proper reflected signal back-coupling, therefore smaller NA, hence a reduced resolution. The working distance, linked to the focal lens, remains also application dependent. With see-through application for instance [30] (see Section IV.3.1) or personal screening [31, 32], at the expense of the resolution, longer working distances are required.

Scaling this simple dual lens setup to larger diameter optics allows for enhanced performances since typical polymer optics with diameters of 3" or 4" remains easily available. Indeed, the use of

larger diameter optics at equivalent numerical aperture, hence similar lateral resolution and depth of field, would allow for larger working distances but will lead to heavier systems. They will thus highly impact the compactness and mechanical obstruction of the transciever. Additionally, the use of OAPMs catabioptric elements would ensure the suppression of the parasitic lens interface reflections.

In our generic implementation, the addition of a 45° angle mirror has been inserted for integration convenience in-between the lens doublet in order to reach an horizontal scanning object plane as displayed in Figure III.13.

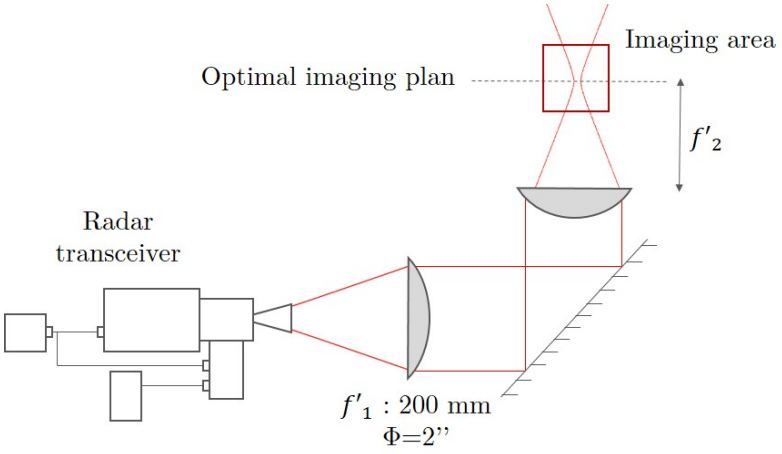

Figure III.13: Typical optical integration for FMCW Radar operation in far-field configuration, featuring a collimation-focalization polymer lens doublet with an additional deflection mirror.

The adaptability of this collimation-focalization system allows for a good versatility of the sensing system, especially with the interchangeability of the focalization lens. Beside on shelf solutions, 3D printed optical components proved their suitability for millimeter waves applications [33] as well. Indeed, printing precision down to several µm remain way below the wavelength so that the slight discontinuities and printing imperfections introduced by the additive manufacturing method remains fully transparent when it comes to low frequencies millimeter-waves applications.

In this work, in order to remedy the limited choice of terahertz and millimeter-waves optics from manufacturers and to provide low-cost custom lenses, the use of classical polymer filament additive manufacturing have been implemented for custom lens design. Among a limited choice of adequate printable materials [34], PP (Polypropylene) and HIPS (High Impact Polystyrene) have been selected as valid candidates with respective refractive indexes of n_{PP}=1.515 and n_{HIPS}=1.561 [35, 36] and low absorption coefficients <0.5 cm^{-1} under 500 GHz. The latter remains more easily printable. Both materials display a very little dispersion level which ensure broadband optical characteristics up to 1 THz where the absorption become the preponderant limiting factor.

Following the Lensmaker's Equation detailed in III.2, with f' the focal length $[m]$, n the refractive index of the lens material, and R_1 and R_2, the respective algebric spherical interface radius of curvature $[m]$ and d, the central thickness of the lens $[m]$, classic plano-convex 2" diameter designs with a 75 mm and 150 mm focal length have been issued as custom low-cost lightweight quasi-optical components using HIPS.

$$\frac{1}{f'} = (n-1)\left(\frac{1}{R_1} - \frac{1}{R_2} + \frac{(n-1)d}{nR_1R_2}\right). \tag{III.2}$$

Additionally, unlike for classical optics conceptions where spherical surfaces remain the norm, the freedom granted by such additive manufacturing techniques allows for exotic designs. Especially, the lens aspherisation (see Equation II.20) does not add any difficulty to the manufacturing process. In this frame of mind, a 2" diameter 40 mm focal lens printed bi-convex aspherical HIPS

optical lens has been designed and its diagram is depicted in Figure III.14. Its high numerical aperture of NA=0.63 makes it highly suitable for lateral resolution oriented applications thanks to the diffraction limited design in the on-axis infinite-focal configuration. Such high surface curvature would have otherwise induced large spherical aberrations, therefore suffering non-negligible achievable resolution limitations.

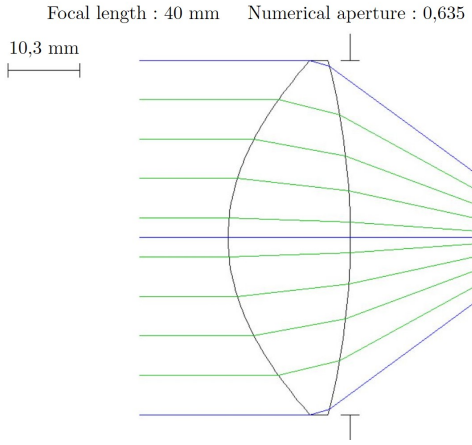

Figure III.14: Optical ray fan simulation of the HIPS aspherical 40mm focal 2" diameter lens, designed with n_{HIPS}=1.495 at 150 GHz to reach a diffraction limited optical component and subsequently manufactured via 3D additive manufacturing.

Beyond lenses, additive manufacturing ensures wider integration flexibility and have been actively investigated in recent works. The relatively low printing precision (size of the printing head and thickness of each layer) nevertheless remains a strong performance limitation factor but satisfactory when it comes to low-frequencies applications. In this context, such technique can easily be considered for the generation of diffracting optics [37], fiber waveguides, off-axis parabolic mirrors or custom reflective elements, providing an additional surface metallization of direct metallic 3D printing [38]. Complex horn antennas [33], and custom waveguide block designs can as well be expected to take advantage of this technology.

Beside those custom developments, no specific focus on the optical configuration optimization has been pursued in this work. When it came to lateral resolution or depth of field considerations, such a simplistic fixed dual-lens focal-focal configuration ensured proper performances for proof-of-work demonstrations. Further work in the investigation of long distance screening, high-speed linear scanning systems for inline-inspection and other specific optical systems tailored to the end-user's requirements are part of the ongoing developments beyond the radar transceiver itself.

Homodyne detection

- LO Provision

On the second arm of the previously introduced power splitter (see Figure III.20), the handling of the LO signal for the homodyne detection is performed. Such harmonic homodyne detection requires quite large power levels for the LO, typically 15 dBm for the integrated mixer. A +24 dB wideband amplifier is then inserted on this arm of the power splitter, where a prior typ. 6.5 dBm power is available, and is followed by a -3 dB attenuator to fit the LO power level specifications. The value of this supplementary attenuator accounts for the amplifier compression at high input power and the additional insertion losses witnessed from the subsequent SMA (SubMiniature Version A) high frequency cables as well as the the high frequency channel of the cascaded diplexer.

Indeed, as the integrated mixer features a single bidirectional SMA for the LO provision and the IF signal retrieval, the integration of a diplexer is required to dissociate those two contributions that remains in very distinct frequency ranges, namely covering the 16-20 GHz window and below several megahertz respectively. Such components feature a common port, in our case directly connected to the mixer LO Input/ IF output, completed by a high pass port (6 GHz-20 GHz), from which is provided the LO, and a low pass port (DC-5 GHz) from which, the IF signal is retrieved as displayed in Figure III.20. Typical insertion losses of 1.5-2.5 dBm are witnessed with port isolation of 90 dB in the MHz range for the high pass port and similarly on the 16-20 GHz frequency window for the low pass port.

- HF Provision

On the other hand, thanks to the previously introduced insertion of a directional coupler, a dissociation of the backward-propagating reflected signal, S_{echoe}, is possible with respect with the up-converted forward emitted probing frequency chirp, S_{probe}. This time-delayed signal is then directed towards the third arm of the coupler as the HF signal for the homodyne detection. Accounting once again for the coupling coefficient and insertion losses, a 20 mW, or 13 dBm power, is retrieved on the sensing arm when inserting a perfectly reflecting sample, i.e. a metallic mirror on the waist point of the optical beam shaping system. This initial power calibration is of upmost importance since mixers can only handle small amount of HF power; 0 dBm or 1 mW in the case of the harmonic mixer selected for our integration. Any excess from this value could irreversibly alter the component performances or destroy it.

In order to safeguard this last central component, a tunable level setting attenuator is inserted to protect the mixer and allow it to operate around its optimum working power point. Its characteristic attenuation level with respect to its micrometric screw position is given in Figure III.15a. Attenuation down to 35 dB is operated and limited by the power sensor noise level. In addition, a 3 dB power margin was taken into account to avoid any damage to the mixer that could occur in slightly different optical configurations. To reach this maximal -3 dBm power level as the HF input over the whole bandwidth (see Figure III.15b), an attenuation of 16 dB was set for standard use. This spectral characterization has been performed through free-space power measurement on the attenuated return port of the coupler, in presence of a unitary reflection sample in the waist plane of the optical setup. Once again, on this spectral characterization, cavity patterns can be witnessed.

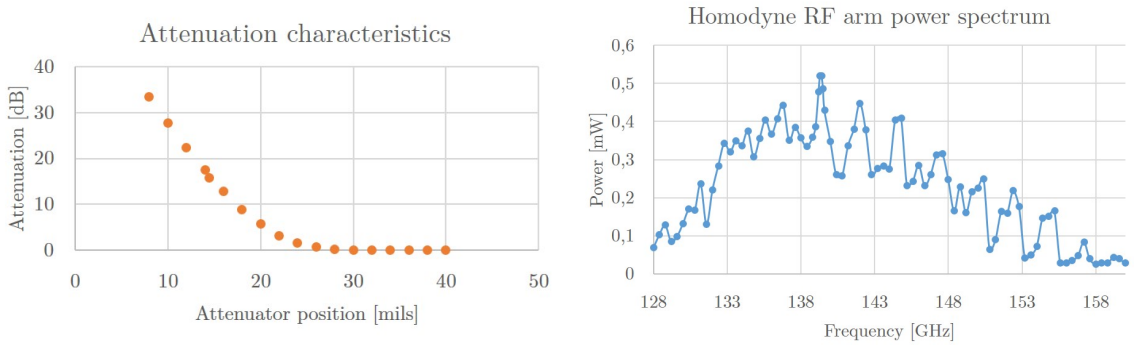

(a) **(b)**

Figure III.15: **(a)** Attenuation characteristic of the WR-06 level setting attenuator and **(b)** Power spectrum measured on the HF reflection arm after the attenuator, featuring a maximal power level of -2.8 dBm, suitable for safe use of the harmonic mixer.

Any major change in the optical configuration would nevertheless require a re-calibration of the attenuation to provide the best performances while preventing any damage to the mixing unit.

In fine, with suitable characteristics for the LO as well as the HF input, the mixing operation can be implemented on the 8^{th} LO harmonics. The generated beating IF signal (see Equation I.8),

featuring the frequency difference between the mixed signals, will then be retrieved through the low frequency port of the diplexer as displayed in Figure III.20 .

The attenuation, introduced on the reflection HF arm, could be perceived as a waste of the high available emitted probing power. Nevertheless, one of the main advantages is the unaltered sensing capabilities on low reflectivity samples such as foams or air-filled structures. Indeed, appropriately tuning down the attenuation level would allows for low reflected power sensing. In anticipation of the full normalization procedure depiction in the following section, considering an adequate low reflectivity referencing procedure, using for instance a low reflectivity pellicle beam splitter as a reference surface, would grant a non-impacted measurement dynamic range of the unit when operating on such low reflectivity samples. *In fine*, an additional 16 dB can therefore be considered in the dynamics performances of the radar unit when targeting implementations on low reflectivity samples. Similarly, such a high available emission power, sacrificed in the general case implementation, could be put to good use to for open beam SAR approached when considering mid-range inspections, where most of the reflected power is not coupled back to the transceiver and would grant a net advantage with respect to the state of the art implementations.

IF signal handling

Now that the harmonic mixing has been operated, and that the IF signal can be retrieved from the multiplexer, data collections and additional processing can be considered.

Accounting for the 25 dBm conversion losses ensured by the harmonic mixer, and the limited acceptable HF input power to the mixer of + 0 dBm, the expected IF signal level should be amplified to a suitable amplitude range so that an adequate data recording could be provided. To do so, and to fit the ± 1V input of the considered ADC (Analog to Digital Converter), a + 24 dB LNA is integrated.

- DAQ Generalities

Subsequently, as the DAQ, a Red Pitaya STEM^{lab}125 – 14 FPGA (Field-Programmable Gate Array) board has been considered for its versatility, price range, compactness and ease of use. It features a multitude IO (input/output) ports with, as a central element, 2 pairs of ADC and DAC (Digital to Analog Converter) operating over 14 bits at 125 M$sample.s^{-1}$, with GPIOs (General-purpose IO), pined IO lines, LED (Light-Emitting Diode) indicators, as well as an Ethernet communication interface.

In its initial Linux configuration, it features numerous already implemented applications for its employment as a versatile instrumentation tool. Among those, one of interest was used for initial data externalization through the streaming server application, allowing for sampling on both input ports with continuous signal recording and transmission up to several MB.s^{-1}. Nevertheless, this solution remains unsuited for performance integration as it required externalized and delayed data handling.

As an alternative, deprived of its native Linux, this board can be used as a blank FPGA thanks to the central integration of a Xilinx Zynq XC7Z010 FPGA chip. Considering the reprogrammable logic aspect, in adequacy with the presence of an ADC and the data externalization IOs through Ethernet, this component is integrated as a data acquisition unit.

A depiction of the chip architecture for Zynq 7000 components family is given in Figures C.1 and C.2 in Appendix C, through detailed block diagrams. On the highest level, the ZYNQ XC7Z010 chip can be separated in 2 main sections with on one side the Programmable Logic (PL) and on the other side, the Processing System (PS) for additional data processing, external communications, and initial Boot handling. A communication between those two distinct architectural regions can be performed through a multitude of AXI (Advanced eXtensible Interface) GPIO and HPIO (High Performance IO) ports.

This section will draw a raw depiction of the implemented FPGA architecture to carry out DAQ functionalities with minimal internal data-processing. For further information on this matter, and

technical choices performed for this design, the reader will find a detailed and quantitative depiction of this architecture in Appendix B.

- FPGA architecture for beating signal recording

This first implementations only targets a data-recording of the IF beating signal, S_{IF}. To do so, an ADC will be put to contribution for data digitalization toward the PL, while the Ethernet socket has been considered for data externalization towards the host processing unit, due to the high required data transfer rate. A depiction of this global architecture is given in Figure III.16. A more complete block diagram depiction of the architecture in the VIVADO environment is given in Appendix B with Figure B.4.

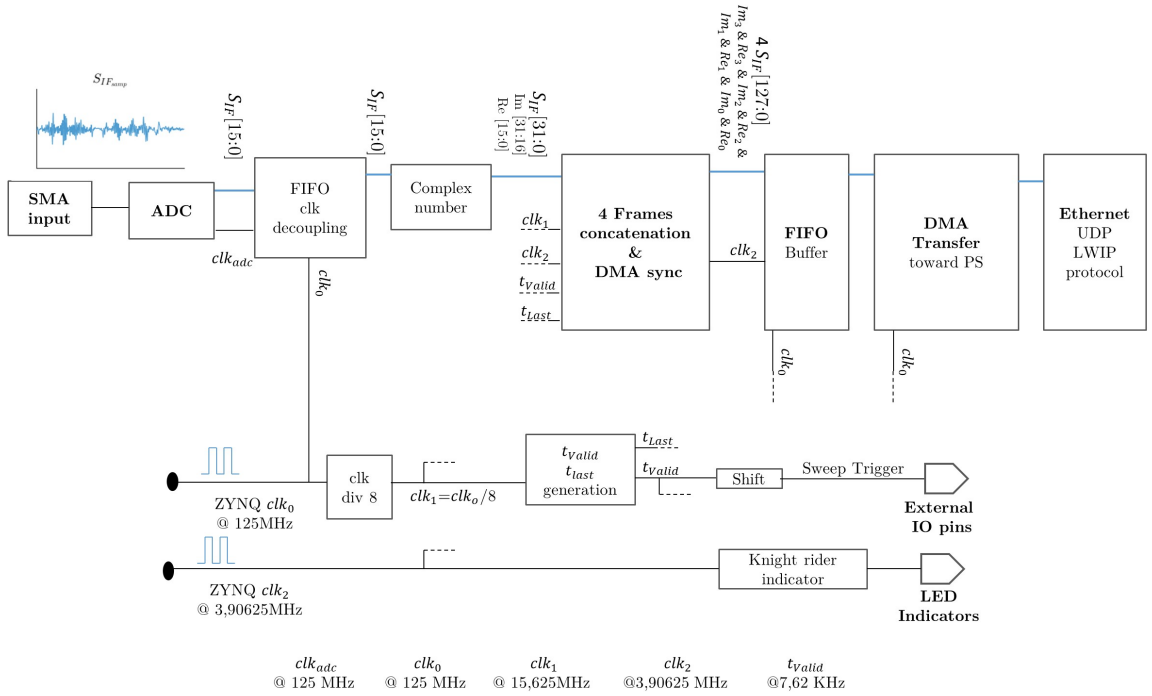

Figure III.16: Diagram of the implemented FPGA architecture as a DAQ module.

- Complex data-frame formatting

At first, the ADC will generate a 14-bit data stream at a rate of 125 M$sample.s^{-1}$. A clock decoupling FIFO (First in, First out) then needs to be considered due to the improper ADC clock. Anticipating further processing and data transfer problematic, the need for a full 125 M$sample.s^{-1}$ full BW recording remains limited since, for a target at 50 cm, the beating frequency would be expected in the order of 1 MHz. A sampling decimation can then be performed without risking information loss. A clock division by a factor of 8 is then considered to reach an effective sampling frequency of F_s = 15.625 M$sample.s^{-1}$.

Forestalling the following signal processing steps to be embeded in the FPGA process, complex signals have to be anticipated. From a signed 16-bit recorded real signal, a concatenation of a null 16-bit imaginary part is performed, as to fit the architecture of a FFT block, for example.

Once again in anticipation of the subsequent signal processing, a signal frame, recorded over a full one-way frequency chirp, should be comprised of a given power of 2 samples. To achieve such minor evolution, from the initial T_s = 100 µs intended initially for the full-sweep rate, a reduction down to T_s = 65 µs is executed, equivalent to an increase of the up-converted chirp rate to Γ = 492 T$Hz.s^{-1}$. This improvement relies on the fact that the PLL can still be operated in locked state at this rate. With this sampling rate, 1024 14-bit samples are recorded over a full one way

sweep frame. Such an optimization leads to a symmetric chirp repetition rate of 7.62 kHz. This initial implementation relies on the sole recording of the beating signal only over a rising chirp, leading to a 7.62 kHz measurement rate.

In addition to the quite simple logic signal handling and formatting, a chirp trigger signal is as well generated to ensure the best synchronization between the DAQ frame acquisition and the sweep emission delivered by the PLL. As a way to provide a strong reliability when it comes to signal front sharpness and jitter performances, a square wave trigger signal is then generated among the FGPA board and linked to the DDS sweep generation unit as a master command to drive either the rising or descending chirp as depicted in Figure III.20.

- Externalization Ethernet transfer

Following those data formatting steps, the retrieval of the numeric signals toward a central unit for processing and Human-Machine Interface rendering, can be considered. Acknowledging the fact that the Gigabit Ethernet (GigE) IO interfaces are linked to the PS, a prior transfer of those data frames towards the PS memory should be carried out. With the high data-rates at stake, a DMA (Direct Memory Access) transfer has been integrated through the HPIO AXI ports. It will allow for the allocation of part of the PS memory where the S_{IF} chirp frames will be subsequently written.

As to fit the DMA transfer 256 clock burst size limitations, and the will to assess a single DMA burst for each measurement chirp frame, a concatenation of 4 subsequent samples is performed along the frame, leading to an increase of the bit count for each sample by a factor 4. Doing so, the consistency of the frame content is preserved. To allow for a maximal transfer throughput towards the PS, the DMA transfer is performed at the fastest available clock, then requiring a clock domain decoupling FIFO, which also operates as a data buffer. Once the DMA transfer towards the PS dedicated memory is completed, the Gigabit Ethernet transfer of a whole FMCW frame is performed and initiated on the PS side towards the host unit through the lwIP (lightweight IP) UDP (User Datagram Protocol) protocol. It indeed remains a simple solution especially suitable to the unidirectional data transfer. Once the full frame packet Ethernet transfer is performed, a feedback status register is updated on the PS side to allows the PL to initiate the subsequent FMCW frame DMA transfer.

The expected transfer data rate of 254 $Mb.s^{-1}$ is then achieved for the externalization of the raw complex data, hence close to the maximal Ethernet link throughput. Each UDP frame, emitted at the cadence of 7.62 kHz then corresponds to a full recording of the beating signal, S_{IF}, over the course of a rising frequency chirp, sampled at the effective sampling frequency of $F_s = 15.625MHz$, hence constituted of 1024 complex samples.

- Recorded raw FMCW beating signals

Thanks to the previously detailed FPGA integration, the collection of full FMCW chirp beating signals is simplified, as each Ethernet transmitted UDP frame corresponds to a desired raw data measurement. A selection of such raw temporal traces, S_{IF} are displayed in Figure III.17, with three configurations of interest. As a reference, $S_{IF_{ref}}$, a measurement is taken with a perfectly reflecting mirror at the waist point of the single point sensing optical system, allowing for a full back coupling towards the transceiver. In the opposite way, for $S_{IF_{back}}$, a background is taken in absence of any object in the sensing area. And lastly, a sample can be recorded, $S_{IF_{samp}}$, with in this case, a 7.5 mm thick Plexiglas plate sample.

As one can notice, even for the simplest signal, which is the reference measurement, the recorded trace remains far from the expected mono-frequency, stable amplitude beating trace that should be recorded in the case of a single reflective interface of the mirror (See Equation I.9). Similarly, in the background signal, a consistent component remains and is not linked to a measurement noise. This is obviously linked to the non-negligible reflectivity of several elements in the radar vicinity. Namely the used optical components, PTFE lenses in our case, from which each reflective interface will then lead to a non-negligible contribution.

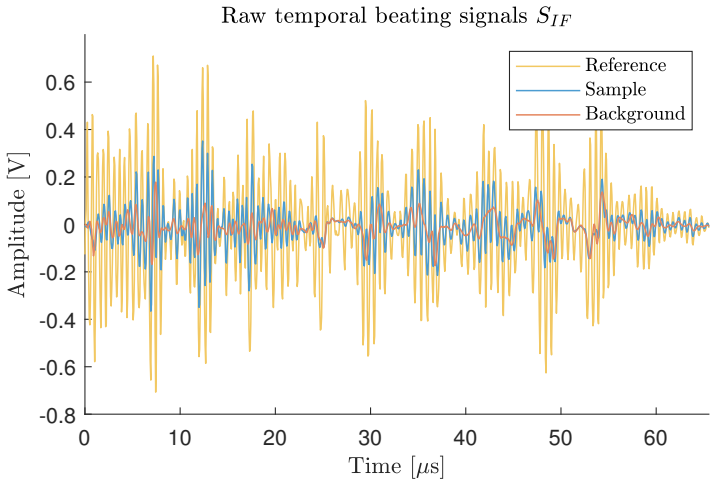

Figure III.17: Raw temporal beating signals S_{IF} for 3 configurations: a reference , a background and a sample measurement featuring a 7.5 mm thick Plexiglas plate.

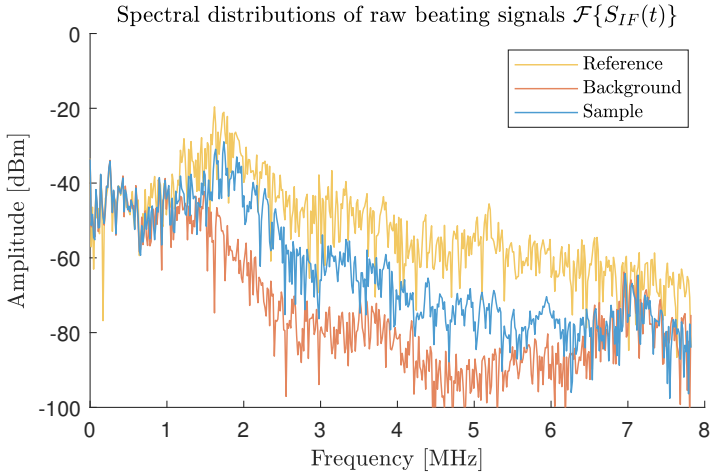

Figure III.18: Single sided spectral distributions of the raw beating signals S_{IF} for 3 configurations : a reference, a background and a sample measurement, featuring a 7.5 mm thick Plexiglas plate.

Those observations originating from the raw temporal signals are corroborated by their spectral power distributions as well, depicted in Figure III.18.

Once again, in the perfect FMCW radar model (see section I.4.1), each reflective interface should lead to a single frequency component. At first glance, one can notice that the recorded signals do not display those characteristics, even in the case of the perfectly reflecting reference.

Nevertheless, such spectral distributions still display features of interest. Specifically, the centering of the beating signal around 1.7 MHz for an object placed at roughly 50 cm from the transceiver is corroborated by Equation I.10, that links the chirp rate $\Gamma = \frac{BW}{T_s}$, and the target distance, to the beating frequency. It was nevertheless initially intended to reach a beating frequency of 1 MHz with a Sweep period of T_s=100 µs for a propagation path of 50 cm. The cadence evolution to T_s=65 µs, as to fit the FPGA implementation, led to an increase of this beating frequency, still perfectly within the sampling capabilities of the DAQ. Additionally, considering the reference signal configuration, it can be observed experimentally that, if one were to simply mechanically shift the reference mirror, a global shift of the major spectral component, initially centered around 1.7 MHz would be witnessed. The expected beating distance/frequency correlation, granted by the FMCW homodyne detection is effective. However, the achievable longitudinal resolution, initially linked to the transceiver BW, remains far beyond the expected theoretical value of 4.6 cm.

Additionally, specific stable spectral components can be as well witnessed in each of those recorded traces. Especially, the fix low frequency components, from 1 MHz and below, can be imputed to steady contributions in the vicinity of the radar, with the optical components. This has been attested with the drastic reduction of those contributions when inserting an absorber at the output of the radar transceiver prior to the beam shaping optics.

To view of those raw signal recordings, the previously depicted technological architecture does not natively allow for optimal and expected performances. Indeed, several imperfections that will be detailed along section III.3.1, led to unexploitable raw signals. Additional data processing is nevertheless practicable to remedy those alteration, namely through a temporal signal normalization procedure, fully detailed in section III.3.

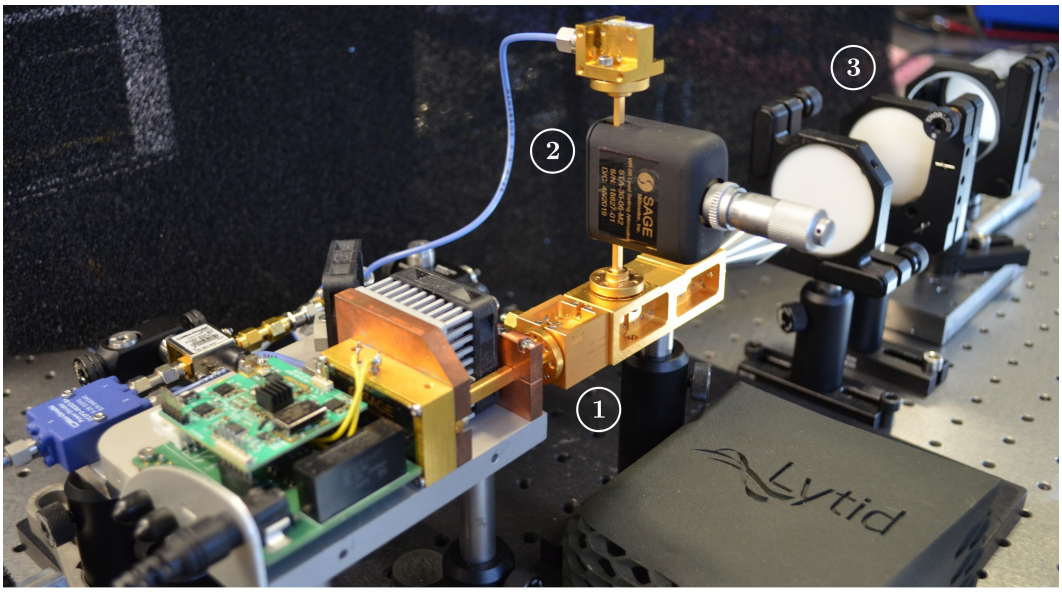

Figure III.19: Picture of most components of the development FMCW radar transciever main HF components, featuring the direct emission chain in the foreground (1), topped by the homodyne detection branch with an attenuator and the mixer (2), completed on the background by the beam shaping optics (3).

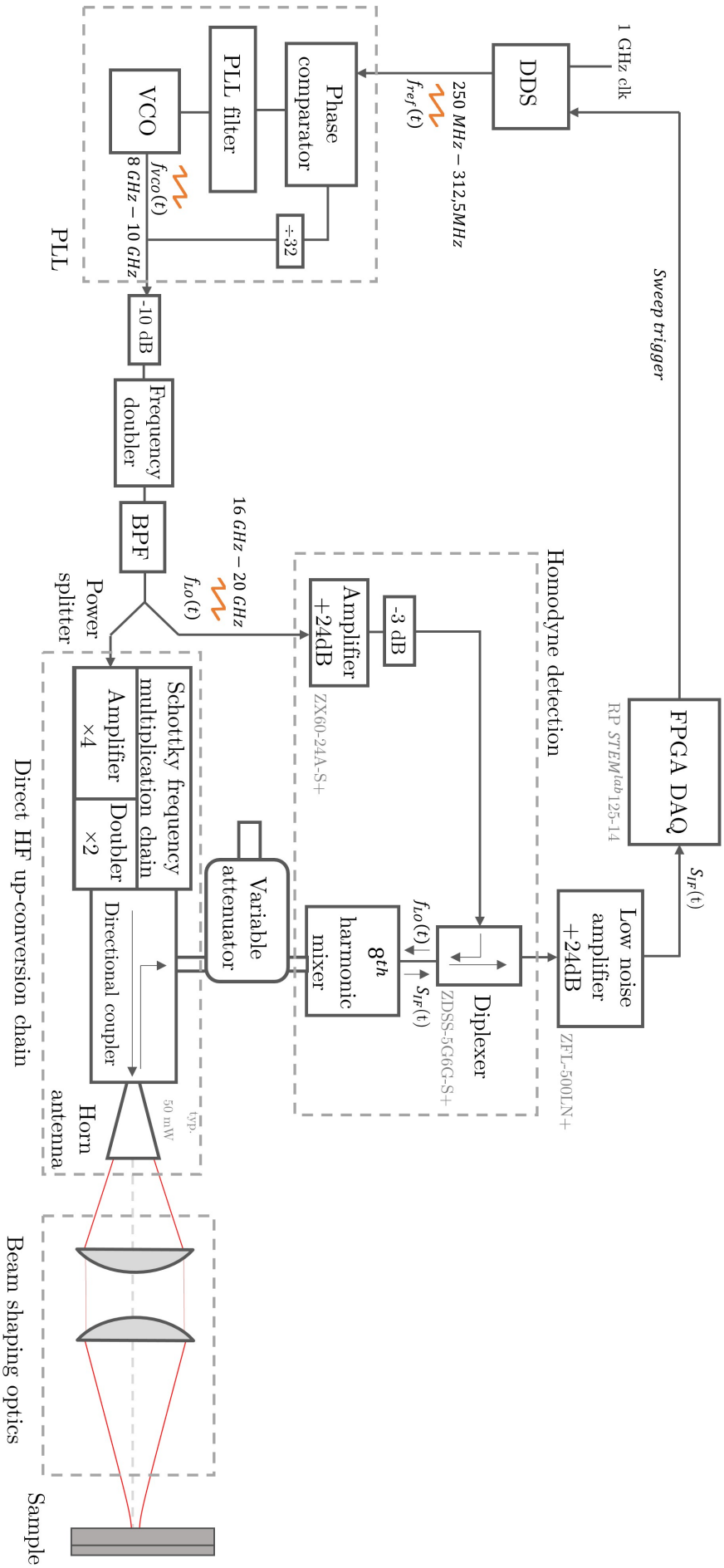

Figure III.20: Full FMCW radar architecture diagram featuring the low frequency chirp generation PLL stage, the direct up-conversion and emission stage, the beam-shaping and coupling optics and the homodyne detection stage.

III.3 Signal Pre-Processing

In the previous section, the final depictions of raw signals highlighted the requirement for additional data processing stages to retrieve exploitable and quantitative information from the FMCW radar unit. Indeed, even considering a careful technological design process to reach optimal characteristics, several limitations are highly impacting the raw achievable performance of the transciever. Namely, the amplitude spectrum of the emission source and LO signal could highly alter the beating signal, leading to convoluted FMCW information. To account for those alterations, further described in section III.3.1, a temporal normalization procedure can be integrated and will be further described along section III.3.2.

III.3.1 Impact of model alterations

In the ideal FMCW model previously described in section I.4.1, several considerations have been neglected.

Fabry-Perot resonator echoes

Namely, resonant echoed contributions can arise from multi-paths travels in between reflective objects. A single interface can then contribute to the generation of several beating frequencies. Indeed, thanks to its range sensing capability, Fabry-Perot cavities generated in free-space (e.g. between object interfaces and beam shaping optics interfaces) or within a material between two reflective interfaces can be resolved and do not appear as usual as interference patterns. Similarly to time-resolved TDS inspection methods, they would lead to the duplication of primal peaks and therefore would induce longitudinal ghosting artifacts.

Chirp non-linearity

Likewise, the previously considered ideal FMCW model excluded the impact of any imperfection to the emitted frequency chirp. Specifically, a non-linearity in the sweep signal or induced by the transmission chain. In most cases, this artifact is generated by the VCO that often presents a non-linear voltage-frequency response. If no attempt to straighten out the frequency sweep is made, several artifacts can appear with mostly a spectral peak broadening and distortion as depicted in Figure III.21, hence, highly degrading the achievable measurement dynamics. This specific point has been addressed in section III.2 with the insertion of the VCO within a PLL to minimize this non-linearity. As an alternative approach, the detailed study of the impact and an algorithmic correction approach can be found in [11, 39].

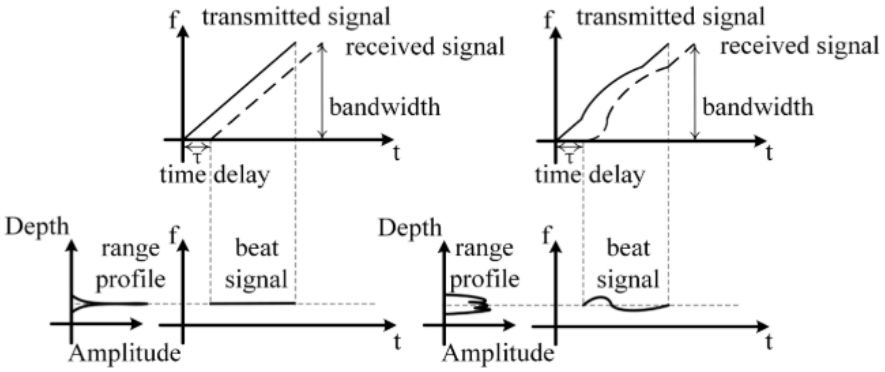

Figure III.21: Diagram representing the impact of a non-linearity in the frequency chirp [11].

Spectral characteristic impact

Additionally, an inconsistency in the emission spectrum of the transceiver can drastically impact the beating signal profile as well. Indeed, altering the ideal FMCW model depicted in Section I.4.1 over the course of a frequency chirp, the spectral profile, $a_{probe}(f)$, will be transposed as a temporal amplitude variation $a_{probe}(t)$. From Equation I.6, it can be considered for the analytical emitted signal as follows:

$$\widetilde{\mathrm{S}}_{probe}(t) = a_{probe}(t)e^{i2\pi f_{min}t + i\pi\frac{\mathrm{BW}}{\mathrm{T}_s}t^2 + i2\pi\phi_0}. \tag{III.3}$$

Hence, in the case of direct mixing, considering an unchanged spectrum after back-coupling, the analytical beating signal will incorporate the following additional terms:

$$\widetilde{\mathrm{S}}_{\mathrm{IF}}(t) = \sum_{i=1}^{p} a_{probe}(t) \times a_{probe}(t-\tau_i) \times r_i e^{i2\pi(f_{min}\tau_i + \frac{\mathrm{BW}}{\mathrm{T}_s}\tau_i t)}, \tag{III.4}$$

with once again, p, the number of target, i the considered target, r_i and τ_i the reflection coefficient of this said target and propagation delay respectively.

Considering the propagation delay τ_i to be small enough with respect to the total sweep time, and a slowly varying amplitude evolution on the spectral characteristic of the source, the following simplification can be performed:

$$\widetilde{\mathrm{S}}_{\mathrm{IF}}(t) \simeq a_{probe}(t)^2 \sum_{i=1}^{p} r_i e^{i2\pi(f_{min}\tau_i + \frac{\mathrm{BW}}{\mathrm{T}_s}\tau_i t)}. \tag{III.5}$$

A modulation of the beating signal is therefore induced and will lead, in the spectral domain, to a convolution of the ideal spectral response of the radar by the Fourier transform of the source power spectrum as follows:

$$\mathscr{F}\{\widetilde{\mathrm{S}}_{\mathrm{IF}}(t)\} = \mathscr{F}\{a_{probe}(t)^2\} * \mathscr{F}\{\sum_{i=1}^{p} r_i e^{i2\pi(f_{min}\tau_i + \frac{\mathrm{BW}}{\mathrm{T}_s}\tau_i t)}\}, \tag{III.6}$$

where $*$ represents the convolution operator. A non-negligible broadening of a single interface frequency response can then be expected with respect to the mono-frequency beating anticipated in the perfect FMCW model. The mitigation of this specific problematics will be further addressed in the following section, with the implementation of a temporal normalization procedure on the beating signal $\mathrm{S}_{\mathrm{IF}}(t)$ to avoid such drastically limiting behaviors.

In our specific case, the harmonic mixing is performed between the low frequency LO which features a flat power response (see Figure III.7a) and the HF signal that will display strong power variations as previously detailed in Figure III.11. Equation III.6 could therefore be assimilated with a linear spectrum convolution instead of the quadratic term. More broadly, the $a_{probe}(t)^2$ term should be more rigorously expressed as $a_{\mathrm{LO}}(t) \times a_{probe}(t-\tau_i)$, with $a_{\mathrm{LO}}(t)$ the LO time dependent spectral distribution as a function of the sweep time.

Beside the amplitude spectral evolution, when considering a real value spectral characteristic $a_{probe}(t)$, this approach can be broadened to the impact of the phase characteristics of the FMCW unit when considering a complex spectral distribution, $a_{probe}(t) = \mathrm{A}_{probe}(t)e^{\phi_{probe}(t)}$. As no phase characterization have been conducted, no discrimination of those two contributions will be addressed.

III.3.2 Normalization procedure

The impact of this latest model alteration, related to the amplitude power spectrum, is the main reason for the drastic raw performance limitations of the radar transceiver. Namely, the severe peak broadening, induced by the convolution depicted in Equation III.6, eradicates the longitudinal resolution of the systems, as witnessed in Figure III.18. Indeed, the flat 7.5 mm thick Plexiglas

sample should display 2 main amplitude peaks related to each interface, while in this case, a convoluted spectral tumult is collected. From the amplitude spectrum impact model, a deconvolution operation of the raw radar spectral response should then be achievable, providing the access to the convolution pattern.

Analytical signals retrieval : single-sided filtering

The previous raw data sampling operation leads to the collection of a real harmonic signals. Hence, when transposed in the frequency domain through the Fourier transform operation, $\mathscr{F}$, the spectral distribution features a symmetric double sided spectrum due to the Hermitian symmetry of a real space signal. A sample with one interface would then give rise to two distinct contributions. Namely, the main contribution at the beating frequency f_{IF_i} and a symmetrical contribution at its negative beating frequency counterpart $-f_{\mathrm{IF}_i}$. In order to avoid this superfluous additional contribution, highly troublesome for subsequent processing steps, a suppression of the negative frequency $[-\frac{\mathrm{F}_s}{2}; 0[$ (or equivalently the $[\frac{\mathrm{F}_s}{2}; \mathrm{F}_s[$) spectral interval should be considered.

To do so, one can acknowledge that any harmonic function can be represented as the real part of a complex analytic function, that therefore will have no negative frequency components [40]. The obtention of such an analytic signal can easily be performed thanks to the Hilbert transform as such: $\widetilde{\mathrm{S}}_{\mathrm{IF}_{samp}} = \mathrm{S}_{\mathrm{IF}_{samp}} + i\mathscr{H}\{\mathrm{S}_{\mathrm{IF}_{samp}}\}$ [40–42]. $\mathscr{H}$, the Hilbert transform operator will give rise to the quadrature signal. $\widetilde{\mathrm{S}}_{\mathrm{IF}_{samp}}$, the experimental analytic signal will then feature a loss of its initial spectral negative frequency components.

An equivalent approach, implemented in this work, consists in straightforwardly nullify the negative frequency component through a simple multiplication by a step function in the frequency domain [41]. A transposition of this single sided spectrum, back in the time domain, through an inverse Fourier transform operation, $\mathscr{F}^{-1}$, will lead to the complex experimental analytic signal as follows :

$$\widetilde{\mathrm{S}}_{\mathrm{IF}_{samp}} = \mathscr{F}^{-1}\Big\{\mathrm{S}tep_{f_\mathrm{L},f_\mathrm{H}}\{\mathscr{F}\{\mathrm{S}_{\mathrm{IF}_{samp}}\}\}\Big\}. \tag{III.7}$$

This approach allows for simplified additional spectral filtering when tuning the two cut off frequencies, f_L and f_H [$\mathrm{H}z$], in the $[0; \frac{\mathrm{F}_s}{2}[$ frequency range . Such an additional spectral filtering allows for a broad primary limitation of the frequency window of interest around the sensing area.

Two points referencing normalization

The prior single sided filtering nevertheless does not solve the spectral convolution issued previously. To remedy this point, a time domain two points referencing normalization procedure can be implemented [41]. This operation will feature a background subtraction followed by a unitary reference normalization step.

As witnessed in the measured S_IF raw beating signals, the main spectral alteration lead to a convoluted FMCW spectrum, as depicted in the altered model of Equation III.6. Alternatively, such a spectral convolution is related to a multiplication in the temporal domain as depicted in Equation III.5. This temporal over-modulation hence directly induces this spectral broadening artifact. The application of a normalization procedure, through the use of a temporal transfer function, can then be considered as a valid solution for the suppression of this over-modulation. The relation between the normalized signal $\widehat{\mathrm{S}}_{samp}(t)$ and the raw analytic beating signal $\widetilde{\mathrm{S}}_{\mathrm{IF}_{samp}}(t)$ should be given by :

$$\widehat{\mathrm{S}}_{samp}(t) = \mathrm{H}(t) \times \widetilde{\mathrm{S}}_{\mathrm{IF}_{samp}}(t), \tag{III.8}$$

with $\mathrm{H}(t) = \frac{1}{a_{probe}(t)^2}$ according to Equation III.5.

In practice, a retrieval of this transfer function should be targeted. This task can be performed when considering a single unitary reflection interface at zero distance. Indeed, this unique contribution would have endured no time delay propagation, hence, the beating signal would then be

reduced to $\widetilde{S}_{IF}(t) = a_{probe}(t)^2 \times 1$. Indeed, in this ideal configuration, one would notice that

$$\sum_{i=1}^{p} r_i e^{i2\pi(f_{min}\tau_i + \frac{BW}{T_s}\tau_i t)} = 1, \tag{III.9}$$

since p=1 for the unique target, r_i=1 thanks to the unitary reflectivity, and $\tau_i = 0$.

The obtention of the unique unitary reflectivity signal can be performed through the recording of a reference signal, $S_{IF_{ref}}(t)$, i.e. a mirror placed at the waist of the sensing optical configuration. Nevertheless, as witnessed previously, this signal still features parasitic reflections from optics and other radar surrounding components. A prior background removal task is then required.

Intended to be subsequently subtracted to any measurement, the recording of a background signal,$S_{IF_{back}}(t)$, in absence of any reflective interface in the sensing area, will ensure the suppression of all the unwanted contributions. This will allow for the consideration of only the sample related spectral contribution as follows:

$$\widetilde{S}_{IF_{samp}}(t) - \widetilde{S}_{IF_{back}}(t) = a_{probe}(t)^2 \sum_{i'=1}^{p'} r_{i'} e^{i2\pi(f_{min}\tau_{i'} + \frac{BW}{T_s}\tau_{i'} t)}, \tag{III.10}$$

with i' and p', denoting the removal of the background related targets.

In this same way, when applied to a reference recorded signal, related to a perfect reflector placed in a given reference plane, hence with p=1 and $r_{i'} = 1$, it will lead to:

$$\widetilde{S}_{IF_{ref}}(t) - \widetilde{S}_{IF_{back}}(t) = a_{probe}(t)^2 1 e^{i2\pi(f_{min}\tau_{ref} + \frac{BW}{T_s}\tau_{ref} t)}. \tag{III.11}$$

$\widetilde{S}_{IF_{ref}}(t) - \widetilde{S}_{IF_{back}}(t)$ then corresponds to the expected unitary reflection, over-modulated by the source frequency spectrum $a_{probe}(t)^2$. Due to the non-zero distance propagation to reach this reference interface, it will be tied to a beating frequency $f_{IF_{ref}} = \frac{BW}{T_s}\tau_{ref}$. Except for this detail, the transfer function could then be considered as $H(t) = \frac{1}{\widetilde{S}_{IF_{ref}}(t) - \widetilde{S}_{IF_{back}}(t)}$.

Accounting then for the subsequent analytic signal generation ($S_{IF_{samp}}(t) \rightarrow \widetilde{S}_{IF_{samp}}(t)$) background subtraction ($\widetilde{S}_{IF_{samp}}(t) - \widetilde{S}_{IF_{back}}(t)$), and temporal normalization ($\times H(t)$), the normalized sample temporal trace can be expressed as:

$$\widehat{S}_{samp}(t) = \frac{\widetilde{S}_{IF_{samp}}(t) - \widetilde{S}_{IF_{back}}(t)}{\widetilde{S}_{IF_{ref}}(t) - \widetilde{S}_{IF_{back}}(t)}, \tag{III.12}$$

A diagram of this procedure is depicted as the central piece of the subsequent FPGA integration given in Figure III.25.

In fine, as expected, this temporal normalization and background removal becomes equivalent to the expected spectral deconvolution by a single reflective plane reference spectral profile. More precisely, this will lead to the following normalized signal formulation, that emerges from the combination of Equations III.12, III.11 and III.10 :

$$\widehat{S}_{samp}(t) = \sum_{i'=1}^{p'} r_{i'} e^{i2\pi(f_{min}(\tau_{i'} - \tau_{ref}) + \frac{BW}{T_s}(\tau_{i'} - \tau_{ref})t)}, \tag{III.13}$$

with i' and p' once again only denoting sample related targets and their respective amplitudes $r_{i'}$, and $\tau_{i'} - \tau_{ref}$, their propagation times, relatively to the reference plane.

As a consequence, this two-points normalization procedure leads to several improvements. Namely, the expected deconvolution is performed for a mitigation of the spectral characteristic impact. Each contribution will then be featured as a Dirac distribution centered at the expected relative beating frequency. Additionally, the background subtraction allows for the suppression of the unwanted contributions. The final trace will therefore not feature the optics and other parasitic reflective elements. Hence, a drastic improvement of the dynamic range is to be expected as a

measurement in absence of reflective object will then only features a measurement noise emerging from the ADC, or outputted by the LNA, unspoiled by parasitic reflective elements. And finally, a beating signal frequency referencing with respect to the position of the reflective reference target plan will be witnessed. Indeed, the time delay difference featured in Equation III.13 will lead to a reduced frequency beating signal following $\widehat{f}_{\mathrm{IF}_{i'}} = \frac{\mathrm{BW}}{\mathrm{T}_s}(\tau_{i'} - \tau_{ref})$. A constant signal will then be observed at $\tau_{i'} = \tau_{ref}$, hence when a reflective interface is positioned in the reference plane. Considering then once again the back and forth propagation time with respect to this plane, in a medium of real refractive indes n, such that $(\tau_{i'} - \tau_{ref}) = \frac{2n\widehat{d_{i'}}}{c_o}$, the following relation ensue :

$$\widehat{d_{i'}} = \frac{c_o \widehat{f}_{\mathrm{IF}_{i'}}}{2n} \frac{\mathrm{T}_s}{\mathrm{BW}}, \tag{III.14}$$

with $\widehat{d_{i'}}$ the relative distance to the reference plane [m], $\widehat{f}_{\mathrm{IF}_{i'}}$ the reduced beating frequency [Hz], and once again BW the sweep bandwidth [Hz] and T_s the sweep time [s], fixed to T_s=65 µs in this implementation. Equation III.14 echoes the distance-frequency relation given in the unaltered ideal FMCW model with Equation I.10, applied to normalized signals.

A depiction of the results obtained after this temporal normalization procedure is given in Figure III.22. They emerge from the raw signals displayed previously in Figure III.17. For the sake of simplicity and illustration purposes, the temporal complex analytic signals are displayed as distinct real and imaginary parts for the normalized signals that are presented. To perform the normalization on such signals, a prior reference and background recording have been performed and then applied to subsequent signals. To corroborate the normalization performances, the sample signals, $\mathrm{S}_{\mathrm{IF}_{samp}}(t)$, have been taken in three configurations with a reference configuration on reflective mirror in the waist sensing point of the optical setup, a background measurement in absence of reflective objects and finally, featuring a 7.5 mm thick Plexiglas sample for which the first interface was placed in the reference plane. From those raw collected signals, the sole application of the normalization procedure, depicted in Equation III.12, give rise to the complex normalized contributions of Figure III.22.

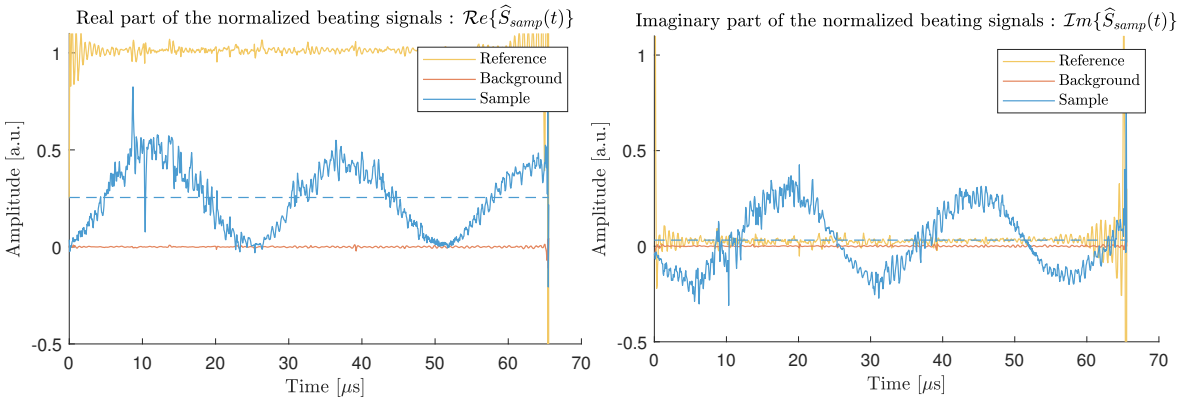

(a) **(b)**

Figure III.22: **(a)** $\mathscr{R}e\{\widehat{\mathrm{S}}_{samp}(t)\}$ real part and **(b)** $\mathscr{I}m\{\widehat{\mathrm{S}}_{samp}(t)\}$ imaginary part of temporal normalized signals in 3 configurations: a reference, a background and, a sample measurement featuring a 7.5 mm thick Plexiglas plate .

When normalizing a reference signal itself, as expected, the result features a constant real value of $\widehat{\mathrm{S}}_{ref}(t) = 1$. This observation can be made by leaving out the high frequency low amplitude noisy components. Additionally, the sweep extremities display unstable behaviors due to the low employed emission powers at the bandwidth extrema, inducing higher levels of incertitude in the normalization transfer function. Such components will contribute as a limitation to the single peak achievable dynamic range. The imaginary part also feature a negligible 0.05 fixed component, emerging from a non-zero static phase between the calibration and measurements, or a subtle displacement of the reflective plane between the two processing and processed reference

measurements. *In fine*, this contribution can be designated as an unitary contribution at the frequency of 0 Hz, the related beating frequency with respect to the position of the reference plane.

Now considering the normalized sample measurement, it features a real continuous component centered around 0.25, combined with a main sinusoidal component of frequency on the order of 0.04 MHz, accompanied by much higher frequency components of lower amplitudes. The continuous component is linked to the first interface of the Plexiglas plate, positioned in the reference plane, hence contributing as a beating signal at the frequency of $\widehat{f}_{\mathrm{IF}'_1} = 0$ Hz since $\tau_{1'} = \tau_{ref}$. The second contribution, on the other hand can be linked to the second interface and features a non-null beating frequency due to the induced relative propagation time with respect to the reference plane, $\widehat{f}_{\mathrm{IF}_{2'}} = \frac{\mathrm{BW}}{\mathrm{T}_s}(\tau_{2'} - \tau_{ref})$ with $\tau_{2'}$ the propagation time required for a back and forth propagation toward the second interface. It will then account for the additional round trip propagation in the 7.5 mm Plexiglas thick layer, that features a real refractive index of $n_{Plexiglas} = 1.59$ at 150 GHz, assessed through literature [43] and TDS investigations.

Finally, considering the background measurement, performed in absence of reflective elements in the measurement field, no significant contributions are recalled as the background subtraction referencing allows for the eradication of any major contribution that could arise from reflective elements such as the optical components interfaces. The reminiscent differential signal, $\widetilde{\mathrm{S}}_{\mathrm{IF}_{samp}}(t) - \widetilde{\mathrm{S}}_{\mathrm{IF}_{back}}(t)$, then only lies on the measurement noise of the system, hence imputable to a low amplitude thermal noise.

Dynamic range improvement : averaging

A reminiscent thermal noise component can easily be witnessed on the normalized reference and background measurements and will be the limiting factors in term of achievable measurement dynamic range. It originates from the different noise sources in the system among the radar transceiver. In the case of a random noise distribution, time averaging can successfully reduce the effective noise level. An improvement of the SNR, and so measurement dynamic range, can then be expected by averaging over several sweeps the measured signal $\widetilde{\mathrm{S}}_{\mathrm{IF}_{samp}}(t)$ or quite similarly the already normalized signal $\widehat{\mathrm{S}}_{samp}(t)$.

Nevertheless, the measured noisy components embedded in the transfer function through the previously recorded signal $\widetilde{\mathrm{S}}_{\mathrm{IF}_{back}}(t)$ and $\widetilde{\mathrm{S}}_{\mathrm{IF}_{ref}}(t)$ will as well impact the measurement dynamic range. Additional averaging on the reference and background transfer function signals should then as well be considered.

The performances granted by such averaging operations will be further detailed in section III.4.5. Typically, large average numbers over the components of the transfer function are practicable as they can be performed only once at the launch of the radar unit, thanks to its long term stability. While averaging over the measurement itself will impact the desired achievable dynamic range, and expected measurement rate.

Rendering additional processing : windowing, zero-padding and Fourier transform

As stated earlier, the frequency domain is obviously much more suited for visualization purposes, as a reflective element should render as a single Dirac frequency contribution. A Fourier transform of the previously normalized sample can then be considered. From the N_s=1024 complex samples signal, a frequency domain representation should be retrieved, but does not offer an adequate frequency resolution as depicted in Figure III.23a. Hence, the distance numerical resolution is also found to be quite limited, caped to the longitudinal resolution of 4.6 mm. The following spectral characteristics are displayed on reduced frequency regions interest. The [-0.5 MHz 0.5 MHz] span, corresponding to a ± 15 cm distance span around the reference plane.

For quantitative visualization purposes, zero padding operations can be performed to artificially improve the numerical frequency resolution [44]. The zero padding operation consist in appending zeros prior to and after the normalized temporal signal. An enhancement of the peaks

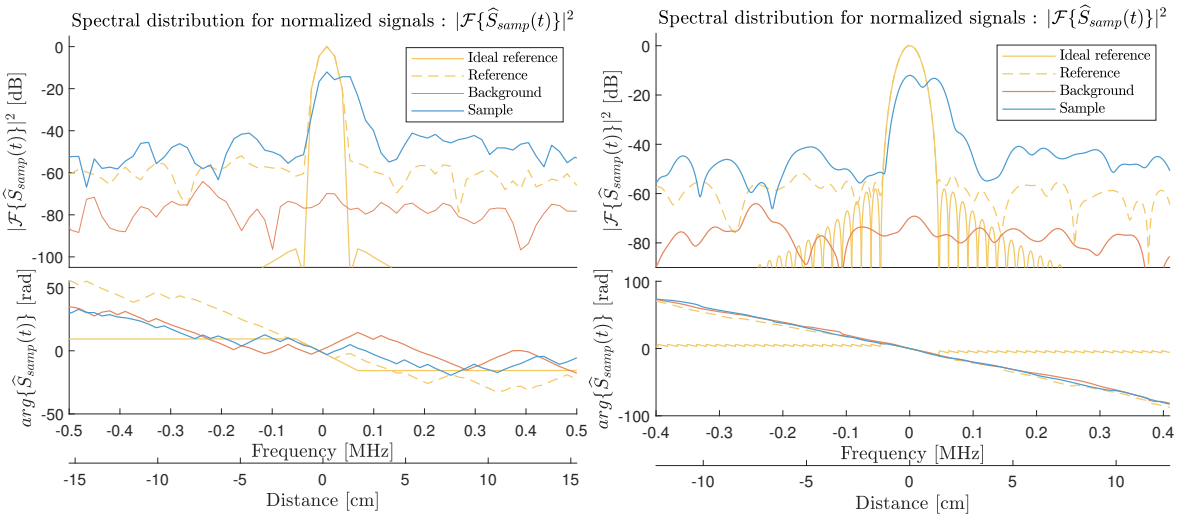

Figure III.23: Spectral visualisation of the normalized signals **(a)** in absence of additional zero-padding and **(b)** considering a $N_{ZP} = 64$ zero padding factor with a Blackman apodization window.

position and respective amplitudes will hence be witnessed as one can see with Figure III.23b. Introduce a zero padding factor, N_{ZP}, hence leading to a final temporal signal of length $1024 \times N_{ZP}$, the subsequent frequency resolution will be accordingly scaled as $\frac{\delta_f}{N_{ZP}}$ where δ_f represents the initial numerical frequency resolution [Hz]. Figure III.23b features a zero padding factor of $N_{ZP} = 64$, hence, Fourier transform operations are performed over 65536 points to reach those representations. Additionally, the improved spectral resolution allows for a relevant unwrapping of the signal phase as established in Figure III.23b

Nevertheless, if no care is taken, and the zero padding operation only consists in concatenating zeros to the signal, a sharp drop will be witnesses at both ends of the recorded signals. This operation would be equivalent to the over-modulation of a signal through a rectangular window. In the frequency domain, it would then result in the convolution of the expected spectrum by the Fourier transform of this square window, hence, a cardinal sine function. With such un-careful zero-padding operations, the appearance of non negligible side-lobe would then be witnessed with amplitudes of -13.26 dB as detailed in Table III.1.

The prior windowing of the signal is then required to smooth the transition toward the concatenated zeros, and will lead to the apodization of the predominant side-lobes [45]. As depicted in Figure III.24b, this will nevertheless have as a harmful consequence to widen the main spectral lobe. The profiles of typical windowing apodisation functions are given in Figure III.24. Their respective features of interest in this work, i.e. main lobe width and secondary lobe amplitudes, are given in Table III.1.

Table III.1: Characteristics for main apodization functions.

	Main lobe width @ -3dB	Secondary lobe height [dB]
Rectangular	$0.87 \times \delta_f$	-13.26
Hamming	$1.28 \times \delta_f$	-43.59
Hann	$1.42 \times \delta_f$	-31.47
Blackman	$1.62 \times \delta_f$	-58.11

Following this global normalization procedure will lead to quantitative visualization of FMCW radar signals as depicted in Figure III.23b. The three normalized reference, background and sample measurements are featured. The rendering operations featured a Zero padding factor of $N_{ZP} =$

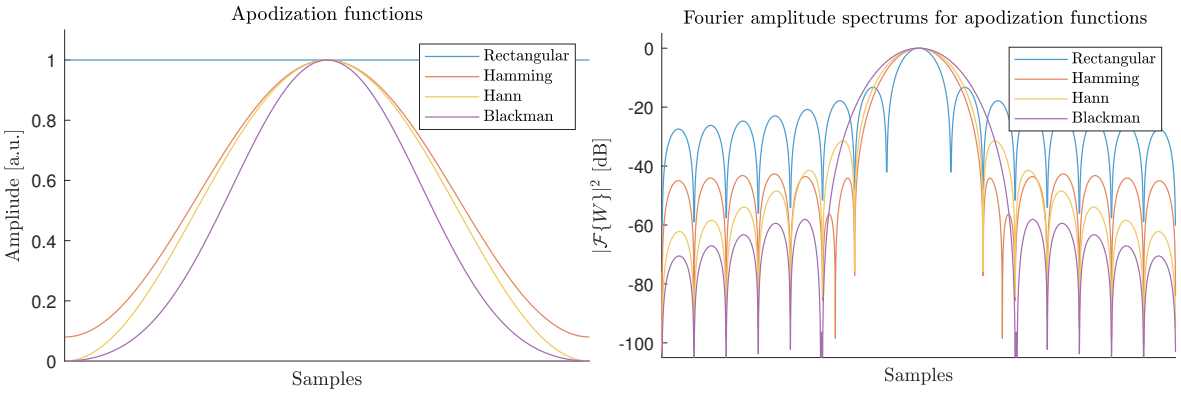

(a) **(b)**

Figure III.24: **(a)** Apodization function representations and **(b)** relative Fourier transform amplitude spectra.

64 with the application of the Blackman window. These measurement has been performed with averaging over 1024 frequency chirps for the sample and 4096 averaging over the transfer function reference and background measurement.

As expected, on the reference measurement, a central peak at the reduiced frequency of 0 Hz is obtained with an unitary amplitude. A reminiscent noise is observed with a measurement dynamic range of over 60 dB on the peak amplitude. On the Plexiglas sample measurement, the two interfaces are clearly observed with the first one in the reference plane and the second one further behind, aroung 0.04 MHz. The first interface reflectivity amplitude corroborates the reflection coefficient expected by an air interface with a material of refractive index $n_{plexiglas} = 1.59$. An additional frequency component, centered at $\widehat{f}_{\mathrm{IF}_3\prime}$=0.08 MHz is relative to a Fabry-Perot echoe induced by the multiple reflections among the flat sample cavity. Finally, on the background measurement, a 80 dB measurement dynamic range can be witnessed corroborating the adequacy of the background removal operation.

III.3.3 FPGA Integration

Considering this efficient normalization procedure, that allows for the deconvolution of the initially un-exploitable FMCW raw signals, a global real-time data processing integration can be considered. The previously described DAQ FPGA unit, detailed in section III.2.2, initially considered as a simple data retrieval tool, can be complemented to integrate additional processing steps among the reprogrammable logic. This consideration is especially suitable as the algorythmic processing remains a linear process, through the cascading of the previously featured steps.

This section will be dedicated to a coarse depiction of the design of this FPGA architecture, for the embedding of the normalization procedure. A global design of this FPGA implementation is given in Figure III.25, while the Vivado block diagram for the full processing project integration is given in Appendix D, Figure D.2. For further information on this integration, the reader can refer to Appendix D where a more detailed FPGA oriented description of the implementation is provided, as this task represents a non-negligible part of the work conducted in this thesis. Namely, this normalization architecture, along with the establishment of the high data rate Ethernet link accounts for few months of work to reach such a streamline architecture.

Data collection and formatting

This first operation lies on the same architecture as for the previously featured DAQ implementation. A 125 M$sample.s^{-1}$ signal sampling is performed by the ADC and fed in the clock decoupling FIFO as to avoid timing issued. For the integration of the subsequent FFT operation, a complex number signal is then generated by concatenating a 16-bit zero imaginary part.

The generation of a decimated clock to the frequency of F_s = 15.625 MHz can be integrated as the working frequency input of the subsequent FFT. It will hence passively operate as the sub-sampling operation as to reduce the data-rate. Once again, the externalization of the chirp trigger signal allows for a synchronization of the PLL frequency sweep. Additionally to this external trigger, a proper internal trigger of the recorded signal frames comprized of 1024 samples is as well of extreme importance. Those t_{Valid} and t_{Last} flags will ensure the reliability of the subsequent time related operations. Additionally, the use of LED indicators will detail the proper functioning of the FPGA board and will integrate status indicators for the collection of normalization signals.

Single-sided filtering

Due to the complexity of integrating an FPGA Hilbert transform, the analytical signal retrieval will be conducted as detailed in Equation III.7, through the application of an double Fourier transform, along with an asymmetrical rectangular window modulation in the frequency domain.

The first step then consists in applying a Fourier transform to the input collected signal. The capability to perform this transform fast enough should then be considered in order to avoid a limitation of the achievable measurement rate. The Pipelined streaming I/O solution allows for such real time processing but obviously represents a demanding operation in term of required logic resource [46]. The resource limitations of this chip led to the limitation of the frame size to 1024 samples, hence setting the decimation factor to 8.

The complex Fourier transform of the input signal can then be fed in the asymmetrical filter to which the two cut-off frequencies, f_L and f_H, have been formerly provided through an initialization procedure. Those two values are stored in dedicated BRAM (Block Random Acces Memory) units, accessible by the filtering unit, as depicted in Figure III.25. As each clock cycle will bring the subsequent frequency component unloading from the FFT unit, the filtering step is performed along the data-flow and is further detailed in Appendix D.

This single sided filtered spectrum can then be back-transposed to the time domain with the integration of an IFFT (Inverse Fast Fourier Transform). Those two Fourier transform operation are accompanied with an additional constant scaling factor for each processed frame to provide an optimal bit-wise resolution. Those scaling coefficients are then accounted for in a subsequent re-scale step.

Normalization

Following such a single sided filtering, the sample analytical complex signals will then transit at this point. Hence, the normalization procedure can be considered.

To do so, a prior recording of the reference and background normalization elements, is performed. At launch, upon the user query, a recording of the filtered reference signal (taken on a perfectly reflective sample placed at the imaging waist) and a background signal (taken in absence of object in the imaging field) is stored in dedicated BRAM units from the output of the single sided filter processing chain. An additional averaging step, typically over 512 frames is performed on each of those two configurations to improve the transfer function effective SNR. Such storage then allows their accessed when needed for the background removal and normalization procedure as depicted in Figure III.25.

The time dependant normalization is then performed, once again accounting for the data-flow, as each clock cycle will bring a subsequent measurement point, along the 1024 samples frame. A flawless timing through t_{Valid} and t_{Last} flags is then once again required for the assessement of the background and reference BRAM access.

Additionally, specific precautions are accounted for since the integration of a division operation in the normalization (see Equation III.12) can leads to bit growth as the divisor becomes small.

Data externalization

From such normalized temporal complex signals, their externalization toward the host central unit can be considered. With respect to the simple DAQ architecture previously detailed, the data-stream to be transferred displays identical characteristics. Namely, a frame of 1024, 32-bit complex samples should be transmitted. These unchanged cadences and bit counts allows for the use of the exact same transfer mechanism as for the sole DAQ integration. Namely, a 4 sample concatenation operation is performed to suite the 256 clock cycle burst size for AXI DMA transfer. Subsequently to the completion of a full frame DMA update toward the PS, the Ethernet packet transfer take place and once completed, will trigger the subsequent DMA transfer.

A fully processed complex frames is then retrievable on the Ethernet port for every chirp cycle, *i.e.* every 130 µs. Those time domain frames are then equivalent to the $\widehat{S}_{samp}(t)$ traces featured in Figure III.22.

Such integration remains exempt of the zero padding and final spectral conversion rendering FFT as those final processing steps have been chosen to be performed outside of the FPGA integration for 2 main reasons. At first, the implementation of high sample count FFT after zero-padding would displays large logic resource requirements, that are not meeting the capabilities of such limited FPGA zynq7010 chips. Secondly, the Ethernet throughput should fit the internal data-rate. In absence of zero-padding operation, transferring 1024 complex samples over 130 µs leads to a 254 kB.s^{-1} transfer rate. The use of a N_{ZP} = 4 would already saturate the Gigabit Ethernet link. A limitation of the transmitted frequency window to a spectral range of interest (typ. [-500 kHz, 500 kHz] equivalent to a ±15 cm measurement span), would nevertheless enable the use of larger zero-padding factors.

Additionally, the externalization of the final zero-padding and FFT operations lies on a versatility-oriented decision. More freedom can then be granted to the integrator if those two operation are deferred. Larger zero padding factors, N_{ZP}, could be considered in accordance with the available processing power. The windowing profile, for the apodization operation, would not be imposed either. Finally, the use of normalized temporal signals, is of interest for specific application cases. Namely, thickness assessment problematics, detailed further in section IV.4. In this approach, the thickness determination process is based on temporal error minimization of physical models with respect to the performed measurement. Hence, such algorithmic considerations would remain incompatible with the use of partial, resolution enhanced spectral signals.

As a current integration, the full normalization architecture displayed in Figure III.25 takes up to 87 % of available logic LUTs in the PL section of the FPGA board. Those resources are mainly employed for the FFT and IFFT transform operations as well as the normalization division.

This full data processing implementation relies on the recording of the beating signal over a rising chirp and further data processing over a full symmetrical chirp period. This integration leads to a 7.62 kHz measurement rate for the FMCW radar unit. No attempt to exploit the descending chirp has been pursued in this work. A parallelization on the processing chain, focused on this descending chirp time, could solve this issue and provide a doubling of the radar measurement rate. However, beside requiring twice as much logic resources that would simply require a larger FPGA chips, this implementation would still be limited by the DMA transfer process and Ethernet link capabilities as bottleneck limitations.

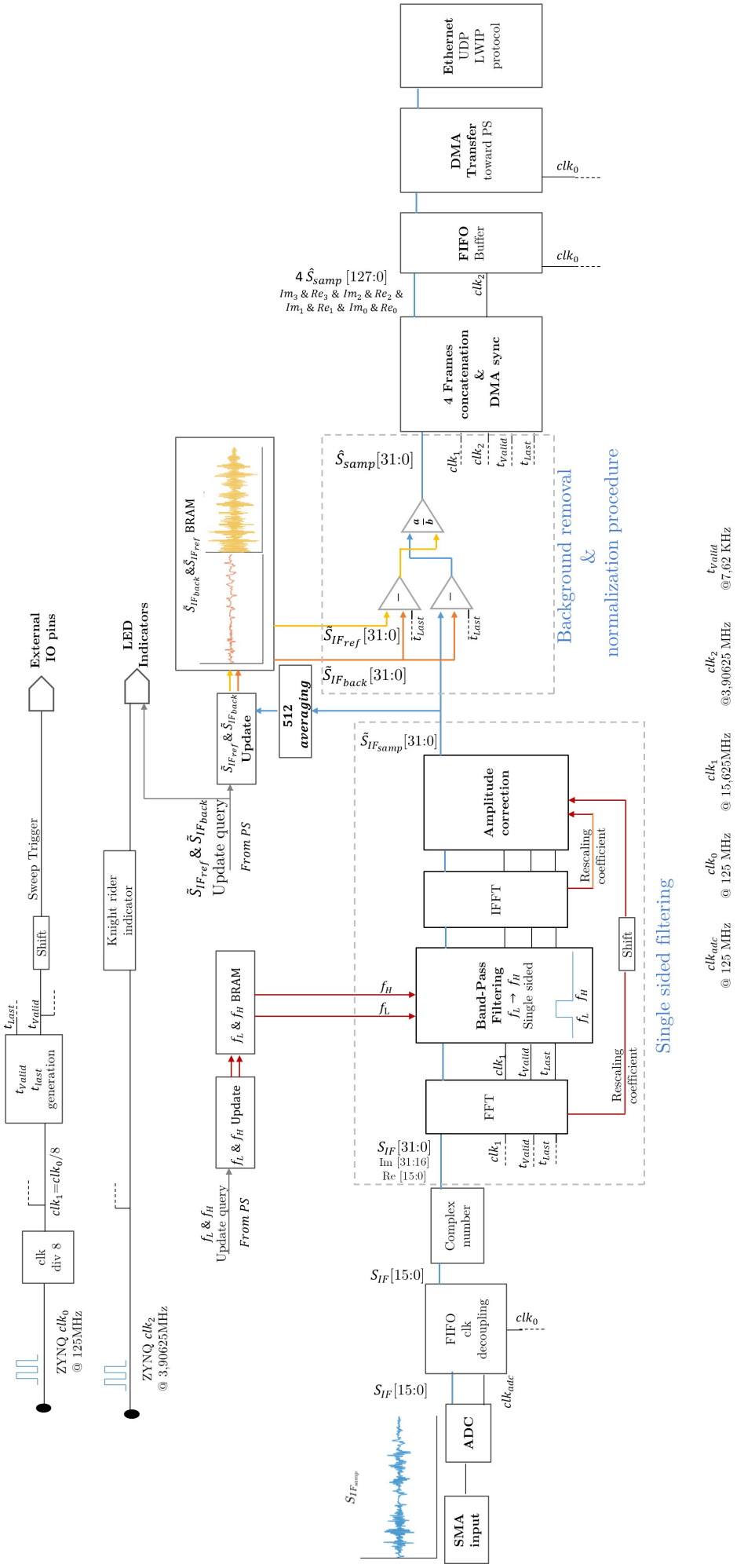

Figure III.25: Depiction of the implemented FPGA architecture as a DAQ module with integrated full FMCW data normalization procedure.

Up to this point, the radar has been used for punctual sensing for the definition and integration of an-optimal data processing procedure. *In fine*, following the FMCW mode of operation with high data-rate processing, each frequency chirp gives access to a whole longitudinal range information.

Given the high measurement rate granted by the FPGA processing integration, this approach can easily extended to 2D scanning of a sample. A focused point sensing imaging optical configuration, combined with a displacement of the object with respect to the radar sensing unit (or vice and versa), will then leads to the reconstruction of the whole sample with an additional longitudinal sensing information.

III.3.4 Visualisation concerns

Indeed, thanks to the inherent in-depth sensing capabilities of FMCW radar, a single point sensing A-Scan, performed over a single frequency sweep, will give access to a full longitudinal sensing of the probed object along the optical axis. Thanks to an adequate processing, depicted earlier in Section III.3, the longitudinal complex information are gathered in the vicinity of the focal point, on a representative depth range (i.e. typ. ± 10 or 15 cm range with respect to the reference plane in the case of focused point sensing) as displayed in Figure III.26b.

Providing a lateral displacement, a B-scan will then give access to a 2D information slice probing of the samples along the displacement direction $\vec{x}$. A simple representation in the form of an image in the $(\vec{x}, \vec{z})$ plane for the amplitude and phase, is then easily achievable as depicted in Figure III.26c, with $\vec{z}$ the longitudinal depth sensing direction.

Nevertheless, when considering a full $(\vec{x}, \vec{y})$ C-scan probing of a sample, a whole volume complex information is collected, as showed in Figure III.26d corresponding to a full A-scan depth sensing relative to each probing point.

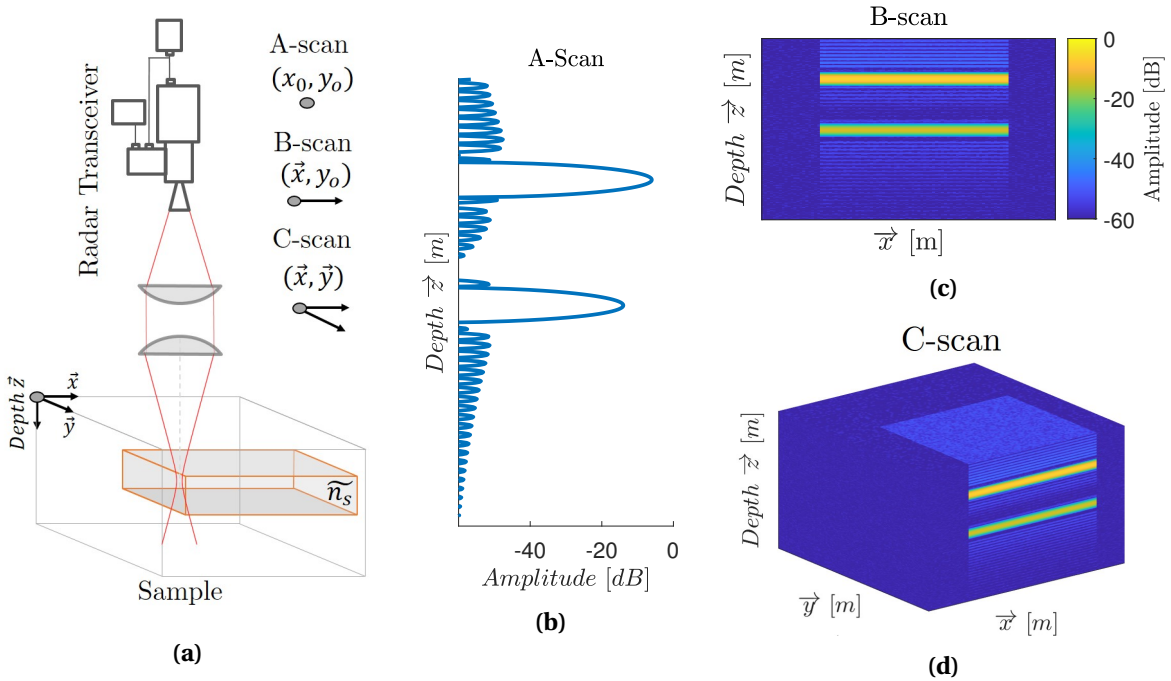

Figure III.26: **(a)** Diagram representation of a sample under inspection depicting the A, B and C-scans mode of operation, and simulations of their respective resulting radar amplitude data-sets for **(b)** a A-scan, **(c)** a B-scan and **(d)** a full volumetric inspection C-scan.

Displaying such 3D complex data sets can turn out to be quite challenging, especially in such a paper format. Inspired from ultrasounds [47], and eddy current NDT C-scan approaches, a simple 2D visualization of the signal maximum amplitude along the depth dimension can lead to a reliable, but non exhaustive representation of a sample in its entirety. Indeed, this maximal ampli-

tude approach will have a tendency to highlight reflective features, and especially first interfaces or metallic elements reflections, while concealing or covering up more subtle artifacts of interests. Even-though it does not lead to a proper phase representation either, it can nevertheless provide a topological information on the sample when considering the depth of this signal maxima on each scanning point.

On the other hand, the most exhaustive approach, the full volume display, would consist in considering every $(\vec{x}, \vec{y}, z_i)$ slice in the depth range as a stack of images for the amplitude and phase signals. An additional animation as videos, or Graphics Interchange Format (GIF) can ensure an effective visualization technique for this consequent amount of data. Additionally, from such a 3D data-set, from a full C-scan, lateral B-scans, in either the $(\vec{x}, \vec{z})$ of $(\vec{y}, \vec{z})$ planes, can easily be retrieved.

As a trade-off between those two visualization approaches, the averaging, in the depth $\vec{z}$ direction, over a given range of interest, to suit a specific sample geometry, represents a tailored solution. It gives rise to optimizes 2D representations when targeting specific artifacts visualization, in terms of amplitude.

For the sake of clarity and to ensure the display of the most exhaustive and quantitative pieces of information, the results features in the following sections will call on those display approaches, unless specified otherwise.

Figure III.27 features visualization approaches applied to a portion of a honeycomb reinforced sample. A scan time of 15 min, highly restricted by the translation stages, was required for the full-volume inspection of the sample. From this unique measurement, Figure III.27 highlights the benefits and drawbacks of each visualisation approach.

Namely, the selection of independent 2D $(\vec{x}, \vec{y}, z_i)$ complex slices (namely z=0 mm, z=4.6 mm and z = 7.5 mm), ensure the independent visualization of the front-face (see Figure III.27c), the honeycomb structure (see Figure III.27d), and the back-face inclusions to be detected (Figure III.27e).

On the opposite, as expected, the maximum amplitude representation depicted in Figur III.27a, mainly showcases the high reflectivity first interface while masking, to some extend the honey comb structure and back-face inclusions. Retrieving the position of this maximum allows as well for a topographic depiction of the sample, in Figure III.27b. Namely, it displays a slight misalignment tilt with respect to the scanning system, leading to a 1 mm shift over the 10×15 cm^2 flat sample. This tilt and sample bend, are as well perfectly visible on the phase image in Figure III.27c. Finally, tailored to this sample, for honeycomb integrity visualization and back-side inclusion sensing, an averaging over the range of interest z=[4 mm, 7.5 mm] gives rise to the optimized representation on Figure III.27f.

Even such simplistic samples demonstrates that, beside proper data processing, data handling and visualization is of extreme importance to exploit the radar to its full capabilities. A dedicated visualization application has therefore been developed for preliminary data-set handling when imaging concerns are at stake.

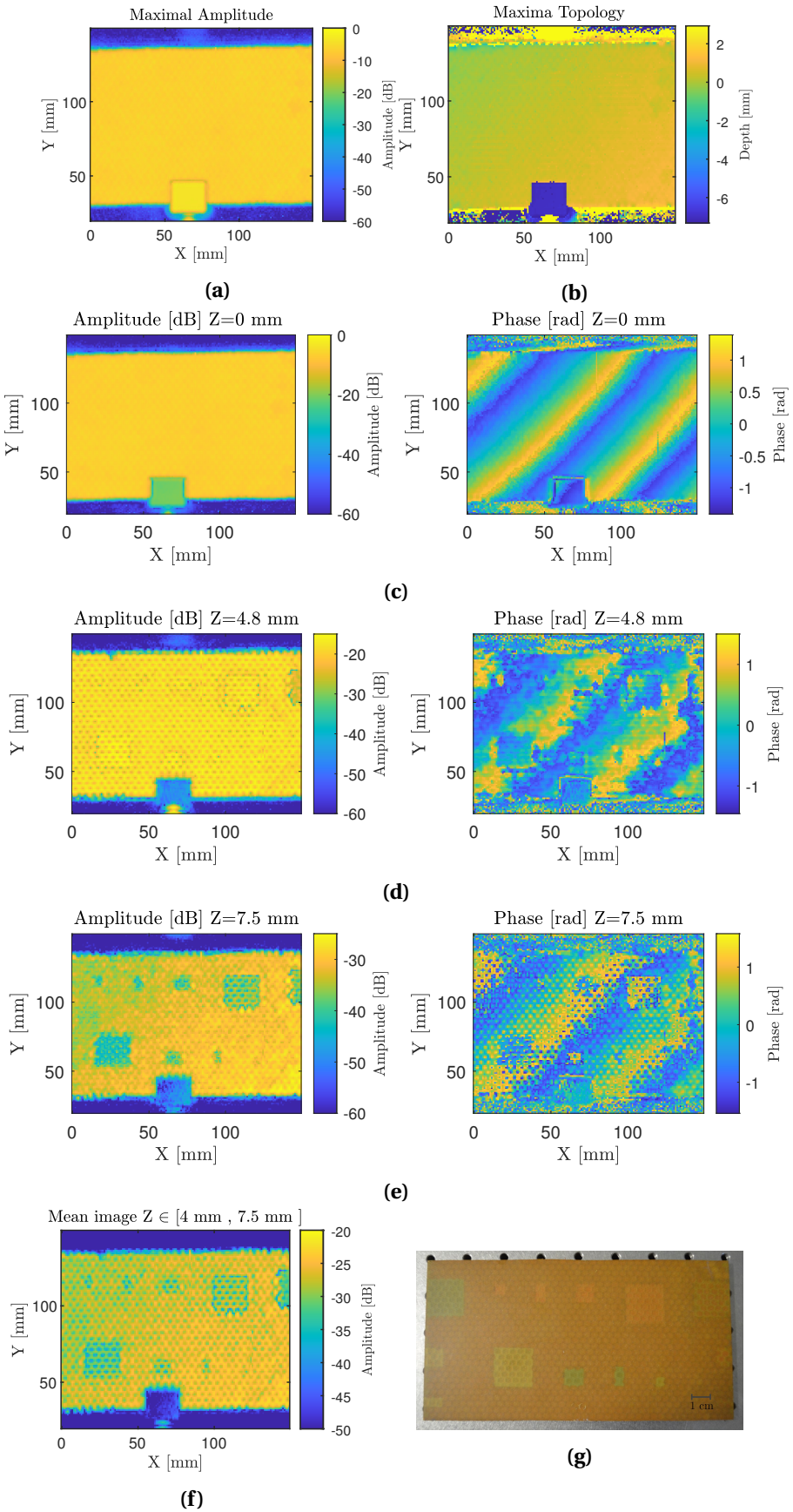

Figure III.27: Composite honeycomb structure reinforced sample, featuring inclusions on its back side, depicted through different visualizations approaches with : **(a)** Maximal reflectivity image, **(b)** related maxima tomography, complex slices at **(c)** z=0 mm ,**(d)** z=4.8 mm, **(e)** z=7.5 mm **(f)**, averaged amplitude image between 4 and 7.5 mm and **(g)** back side photograph of the sample.

III.4 Performances and Characterizations

Following the detailed depiction of the mode of operation of the radar transceiver along with its integrated architecture, an quantitative characterization of its performances can be envisaged. Namely, as a three-dimensional sensing method, a proper assessment of the lateral and longitudinal resolutions of this unit, with respect to the expected performances, represents a ineluctable operational validation factor. This should hence be considered alongside with the longitudinal sensing accuracy and precision. The effective sensing dynamic range designates as well a central performance factor for any sensing unit. Finally, the stability and effective measurement rate of the FMCW transceiver will be detailed as integration-oriented characteristics.

III.4.1 Effective measurement rate

With the fully integrated data normalization FPGA implementation, a measurement rate of 7.62 kHz is achieved. Nevertheless, included in a whole system, the data-collection and processing power of the receiving unit should at least match the data-transmission potential displayed by the transceiver.

For data-collection and imaging acquisition purposes, a Labview interface has been optimized to match the measurement rate potential of the transceiver unit. Namely, it incorporates an Ethernet UDP read block that allows for the collection of the measurement frames at full speed. Additionally, it integrates the translation stages control, the application of final rendering data-processing steps (sample averaging, zero padding and windowing, Fourier transform, *etc.*), and targeted display and visualization tools.

The global system achievable cadency performances will then obviously depend on the work load imputed to this receiving unit during the measurement phase since dealing with high data-rates as the one considered at full speed, 254 M$b.s^{-1}$, remains quite challenging.

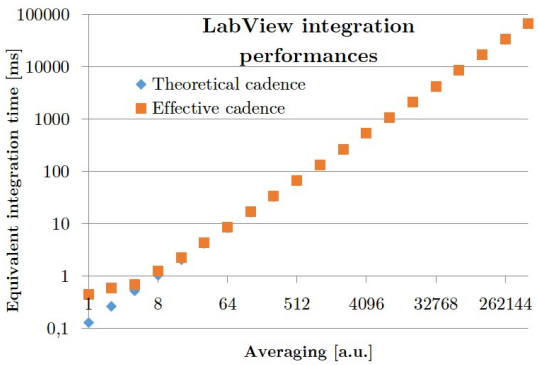

Figure III.28: Evolution of the effective equivalent integration time with respect to the sample averaging level.

Strong cadence limitations were initially found in absence of task parallelization with a un-optimized maximal effective measurement rate of 40 Hz. Subsequently, The decoupling of the data collection and processing scheme brought strong improvement. It featured a full speed data collection over the forward displacement of the translation stage followed by a parallelized data-processing and display during the backward return of the translation stage. Similarly, the parallelization of the position assessment during the continuous forward motion allowed to reach the performances displayed in Figure III.28. A maximal effective measurement rate of 2.22 kHz is then achieved. This limitation at very low averaging is nevertheless not tied to the radar transceiver performances as it solely relies on the feedback positioning integration. Indeed, the USB communication protocol, used for the translation stage position query, imputes a non-negligible delay, even when the task is fully parallelized. For imaging purposes, an upgrade toward high speed communication protocols compatible translation stages or positioning units would grant a mitigation of this technical issue. However, when considering higher averaging, often implemented due to the translation stage speed limitation, from a factor of 16, the 7.62 kHz measurement rate is fully exploited. Likewise, for static measurements, when no positioning feedback is required, even at very low averaging factors, full speed investigations can be performed.

III.4.2 Lateral resolution

Similarly to CW investigations, the longitudinal resolution remains a criteria of interest for punctual sensing or, in the simplest integration, for imaging purposes when featuring raster scanning.

As detailed in section II.2.1, this assessment has been performed using an USAF test chart, implementing the optical configuration described in section III.2.2 and Figure III.20. As a resolution oriented investigation, a high NA beam focusing was performed using a 2" diameter f'=50 mm aspheric lens leading to NA=0.5.

From the previously detailed Gaussian beam model, and more precisely Equation II.14, it ensue that the lateral resolution solely rely on the operation wavelength, 2 mm in this case at 150 GHz, and the optical configuration, and more specifically the NA.

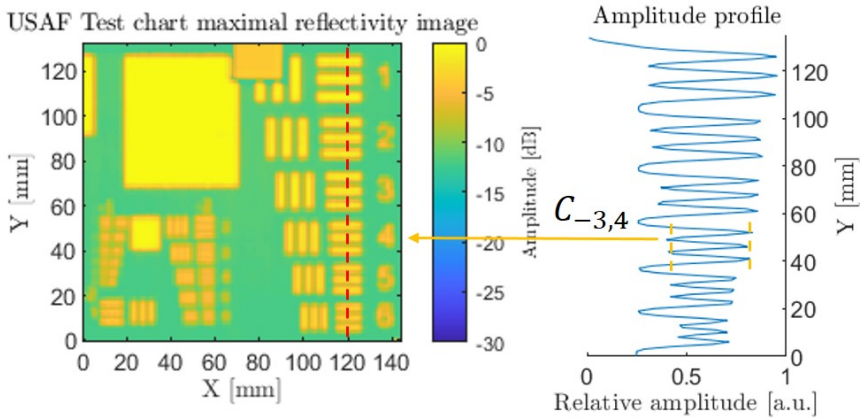

Figure III.29: Estimation of the lateral resolution using a 1951-USAF test chart.

Figure III.29, displays the resulting maximal amplitude image, corresponding to the surface of the used PCB USAF test chart, from which the contrast on each element can be assessed.

Similarly to real-time recorded images of section II.3.5, the contrast assessment are not performed on logarithmic images but on linear-scale amplitude normalized profiles such as with the left sub-plot of Figure III.29. Similarly to the real-time non unitary target contrast ration, one should establish the normalized contrast ration as $\widehat{C}_{Grp,El} = \frac{C_{Grp,El}}{C_t}$ with in this case $C_t = \frac{1-0.26}{1+0.26} = 0.586$. Indeed, for this test chart, the maximal reflectivity value equals to a unitary amplitude thanks to the metallized surface, and the low level equals to 0.26 (-11.7 dB in intensity) relative to the PCB non-null reflectivity.

In this configuration, a resolution comprised in-between 2.8 and 2.5 mm is achieved with measured normalized contrast rations of $\widehat{C}_{-3,5} = 0.468$ and $\widehat{C}_{-3,4} = 0.575$ respectively. Nevertheless, considering such stable high contrast ratio measurements, a visual resolution of the element 1 group -2 remains practicable, for an effective latteral resolution of 2 mm. This difference displays the limit of arbitrary contrast threshold of 0.5, that should depend on several parameters such as the used color-scale, the transparency of the substrate, or, as in this case, the use of a logarithmic amplitude scale.

From the Gaussian beam model, an estimated resolution of 1.5 mm is expected at this frequency and working NA. This mismatch can be explained by several factors. At first, the exact validity of this simplest Gaussian beam model for such high aperture beams, hence beyond the paraxial approximation, can be questioned [48–50]. Additionally, the use of a diagonal horn antenna on the transceiver leads to a non-rigorously Gaussian beam profile. The coverage of the focusing lens should as well be extensively investigated for quantitative model fitting. Finally, with such a high aperture, short Rayleigh range configuration, a slight defocusing of less than 2 mm over part of the 15 × 15 cm scanning area, would lead to such a resolution degradation. The strict adequacy of the used aspherical lens profile has not been overlooked either and could hence lead to resolution degradation.

Accounting for all those uncertainties, the assessment of the Gaussian model nevertheless leads to a close estimation of the effective resolution.

III.4.3 Longitudinal resolution

Beside the lateral resolution, solely linked to the optical configuration and operating wavelength, the longitudinal resolution represents as well a parameter of interest for a radar transceiver. This resolution relates to the capability of the transceiver to differentiate two consecutive interfaces along the sensing optical axis and is solely tied to the transceiver achievable bandwidth (see Equation I.11).

Obviously, this quantity will be limited by the numerical frequency resolution. In the data acquisition process, as long as the signal is recorded over a full unidirectional sweep, the resulting numerical frequency resolution after the Fourier transform operation, will remain constant as $\delta_f = \frac{F_s}{N_s}$ [Hz], regardless of the sampling frequency, F_s. The numerical distance resolution can be defined as $\delta_d = d_{k+1} - d_k$ [m], with k and k+1 the subsequent numerically spaced frequency or distance bins. Considering then a numerical depiction of the frequency as $f_{IF_i} = k\delta_f$, and the frequency to distance conversion of Equation I.10, one can deduce as follow that the distance resolution is directly linked to the frequency resolution:

$$\delta_d = \frac{c_o\left((k+1)-k\right)\delta_f}{2n}\frac{T_s}{BW} = \frac{c_o\delta_f}{2n}\frac{T_s}{BW}. \tag{III.15}$$

From there, since $\delta_f = \frac{F_s}{N_s}$ and $\frac{F_s T_s}{N_s} = 1$, one can easily get back to the initial range resolution definition of Equation I.11, solely tied to the effective chirp bandwidth. The numerical longitudinal resolution is then equal to the longitudinal resolution of the radar, the expected 4.6 mm according to the 32 GHz bandwidth.

Now considering the previously introduced windowing and zero-padding operation, a frequency resolution enhancement will be artificially accessed. The numerical frequency bin resolution will then be reduced by a factor equal to the N_{ZP} zero-padding factor as $\frac{\delta_f}{N_{ZP}}$, hence leading to a distance numerical resolution of $\frac{\delta_d}{N_{ZP}}$. A typical factor $N_{ZP} = 64$ in this implementation then leads to a numerical distance resolution of 71 µm.

This improvement only applies to the numerical resolution, hence the spacing between two distinct frequencies. But the radar longitudinal resolution obviously does not follow such improvement when enduring the zero-padding operation, due to the convolution of its spectral profile by the Fourier transform of the chosen apodization profile (i.e. rectangular window, Hamming, Hann or Blackman windows, *etc.*). As detailed in Table III.1, the main lobe width can be related to the effective -3 dB longitudinal resolution, through the following equation, directly reformulated from Equation III.15:

$$\delta_{d_{eff}} = \frac{c_o\delta_{f_{-3dB}}}{2n}\frac{T_s}{BW} \tag{III.16}$$

In the case where no apodization is performed, with the intrinsic use of a rectangular windows, a squared sinus cardinalis, $sinc^2$, function will be convoluted with the expected Dirac spectral response. A $0.87 \times \delta_f$ -3 dB main peak width will be reached, leading to an achievable longitudinal resolution of 4 mm. Such a measurement will nevertheless be highly limited by the -13 dB sidelobes.

Respectively, 5.9 mm, 6.5 mm and 7.4 mm effective resolutions will be accessible when integrating the Hamming, Hann and Blackman apodization windows. A trade-off between achievable measurement dynamic range, limited by the side lobes amplitude, and longitudinal resolution then directly emerges from the values given in table III.1.

The assessment of those longitudinal resolutions through theoretical values is guaranteed by the addequation of the measurement profile with respect to the ideal spectral profiles of those windows, as depicted in Figure III.23b. This profile match ensues from the robustness of the normalization operation and the PLL non-linearity correction that would otherwhise irremediably alter the measurement main lobe profile.

III.4.4 Longitudinal precision and accuracy

Longitudinal precision

Unlike the longitudinal resolution that details the capability of the transceiver to discern two distinct targets, the longitudinal precision should depict the stability performances of the radar to output the longitudinal position of a given reflective interface. It would then be equivalent to the frequency jitter witnessed on the main signal peak.

At first glance, the longitudinal precision could be considered as the stability of the maximum of reflectivity of an interface. Nevertheless, the zero-padding processing step, leads to a finite distance resolution.The higher the zero padding factor, N_{ZP}, the finer the numerical distance resolution. Figure III.30a nevertheless demonstrates that even at high zero-padding factor, the achieved numerical resolution remains insufficient, especially for stable high averaging sensing. Typically, for such type of resolution oriented measurements, the integrated $N_{ZP} = 512$ factor leads to a numerical resolution of $\delta_{f_{N_{ZP}}} = \frac{\delta_f}{512} = 30$ Hz hence a longitudinal numerical resolution of 9 µm. Further sub-sampling could be performed but would therefore require additional unnecessary processing resources.

To overcome this longitudinal resolution limitation, another approach to assess the peak stability, or precision, lies on the consideration of the peak in its entirety, and not only consider the maximal point. As the peak profile is well established by the apodization window (see Figure III.24), an intercorrelation between the measurement and the ideal peak profile will return a maximal amplitude at the position where both are coinscidents. By interpolating the numerical measurement, this estimation can be as well extended below the longitudinal numerical resolution of $\frac{\delta_f}{N_{ZP}}$. Operating this algorythmic approach over subsequent measurements will allow to precisely assess the position of the peak over time, as displayed in Figure III.30b. The consideration of the position Root Mean Square (RMS) evolution then leads to the longitudinal precision.

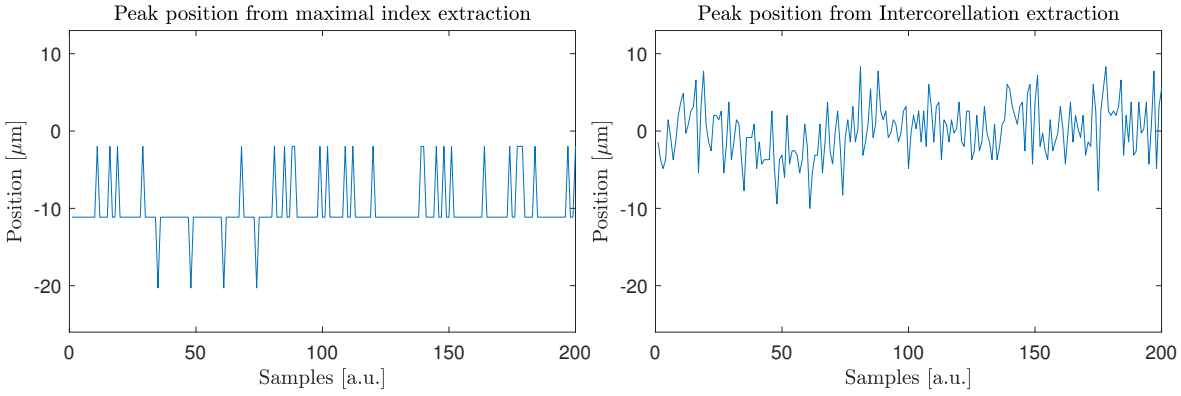

(a) **(b)**

Figure III.30: Depiction of the main peak position over 200 consecutive measurements, on a fixed reflective sample, retrieved through **(a)** the maximum of reflectivity implementing $N_{ZP} = 512$, or **(b)**, through an apodization window intercorrelation.

Obviously, a major parameter for this performance is the averaging level imputed to the sample measurement. Figure III.31 details the evolution of such assessed longitudinal precision with respect to the averaging level over the measured sample, hence, the measurement integration time. The RMS assessment has been performed over 200 successive measurements at each averaging level for a transfer function averaging factor of 1024 over the reference and background normalization measurements. A Blackman windows was integrated with the previously mentioned zero-padding factor of N_{ZP}=512. The numerical resolution of 9 µm then prevents the maximal reflectivity index approach to provide relevant information below this value, similarly to Figure III.30a. A global undervaluation of the precision is then highlighted with this approach as depicted on Figure III.31.

Considering the inter-correlation extractions, the measurement precision then ranges from 50 µm for single shot measurements down to 3.6 µm when considering a 4.2 s integration time, hence, considering an object placed at roughly 50 cm, less than 0.001% positioning instability. Such fluctuations can be tied to a variety of factors, either linked to the transceiver itself or its environment. Namely, mechanical vibrations of the workstation can be recorded as a strongly impacting factor for this measurement. Additionally, thermal effect can affect the electronic components among the transceiver and might as well induce a subtle changes in the refractive index of the propagation media, in the order of several parts in a million (1×10^{-6}) for a 1°C temperature variation [51].

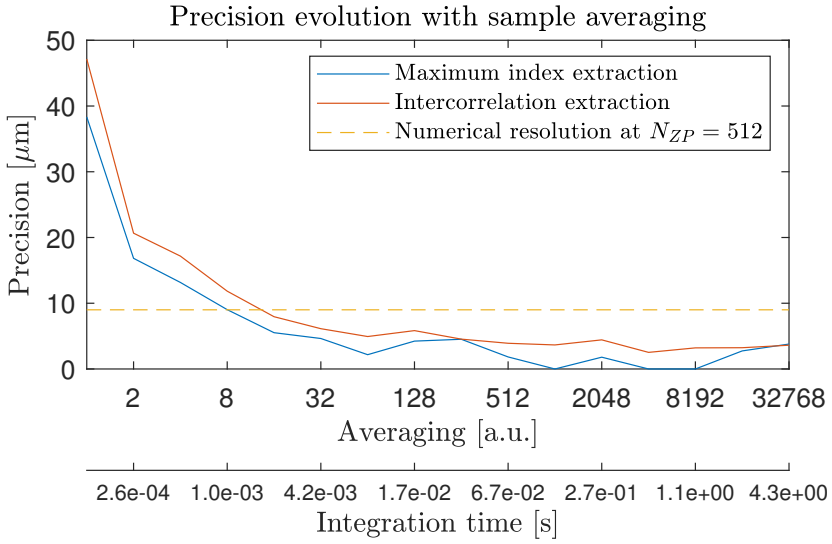

Figure III.31: Evolution of the longitudinal precision with respect to the sample measurement averaging factor.

Longitudinal accuracy

As depicted between Figure III.30b and III.30a, the subtle mean value variation between those two measurements bring up the difference between precision and accuracy. The accuracy relates to the effective position assessment, hence the capability of the transceiver to procure correct values while the precision details the spreading around the mean returned value.

From the previously introduced normalization algorythmic process, the position outputted by the radar is given with respect to the reference plane, as the reduced beating frequency $\widehat{f}_{\mathrm{IF}_{i'}}$ is considered. An absolute accuracy assessment is then impracticable. However, a relative assessment has been carried out through the use of a step metallic target, displayed in Figure III.32. The sample is composed of a flat reference surface for post-processing alignment purposes and subsequent steps of different heights given in column 1 of Table III.2. Manufacturing mechanical uncertainty in the order of ± 10 µm, from the numerical positioning tool, should additionally be highlighted.

A full scan of the sample has been performed and the topographic image, resulting from the previously detailed intercorrelation extraction approach is given in Figure III.33. To reach a suitable total recording time below 5 minutes using a 1mm scan pitch, an averaging factor of 256 over the sample measurement has been performs with a 512 averaging level over the background and reference measurements. The rendering process have been applied with N_{ZP} = 512 and a Blackman windowing to remain consistent with the previous precision measurements. The extracted step size lies on the differential depth measurement performed on the averaged central region of each step to avoid any edge effects. Considering a 10% relative error as the resolving threshold [52, 53], in accordance with the ± 10 µm mechanical imprecision, a relative longitudinal accuracy of 110 µm step is then achieved as depicted in Table III.2. A consistent measurement is as well

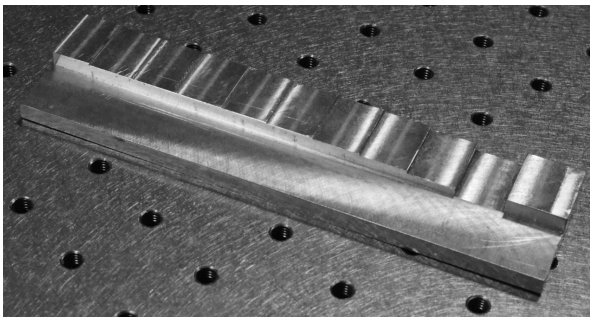

Figure III.32: Photograph of the step target under inspection.

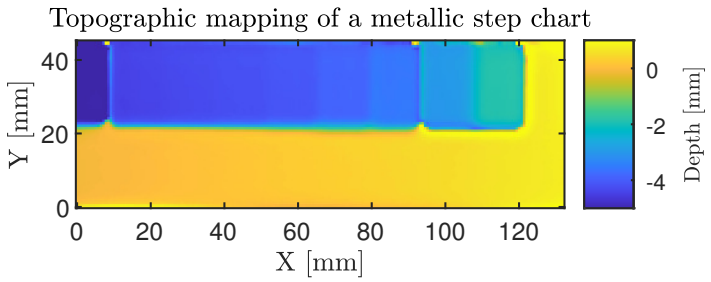

Figure III.33: Topographic mapping of step target under inspection.

achieved for a step of 25 µm, even though, below 50 µm step sizes, the 10 µm mechanical machining uncertainty already induces a 20% relative error.

Table III.2: Longitudinal accuracy assessment.

Theoretical step size [µm]	Extracted step size [µm]	Error [µm]	Relative error [%]
2500	2296	204	8.2
1000	955	45	4.5
500	489	11	2.2
250	250	10	4.2
110	100	10	9.1
50	32	18	36
25	23	2	8
10	7	3	30

Such accuracy limitation can emerge from two main considerations. The integration of the noisy components around the main measurement peak in the intercorellation extraction can lead to slight peak shift. A peak distortion can as well be induced by a reminiscent non-linearity among the frequency chirp, hence, the intercorellation with an ideal Blackman window could lead to this considered shift with respect to the maximum peak position.

The assessment of the longitudinal accuracy and precision have been performed only through a sole consideration of the amplitude profile. A whole complex signal consideration, especially accounting for the embedded phase, should lead to higher precision levels.

III.4.5 Measurement dynamic range

Beside the previously detailed performance figures of merit, the measurement Dynamic Range (DR) granted by a system remains a central characteristic. This quantity solely relies on signal amplitude considerations.

Obviously, an averaging operation over several sensing frequency chirp will have a tendency to

improve the effective SNR on this given signal. This impact is directly perceptible on Figure III.34 which displays amplitude signals in absence of any numerical mean operation, hence allowing for the highest measurement rate in Figure III.34a and in the case of high levels of averaging in Figure III.34b, targeted for high dynamic range measurements.

From the previously introduced normalization procedure, two types of numerical mean can be considered. At first, with the calibration of the radar for the generation of the temporal normalization transfer function H(t), an averaging over the recorded normalization reference and background signals, $\widetilde{S}_{\mathrm{IF}_{ref}}(t)$ and $\widetilde{S}_{\mathrm{IF}_{back}}(t)$, can be performed. This data recording can be considered only once in the calibration phase. And secondly, an averaging over the measured sample, either before or after the normalization, will as well highly impact the achievable dynamic range. However, considering the raw sensing acquisition rate of the radar, 7.62 kHz, the sample averaging can be related to an effective integration time, hence impacting the effective measurement rate as detailed in section III.4.1.

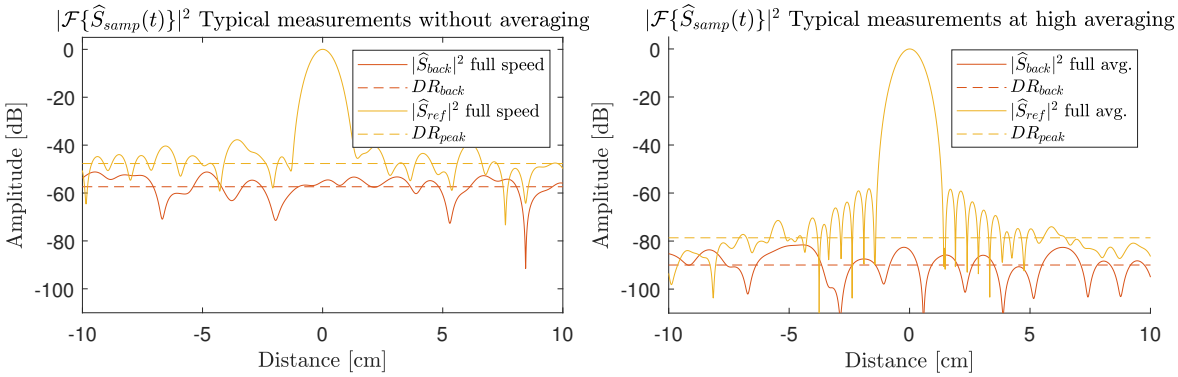

(a) **(b)**

Figure III.34: FMCW radar amplitudes spectrum for normalized references and background measurements **(a)** when no averaging is considered for high cadence measurements and **(b)** at high averaging levels, for high dynamic range sensing equivalent to a 1 minute equivalent integration time.

Additionally, two DR configurations can be observed from Figure III.34. A global measurement dynamic range, DR_{back}, that best suits the effective definition of the dynamic range, which then depicts the ratio between the smallest reflectivity object detectable with respect to the unitary reflectivity element. The assessment of this quantity is performed on a background measurement. In addition, a DR on reference, DR_{peak}, can be established and will be estimated as the smallest reflectivity signal detectable, in presence of a highly reflective element. The assessment of this quantity is hence performed on a reference measurement.

In each of those cases, their values are assessed as the mean noise value over a window of interest. Precisely, a ± 10 cm longitudinal measurement range is considered. For DR_{back}, the mean value over the whole range is considered to assess the noise level. In the case of DR_{peak}, the central lobe of the peak is not considered. DR_{peak} is then attributed as a mean noise level surrounding the central lobe.

An evaluation of those two quantities with respect to the imputed averaging levels have been explored and the results are displayed in Figure III.35. At first glance, one can notice that as expected, the DRs features an improvement tendency with respect to the two averaging operations.

The effective DR, DR_{back}, ranges from 60 dB at full speed over a 125 µs symetrical chirp, down to over 90 dB when considering integration times above several second for averaging levels over 65536. An optimal value of 98 dB has been recorded for an 8.5 s integration time and 16384 averaging over the reference and background measurements.

The DR over peak, DR_{peak}, on the other hand, reaches a value of 46 dB in absence of averaging and features a saturation around 75 dB as the Blackman window then displays predominant limiting side lobes. This saturation occurs above an averaging factor of 4096, hence a measurement cadence of 1.9 Hz, from the moment where DR_{peak}, reaches the sidelobes levels at - 60 dB . This

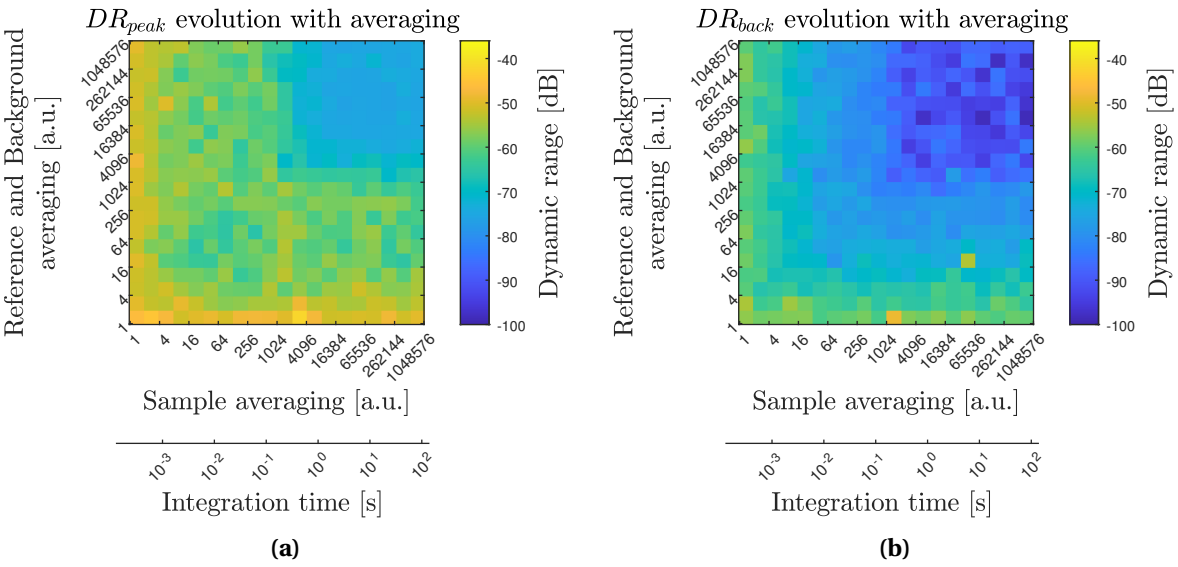

Figure III.35: **(a)** Impact of the sample and normalization signal averaging over **(a)** the Dynamic range over reference measurement DR_{peak} and **(b)** the Dynamic range over background measurement DR_{back} .

saturation is effectively displayed in Figure III.34b, with the appearance of the Blackman pattern.

The offset between the two dynamic ranges comes from the additional noise components introduced by the normalization procedure in presence of highly reflective sample. In imaging conditions, this could relate to a longitudinal glare noise.

As expected, a clear trade-off between achievable measurement dynamic range and measurement rate can be drawn. Those measurements can then be provided as abacus data for such considerations. The optimal windowing apodization profile can then as well be assessed according to the achievable DR_{peak}. Indeed, thinner main peak profile can be considered for lows dynamic range measurements (see Table III.1). On the opposite, long integration high dynamic measurements could make use of side-lobe minimization oriented windowing profiles with for example the Nuttall window [54] that features side-lobes below 95 dB at the expense of a larger main lode.

The state of the art published III/V FMCW radar transceivers in the 150 GHz band features a 40 dB dynamic range, for an acquisition time of 100 µs, 60 dB at acquisition time of 10 ms and 70 dB for a 100 ms acquisition rate. Those values have been extracted from the DOTNAC project final report [1] and [25]. For comparative purposes, at similar integration times, of 100 µs, 10 ms and 100 ms, and practicable background and reference averaging of 2048, the developed transceiver features respective dynamic ranges DR_{back} of over 57 dB, 77 dB and 85 dB. Further III/V FMCW radar sources, operating in various frequency windows, demonstrated measurement dynamic ranges around 60 dB without integration time specifications. Several other systems can be highlighted with [32] operating at at 675 GHz leading to 63 dB with chirp times of 100 µs and unspecified amount of averaging, 60 dB for a transceiver operating at 100 GHz [41] over 5 ms acquisition rate or again 60 dB operating at 200 GHz [55]. The dynamic range performances nevertheless remain quite often access limited when it comes to commercially available systems, hence the absence of more recent systems capabilities in this comparative study.

The lack of such quantitative performance assessments is as well witnessed in the recent development of silicon based FMCW transceivers. In the case of the Silicon-radar transceiver, beside the range accuracy [4], and electronic integration oriented developments [2, 3], no short range sensing performances oriented studies have been performed. From internally performed tests, typical dynamic ranges up to 50 dB can be achieved depending on the implementation with a measurement rate of several hertz (up to 20 Hz). This can partially be explained by the targeted design of this component, better suited to longer measurement ranges considerations where 70 dB dynamic ranges can be obtained. Beside their typically reduced achievable bandwidth, hence longitudinal resolution, their considerably lower emission power remains as well an intrinsic limitation.

Lastly, the assessment of the FMCW radar transceiver DR detailed in this section has been performed in a focused point configuration, hence, requiring the insertion of a 16 dB attenuation for the safe operation of the frequency mixer. Those additional 16 vdB of potentially available power could then be accounted for in the performances of the radar in specific configurations such as when investigating low reflectivity targets. The large available emission power, in contrast with Si-based radar transceivers, can as well present a net advantage for far field open beam SAR investigations where most of the emitted power is not back-coupled toward the transceiver, preventing the mixer to endure any damage.

III.4.6 Stability

Beside the effective dynamic range, stability performances remain of strong interest for system integration and operation oriented problematics. Namely, this characterization should assess the validity time of the normalization procedure and highlight the requirement of an eventual periodic re-calibration of the system. Indeed, a slight evolution of the reminiscent non-lineatities of the transceiver or spectral characteristics for the LO and/or source spectrum should impact the measured normalization reference, $\widetilde{\mathrm{S}}_{\mathrm{IF}_{ref}}(t)$, and background, $\widetilde{\mathrm{S}}_{\mathrm{IF}_{back}}(t)$. A regular update of those signals should then be considered if such variations were to be endured.

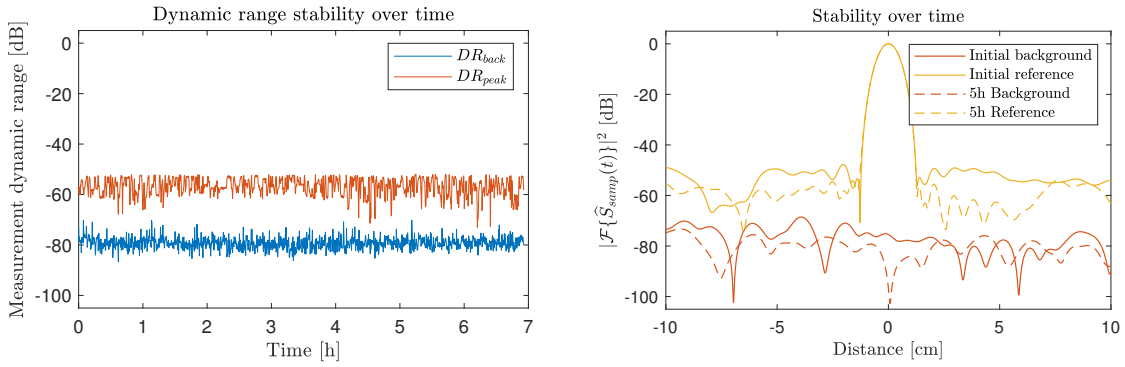

(a) **(b)**

Figure III.36: **(a)** Dynamic range stability over time, and **(b)** and arbitrary signals taken respectively shortly after the calibration and after 5h of operation.

Figure III.36a displays the evolution of the background DR, DR_{back}, and the DR on reference, DR_{peak}, as a function of time over a long operating period. The considered reference and background normalization signals have been taken right at the beginning of this measurement period after several hours of operation of the radar for settling purposes. Averaging levels of 256 have been considered as to fit a typical imaging configuration. Those extractions have been performed by consistently measuring 2 signals in a reference and background configuration respectively over several hours in a controlled environment. No significant drifts and degradations of the respective dynamic ranges is witnessed over a measurement period of 7 hours.

Alongside, arbitrary signals taken respectively right after the calibration and after 5 hours of operation are displayed in Figure III.36b. No noticeable peak distortion or significant noise level rise are observed. Figure III.36b nevertheless features a DR_{peak} variation of several dB when considering a distance of 3 cm over the initial reference and the 5h reference measurements. This discrepancy emerges from the higher variation level witnessed over the DR_{peak} evolution displayed in III.36a and emanates from the sensitivity of the raw signal normalization procedure to subtle target displacements or vibrations.

In fine, featuring such a stability up to several hours, no additional re-calibration seems to be required when operating in a controlled environment, especially regulated in temperature.

This specific performance assessment endorses the capability of the PLL to mitigate very efficiently the VCO characteristic variations. Such a stability nevertheless requires that no other

components endure drifts, namely the up-conversion HF stage and mixer, or the LO provision low frequency chain after the PLL. Ultimately, a settling time is nevertheless required upon the transceiver start-up to allow for each component to reach thermal stability.

Warm up settling time

Indeed, the effective normalization transfer function might be ever so slightly impacted by the characteristic of each component in the transceiver architecture. Namely, a thermal stabilization of each element at start-up is a considerable factor; leading to the settling time as a parameter of importance.

Considering a normalization signal taken after several hours of operation, a 10 to 15 dB settled improvement can been witnessed on DR_{back}, with respect to the initial signal. A total stabilization of 1 hour of operation prior to the recording of the normalization signals would grant optimal performances.

Nevertheless, the transceiver operation right after start-up still features ideal performances when ensuring regular re-calibration over the first 15 to 30 minutes of operation.

Additionally, after settling time, the reference and background remains perfectly stable and feature a total consistency from one day to another after an interruption period. This should ensure the integration of a fixed effective transfer function for the operation of the transceiver given stable operating conditions, then only requiring an initial optimal calibration measurement.

No further in depth investigations has been pushed on those matters as the integration status of the current transceiver does not allow for optimal repeatably. Namely, the current temperature stability of the different chips highly lies on the environment. A proper implementation packaging would drastically reduce such environment related perturbations, allowing for a higher measurement reliability.

III.5 Conclusion

Following the developments in the continuous wave mode of operation, for full field and focused point sensing, the progression toward coherent sensing has been operated through the depicted advancements on a millimeter-wave homodyne FMCW transceiver. Driven by the settled capabilities of such tools, this transition hinged on the technical upgrade of a high power Schottky based tunable source, along with the establishment of the frequency modulation sensing mode of operation. Namely, this alteration lies on the development of a 150 GHz mono-static reflection module featuring a harmonic mixing detection scheme.

As the fundamental component of the targeted FMCW mode of operation, a strong effort has been deployed on the optimization of the frequency chirp generation unit with the development and characterization of a DDS driven hybrid PLL. Indeed, the high requirements for the sweep cadences and sweep frequency rates, prevented the use of commercially available solutions. The integration of a fixed integer-N PLL, locked on a fast chirp generation DDS allowed for a total suppression of the predominant VCO non linearity, along with the granting of a perennial stability of the command chirp. On this specific point, in response to the fickle VCO behavior, the requirement for such a PLL synchronization stage turned out to be extremely efficient when assessing the stability and repeatibility performances of the radar transceiver. In fine, with the addition of a frequency doubler and band-pass filter, the full 16-20 GHz modulation provision stage featured the generation of a suitable HF stages driving signal, assessed through multiple spectral characterizations.

To attain the mono-static integration, the direct emission arm subsequently features the up-conversion multipliers to reach the 128-160 GHz frequency band of interest, followed by a 3-port coupler, terminated with a diagonal horn antenna, for free-space coupling. Thanks to this additional asymmetrical component, a redirection of the back-coupled reflected signal can be performed toward the mixer. Even-though it represents a net advantage with respect to the lower

power state of the art FMCW radar systems, the high available probing power of 50 mW nevertheless induces the insertion of a variable attenuator on the reflection probing arm, prior to the mixer. From there, on this collected reflection signal, the homodyne detection can be implemented with the provision of a local oscillator to the mixer. Through the chosen 8^{th} harmonic mixing, the use of the splitted and amplified low frequency driving signal as the LO provides a full chirp coherence with the up-converted probing signal.

The linear frequency modulation then grants the procurement of the valuable time-of-flight to beating frequency relation, hence, leading to the intrinsic longitudinal sensing capability of the FMCW scheme.

Nevertheless, at this point, even through a carefull transceiver design has been operated, no exploitable high dynamics longitudinal measurements can be retrieved due to the non-negligible performances alterations induced by the discrepencies with respect to the ideal FMCW model. Namely, the non-ideal spectral characteristic of the emission HF chirp and LO lead to a full convolution of the expected sensing spectral profiles. As a solution, a temporal normalization procedure can nevertheless mitigate and rectify this broad unitary spectral response. Based on the prior recording of a background and reference signal, it allows for the deconvolution of the signal, supported by a background subtraction to reach optimum operable sensing performances.

From this academic operational numerical data handling, the transceiver integration process led to the development of a full FPGA architecture to ensure an optimum measurement cadence. Initially intended as a simple dedicated DAQ, it has been ultimately complemented with full embedded processing to reach a compact dedicated targeted hardware processing unit.

Following such a targeted integration in the pursue of further applicative proof of work developments, an assessment of the capabilities of this FMCW unit have been carried out. A variety of considerations, specific to the FMCW sensing method, brought up an extensive and quantitative performance evaluation. Namely, the theoretical longitudinal resolution of 4.6 mm have been attested with a reduction down to 4 mm a -3 dB when considering a $sinc^2$ apodization window or an effective resolution of 7.4 mm for high dynamic measurement with the application of the high dynamic range Blackmann window. Precision levels down to 3.6 µm and a relative accuracy level of 110 µm have been assessed for the transceiver in typical sensing configurations, along with the achievable measurement dynamic range ranging up to 100 dB for a few seconds integration time. As a prominent, performance marker, the later displayed a 15 dB improvement over the state of the art systems featuring similar technology at equivalent measurement cadences. In a more system oriented consideration, the effective measurement cadence of 7.62 kHz has been successfully tested along with the long term stability of the system. While the prior rely on the FPGA integration, the later is granted by the ability and robustness of the PLL to ensure a stable LO and emission chain driving signal after thermal settling.

With an exhaustive technical and processing architecture depiction, completed by the sensing specification capabilities of the transceiver, a transition toward applicative proof of work can be initiated.

III.6 Bibliography

[1] https://cordis.europa.eu/docs/results/266320/final1-final-report-dotnac.pdf. ix, 92, 134

[2] K Schmalz, W Winkler, J Borngraber, W Debski, B Heinemann, and C Scheytt. A 122 ghz receiver in sige technology. In *2009 IEEE Bipolar/BiCMOS Circuits and Technology Meeting*, pages 182–185. IEEE, 2009. 93, 134

[3] K Schmalz, W Winkler, J Borngräber, W Debski, B Heinemann, and JC Scheytt. 122 ghz ism-band transceiver concept and silicon ics for low-cost receiver in sige bicmos. In *2010 IEEE MTT-S International Microwave Symposium*, pages 1332–1335. IEEE, 2010. 134

[4] Mario Pauli, Benjamin Göttel, Steffen Scherr, Akanksha Bhutani, Serdal Ayhan, Wolfgang Winkler, and Thomas Zwick. Miniaturized millimeter-wave radar sensor for high-accuracy applications. *IEEE Transactions on Microwave Theory and Techniques*, 65(5):1707–1715, 2017. 93, 134

[5] Alain Maestrini, John S Ward, John J Gill, Choonsup Lee, Bertrand Thomas, Robert H Lin, Goutam Chattopadhyay, and Imran Mehdi. A frequency-multiplied source with more than 1 mw of power across the 840–900-ghz band. *IEEE transactions on microwave theory and techniques*, 58(7):1925–1932, 2010. 93

[6] Alain Maestrini, Bertrand Thomas, Hui Wang, Cécile Jung, Jeanne Treuttel, Yong Jin, Goutam Chattopadhyay, Imran Mehdi, and Gérard Beaudin. Schottky diode-based terahertz frequency multipliers and mixers. *Comptes Rendus Physique*, 11(7-8):480–495, 2010.

[7] A Maestrini, L Gatilova, J Treuttel, F Yang, Y Jin, A Cavanna, D Moro Melgar, F Tamazouzt, T Vacelet, A Féret, et al. 1200ghz and 600ghz schottky receivers for juice-swi. In *proceedings of the 27th International Symposium on Space Terahertz Technology*, volume 3, 2016.

[8] John Ward, Erich Schlecht, Goutam Chattopadhyay, Alain Maestrini, John Gill, Frank Maiwald, Hamid Javadi, and Imran Mehdi. Capability of thz sources based on schottky diode frequency multiplier chains. In *2004 IEEE MTT-S International Microwave Symposium Digest (IEEE Cat. No. 04CH37535)*, volume 3, pages 1587–1590. IEEE, 2004.

[9] Goutam Chattopadhyay, Erich Schlecht, John S Ward, John J Gill, Hamid HS Javadi, Frank Maiwald, and Imran Mehdi. An all-solid-state broad-band frequency multiplier chain at 1500 ghz. *IEEE Transactions on Microwave Theory and Techniques*, 52(5):1538–1547, 2004. 93

[10] M Vandewal, J Depauw, K Rombaut, R Beigang, J Jonuscheit, P Mounaix, I Sáez de Ocáriz, R Martínez Edo, A Priegue, and Y Sternberg. Development and optimization of thz ndt on aeronautics composite multilayered structures. In *Terahertz Physics, Devices, and Systems VI: Advanced Applications in Industry and Defense*, volume 8363, page 83630Y. International Society for Optics and Photonics, 2012. 94

[11] Yade Li, Weidong Hu, Xin Zhang, Yunzhang Zhao, Jiaqi Ni, and Leo P Ligthart. A non-linear correction method for terahertz lfmcw radar. *IEEE Access*, 8:102784–102794, 2020. x, 94, 113

[12] Ruben Undheim. Design of a linear fmcw radar synthesizer with focus on phase noise. Master's thesis, Institutt for elektronikk og telekommunikasjon, 2012. 94, 95

[13] Curtis Barrett. Fractional/integer-n pll basics. 1999. 95

[14] Pratap Tumkur Renukaswamy, Nereo Markulic, Sehoon Park, Anirudh Kankuppe, Qixian Shi, Piet Wambacq, and Jan Craninckx. 17.7 a 12mw 10ghz fmcw pll based on an integrating dac with 90khz rms frequency error for 23mhz/µs slope and 1.2ghz chirp bandwidth. In *2020 IEEE International Solid-State Circuits Conference - (ISSCC)*, pages 278–280, 2020. 96

[15] https://www.ti.com/product/lmx2594. 96

[16] https://www.ti.com/product/lmx2492. 96

[17] https://www.analog.com/media/en/technical-documentation/data-sheets/hmc734.pdf. ix, 97, 99

[18] https://www.renesas.com/us/en/document/whp/integer-boundary-spurs-fractional-feedback-phase-locked-loops-plls. 97

[19] https://www.analog.com/en/analog-dialogue/articles/analyzing-integer-boundary-spurs.html. 97

[20] Andrey V Khudchenko, Valery P Koshelets, Pavel N Dmitriev, Andrey B Ermakov, Pavel A Yagoubov, and Oleksandr M Pylypenko. A cryogenic phase locking loop system for a superconducting integrated receiver. *Superconductor Science and Technology*, 22(8):085012, 2009. 98

[21] https://anteral.com/datasheets/standard-gain-horn-antenna-wr06-26-dbi-gain.pdf. 102

[22] Jinshan Ding, Matthias Kahl, Otmar Loffeld, and Peter Haring Bolívar. Thz 3-d image formation using sar techniques: simulation, processing and experimental results. *IEEE Transactions on Terahertz Science and Technology*, 3(5):606–616, 2013. 103

[23] Ian G Cumming and Frank H Wong. Digital processing of synthetic aperture radar data. *Artech house*, 1(3), 2005. 103

[24] James D Taylor. *Advanced ultrawideband radar: signals, targets, and applications*. CRC press, 2016. 103

[25] Edison Cristofani, Fabian Friederich, Sabine Wohnsiedler, Carsten Matheis, Joachim Jonuscheit, Marijke Vandewal, and René Beigang. Nondestructive testing potential evaluation of a terahertz frequency-modulated continuous-wave imager for composite materials inspection. *Optical Engineering*, 53(3):031211, 2014. 134

[26] Arindam Sengupta, Feng Jin, Reydesel Alejandro Cuevas, and Siyang Cao. A review of recent advancements including machine learning on synthetic aperture radar using millimeter-wave radar. In *2020 IEEE Radar Conference (RadarConf20)*, pages 1–6. IEEE, 2020.

[27] Sang-Hoon Jung, Yong-Sun Cho, Rae-Seoung Park, Jong-Mann Kim, Hyun-Kyo Jung, and Young-Seek Chung. High-resolution millimeter-wave ground-based sar imaging via compressed sensing. *IEEE Transactions on Magnetics*, 54(3):1–4, 2017. 103

[28] M Naftaly, RE Miles, and PJ Greenslade. Thz transmission in polymer materials—a data library. In *2007 Joint 32nd International Conference on Infrared and Millimeter Waves and the 15th International Conference on Terahertz Electronics*, pages 819–820. IEEE, 2007. 103

[29] Mohammed N Afsar, Hua Chi, and Igor I Tkachov. Millimeter-and submillimeter-wave transmission and dielectric properties of radome materials. In *Millimeter and Submillimeter Waves II*, volume 2558, pages 73–85. International Society for Optics and Photonics, 1995. 103

[30] Adrien Chopard, Joyce Sleiman, Q Cassar, P Fauché, J Guillet, Patrick Mounaix, Perraud Jean-Baptiste, and A Susset. Millimeter waves radar: A way to see through the airplane covering? In *11 symposium international: NDT in Aerospace*, 2019. 103

[31] David M Sheen, Thomas E Hall, Ronald H Severtsen, Douglas L McMakin, Brian K Hatchell, and Patrick LJ Valdez. Standoff concealed weapon detection using a 350-ghz radar imaging system. In *Passive Millimeter-Wave Imaging Technology XIII*, volume 7670, page 767008. International Society for Optics and Photonics, 2010. 103

[32] Ken B Cooper, Robert J Dengler, Nuria Llombart, Bertrand Thomas, Goutam Chattopadhyay, and Peter H Siegel. Thz imaging radar for standoff personnel screening. *IEEE Transactions on Terahertz Science and Technology*, 1(1):169–182, 2011. 103, 134

[33] Bing Zhang, Yong-Xin Guo, Herbert Zirath, and Yue Ping Zhang. Investigation on 3-d-printing technologies for millimeter-wave and terahertz applications. *Proceedings of the IEEE*, 105(4):723–736, 2017. 104, 105

[34] AD Squires and RA Lewis. Mechanical and optical viability of eighteen filaments for 3d printing of terahertz components. In *2017 42nd International Conference on Infrared, Millimeter, and Terahertz Waves (IRMMW-THz)*, pages 1–2. IEEE, 2017. 104

[35] Lu Rong, Fangrui Tan, Dayong Wang, Yaya Zhang, Kunlun Li, Jie Zhao, and Yunxin Wang. High-resolution terahertz ptychography using divergent illumination and extrapolation algorithm. *Optics and Lasers in Engineering*, 147:106729, dec 2021. 104

[36] SF Busch, M Weidenbach, M Fey, F Schäfer, T Probst, and M Koch. Optical properties of 3d printable plastics in the thz regime and their application for 3d printed thz optics. *Journal of Infrared, Millimeter, and Terahertz Waves*, 35(12):993–997, 2014. 104

[37] AD Squires, E Constable, and RA Lewis. 3d printed terahertz diffraction gratings and lenses. *Journal of infrared, millimeter, and terahertz waves*, 36(1):72–80, 2015. 105

[38] Daniel B Fullager, Serang Park, Clark Hovis, Yanzeng Li, Jesse Reese, Erin Sharma, Susanne Lee, Christopher Evans, Glenn D Boreman, and Tino Hofmann. Metalized poly-methacrylate off-axis parabolic mirrors for terahertz imaging fabricated by additive manufacturing. *Journal of Infrared, Millimeter, and Terahertz Waves*, 40(3):269–275, 2019. 105

[39] Duncan A Robertson, Scott L Cassidy, and David R Bolton. Nonlinearity and phase noise effects in 340 ghz 3d imaging radar. In *Passive and Active Millimeter-Wave Imaging XVI*, volume 8715, page 87150M. International Society for Optics and Photonics, 2013. 113

[40] J Smith. Analytic signals and hilbert transform filters. In *Mathematics of the Discrete Fourier Transform (DFT): with Audio Applications*. 2007. 115

[41] J Detlefsen, A Dallinger, S Schelkshorn, and S Bertl. Uwb millimeter-wave fmcw radar using hubert transform methods. In *2006 IEEE Ninth International Symposium on Spread Spectrum Techniques and Applications*, pages 46–48. IEEE, 2006. 115, 134

[42] N Schreiner, A Keil, W Sauer-Greff, R Urbansky, and F Friederich. Comparison of signal processing algorithms for high-resolution fmcw terahertz thickness measurements. In *Journal of Physics: Conference Series*, volume 1537, page 012018. IOP Publishing, 2020. 115

[43] Radoslaw Piesiewicz, Christian Jansen, S Wietzke, Daniel Mittleman, Martin Koch, and Thomas Kürner. Properties of building and plastic materials in the thz range. *International Journal of Infrared and Millimeter Waves*, 28(5):363–371, 2007. 118

[44] Qi Guoqing. High accuracy range estimation of fmcw level radar based on the phase of the zero-padded fft. In *Proceedings 7th International Conference on Signal Processing, 2004. Proceedings. ICSP'04. 2004.*, volume 3, pages 2078–2081. IEEE, 2004. 118

[45] Kevin J Parker. Correspondence: apodization and windowing functions. *IEEE transactions on ultrasonics, ferroelectrics, and frequency control*, 60(6):1263–1271, 2013. 119

[46] Fast Fourier Transform Xilinx. v9. 1 logicore ip product guide, 2019. 121

[47] Angelika Wronkowicz, Krzysztof Dragan, and Krzysztof Lis. Assessment of uncertainty in damage evaluation by ultrasonic testing of composite structures. *Composite structures*, 203:71–84, 2018. 124

[48] CJR Sheppard and S Saghafi. Electromagnetic gaussian beams beyond the paraxial approximation. *JOSA A*, 16(6):1381–1386, 1999. 128

[49] CJR Sheppard and S Saghafi. Electric and magnetic dipole beam modes beyond the paraxial approximation. *Optik*, 110(10):487–491, 1999.

[50] Akifumi Yoshida et al. Electromagnetic field near the focus of gaussian beams. 1974. 128

[51] James C Owens. Optical refractive index of air: dependence on pressure, temperature and composition. *Applied optics*, 6(1):51–59, 1967. 131

[52] Tak Ming Wong, Matthias Kahl, PH Bolívar, and Andreas Kolb. Frequency modulated continuous wave (fmcw) thz image 3-d superresolution. *arXiv preprint arXiv:1802.05457*, 2018. 131

[53] Tak Ming Wong, Matthias Kahl, Peter Haring Bolívar, and Andreas Kolb. Computational image enhancement for frequency modulated continuous wave (fmcw) thz image. *Journal of Infrared, Millimeter, and Terahertz Waves*, 40(7):775–800, 2019. 131

[54] Albert Nuttall. Some windows with very good sidelobe behavior. *IEEE Transactions on Acoustics, Speech, and Signal Processing*, 29(1):84–91, 1981. 134

[55] Duncan A Robertson, David G Macfarlane, and Tomas Bryllert. 220ghz wideband 3d imaging radar for concealed object detection technology development and phenomenology studies. In *Passive and Active Millimeter-Wave Imaging XIX*, volume 9830, page 983009. International Society for Optics and Photonics, 2016. 134

Chapter IV

FMCW Proof of Principle and Targeted Implementations

«In the long history of humankind, those who learned to collaborate and improvise most effectively have prevailed.»

Charles Darwin

IV.1 Introduction

Following the development of the FMCW radar unit, and to the view of its performances, the fourth chapter, *FMCW Proof of Principle and Targeted Implementations*, will henceforth focus on specific study cases of interest.

Such applicative executions, tightly linked to the millimeter-wave application fields, are set as proof of concept, aiming to advocate for the potential of the FMCW sensing approach. Namely, a non-exhaustive selection of NDT oriented problematics, emerging from several industrial fields, have been considered as to provide illustrations over the broad abilities enabled through the FMCW procedure with the use of the previously featured 150 GHz transciever. In contrast with CW operations and other NDT systems, those study cases then mainly rely on the longitudinal sensing aptitude, coupled with the contactless penetrating inspection capabilities available in the millimeter-wave spectral range for volumetric inspection on a variety of materials.

Anticipated in parallel of the development of the FMCW radar unit, simplified guided FMCW integrations will be featured as a development toward compact and portable sensing tools for remote or long range inspection in the vicinity of the waveguide. Likewise based on already existing FMCW sensing units, the targeted implementation of penetrating imaging for see-through defect detection will be assessed as to fulfill explicit needs in the aeronautics and automotive industries. Specifically, simplified *in-situ* health monitoring is targeted for a reduction of the maintenance airplane on ground delays and costs.

Thirdly, with once again the purpose of demonstrating the adequacy of the developed FMCW transceiver, the main section of this chapter will be dedicated to the advanced development and numerical methods on the topic of thickness derivation from FMCW sensing signals. Namely, a parallel with TDS-based extractions will be drawn, along with the evaluation of the algorithm performances for the assessment of single-layer and multi-layered stratified samples, as proof of concept to answer the growing interest on this topic.

IV.2 Volumetric Imaging for Inspection, Using Newly Developed FMCW Transceiver

Initially intended as one of the intrinsic application for the FMCW scheme, thanks to the longitudinal sensing availability, three dimensional volumetric testing grants a perfect demonstration of the inspection capabilities embedded with such approaches.

Accounting for the performances of the previously featured 150 GHz transceiver, detailed in section III.4, namely the high dynamic range and millimeter-level resolutions, a variety of challenges can be tackled, providing that the inspected material remains suitable. Specifically, in absence of metallic parts, a broad spectrum of dry dielectric materials, ranging over polymers, textiles, ceramics, plasters, glass fiber-based composites *etc.*, are appropriate for the detection of breaking or stress marks, foreign material inclusions, delaminations, density variations, humidity traces, or more generally, health and structural monitoring.

A first approach of such volumetric inspection has been mentioned in section III.3.4 with Figure III.27 on the inspection of a honey-comb multi-layered sample featuring inclusions. The 150 GHz frequency band demonstrated an expected adequate material penetrability and suitable lateral resolutions along with a 80 dB measurement dynamic range in the chosen averaging configuration, when considering integration times around 100 ms. The longitudinal resolution of 4.6 mm also ensured depth sensitive sensing on this flat 7 mm thick sample. The adequacy of fiber-glass-based composite materials has been further successfully investigated with thicker filled samples displaying foreign inclusions, delaminations of impact marks, all answering to specific industrial concerns along the DOTNAC Project [1].

For such proof of work demonstrations, through the variety of samples and their relative complexity, far-field scanning implementation remains the most versatile approach. The implementation previously detailed in Figure III.13 has been considered for the initial integration of the newly introduced FMCW transceiver. Far for the high available optimal measurement rate, a 30 minutes recording time is required for a 15 cm × 15 cm surface area scan, with a 1 mm pitch, hence a 150 × 150 recording grid, highly restricted by the displacement speed of the translation stages. Through this initial transitional setup, the inspection results, gathered on a selection of samples, will highlight the global capabilities of the developed 150 GHz transceiver for volumetric inspection with the consideration of few very pragmatic and concrete problematics, encountered by industrial actors.

Polymer injected sample monitoring

In order to bridge with the QCW mode of operation detailed in Chapter II and pinpoint the enhancement provided by the FMCW radar mode of operation, the polymer injected sample pictured in Figure IV.1d is once again under inspection as a three dimensional test target. As a large majority of polymers, this sample remains quite suitable for millimeter-wave inspection thanks to its high transparency.

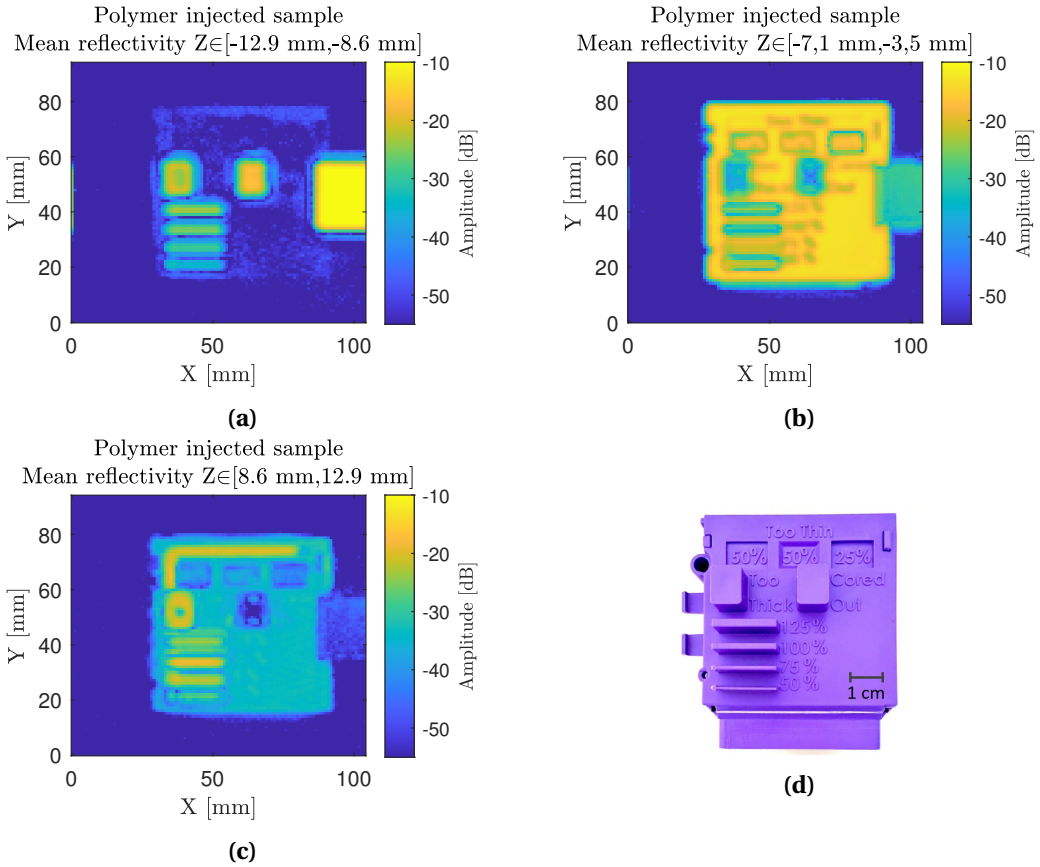

Figure IV.1: Polymer injected sample, featuring several geometrical test structures, depicted in different longitudinal ranges of interest. Namely, **(a)** centered on the foreground protrusions, **(b)** on the main sample plane, **(c)** over the background features and **(d)**, photograph of the sample in the visible range.

On the lateral resolution side such a measurement is to be compared with Figure II.7b, where the transmission QCW image of this same sample has been recorded at 150 GHz. A resolution of 2 mm for a NA=0.5 configuration is once again achieved through a typical focused point raster scan scheme, previously featured in Figure III.13.

Over such a simplistic multi-plane sample, already assessed through several sensing approaches, a large amount of information can be gathered from the FMCW inspection. Figure IV.1a, IV.1b

and IV.1c, perfectly describe the depth sensing capabilities of the transceiver with the respective consideraion of each sample main plane. The first plane, in Figure IV.1a, features the foreground elements first interface, and the sample holder, elevated from roughly 11 mm with respect to the main sample plane. The main sample plane itself is depicted in IV.1b with the visualization of the various inscriptions featured on the front face. While the background, displayed in Figure IV.1c features the background polymer ridge on the top of the sample, as well as the back side of the thick cubic polymer protrusions, and parallel stripes. Due to the larger optical thickness crossed through those components, their back interfaces appear further than their actual position. This additional optical propagation delay induces a drastic contrast between the two hollow cored and the polymer filled cubic protrusions in this representation

Considering the maximal reflectivity image, once again, a pseudo-topographic map of the sample could be collected. The 4.6 mm longitudinal resolution, however, does not allow for the differentiation of each intermediate layer, such as the front and back interfaces of the 2.2 mm thick main plane. A careful thickness assessments would nevertheless allow for the extraction of such sub-resolution thicknesses and will be fully detailed in section IV.4

From those preliminary visualisation results on a complex shape sample, several very pragmatic problematics can be already addressed with dimensioning topics, in the lateral and longitudinal directions, fault detection with the detection and spatial assessment of inclusions, bubbles, lack of mater for injected samples, cracks or delaminations, as well as homogeneity inspection.

Polymer gluing and welding inspection

Beside structural monitoring, such penetrating inspection can deliver significant information for the assessment of joints, and junctions on polymer or composite dielectric materials, as long as their absorption levels allow it. Namely, the assessment of the homogeneity and regularity of the glue or welding traces is of interest to generates a corrective feedback on production lines, hence limiting the excessive use of active matter while ensuring the integrity of the component. Namely, the expected mechanical proprieties of welds are at stake along with the joints hermetycity, which represents a challenging topic ranging from the field of pharmaceutical components such as blood bags, down to the food industry.

Figure IV.2 features the scan over the central portion of two 5 mm thick polymer plates glued together inducing a 2 mm interstice. Once again, to avoid the predominant first interface reflection, the glue trace can be precisely defined through the averaging over a longitudinal range of interest, encapsulating the interstice. The refractive index difference within the gap can be witnessed through the lowered interfaces reflectivity in presence of glue with respect to the polymer-air interfaces.

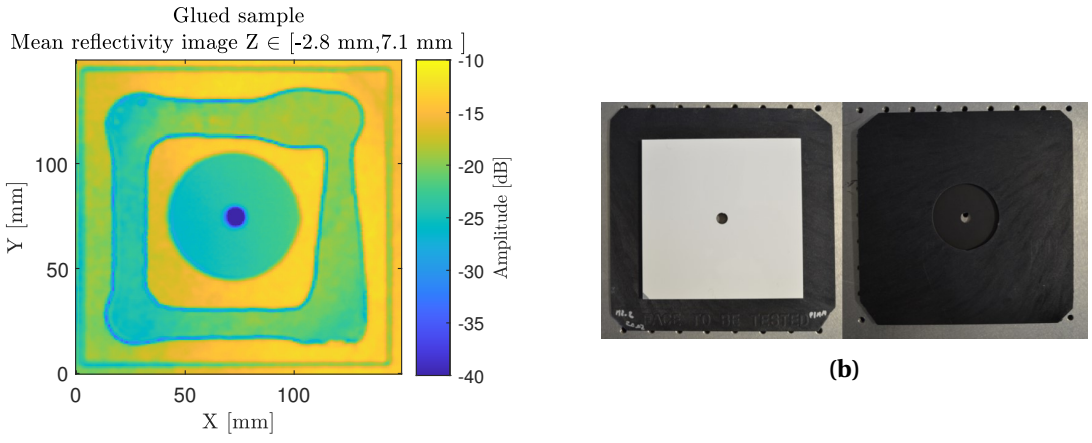

(a) **(b)**

Figure IV.2: **(a)** Glued plates scan, averaged over the longitudinal range of interest, **(b)** front and back views of the sample, featuring the central holes, and the two glued polymer plates.

Similarly, Figure IV.3 displays the measurements performed on polymer-on-polymer welded parts, featuring assembly specific artifacts. For such test samples, the assessment of welding defects, through a lack or excess of welding material or a deformation of the trace to actively rectify the welding parameters, are of interest for the mechanical integrity of the sample. Namely, a lack of welder can be very well distinguished in Figure IV.3b along the red line with respect to the reference sample depicted Figure IV.3a. The transverse representation, on the C cuts delivers a convincing depiction of the glue distribution but required a full 2D scan of the sample to provide a sensible information. Alternatively, a simple line B-scans, collected on the glue trace, ensure a full longitudinal inspection while only requiring a unidirectional sample assessment and still leading to a clear distinction between both samples. An individual inspection of both symmetrical sample flanges, in the foreground and background of the contact section, can as well be intended through the FMCW mode of operation, that could not be considered in the case of QCW systems.

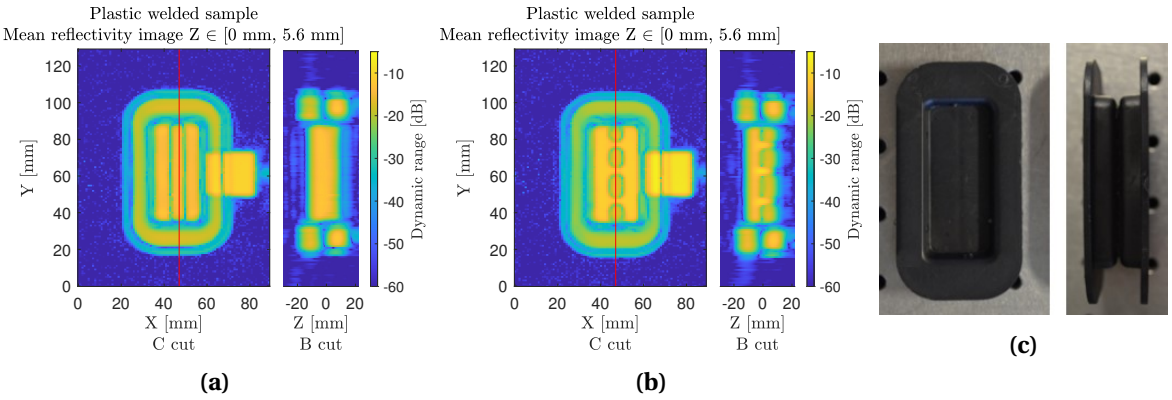

Figure IV.3: **(a)** Standard plastic welded part scan, averaged over a longitudinal range of interest, complemented with its respective longitudinal B-scan along the welding line, red line, **(b)** similar representation for an altered part, **(c)** front and side views of a polymer welded part.

Pharmaceutical packaging assessment.

To demonstrate once again the versatility and wide application field reachable through this homodyne sensing scheme, a pharmaceutical packaging inspection has been successfully undertaken with the simultaneous inspection of the leaflet presence and pills count. In this specific scope of application, the weakly interacting nature of millimeter-waves offers a strong argument to ensure the integrity of the chemical compounds after inspection. Indeed, in the tightly controlled pharmaceutical industry, radiography testing remains proscribed as an alteration of the chemical compound integrity is to be feared, along with the thermal effect that could be induced by thermography inspections.

At first glance, in the longitudinal range corresponding to the front of the packaging cardboard box, displayed on Figure IV.4b, the inspection of the sealing packaging flap can be conducted along with the assessment of the leaflet presence. This plane correspond to the yellow marker on the two B cuts.

Additionally, within the sample, beyond the cardboard packaging, with Figure IV.4c, the pill count can as well be easily assessed through the protection blister. This vizualization is performed when considering the contribution of the tablet blister pack, relative to the green markers on the B cuts. Counter-intuitively, due to the high transparency, and low refractive index of the pill themselves, the signal witnessed over the tablet does not emerge from a direct reflection of the pills, but relates to the reflection on the back metallic sheet, propagated back and forth through the pill. The additional propagation delay can indeed be witnessed on the second B cuts in the orange squared section. In presence of a pill, the metallic sheet interface appears further than in absence of a pellet. The refraction on the rounded edges of the pill nevertheless ensure a reliable pellet boundary detection, as detailed in the orange squareed section of the C cut of Figure IV.4c.

(a)

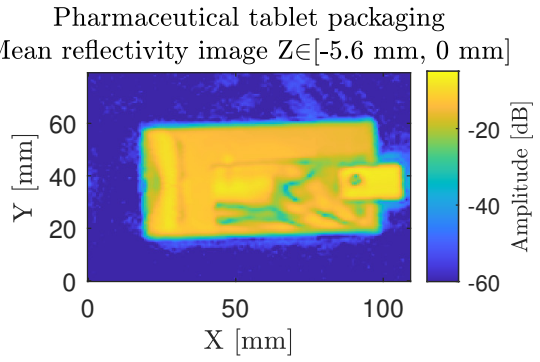

(b)

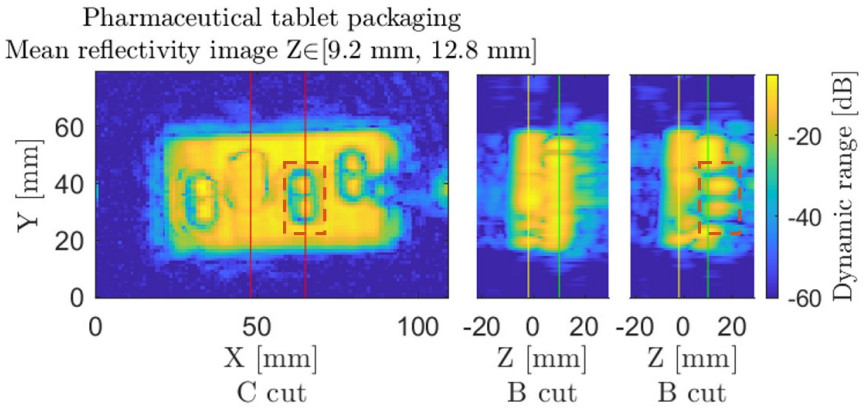

(c)

Figure IV.4: **(a)** Pharmaceutical sample under inspection featuring a missing tablet, and scanned ranges of interest featuring **(b)** the front packaging and instruction leaflet, and **(c)** the tablets in their blister pack, completed by two b cuts along the vertical lines red markers at x=50 mm and x=65 mm. Yellow and Green markers feature the cardboard interface and the blister pack metallic interface respectively on the B cuts. One pill is highlighted through the orange dotted box on both cuts.

This section aimed to provide, through the consideration of few representative samples, a glimpse of the wide advanced problematics that are accessible through millimeter waves FMCW radars on pragmatic and concrete industrial topics. For such industrial applications, even at such attainable high recording cadence of 7.62 kHz, raster-scan operations remain non-viable beyond academic proof of work demonstrations. Even-though a scan takes less than 15 min, for a full three dimensional contactless monitoring of the sample, once again highly limited by the scanning unit; itself improved from several hours for a QCW two dimensional inspection, the transposition to the industrial sector would require full in-line inspection capabilities. At this point, the integrability of such systems does not rely on the radar mode of operation and performances, but remains tied to the imaging system capabilities. Efforts toward line-scanning setups are part of the ongoing scope of development to take the full advantage of the high measurement rate while suppressing the mechanical limitations of the imaging unit integrating the newly introduced FMCW transceiver.

IV.3 Targeted Instrumentation Approaches, Using Generic Available FMCW Units

In anticipation to the outcome and results gathered in Chapter III on the development of the 150 GHz FMCW transceiver, several specific topics have been tackled in preliminary feasibility studies through the employment of available FMCW sensors. Indeed, in parallel to the design and characterization phases of the previously detailed newly developed transceiver, the FMCW systems accessible among the IMS terahertz platform have been put to good use to target explicite

industrially encountered technological issues.

Specifically, the previously featured, fully integrated PCB 122 GHz Silicon-radar chip, subsequently optimized for short range operation was available as a low-cost compact sensing solution. Oppositely, the III-V based SynView scanner, embedding 100 GHz and 300 GHz FMWC sensors, featuring 60 dB and 40 dB measurement dynamic ranges respectively, with transmission and reflections configurations, was accessible as a reference imaging system which offers a large achievable scanning area.

The respective capabilities of those systems have been operated as to consider few specific topics of interest for industrial actors. Namely, wall see-through inspection will be addressed as an actively encountered problematic in the aeronautics field. For instrumentation simplifications, to allow for inaccessible remote sensing, the assessment of guided transceivers geometries have as well been explored.

IV.3.1 See-through imaging

Focusing on see-through imaging problematics, specifically in the aeronautics application field, further brings to light a few additional challenges beyond the simple measurement rate. This specific topic is brought up as an alternative to the teadious and costly integration of X-ray inspection during airplane on ground maintenance time frames. Targeting *in-situ* direct health monitoring while avoiding the internal cover dismantlement, the reflection geometry represents the only adequate implementation due to the metallic plane fuselage. The focused-point sensing integration then enables a simplified optimization of the beam waist point on the object of interest, beyond an eventual extra partially transparent cover, to reach the optimum returned power and resolution. In such a configuration, at a given working frequency, a trade-off between achievable lateral resolution and optimum imaging distance then once again needs to be considered. Suiting material absorption, the frequency band selection also represents one of the key optimization to be accounted for. Lying on the trade-off between material penetrability and targeted resolution according to the defect size, lowered material absorption levels highlighted the adequacy of the 100 GHz band SynView radar transceiver. As it minimizes the losses when passing back and forth through the fiber-glass panel, it can guarantee adequate lateral resolutions in the order of a few millimeters [2, 3].

As expected, over a scan, the maximal reflectivity image will mainly feature the predominant fiber-glass cover first interface reflection. The use of a longitudinal averaging in the Region Of Interest (ROI) beyond the cover brought significant improvement as depicted in Figure IV.5a, with the clear depiction of reflective elements. Reminiscences of the panel geometry remain nevertheless discernible.

Indeed, as a result, Figure IV.5a displays the first demonstration of this approach, in a complexified configuration of see-through plane cover imaging. Distances up to 150 mm between the samples area and the covering panel have been assessed, leading to resolution levels below 1 cm.

An object presence evaluation, can easily be performed along with a position, depth and shape assessment for each of the metallic reflective components, with the wrench, the sample holders and $\frac{1}{2}$" holder posts. The complex shape of the plane cover nevertheless induces a non-negligible signal loss along the cover edges, naturally introduced by refraction. Deepening the investigation, the insertion of an extra thermal insulation layer demonstrated to have very little effect on such sensing capabilities. Indeed, these fiber-based low density materials display little reflectivity and a full transparency in the sub-terahertz range, confirmed through succinct terahertz TDS investigations. Additionally, aiming to check for water content detection capabilities, in case of cracks or fissures inducing any fluid leakage, dry and moist sponges are held below the metallic wrench and feature an expected reflectivity contrast. A clear distinction of the moisture status is achieved between the two sponges. Further investigations have been carried out with the detection of cracks broken components or alterations on aluminum and glass-fiber composite tubes, and are further detailed in [2].

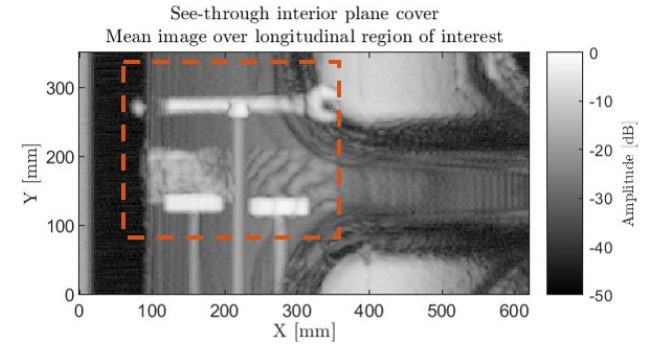

(a)

(b)

Figure IV.5: **(a)** 100 GHz FMCW large field scan for see-through purposes on interior plane cover. **(b)** Relative implementation, side view and top view, featuring the metallic samples and sponges on the low right side, beyond the cover.

The FMCW embedded longitudinal sensing demonstrated its adequacy for see-through imaging thanks to the sole consideration of contributions over a given region of interest, hence excluding the unwanted cover reflected signal. Beside the reduced resolution, and refracted beam distortion through the cover, the visualization of defects, foreign object, alterations or moisture contamination is made possible through a glass-fiber plane cover.

IV.3.2 Guided FMCW radar remote imaging and sensing

The volumetric inspection granted by the FMCW mode of operation demonstrated its suitability to several application cases. Nevertheless, the use of optical components involves tedious alignment and imposes mechanical restrictions along the propagation path. Hence, such coupling methods limit the development of compact and portable terahertz measurement systems to a broader scope of applications with remote sensing capabilities.

To address this issue, a terahertz waveguide [4] can be considered as an alternative solution. The guided reflectometry concept has already been investigated with CW sources or pulsed sources [5, 6] in conjunction with different waveguide conceptions. A variety of waveguide geometries have been assessed [7–10] to demonstrate the feasibility and the potential of THz guided reflectometry systems for large applicative fields.

To remedy the complexity of those coupling setups, the guided reflectometry configuration can be highly simplified by matching a compact FMCW transceiver with a dielectric thin-wall hollow-core waveguide of suitable dimensions. An optic-free transmission channel between the transceiver and the sample is then ensured with all the benefits of the FMCW radar sensing technique. Namely, the phase information granted by the guided FMCW technique allows a differentiation of the contributions generated along the waveguide, unlike with guided QW integrations where the detected signal results from a superposition of all those contributions. Hence, beside a sensing capability along the waveguide, it ensures a drastic improvement of the signal-to-noise ratio thanks to the selection of the sensing distance, leading to the suppression of unwanted parasitic contributions. The relatively low longitudinal resolution of the considered radar units nevertheless does not allow volumetric sensing at the waveguide's output.

As a proof of adequacy and universality of this approach regarding the front-end of the FMCW

transceiver, two guided reflectometry configurations have been investigated [11] with a high end III/V based 100 GHz SynView system and a low-cost solution with the 122 GHz Silicon radar chip. The prior features a suitable regular emission profile thanks to the horn antenna integration, with a maximum directivity of 20 dBi, for 14.4° and 24.1° angular width in both normal planes respectively. The later, on the other hand, features a broad emission profile in nearly a half space (11 dBi with angular width of 47°), that suits the typical emission profile of such double patch antenna front-ends [12]. As a simplified guided configuration, an optics-free single communication path between the FMCW module and sample is solely provided by the above-mentioned dielectric waveguide, properly centered on the transceiver. As a simple optimization, a foam support, acting as terahertz absorber, is placed in the vicinity of the coupling area to neutralize the parasitic signals of non-coupled echoes.

Waveguide for remote sensing

The development of terahertz waveguides benefits from the technological advancement witnessed in the IR and microwaves regions. However, the absorption losses witnessed in the propagation materials highly limits their performances. Considering that dry-air is the most transparent terahertz medium, a thin-wall hollow-core Polypropylene waveguide has been selected to be implemented due to its simple structure, low-loss propagation properties of the cladding material and availability on the market. Such waveguides exploit the anti-resonant reflection guiding mechanism [13]. The cladding layer then acts as a Fabry-Perot etalon, allowing terahertz waves to propagate inside the air core at non-characteristic frequencies that are defined as [14]:

$$f_{c_m} = \frac{m\, c_0}{2\, t_{cl}\, \sqrt{n_{cl}^2 - 1}}, \tag{IV.1}$$

with m an integer, t_{cl} [m] and n_{cl} the thickness and real part of the refractive index of the cladding material respectively.

One of the additional parameters for the waveguide selection relies on its diameter as it will impact the power coupling between the transceiver and the waveguide. Accounting for the complexity of the involved anti-resonant guiding mechanism and complex transceivers emission profiles, electromagnetic simulations have been conducted to investigate the impact of the waveguide diameter on the coupling capabilities on both radar units front ends.

In addequation with simulated trends, experimentally, a commercially available 3 mm radius Polypropylene (n_{cl} = n_{PP} =1.515) pipe waveguide with a cladding thickness of t_{cl}=158 µm has been selected and should display characteristic resonant frequencies around f_{c_1}=860 GHz and f_{c_2}=1.72 THz [5] according to Eq. IV.1. A TDS investigation displayed the associated losses peaks around 840 GHz and 1.7 THz, hence, allowing the 100 GHz wave propagation without significant impacts on the considered FMCW radars bandwidth.

100 GHz SynView transceiver reflectometry unit

- Propagation and coupling-in issue

Alongside the experimental setup implementation depicted in Figure IV.6b, full-wave electromagnetic field distribution simulations have been performed and provided substantial information concerning the propagation behaviors of guided waves as detailed in Figure IV.6a. Through the three dimensional full-wave simulation suite CST microwave studio, a time-domain solver applying finite integration technique is used to retrieve those field distributions. It should be noted that no material absorption has been considered. With the W-Band conical horn antenna, the 30 cm long hollow-core waveguide and a 5 cm long air block, such an integration demonstrated a strong dependency on the profile of the injection source and position of the waveguide.

Over the first part of the propagation, a stabilization of the guided signal is noticeable, while towards the end of the 30 cm waveguide, a steady field distribution is retained which corroborates

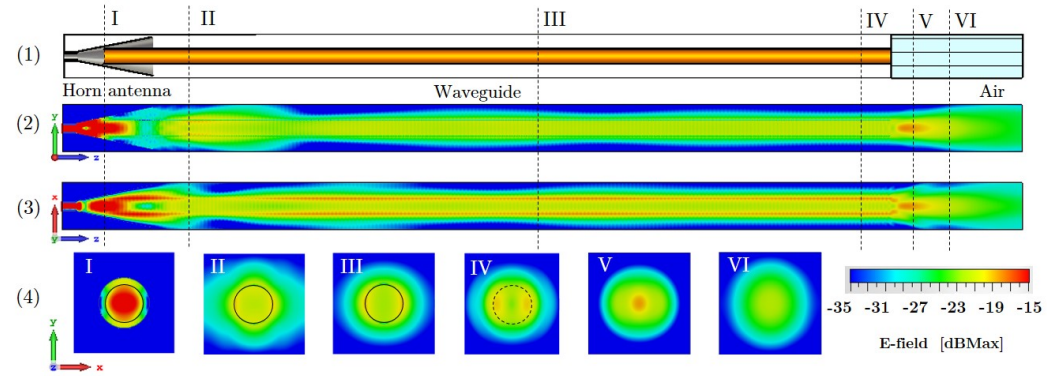

(a)

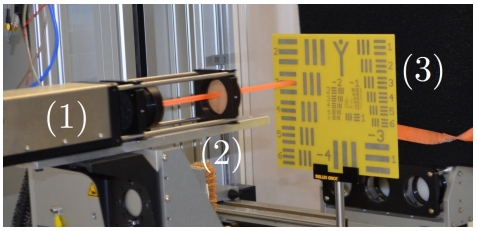

(b)

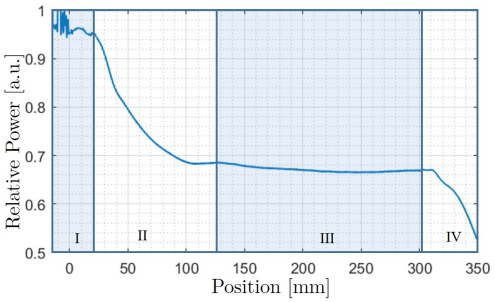

(c)

Figure IV.6: (a) (1) Diagram of the 100 GHz SynView guided reflectometry radar unit, simulated electric field magnitude profile along both plans **(2)** $\vec{y}$-$\vec{z}$ and **(3)** $\vec{x}$-$\vec{z}$ and **(4)** $\vec{x}$-$\vec{y}$ cut of the electric field magnitude profile at respectively z=0 mm, z=30 mm, z=190 mm, z=300 mm along the waveguide and 5 mm, 20 mm from the waveguide's output. **(b)** Related experimental setup with **(1)** the transceiver unit, **(2)** the waveguide support and **(3)** the test target. **(c)** Simulation of the enclosed power as a function of the propagation distance.

the guidance capacity of the waveguide. The field distribution also reveals that cladding modes are excited, resulting in the significant field confinement in the two sides of the cladding in the $\vec{x}$-direction. The low effective refractive index, induced by the thin cladding, should prevents any significant back-reflection from the output waveguide-air interface to restrain the generation of a standing wave. Additionally, with the low guiding mode confinement, an external field spillage enables an additional beneficial sensing capability along the waveguide. Indeed, combined with the high sensitivity and the FMCW longitudinal sensing, this external field distribution allows for sensing and differentiation of inserted perturbations in the vicinity of the waveguide.

Beside spatial distribution concerns, power coupling remains of importance to assess the sensing capabilities of this system. The coupling is simply achieved directly by inserting the waveguide into the conical horn antenna to get a proper centering and field collection. Figure IV.6c depicts the simulated enclosed power as a function of the propagation distance. Over the first 30 mm, (phase I), the excitation signal is confined in the metallic horn antenna. The subsequent gradual decrease, (phase II), relates to the non-coupled waves radiation losses. The stable guided propagation then takes place along the waveguide (phase III) where no significant power losses are noticed. The coupling efficiency, dictated by Equation IV.2, as the ratio between the coupled guided power, P_{Guided} [W], and the initial excitation Power, $P_{Excitation}$ [W], is hereby directly deduced from the simulation steady state, then approaching 70%. Once the radar signal propagates out of the waveguide (phase IV), the enclosed power reduction occurs due to the beam expansion in free space.

$$\eta = \frac{P_{Guided}}{P_{Excitation}}, \tag{IV.2}$$

- Sensing capabilities : dynamic range and lateral resolution

The measurement dynamic range of the unit is one of the main performance indicators for sensing purposes. The 100 GHz SynView FMCW Radar unit offers a maximum 70 dB dynamic range when used in standard quasi-optical imaging configuration. Nevertheless, the implementation of the waveguide will ineluctably induce a limitation on this dynamic range. Indeed, impacting the signal as a constant background noise, the unavoidable signal reflection from the open probing end will be the main limiting factor. Appropriate simulations have been conducted to assess this impact via the comparison of the reflected power for two extreme cases. The open-end waveguide, as a background signal, featured a -28.5 dB amplitude reflection coefficient from the effective index mismatch back-reflection. Secondly, the implementation of a perfect reflector at the end of the waveguide will assess the optimum achievable signal level. A -1.5 dB return signal coefficient has been deducted from those simulations, mainly impacted by the imperfect coupling from the horn antenna to the waveguide. A total maximum achievable dynamic range of 27 dB can then be expected.

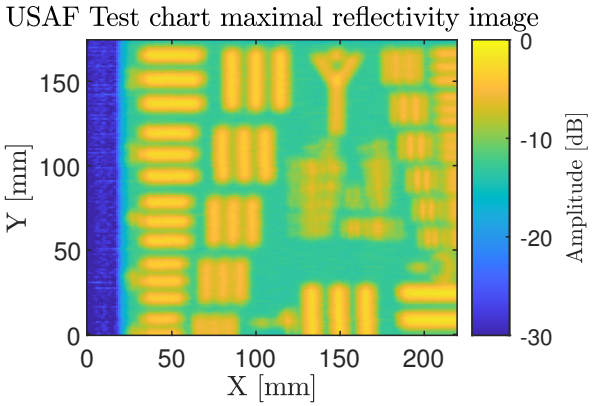

Figure IV.7: Guided unit lateral resolution assessment on USAF test chart.

The free space propagation behavior after the waveguide is obviously of interest to assess the sensing and imaging capabilities of the transceiver. Indeed, the maximum sensing distance is related to the back-coupling efficiency, while the lateral resolution capabilities is established by the beam profile. It can be observed that, although the back-coupling efficiency is optimized in the vicinity of the waveguide's output, the beam profiles of Figure IV.6a(4) (IV) display two main amplitude lobes oppositely confined on the cladding. This inhomogeneity leads to ghost imaging artifacts causing a duplication of the object when using the system in such a close configuration as depicted in Figure IV.7, on the scan of an USAF test chart performed with a 1 mm working distance.

After propagation, the beam profile is then smoothed thanks to the spreading of the two lobes. It reaches an optimum imaging resolution of 4.5 mm at FWHM at an optimum working distance of 5 mm. Working at larger distances, the back-coupling efficiency along with the resolution will decrease due to the free space beam spreading. A classical far field image at this frequency would grant a resolution in the order of 2.5 mm for a numerical aperture of NA=0.5 [11].

- Optical resolution improvement: solid immersion lens implementation

To address the limitations of the imaging resolution, linked to the waveguide's diameter, while avoiding heavy configuration with optical components, an end-of-waveguide solid immersion lens has been selected. It allows for high NA focusing for high resolution imaging at short working distance. Specifically, a 9 mm diameter hemispherical HDPE lens is inserted at the output of the waveguide. Its relatively low refractive index induces a moderate unwanted signal return from the lens interfaces, still leading to a slight decrease of the achievable dynamic range. Through simulations, as detailed in Figure IV.8a a beam optimum spot size of 2 mm at FWHM is obtained at

a frontal working distance of 2.5 mm, while residual low amplitude side lobes at -25 dB are induced by the waveguide spillage. This simulated profile corroborates the resolution improvement witnessed in Figure IV.8a, with the resolution of element 1, group -2 at 2 mm working distance. This configuration nevertheless leads to a highly reduced depth of field, along with a drastic back-coupling losses and resolution decrease beyond the optimum sensing distance.

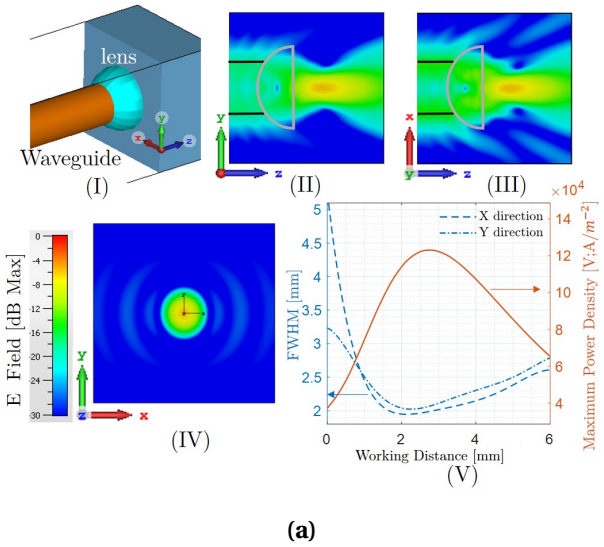

(a)

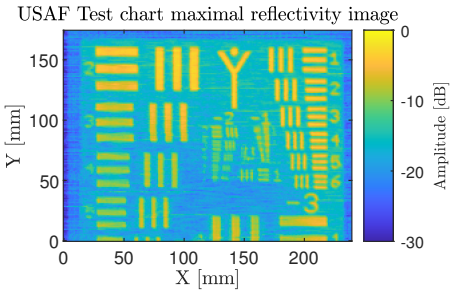

(b)

Figure IV.8: (a) (I) Diagram and (II), (III), (IV) simulations performed on the solid immersion lens SynView guided unit following different plane cuts, supplemented by (V) the extracted evolution of the beam FWHM and maximal power density evolution. **(b)** Related lateral resolution assessment on USAF test chart.

122 GHz Silicon radar chip reflectometry unit

In contrast with the previously detailed unit, the integration of the 122 GHz silicon radar chip will allow for a low cost and compact alternative. As a front-end,it displays a double patch antennas with a much broader emission pattern. The significant alteration of the electric field distribution along the waveguide is depicted in Figure IV.9. Obvious signal reflections on the waveguide's cladding can be observed through the oscillating behavior during the propagation. This can be explained by the decentering of the transmitter with respect to the waveguide, the excitation conditions not being symmetrical anymore.

Owing to the wide, near-isotropic, emission pattern of the patch antenna design, a considerable power fraction is radiated into free space rather than coupled into the waveguide. Figure IV.9b phase I depicts this power loss, while phase II indicates that the radar signal reaches guided power stabilization after a 50 mm propagation, leading to a reduced coupling efficiency of 18%. Assessed in the same way as previously, full dynamic range is expected to reach up to 27.6 dB even though a much larger coupling loss is witnessed, once again limited by effective index miss-match reflection at the end of the waveguide.

On imaging perspectives, through an open waveguide configuration, an achieved resolution of 2.8 mm, corroborating the simulated FWHM beam diameter. The power confinement on one side of the cladding (see Figure IV.9(4)IV) ensures this resolution improvement with respect to the previously witnessed two lobes profile, and is induced by the asymmetrical coupling-in geometry. This TX asymmetry, completed by the complex back coupling toward the decentered RX antenna, are additionally inducing a non-negligible shadowing effect.

This artifact is highly mitigated with the addition of the resolution enhancing, hemispherical HDPE solid immersion lens. Figure IV.9c displays such a raster scan acquired image of the UAF test chart featuring a 1.4 mm resolution (group -2 element 4) in accordance with the conducted beam profile simulations. Nevertheless, ghost artefacts are still noticeable and induced by beam profile inhomogeneities leading to an improper beam focusing with non-negligible side lobes.

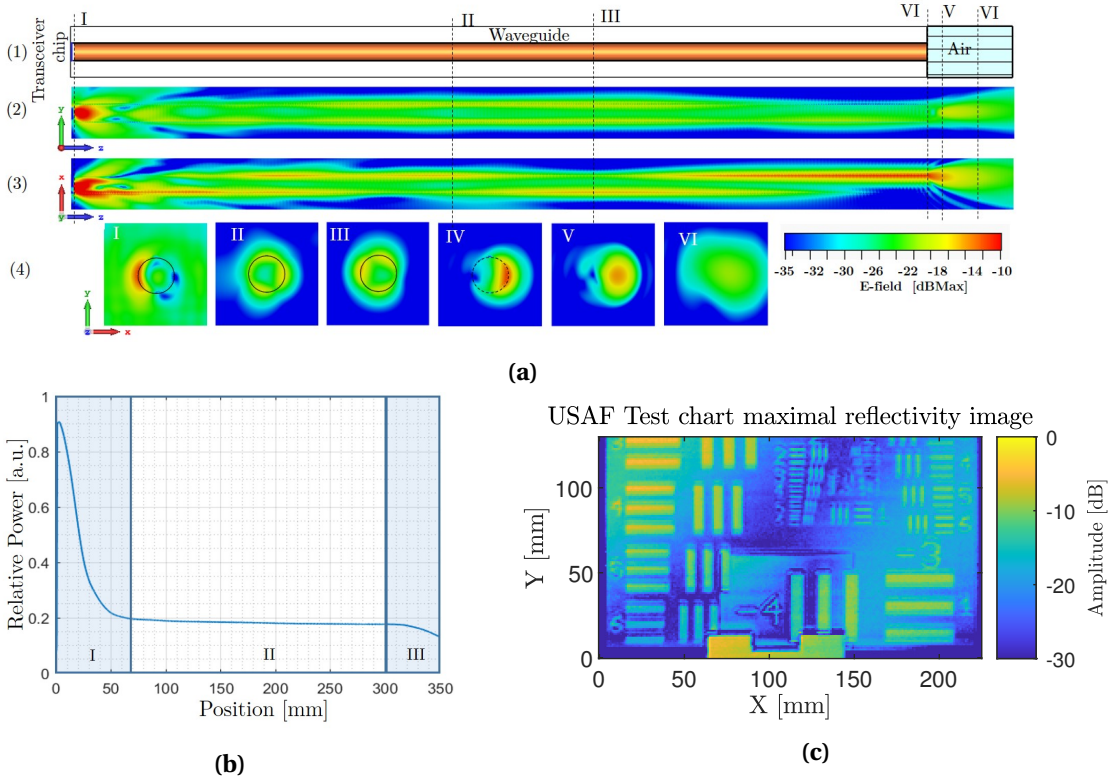

Figure IV.9: **(a)(1)** Diagram of the 122 GHz Silicon radar guided reflectometry radar unit, simulated electric field magnitude profile along both plans **(2)** $\vec{y}$-$\vec{z}$ and **(3)** $\vec{x}$-$\vec{z}$ and **(4)** $\vec{x}$-$\vec{y}$ cut of the electric field magnitude profile at respectively z=0 mm, z=40 mm, z=180 mm, z=300 mm along the waveguide and 3 mm, 20 mm from the waveguide's output.**(b)** Simulation of the enclosed power as a function of the propagation distance. **(c)** Resulting USAF test chart scan implementing the resolution enhancing solid immersion lens.

With a similar pursue of low-cost terahertz systems developments, also based on the integration of the 122 GHz silicon radar transciever, a open-source focused point scanning system is succintly featured in Appendix E.

IV.4 Thickness Evaluation Through FMCW Sensing

Although the use of FMCW radars has demonstrated to be effective for contactless and non-destructive volumetric inspection, as depicted in Section IV.2, the thickness of the investigated samples proved to be a characteristic of interest for numerous industrial actors.

Capitalizing on the longitudinal sensing capability of the FMCW mode of operation, the range localization of reflective interfaces is ensures and provides a powerful tool for thickness assessment in stratified samples [15–17]. Indeed, when reaching a dielectric interface, a portion of the incident frequency-chirp is transmitted through the following layer, while another portion would be reflected back. Eventually, a spectral analysis, equivalent to a time-of-flight investigation, can then be conducted to evaluate the respective thicknesses.

The intuitive and naive approach would simply rely in the investigation of subsequent maxima in the amplitude spectrum. This would impose a strong limitation on the achievable resolution, in the order of 4.6 mm, as already discussed in Section III.4.3. Unlike section IV.3, this section does not lean on the instrumentation optimization previously featured to fit specific problematics, but will be focused on the development of targeted numerical processing for thickness sensing beyond the intrinsic numerical resolution, employing the newly developed 150 GHz transceiver unit in its standard single point sensing configuration depicted in Figure III.13.

IV.4.1 Technological analogy

Several technological parallels can be drawn with already well established stratified structures inspection approaches. Namely, ground penetrating radars [18], through low frequencies FMCW, pulsed or ultra-wide-band systems in the Gigahertz range, have been extensively applied to the consideration of layered structure with characteristic thicknesses ranging from several centimeters to a few meters. Specifically, it has been applied to pavements investigations [18–21], as depicted in Figure IV.10, or ice layers thickness assessment [22, 23].

To another extent, when considering 100 µm thick layers, pulsed TDS terahertz systems [24] offer unrivalled performances for the contactless investigation of thicknesses in aircraft, or automotive paint coatings. The sensitivity of pulsed terahertz radiations to individual coatings forming a stratified structure was reported for numerous study cases, as in automotive [25, 25–27], aeronautics [28], art science [29] and pharmaceutical [30].

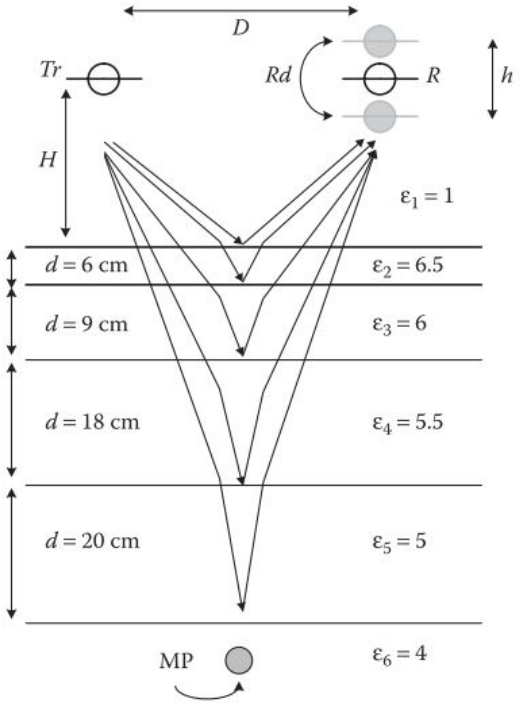

Figure IV.10: Diagram of the investigation of a five-layer pavement and a metal cylinder (MP) beneath the lowest layer, through ground penetrating radar employing frequencies typically in the Gigahertz range. [18, 19].

A clear analogy between FMCW signals and TDS time resolved terahertz electric fields measurements is highlighted in Figure IV.11. As it displays side-by-side a classical logarithmic amplitude and phase complex FMCW representation (Figure IV.11a), as well as a real-part/imaginary-part depiction (Figure IV.11b) of the same signal, the later features a strong resemblance with typical stratified TDS structures investigations time domain signals.

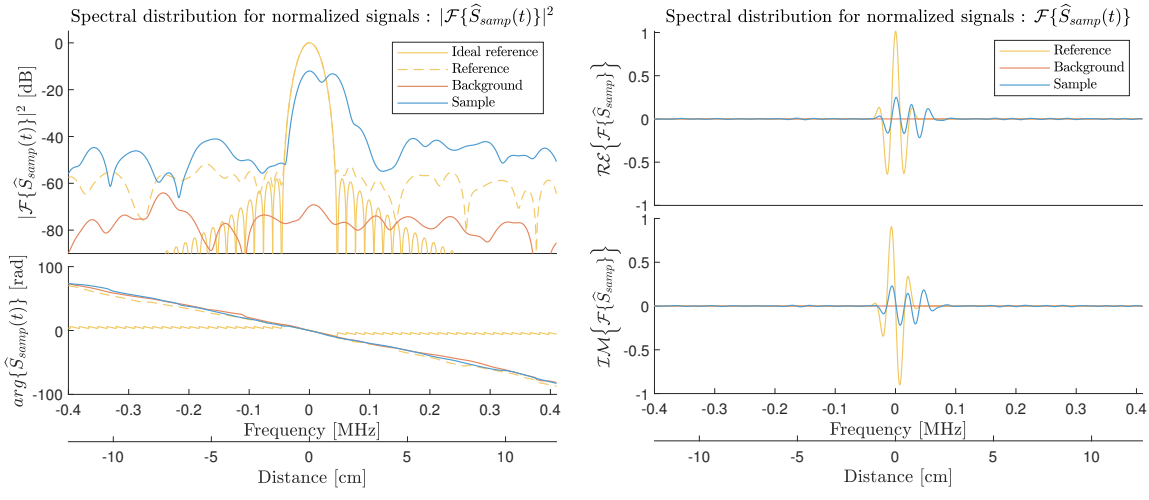

Figure IV.11: Spectral visualisation of the normalized FMCW down-converted signal **(a)** through a typical amplitude and phase representations and **(b)** with distinct real and imaginary parts for a 7.5 mm thick Plexiglas plate.

From there, a time-frequency duality can be expected between TDS and FMCW approaches and is simplistically detailed in Figure IV.12. For the TDS approach, depicted in Figure IV.12a, the time domain convolution of a reference signal by a sample impulse response, $\mathscr{F}^{-1}\{H(\omega)\}$, lead to the sample time domain trace. Hence, a frequency transfer function, $H(\omega)$, can be considered as to describe the sample itself [31]. Contrariwise, for the FMCW mode of operation, the sample related transfer function should be temporal, $H(t)$ and lead to the expected frequency impulse response convolution. This specific duality transposition will be further detailed through the sample model in section IV.4.2, applied for the FMCW thickness extraction.

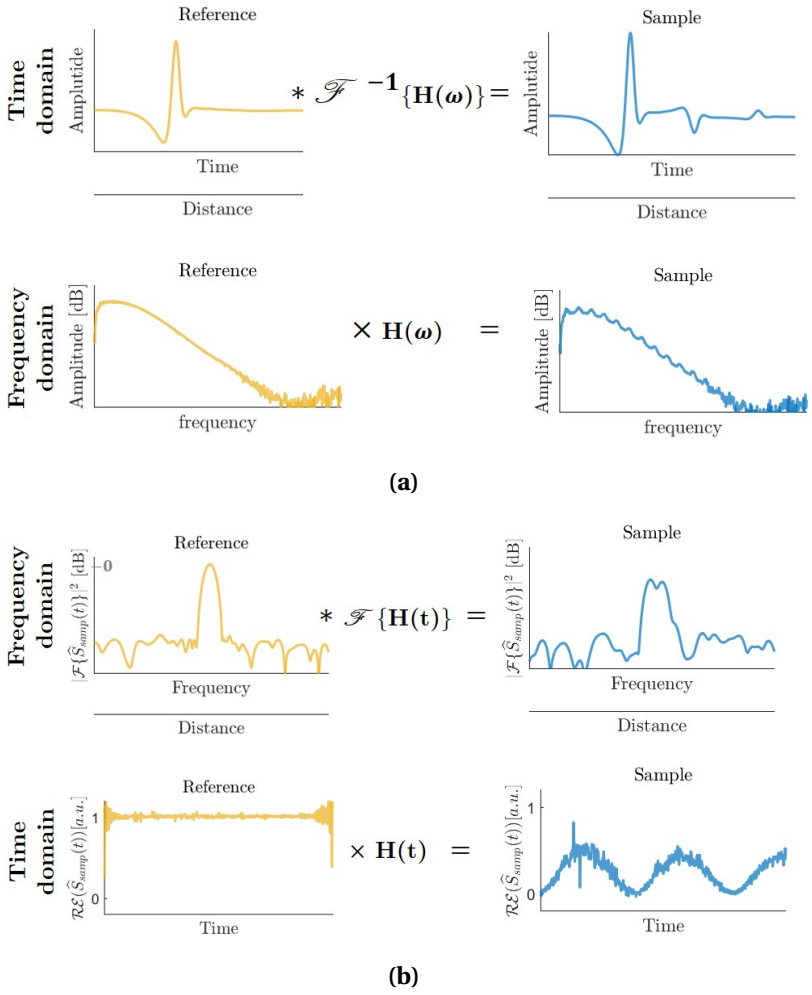

Figure IV.12: Diagrams representing the correlation between **(a)** TDS and **(b)** FMCW radars for the modelling of the sample interaction through the consideration of a transfer function.

Accounting for this analogy with the TDS mode of operation, stratified samples assessment should be achievable from FMCW radars for thicknesses ranging from sub-millimeter levels up to several centimeters. With well-established technological approaches, Inverse Electromagnetic Problems (IEP) are commonly performed to extract individual layers dielectric properties and thicknesses [32] from a recorded trace. Usually, it consists in minimizing an objective function that denotes the discrepancies between the experimental waveform and the ones computed through set of candidate parameters. Namely, the individual thicknesses and complex refractive indexes of each layer are the parameters of interest that will impact the simulated signal.

In addition to the recorded experimental transfer function, $H_m(t)$, the definition of a model transfer function, $H_s(t)$, to depict the behavior of the sample in response to an incoming electric field is then required.

IV.4.2 Sample modelling : Rouard's recursive model

Lying on the elementary propagation and refraction macroscopic interactions, the Rouard's model can lead to the definition of a spectral response of a given stratified sample. It is usually based on an interface-by-interface iterative construction of the sample response [33–35].

Reflection considerations

Of interest for this work due to the geometry of the radar transceiver, the reflection spectral characteristic of a sample can then be derived. Initiating from the farthest interface, the subsequent iterative addition of layers ([1⇒p]) will lead to a whole depiction of the sample. A schematic representation of this process is detailed in Figure IV.13.

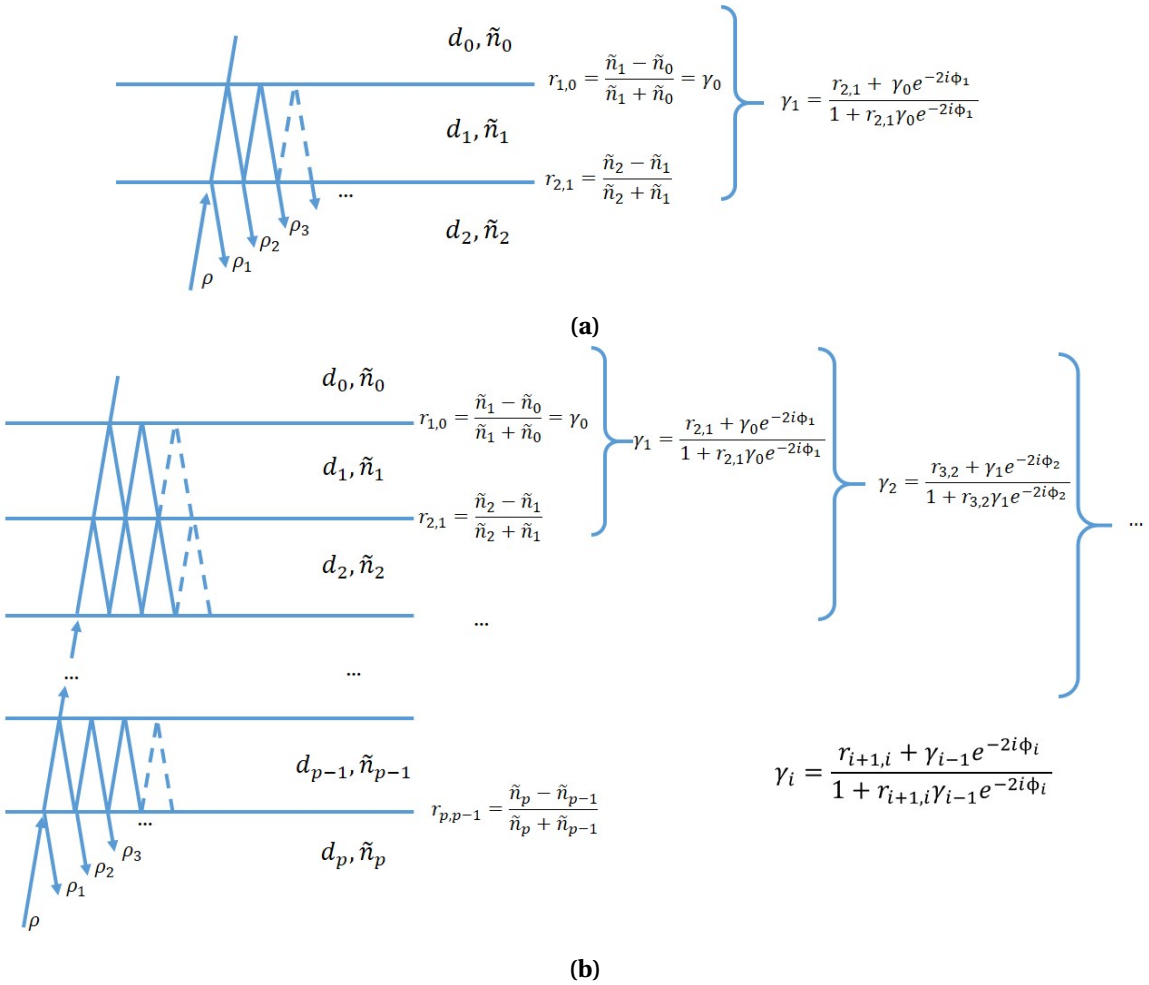

Figure IV.13: Diagram of the optical paths within stratified samples and relative Rouard models for **(a)** a single layer consideration and **(b)** a generic multi-layer sample.

Starting from the final interface, and according to Equation II.10, we can establish, $r_{1,0} = \frac{\tilde{n}_1 - \tilde{n}_0}{\tilde{n}_1 + \tilde{n}_0}$. Relative to the first layer, as depicted in Figure IV.13a, the insertion of a second interface, will generate a Fabry–Perot cavity where multiple round-trip reflections, ρ_k, have to be considered. Accounting for the successive reflections and transmissions occurring at each interface, as well as

the propagation-induced phase, the consecutive contributions can be expressed as:

$$\begin{aligned}
&\rho_1 = r_{2,1},\\
&\rho_2 = t_{2,1} r_{1,0} e^{-i2\Phi_1} t_{1,2} = (1 - {r_{2,1}}^2) r_{1,0} e^{-i2\Phi_1},\\
&\rho_3 = t_{2,1} {r_{1,0}}^2 r_{1,2} e^{-i4\Phi_1} t_{1,2} = (1 - {r_{2,1}}^2) {r_{1,0}}^2 r_{1,2} e^{-i4\Phi_1},\\
&...,\\
&\rho_k = t_{2,1} {r_{1,0}}^{k-1} {r_{1,2}}^{k-2} e^{-i2(k-1)\Phi_1} t_{1,2} = (1 - {r_{2,1}}^2) {r_{1,0}}^{k-1} {r_{1,2}}^{k-2} e^{-i2(k-1)\Phi_1},\\
&...,
\end{aligned} \tag{IV.3}$$

since, from power conservation $t_{2,1} t_{1,2} = (1 - {r_{2,1}}^2)$, with $r_{1,0}$ and $r_{1,2} = -r_{2,1}$ the reflection coefficients of the first and second interface respectively and $\Phi_1 = \frac{2\pi \tilde{n}_1 d_1}{\lambda_0} = \frac{\omega \tilde{n}_1 d_1}{c_0}$, the one-way phase shift[rad]. For simplification purposes, this process has been described in the case of a normal incidence beam.

From ρ_2, those successive contributions are therefore following a geometric series with first term $\rho_2 = (1 - {r_{2,1}}^2) r_{1,0} e^{-i2\Phi_1}$ and a constant ratio between successive terms, $\chi_1 = r_{1,0} r_{1,2} e^{-i2\Phi_1}$. Considering then the total reflection as a coherent sum of those successive contributions, this specific series can be expressed as an infinite sum of terms $\sum_{k=1}^{\infty} \rho_n$ which leads to :

$$\sum_{k=1}^{\infty} \rho_n = \rho_1 + (1 - {r_{2,1}}^2) r_{1,0} e^{-i2\Phi_1} \sum_{k=0}^{\infty} \chi_1^n. \tag{IV.4}$$

A global reformulation of this infinite sum will therefore lead to the following expression for the reflection coefficient of the first layer:

$$\gamma_1 = \frac{r_{2,1} + r_{1,0} e^{-2i\Phi_1}}{1 + r_{2,1} r_{1,0} e^{-2i\Phi_1}}. \tag{IV.5}$$

This expression can therefore be integrated as a global reflection coefficient for the second interface that will account for all the contributions among the first layer. Hence, as depicted in Figure IV.13b, a layer-by-layer iteration can be conducted to develop analytically the whole multilayer sample reflection coefficient following Equation IV.6 :

$$\gamma_i = \frac{r_{i+1,i} + \gamma_{i-1} e^{-2i\Phi_i}}{1 + r_{i+1,i} \gamma_{i-1} e^{-2i\Phi_i}}. \tag{IV.6}$$

This reflection coefficient then accounts for all the subsequent layers [i, 1] and is based on the reflection coefficient of the antecedent stack γ_{i-1}, the reflectivity of the newly added interface $r_{i+1,i}$, as well as the one-way phase shift induced by the optical path among this i^{th} layer, $\Phi_i = \frac{2\pi \tilde{n}_i d_i}{\lambda_0} = \frac{\omega \tilde{n}_i d_i}{c_0}$ [rad]. The introduction of the complex refractive index, $\tilde{n}_i$, ensures the consideration of the imaginary part of the refractive index, κ, mainly to account for the attenuation among each layer. Thanks to the limited bandwidth consideration granted with the use of FMCW radars, non-dispersive dielectric parameters can be assumed.

Extended Rouard's model for transmission configuration

In a similar fashion, an iterative construction of the global transition coefficient of a stratified sample can be derived, but requires additional steps. Contrary to the previous considerations, the iterative construction is preformed from the first layer to the last along the propagation direction of the wave. A derivation the backward reflection coefficients, $\gamma_{i+1,i}$, that accounts for all the contribution in reflection up to the i^{th} layer in the backward propagation direction, is necessary and can be performed following the above mechanism. Following the same infinite coherent sum of contributions, iteratively after each layer, Equation IV.7 can be derived. Beyond this description, that depicts the iterative construction of the transmission coefficient, μ_i, of each subsequent layers, this approach will not be further detailed since no measurements in transmission have been

performed in this work on this thematic.

$$\mu_i = \mu_{i-1} \frac{t_{i,i+1} e^{-i\Phi_i}}{1 + \gamma_{i-1} r_{i,i+1} e^{-2i\Phi_i}}. \tag{IV.7}$$

As a simple application case, an anti-reflecting coating optimum thickness and refractive index (see Equation I.4) can therefore be deducted from this model. It can be extensively used as well for engineered thin film anti-reflective coatings. It is widely applied over the whole electromagnetic spectrum [36] with visible photographic lenses or eyeglasses coatings, selective or broadband IR filters, or again for UV and X-rays grazing angle mirrors [37].

Beside single layers Parylene coatings, such technologies have not yet been extended to the terahertz spectral region due to the lack of suitable materials and the requirements for thick layer depositions. Nevertheless, along with propagation matrix modeling, [31, 38], this approach finds itself extremely useful in the terahertz application field as a physical model for single-layer or stratified samples. Notably, such a mechanism can be integrated for TDS dielectric constants extraction, implemented for spectroscopic measurements [39–41]. In more recent works, among other methodologies such as sparse deconvolution stratigraphy [42, 43], an extensive use of these approaches have been made for thickness extraction on multi-layered paint coatings [25, 44], one of the lately targeted and successful application for terahertz TDS inspection.

This representative physical model of the sample should then allow for the implementation of an IEP for the determination of the sample characteristics from FMCW measurements. Namely the complex refractive index and thicknesse of each individual layer in the sample under test are of interest.

IV.4.3 IEP FMCW extraction

As the FMCW sensing information ensue from a homodyne detection scheme, followed by a prior normalization procedure, the link between the Rouard's sample depiction and the experimental information is not as straightforward as for TDS time traces. Indeed, for the later as a direct measurement scheme, a simple consideration of $H_s(\omega) = \gamma_p(\omega)$, would grand an adequate physical representation for the conducted frequency domain investigations. It would then be subject to the angular frequency, as well as the complex refractive index and thickness of each layer.

However, due to the homodyne down conversion, temporal transfer functions should be considered for the application of the IEP in the FMCW mode of operation.

Transfer functions definition

Indeed, the frequency domain convolution process, depicted in Figure IV.12b, between a unitary reference and the sample impulse response will lead to the sample measurement. Hence, in the time domain, a transfer function relative to the measurement can be described as:

$$H_m(t) = \frac{\widehat{S}_{samp}(t)}{\widehat{S}_{ref}(t)}. \tag{IV.8}$$

The consideration of the normalized reference and sample signals, $\widehat{S}_{samp}(t)$ and $\widehat{S}_{ref}(t)$, accounts for the embedded pre-processing 2-points referencing previously detailed in section III.3.2. Namely, the background removal ensures the sole consideration of the sample contributions. Additionally, from this prior normalization, it ensues a convenient simplification as a reference measurement is to be equivalent to a unitary signal $\widehat{S}_{reference}(t) = 1$. This reduction can be performed in the case where this reference is recorded in the initial normalization reference plane. A frequency shift and phase component has then be accounted for otherwise.

Following the IEP mode of operation, the simulated transfer function remains to be defined, as an algorithmic minimization of the difference between the measurement transfer function $H_m(t)$ and a simulated transfer function $H_s(t)$ is to be performed.

Assimilating then the Rouard's model thicknesses, d_i, as the relative propagation distances with respect to the reference plane, $\widehat{d_{i'}}$, the following variable change can be operated to account for the homodyne detection : $\omega = -2\pi(f_{min} + \frac{\mathrm{BW}}{\mathrm{T}_s} t)$. This will indeed operate a rescaling and transposition in the time domain of the Rouard's sample model to fit with the FMCW model of Equations III.13 and III.14.

In fine, bridging with the sample model, γ_p, defined through Equation IV.6, the simulated transfer function, related to a multi-layer stratified sample should be described as :

$$\mathrm{H}_s(t) = \gamma_p\big(\omega = -2\pi(f_{min} + \frac{\mathrm{BW}}{\mathrm{T}_s} t)\big). \tag{IV.9}$$

Following Equation IV.6, one can consider three parameters that are going to impact such a complex transfer function. The layer thickness, d_i, as well as the dielectric proprieties of the considered material, with its refractive index, n_i, and extinction coefficient, κ_i, should then be investigated.

Inverse electromagnetic problem

Knowing both an expression of the analytical function, $\mathrm{H}_s(t)$, and the measured transfer function, $\mathrm{H}_m(t)$, one can aim to extract the intrinsic properties of the sample by applying an IEP.

Accounting for the complex character of the two considered transfer functions, a minimization of the difference between the experimental and analytical data for both the amplitude and the phase should be performed. However, a direct assessment of the zeros of the complex function $\mathrm{H}_s(t) - \mathrm{H}_m(t)$ would lead to an infinite number of solutions due to the 2π modulo character of their respective phase. For TDS inspections, a variety of work [31, 40, 45, 46] demonstrated the suitability of the introduction of an objective function that can be transposed as follows :

$$\Lambda(t) = \delta\rho(t)^2 + \zeta\delta\phi(t)^2, \tag{IV.10}$$

with $\delta\rho(t)$ and $\delta\phi(t)$ the amplitude and phase relative penalties defined in Equations IV.11 and IV.12, and ζ an optional regularization parameter.

$$\delta\rho(t) = ln(|\mathrm{H}_s(t)|) - ln(|\mathrm{H}_m(t)|), \tag{IV.11}$$

$$\delta\phi(t) = arg(\mathrm{H}_s(t)) - arg(\mathrm{H}_m(t)). \tag{IV.12}$$

Due to the higher incertitude on the signal phase, introduced by the low sample position reliability in reflection configuration, the logarithmic amplitude ratio is especially suitable as it is more penalizing. Additionally, $\delta\phi(t)$, should account for the 2π modulo aspect of the transfer function.

Knowing that $\mathrm{H}_s(t)$ depends on the set of bounded parameter n_i, κ_i, d_i with i$\in$[1, p], a vectorial space of dimension $3 \times p$ would then consider the whole set of conceivable combinations, accounting for every layers. For numerical considerations, the size of each dimension,is related to its boundaries and numerical increments, such that $n_i \in [n_i^{min}, n_i^{max}]$, $\kappa_i \in [\kappa_i^{min}, \kappa_i^{max}]$, $d_i \in [d_i^{min}, d_i^{max}]$ with respective numerical increments Δn_i, $\Delta\kappa_i$, Δd_i for each layer i$\in$[1, p].

The injection of those parameters in the analytical transfer function expression, $\mathrm{H}_s(t)$, will then allow to assess the temporal objective function. Nevertheless, one can consider that the dielectric parameters can be considered as non-dispersive along the sweep bandwidth, hence, along a full sweep time. Obviously, the layer's thicknesses do not exhibit any frequency dependency either. *In fine*, a global objective function can be obtained thought a time integration as follows :

$$\Lambda = \int_0^{\mathrm{T}_s} \Lambda(t)\,dt = \int_0^{\mathrm{T}_s} \delta\rho(t)^2 + \zeta\delta\phi(t)^2\,dt. \tag{IV.13}$$

From there, the minimal value taken by Λ, should lead to the solution of the conducted IEP.

Objective function minimization approaches

To perform this minimum assessment, one can nevertheless distinguish several main different approaches [47]. In the following, a few methods are succinctly introduced along with their advantages and main drawbacks.

- Full-volume test

As the most intuitive option, a full-volume test successively considers the objective function for all possible parameters combinations allowed in the $3 \times p$ dimension space. The method is then expected to converge to the physical solution as the one to return the minimal objective function. This direct mode of computation makes it extremely adequate to computational parallelization.

However, it is of interest to note that the combinations to be tested can scale up dramatically as the number of layers grows. The process can then become extremely cumbersome and tedious to a point that it would not be able to return the physical parameter set in a decent period of time. This process nevertheless remains extremely adequate for single layer samples as it convergence is guaranteed by the consideration of each possibility.

- Dynamic stochastic assessment

In comparison to the previous method, the stochastic process relies on the random selection of different combinations of parameters that are subsequently injected into the objective function. The goal is then to reach a suitable candidate in a lower number of tests with respect to the prior method.

The best parameter set can then be chosen as the one returning the smallest objective function after a given number of tries, or as the first one to reach a correlation error threshold, considered then as satisfactory, hence interrupting the algorithm. Through those two random selection processes, the convergence toward a viable solution, or in an adequate computing time, remains erratic and unpredictable. This mode of operation nevertheless find itself useful for a coarse assessment IEP, when large numbers of parameters are at stake.

- Incremental descending gradient and Newtonian methods

With respect to the two previous approaches, instead of only pinpointing a parameter set at each try, the descending gradient and Newtonian methods [48] will explore the vicinity of an initial parameter set by assessing the gradient and curvature of the objective function. It will then iteratively converge toward a set of lesser error. In the case of a convex object function space, the convergence is guaranteed toward the physical solution. Nevertheless, with the introductions of local minima, this guarantee fades away as the convergence of the descent might come to a stop to one of those non-physical solutions. Pairing this process with a repeated stochastic selection of the initial parameter set will allow to optimize the chances to reach the global minimum, hence the physical solution. The amount of initial candidates to consider should nevertheless be much lower than for a fixed stochastic assessment as each tentative should converge toward a minima, local or global. However, the required gradient and Hessian estimation requires larger computation resources than the sole transfer function assessment.

- Genetic inspired selective algorithm

As an exploratory approach, the genetic minimization algorithm [47, 49, 50] relies on the improvement of a population of parameter set, following natural selection rules along a given number of generations. An initial population is formed according to a stochastic selection process as to cover the full parameter space. Each member of this population will be attributed a genetic code relative to its parameter set. A natural selection process then occurs as to eliminate the unfit candidates, hence candidates with too high objective function values. With a given probability, a

breeding between fit parents can then occur as to generate several children. This breeding process should lead to an improvement of the objective function for the subsequent generation, hence, in favor of the convergence of the algorithm. In parallel, following a given probability, mutations can as well be considered, as to ensure an exploration of the parameters space. Additionally, to allow for a stable population emerging from the previous steps, a stochastic population reinforcement is performed. This point will as well ensure a random exploration. A subsequent natural selection process can then occur and lead to the consecutive generation. Along all the generations, the best population member will then be considered as the IEP solution.

With respect to the previous method, a larger number of tunable selection criterion are available to optimize the convergence of the algorithm. Namely, the mutation and breeding probabilities, as well as the natural selection threshold, should lead to either a convergence oriented approach or an exploratory assessment. The population size can as well be scaled to suite the parameter space. The number of generations to consider could be either fixed beforehand or an interruption can occur upon achievement of a correlation threshold. And finally, the breeding genetic code handling is also expected to drastically impact the convergence of this method.

Nevertheless, once again, the embedded stochastic approach does not ensure the convergence toward the physical solution.

IV.4.4 Single layer proprieties extractions

Full volume extraction

When considering single layer samples, the use of the full-volume test remains feasible as the parameter set will only feature 3 dimensions, namely, d, n and κ. With a prior knowledge of the raw parameters ranges, the amount of combinations then remains bounded to practicable quantities for such types of minimization methods, and should lead to the physical solution.

As an adequate initial target, the previously investigated 7.5 mm Plexiglas plate is considered. Its relatively large optical thickness allows for a proper definition of the two interfaces, ideal to question the reliability of the algorithm, before considering more challenging geometries. For this specific IEP, the minimization procedure has been specified as follows:

$$min_{n,\kappa,d} \quad \Lambda, \qquad subject\ to: \begin{cases} \zeta = 1 \\ n = [1.45, ..., 1.7], \quad \Delta_n = 1.25e^{-4} \\ \kappa = [0, ..., 2e^{-3}], \quad \Delta_\kappa = 1e^{-4} \\ d = [7, ..., 7.8]\ mm, \quad \Delta_d = 4\,\mu m \end{cases} \tag{IV.14}$$

Numerically, the single-layer full volume algorithm subsequently tests each considered thickness, d, for which it finds the optimal complex index couple $\tilde{n} = n - i\kappa$, hence the one minimizing Λ according to Equation IV.13. The evolution of the extraction minimal objective function with respect to the sample thickness is represented in Figure IV.14, and is calculated as the value of Λ for the optimal extracted $\tilde{n}$ at the given thickness. This figure highlights the convex shape of the chosen objective criterion along the thickness dimension. The subtle wobbling of this quadratic function is ties to the finite numerical resolution of n and κ. Subsequently, the thickness minimizing this projection is selected by the algorithm as the IEP solution, hence leading to the n, κ, d physical solution triplet, denoted by the arrow on Figure IV.14. A finer numerical pitch for the refractive

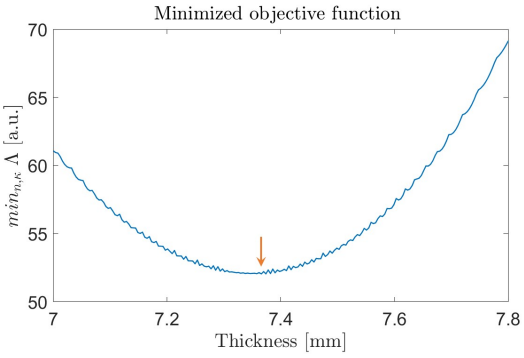

Figure IV.14: Evolution of the objective function at the optimal complex index with respect to the layer thickness.

index parameters smooths this curve, hence minimizing the chances to converge toward an ill-defined local minimum. Namely, a thickness of 7.397 mm, is reported by the algorithm, leading to a refractive index of $\tilde{n}_{Plexiglas} = 1.595 - i8e^{-4}$. For comparative purposes, a mechanical caliper assessment of the thickness lead to a value of 7.42 mm with an imprecision above 10 microns. A TDS evaluation of the refractive index of this sample, as well as literature work [51], corroborated the extracted value, without allowing enhanced precision due to the quite limited sensitivity at 150 GHz.

Along with the measurement transfer function, $H_m(t)$, the resulting optimum temporal transfer function, $H_s(t)$, that emerges from the Rouard model based IEP, is displayed in Figure IV.15a. On this depiction, several pragmatic aspects have to be highlighted. Such a representation is fully equivalent to the ones previously given in III.22 as they assess the exact same quantity, the temporal normalized beating signal, since $H_m(t) = \frac{\widehat{S}_{samp}(t)}{1}$. Nevertheless, an amplitude-phase display is chosen to corroborate the objective function definition, based on distinct amplitude and phase penalty functions, $\delta\rho(t)$ and $\delta\phi(t)$ respectively. As one can notice, to avoid any phase jump incoherences between the measurement and sample Rouard's model, the wrapped [-π, π[phase is considered for the assessment of $\delta\phi(t)$. A subtle continuous phase difference remains noticeable, as an reminiscence of the imperfect phase correction on the sample measurement, impacted by its noise level. Additionally, due to the low power available at the extremities of the sweep spectrum, hence leading to higher uncertainties through the normalization procedure, the objective function integration is actually performed on a reduced temporal window as follows:

$$\Lambda = \int_{\delta T}^{T_s - \delta T} \delta\rho(t)^2 + \zeta\delta\phi(t)^2 dt. \tag{IV.15}$$

with δT the time window limitation [s], in the typical order of $\delta T = 0.02\ T_s$. This cropping leads to a slight effective longitudinal resolution lessening.

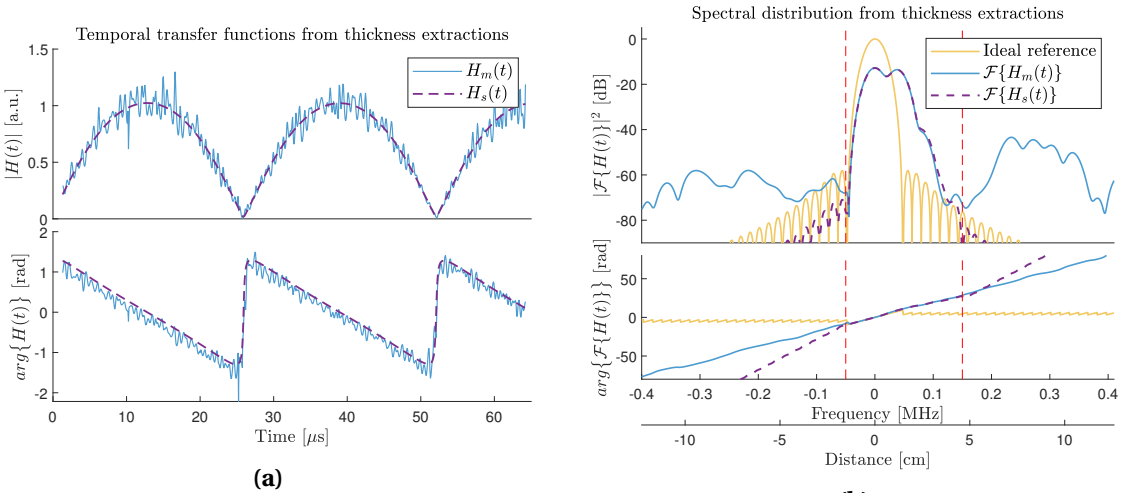

Figure IV.15: **(a)** Temporal complex representation of the considered transfer functions. **(b)** Relative frequency domain representation showing the proper correlation between the measured and optimal simulated transfer functions.

Considering this optimized configuration emerging from a time related IEP, these simulated and recorded signals can hence be transposed to the frequency domain for FMCW distance related visualization purposes. Those representations are displayed in Figure IV.15b.

As one can notice, even in a logarithmic visualization, the correlation between the two amplitude spectrum corroborates the proper convergence of the IEP full volume algorithm. Additionally, when it comes to the complex argument of the signals, the phase information becomes totally irrelevant beyond the frequency range where the amplitude remains non-negligible. This hence leads to a pertinent phase range limited to the [- 0.05, 0.15] MHz reduced beating frequency span,

delimited through the two dashed lines. A fit between the model and measurement in this range supports the validity of the solution.

Within the main frequency window, a slight divergence can nevertheless be observed on the amplitude trace of the Fabry-Perot echo situated at 0.08 MHz. The measurement, $\mathscr{F}\{H_m(t)\}$ features a subtly lower amplitude with respect to the model tranfer function, $\mathscr{F}\{H_s(t)\}$. This is induced by the limited sensing depth of field related to the focused sensing scheme. Indeed, the Rouard model does not integrate beam shaping considerations, hence, a unitary back-coupling is expected. In the far-field sensing scheme, every interface of the sample is then required to be within the Rayleigh range, as to avoid unconsidered power losses for each contribution. On main contribution peaks, such subsequent power losses, could lead to an over evaluation of κ for the material as well as an under evaluation of the refractive index, hence leading to a wrong estimate of the thickness. An amplitude correction profile, with respect to the optical geometry could be implemented to address this limitation to overcome the altered back coupling beyond the depth of field. This issue becomes non-negligible when considering optically thick samples with respect to the Rayleigh range, hence, physically thick samples or samples displaying a high refractive index.

Additionally, one could point out the significant signal level in the [- 0.25, 0.35] MHz reduced frequency range. This results as well from a Fabry-Perot cavity between the focalization optic interface and the sample. Indeed, as a non-existing contribution at the recording of the background and reference normalization signals, the background removal step then does not account for such ghosting artifact. This contribution can as well be witnessed on the temporal beating signal display, as the high frequency noisy component supplemented to the main modulation. To mitigate the impact of such non negligible parasitic contributions in the convergence of the IEP algorithm, a prior selective spectral band pass filtering step is applied. It will ensure a proper suppression of unwanted Fabry-Perot contributions and an additional reduction of the global noise level. Typical steep cut-off frequencies around -0.1 MHz and 0.20 MHz can be chosen and tuned in accordance with the sample geometry and optical configuration. This step will then dampen the influence of those unwanted contributions in the assessment of the objective function, while impacting as little as possible the sample relates frequency contributions.

Thickness mapping and performances assessment

From the prior punctual sensing approach, a raster scan of the sample, once again, leads to the collection of a full longitudinal assessment of its structure.

Beside simple mapping purposes, the examination of specific samples allows for deepened capabilities appraisal for the IEP convergence. Namely, two polymer thickness charts have been considered for such evaluations and are pictured in Figure IV.16. With mechanical thicknesses ranging from 1 cm down to 1 mm, those two test designs allow for a coverage of the thickness range of interest. Namely, it features steps above the effective longitudinal resolution of the FMCW unit of 4.6 mm, as well as below this resolution limit. They nevertheless display slightly different dielectric proprieties due to their different polymeric constitutions. Hence a prior assessment of the dielectric constants of the sample, through subsequent full-volume FMCW IEP on different portions of various thickness led to $\tilde{n}_{\mathrm{HDPE}} = 1.523 - i1e^{-3}$ and $\tilde{n}_{\mathrm{POM_c}} = 1.672 - i0.120$, respectively for the spiral shaped

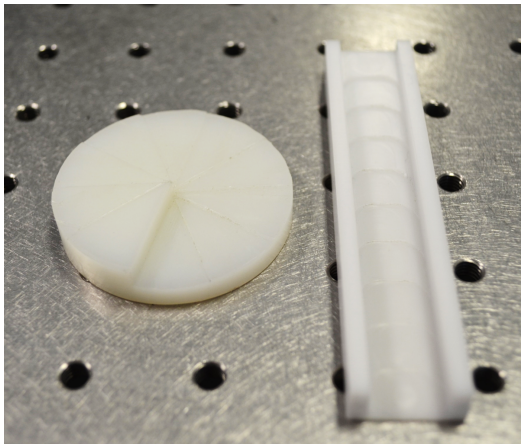

Figure IV.16: Photograph of the two considered thickness charts for mapping and performances assessment.

HDPE sample and the longitudinal Polyoxymethylene copolymer (POM_c) step charts. A corroboration of those extractions have been collected through existing literature [51, 52] and TDS conducted investigations.

As to ensure an adequate processing time for the thickness mapping extraction, from such pre-characterizations, an IEP reduction can hence be considered. Indeed, such a prior evaluation of the sample dielectric parameters allows for the consideration of an uni-dimensional IEP, with only the layer thickness to be considered in the objective function minimization process. It then drastically reduces the computation time for a full-volume assessment. With respect to the subsequent layer thicknesses, detailed in the first column of Table IV.1,the numerical ranges have been defined as $d_{\mathrm{HDPE}} = [4.5, ..., 10.5]$ mm, $\Delta_d = 3$ µm and $d_{\mathrm{POMc}} = [1, ..., 5.5]$ mm, $\Delta_d = 2.25$ µm, to ensure an adequate numerical resolution for each sample. The evaluation of the individual thicknesses for each step was performed using a mechanical micrometer caliper through a repeatability approach. Namely, 10 distinct probing have been performed on each step of the samples as to assess the average thickness, d_m, in column 1 of Table IV.1, as well as the mechanical measurement Standard Deviation (SD), σ_{SD_m}, in column 2 of Table IV.1. On the first helicoidal step sample, on average, a 46 µm SD is witnesses, highly impacted by the mechanical manufacturing process surface imperfections. The better surface quality on the second longitudinal sample is easily witnessed through the mechanical measurement standard deviations with an averaged SD of 28 µm. Additionally, the mechanical imprecision of the caliper would range over 10 µm, due to the limited reliability level of the micrometric screw tightening on the sample.

On the integration side, the optical configuration is also of interest to ensure the adequacy between the Rayleigh range and the characteristic thickness. A f/2 optical configuration with a 2" diameter f'= 100 mm focalization lens brought consistent results up to the highest sample thickness. A lateral resolution of roughly 4 mm is then expected. Additionally, a careful alignment of the sample is required such that the first interface coincides with the reference plane at the beam waist, as to avoid the addition of a corrective phase term in the IEP extraction process. Nevertheless, a $\zeta = 0.01$ regulation parameter is considered as to mitigate the reminiscent additional phase error impacted by the imperfect positioning and alignment.

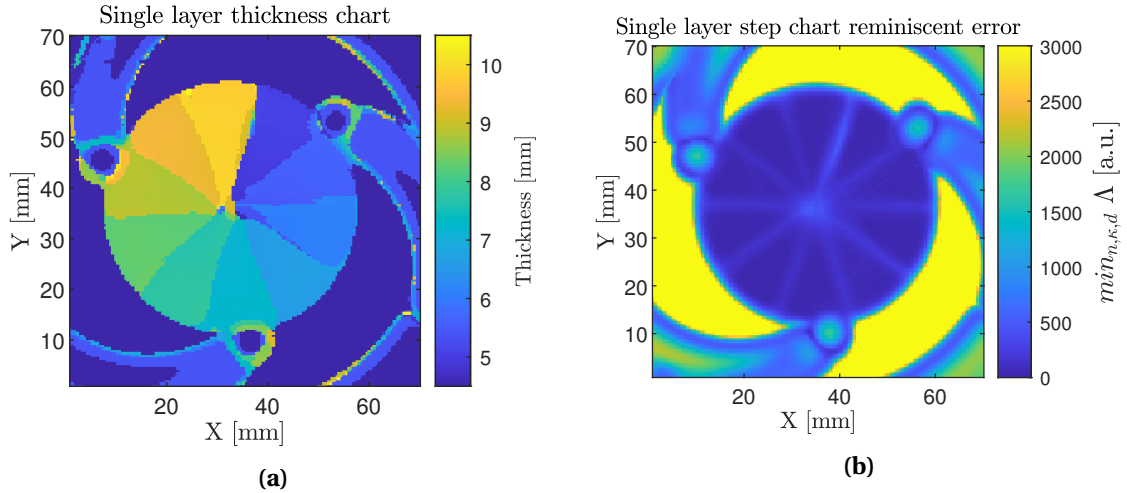

(a) **(b)**

Figure IV.17: **(a)** Extracted thickness map for the spiral step chart sample and **(b)** relative mapping of the reminiscent objective criteria error $min_{n,\kappa,d}\ \Lambda$.

From such parametrization, the resulting extracted thickness map is displayed in Figure IV.17a for the HDPE helicoidal step chart. In this image, a threshold below 5 mm allow for a saturation of the insignificant scan sections, with a sole appeal on the sample ROI. Indeed, in the scanning areas, external to the sample, the algorithm will have a tendency to converge toward a thickness extremum, 4.5 mm millimeter, in this case. Irrelevant thickness extractions are still noticeable on the three metallic holder arms, but remain tied to high optimal objective function values, hence, discriminated as inappropriate. For each step, the mean thickness is as well assessed on a central

3 mm × 3 mm ROI and detailed in column 3 of Table IV.1. The size of this investigated area is tied to regions of proper convergence of the algorithm, in the center of each step.

Figure IV.17b emerges from the consideration of the optimal objective function at each pixel, hence reminiscent error, $min_{n,\kappa,d}\ \Lambda$, represented by an arrow in Figure IV.14, at the optium n, κ, d triplet value. A saturated color-scale is featured as to discard unnecessary sections and allow a visual assessment of the algorithmic convergence. Specifically, reminiscent error levels, on the three sample holder arms disclose the irrelevance of the extraction in those regions. More accurately, the 4 mm lateral resolution induces some extraction uncertainty when a non-strictly mono-layer signal is recorded. Namely, along the segment ridges or at the sample edges as depicted in Figure IV.17b, when the radar signal features a combination of two geometries, it displays an increase in the IEP minimized objective function criteria, $min_{n,\kappa,d}\ \Lambda$. A higher uncertainty, with respect to the well estimated central individual step sections is observed.

Similarly, over each step ROI, an estimation of the standard deviation, $\sigma_{SD_{FMCW}}$, is as well performed and displays much lower values with respect to the mechanical estimation, as detailed in column 4 of Table IV.1. This lower SD level can be explained by the low lateral resolution of the FMCW probing beam, leading to a smoothing of all the surface imperfections that can be witnessed mechanically. It also enlightens the stable convergence of the algorithm as well as the high homogeneity of the sample material.

Table IV.1: Thickness extraction.

Thickness spiral step chart HDPE : $\tilde{n}_{HDPE} = 1.523 - i1e^{-3}$				
Palmer thickness d_m [µm]	SD palmer σ_m [µm]	FMCW thickness d_{FMCW} [µm]	SD FMCW σ_{FMCW} [µm]	Relative error δ [%]
9930	11	9920	9	0.105
9486	57	9475	10	0.114
8932	49	8909	10	0.253
8378	58	8372	8	0.064
7849	58	7835	10	0.179
7293	64	7268	12	0.35
6705	36	6707	4	-0.039
6167	41	6164	4	0.062
5641	48	5657	11	-0.28
5132	38	5108	13	0.46
Thickness longitudinal step chart POMc : $\tilde{n}_{POMc} = 1.672 - i0.120$				
Palmer thickness d_m [µm]	SD palmer σ_m [µm]	FMCW thickness d_{FMCW} [µm]	SD FMCW σ_{FMCW} [µm]	Relative error δ [%]
5496	33	5500	$3e^{-12}$	-0.08
4585	36	5491	6	-0.138
3787	31	3778	8	0.246
3097	56	3081	4	0.507
2519	44	2526	1	-0.254
2048	32	2044	4	0.189
1677	5	1745	179	-4.1
1375	7	1381	3	-0.411
1186	9	1185	3	0.027

Lastly, the consideration of the estimation relative error, δ, defined through Equation IV.16 should highlight the accuracy of the extraction method as well as the thinner attainable thickness

measurement.

$$\delta = \frac{d_m - d_{\text{FMCW}}}{d_m}, \tag{IV.16}$$

with d_m the reference mechanically extracted thickness [µm], and d_{FMCW} the FMCW IEP extracted thickness [µm]. As detailed in column 5 of Table IV.1 a relative error of below 1 % is achieved on every single step measurement from 1 cm down to 1.2 mm, hence optically below the theoretically bandwidth limited resolution limit of 4.6 mm.

An exception can be observed with the 1.7 mm step where the minimization algorithm did not return a coherent and stable value. Indeed, the returned SD, σ_{FMCW}, is several orders of magnitude higher than the surrounding values. The relative error was then expected to be way over the effective FMCW IEP extraction performances on this specific step. This flawed convergence was induced by the appearance of a phase jump at the temporal extremity of the temporal transfer function, leading to a strong uncertainty on the estimation of $\delta\phi(t)$.

In fine, on the helicoidal step sample, a global average error of 13.5 µm is witnesses on the individual extraction of the step thicknesses and subtly rises to 14.5 microns for the second linear step chart, both in the range of the mechanical assessement imprecision of 10 µm.

With no significant measurement capability losses below 2 mm thick mono-layer samples, a pursue of the minimal resolvable thickness through the FMCW IPE algorithm is currently under investigation with the use of thickness calibration standards as to avoid mechanical measurement uncertainties. Namely, grade 1 ceramics Zirconium dioxide thickness standards are used. Nevertheless, the crystalline structure and high density of such a material lead to a large refractive index, primarily extracted through the FMCW IEP at $\tilde{n}_{ZrO_2} = 5.78 - i7e^{-3}$, and corroborated by TDS measurements. Such a large refractive index hence leads to a preponderance of the Fabry-Perot echoes and the considerations of larger optical thicknesses for a given mechanical dimension. Further efforts focuses on the consideration of those problematics, highly tied to the limited sensing depth of field, and the subsequent consideration of much thinner samples for polymer based layers beyond the millimeter optical thickness, hence well below the 4.6 mm theoretical radar longitudinal resolution.

Little work has yet been witnessed toward thickness extraction below the resolution limit using FMCW sensors, or even on the elucidation of advanced thickness extraction algorithms. Beside simulated and measurement correlation approaches based on highly simplified sample models only considering main interface frequency contributions [15, 16, 53], no further development have been tackled to the best of our knowledge.

Nevertheless, through such streamlined processes, sample estimation down to 770 µm have been considered using a 100 GHz 40 GHz BW radar transceiver [16]. In each of those work, at the expense of performances assessments, a focus on the multi-layer capabilities of such systems was preferred but still quite succinctly detailed.

IV.4.5 Multi-layers generalization

A consideration of multi-layered stratified structures has naturally been employed as an extension of the single-layer IEP approach. Indeed, as a highly scalable problem, injecting several layer in the iterative Rouard's model will give access to a physically representative complex transfer function, $\mathrm{H}_s(t) = \gamma_p\left(\omega = -2\pi(f_{min} + \frac{\mathrm{BW}}{\mathrm{T}_s}t)\right)$, hence incorporating each main interface contribution and Fabry-Perot echoes.

This transfer function will now be subject to the thickness and dielectric proprieties of each individual layer material. Hence, ranging from a 3 dimensional parameter space for the mono-layer sensing, a 3 × p dimensions parameter space has to then be assessed through the previously described IEP. Unless with extremely reduced parameter ranges to be tested, or with low numerical parameter resolutions to reach small length dimensions, a full-volume inspection remains impracticable.

The descending gradient approach has then been implemented as an iterative minimization method. A stochastic selection of the starting parameter set is followed by a gradient estimation

at this point. A straight objective function descent is then initiated in the optimal gradient direction until a local minimum is reached or along a given number of descent steps. The reach of this specific point is depicted through red markers in Figure IV.18. A subsequent optimum gradient direction estimation and descent is performed, until a minimum is reached. An improvement with respect to the starting parameter is then ineluctable, as detailed in Figure IV.18. This Figure depicts such an error minimization process through the objective function evolution on an arbitrary initial parameter set. It features several gradient descent direction change at each curve derivative discontinuity point, accompanied by a vertical red marker.

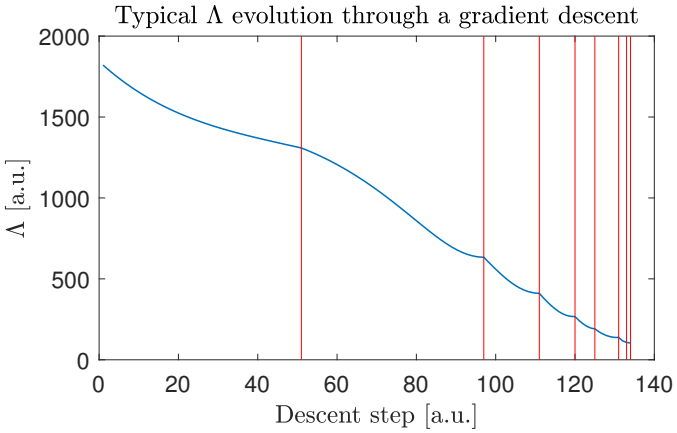

Figure IV.18: Evolution of the objective function Λ along a gradient descent for a given starting parameter set, featuring subsequent gradient direction changes, depicted through the red delimitations.

Due to the addition of numerous dimensions, the convexity of the objective function in the parameter space cannot be guaranteed. Hence, to alleviate the eventuality of converging toward a local minimum, this process is repeated for a given number of stochastic throws in the selection of the initial parameter set as to ensure the identification of the global minimum. It is worth to note that this descent can nevertheless be highly disturbed by discontinuities in the objective function due to the appearance of temporal phase jumps.

As a representative sample, a 3-layered stack has been considered with a Plexiglas-Air-Plexiglas structure. The two Plexiglas plates thicknesses have been mechanically extracted with a caliper and displayed a thickness of 4.43 mm respectively. A 2.8 mm ring spacer was used as to assess a layer thickness below the longitudinal resolution of the radar. A measurement accuracy below 10 µm has to be considered on those estimations due to the mechanical measurement approach.

In order to once again reduce the IEP problem to a 3 dimensional minimization process, the dielectric parameters of the Plexiglas material is fixed to the previously investigated $\tilde{n}_{Plexiglas} = 1.595 - i8e^{-4}$. Hence, evolving from a 9 dimension minimization process subject to $(d_i,\ n_i,\ \kappa_i)$ with $i \in [1,2,3]$, the mathematical formulation can be posed as :

$$min_{d_1,\,d_2,\,d_3} \quad \Lambda, \qquad subject\ to : \begin{cases} \zeta = 0.01 \\ \tilde{n}_1 = \tilde{n}_3 = \tilde{n}_{Plexiglas} \\ \tilde{n}_2 = \tilde{n}_{air} = 1 \\ d_1\ and\ d_3 \in [3.5,\ 5.5]\ mm \\ d_2 \in [2,\ 3]\ mm \end{cases} \tag{IV.17}$$

Coarsely, a total of 1000 throw is usually implemented for such a 3-dimensional problem with an average of 50 descent steps for each throw. Hence, it leads to a total of 50 000 objective function calculation operations, to be compared to the $1e^9$ operations that would be required for a full volume assessment of a typical $1000 \times 1000 \times 1000$ parameter space. Such parametrization gave rise to a high global minimum identification rate. Nevertheless, due to the initial stochastic selection process, the appraisal of the physical IEP solution global minimum remains uncertain.

The optimum simulated temporal beating transfer function, $H_s(t)$, along with the measurement transfer function $H_m(t)$ are displayed in Figure IV.19a as to highlight the suitable aspect of the amplitude and phase objective function.

As one can notice, the selective filtering step smooths the temporal transfer function by removing the frequency contributions that are not directly tied to the sample. Namely, a [-0.2, 0.2] MHz

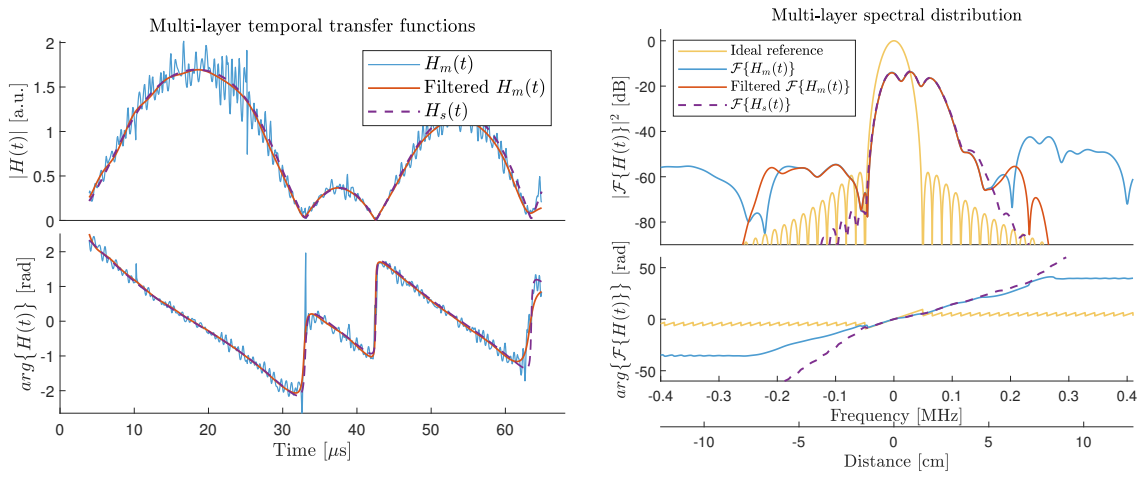

Figure IV.19: **(a)** Temporal complex representation of the considered transfer functions for a multi-layered sample, and **(b)** relative frequency domain representation showing the proper correlation between the measured and optimal simulated transfer functions.

band pass filter allows for the efficient removal of the unwanted Fabry Perrot echoes induced by the optical components, witnessed above 0.2 MHz. The considered phase also remains bounded to the [-π, π[interval as to avoid the 2π modulo aspect of such complex transfer functions that could impact the objective function minimization. A time window reduction is as well performed once again to remove the uncertain low sensing power extremities of the normalized beating signals.

Table IV.2: Thickness extraction in multi-layer configuration.

Layer	Palmer thickness d_m [µm]	FMCW thickness d_{FMCW} [µm]	Relative error δ δ [%]
d_1	4430 ± 10	4419	0.25 ± 0.31
d_2	2800 ± 10	2844	-1.57 ± 0.50
d_3	4430 ± 10	4423	0.16 ± 0.31

The extracted thicknesses, d_{FMCW} [µm], for a given stochastic gradient evaluation are given in Table IV.2 as to be compared with the mechanically estimated parameters, d_m [µm]. The error witnessed on the plexiglass layers remains in the range of the mechanical measurement uncertainty. A relative error maxing at 1.5 % for the air gap can nevertheless be witnessed and is tied to the absence of tightening structure to ensure a contact between the Plexiglas plates and the spacer ring, hence a slight over-evaluation of the air gap.

The spectral transposition, displayed in Figure IV.19b features 3 main, correctly estimated, interface contributions as the air layer thickness remains below the longitudinal resolution power of the FMCW unit. The second main amplitude contribution then relates to the unresolved central Plexiglas-air and air-Plexiglas interfaces, 2.8 mm appart. Once again, the coherency of the phase in the frequency domain between the measurement and the simulated transfer function, is only ensured on the [-0.05, 0.15] MHz reduced frequency range, where non-negligible amplitude levels are witnessed. Additionally, due to the thick nature of the sample, the adequacy of the optical setup should once more be ensured. The final Fabry-Perot echo, witnessed at the frequency 0.13 MHz, displays a slight over-estimation of its amplitude due to the non-consideration for the limited Rayleigh range in such a configuration.

Following this proof of work with suitable and standard layers, on an optimized Plexiglas-air-Plexiglas contrasted configuration, subsequent advanced investigations are part of the ongoing

explorations. Namely, the consideration of different material proprieties combinations, to assess the sensitivity to more subtle refractive index changes, or the examination of drastically different thickness ranges are part of the current prospective work. The assessment of minimal thicknesses represents as well a preponderant element of interest as to draw the limitations of such an inspection method.

As an already discussed alternative view, to the usual amplitude representation of Figure IV.19b, the distance related real-part and imaginary-part representation offers a visual tool to corroborate the convergence of the IEP minimization process. It could as well be used for the implementation of a correlation threshold as to speed-up the stochastic descending gradient operation. Through the convoluted sample signals, it also perfectly emphasis the parallel between the TDS approach and the FMCW IEP extraction process, of course providing a proper variable re-scaling such that $\omega = -2\pi(f_{min} + \frac{BW}{T_s} t)$. Such approach should then enable the investigation of layered stacks with thicknesses ranging down to sub-millimeter levels from a 4.6 mm longitudinal intrinsic resolution.

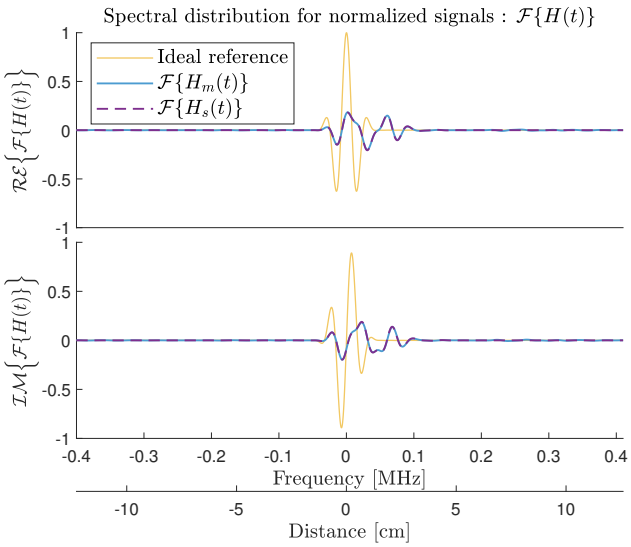

Figure IV.20: Spectral real-part and imaginary-part depiction of the optimum extracted signals on a multi-layered stack.

IV.5 Conclusion

In the wake of the development of the 150 GHz transceiver, detailed in Chapter III, this Chapter, *FMCW Proof of Principle and Targeted Implementations*, focused on the assessment of specific application oriented issues. As a central motivation for this work, contactless Non-Destructive Testing and inspection have been considered as to affirm the FMCW effectiveness toward explicit problematics in broad application fields.

Capitalizing on the longitudinal sensing capability of the FMCW transceiver, as a drastic advantage over conventional CW approaches, volumetric inspection has been intended as a center of interest for this development. The implementation of a standard focused beam scanning integration, featuring the newly developed transceiver, ensured a total versatility for the investigation of a variety of sample geometries, as to conduct feasibility studies. The high intrinsic measurement rate additionally allowed for practicable inspection times, still strongly limited by the mechanical scanning unit. Namely, a non-exhaustive selection of samples of interest, with targeted structural characteristics, has been outlined. Providing proper visualization dispositions, mainly tied to the longitudinal dimension, the specific features of interest have been successfully assessed. Notably, two study cases have been considered as proof of work, with, at first, the examination of joint bondings on polymer parts, and subsequently, a focus on pharmaceutical packaging monitoring.

The results of preliminary case studies on generic available FMCW transceivers have also been detailed. Pinpointing a particular issue, the intrinsic longitudinal sensing capability can be put to good use for see-through thematics. Namely, it demonstrated a specific adequacy for health monitoring through glass-fiber interior plane covers, using a 100 GHz transceiver as to minimize material losses. Additionally, as an alternative way to assess remote-sensing applications, the feasibility for simplified guided FMCW transceivers have been explored in this section as well. Namely, a high performance III/V FMCW radar unit was integrated with a flexible polymer wave guide in a compact and minimalist configuration. The complexity of the coupling and propagation principle

required electromagnetic simulations that corroborated the recorded imaging results. Beside end of guide inspection, the low confinement of the field distribution brought up the sensing capability along the wave-guide vicinity. The addition of an end-of-guide solid immersion lens brought a drastic longitudinal resolution improvement down to 2 mm, working at 100 GHz. A low-cost oriented development led to the use of a compact 122 GHz FMCW Silicon radar unit for the integration of such a simplified guided transceiver and displayed encouraging measurement and simulations results with a lateral resolutions down to 1.4 mm.

Beside the unequivocal performances of FMCW radars for volumetric imaging and contactless flaws inspection, on a multitude of adequate materials, this range-sensitive homodyne detection scheme has been profitably employed for stratified sample thicknesses evaluation.

In contrast with the current approaches, a deepened consideration of the similarities with TDS stratified structures inspection is performed to orient and corroborate the main algorithmic extraction procedures. With the employment of drastically different technological approaches, necessary adjustments are nevertheless required and have been justified throughout this dedicated section. Up until now, the spars work performed on this topic relied on the investigation of simplified layered sample models, coupled to correlation-based extraction procedures. In contrast, the work detailed in this chapter implements the well established Rouard's stratified model for the implementation of the retrieval Inverse Electromagnetic Problem. An initial approach on a full-volume extraction for mono-layer samples featured favorable results. Namely, thicknesses well below the intrinsic longitudinal resolution of the radar are accurately evaluated down to 1.2 mm on polymer samples.

The implementation and bridging of the physical Rouard model additionally allows for a simplified scaling up for the consideration of multi-layered sample. With the investigation of such complexified structures, additional optimal model parameters have then been retrieved on a three-layered sample through dedicated IEP minimization procedures, such as the descending gradient method.

IV.6 Bibliography

[1] https://cordis.europa.eu/docs/results/266320/final1-final-report-dotnac.pdf. 144

[2] A. Chopard, J. Bou Sleiman, Q. Cassar, J.P. Guillet, M. Pan, J.B. Perraud, A. Susset, and P. Mounaix. Terahertz waves for contactless control and imaging in aeronautics industry. *NDT E International*, page 102473, 2021. 149

[3] Adrien Chopard, Joyce Sleiman, Q Cassar, P Fauché, J Guillet, Patrick Mounaix, Perraud Jean-Baptiste, and A Susset. Millimeter waves radar: A way to see through the airplane covering? In *11 symposium international: NDT in Aerospace*, 2019. 149

[4] Georges Humbert. *Optical Fibers in Terahertz Domain*, pages 1–49. Springer Singapore, Singapore, 2019. 150

[5] Mingming Pan, Quentin Cassar, Frédéric Fauquet, Georges Humbert, Patrick Mounaix, and Jean-Paul Guillet. Guided terahertz pulse reflectometry with double photoconductive antenna. *Appl. Opt.*, 59(6):1641–1647, Feb 2020. 150, 151

[6] Mingming Pan. *Terahertz wave-guided reflectometry system*. PhD thesis, Université de Bordeaux, 2020. 150

[7] Yuan Gao and Reza Zoughi. Millimeter wave reflectometry and imaging for noninvasive diagnosis of skin burn injuries. *IEEE Transactions on Instrumentation and Measurement*, 66(1):77–84, 2017. 150

[8] Borwen You and Ja-Yu Lu. Remote and in situ sensing products in chemical reaction using a flexible terahertz pipe waveguide. *Optics express*, 24(16):18013–18023, 2016.

[9] J-P Guillet, L Chusseau, R Adam, T Grosjean, A Penarier, F Baida, and D Charraut. Continuous-wave scanning terahertz near-field microscope. *Microwave and Optical Technology Letters*, 53(3):580–582, 2011.

[10] Pallavi Doradla, Karim Alavi, Cecil S Joseph, and Robert H Giles. Flexible waveguide enabled single-channel terahertz endoscopic system. In *Terahertz, RF, Millimeter, and Submillimeter-Wave Technology and Applications VIII*, volume 9362, page 93620D. International Society for Optics and Photonics, 2015. 150

[11] Mingming Pan, Adrien Chopard, Frederic Fauquet, Patrick Mounaix, and Jean-Paul Guillet. Guided reflectometry imaging unit using millimeter wave fmcw radars. *IEEE Transactions on Terahertz Science and Technology*, 10(6):647–655, 2020. 151, 153

[12] Mario Pauli, Benjamin Göttel, Steffen Scherr, Akanksha Bhutani, Serdal Ayhan, Wolfgang Winkler, and Thomas Zwick. Miniaturized millimeter-wave radar sensor for high-accuracy applications. *IEEE Transactions on Microwave Theory and Techniques*, 65(5):1707–1715, 2017. 151

[13] Chih-Hsien Lai, Yu-Chun Hsueh, Hung-Wen Chen, Yuh-jing Huang, Hung-chun Chang, and Chi-Kuang Sun. Low-index terahertz pipe waveguides. *Optics letters*, 34(21):3457–3459, 2009. 151

[14] Chih-Hsien Lai, Borwen You, Ja-Yu Lu, Tze-An Liu, Jin-Long Peng, Chi-Kuang Sun, and Hung-Chun Chang. Modal characteristics of antiresonant reflecting pipe waveguides for terahertz waveguiding. *Optics express*, 18(1):309–322, 2010. 151

[15] Nina S Schreiner, Wolfgang Sauer-Greff, Ralph Urbansky, Georg von Freymann, and Fabian Friederich. Multilayer thickness measurements below the rayleigh limit using fmcw millimeter and terahertz waves. *Sensors*, 19(18):3910, 2019. 155, 168

[16] NS Schreiner, B Baccouche, W Sauer-Greff, R Urbansky, and F Friederich. High-resolution fmcw millimeter-wave and terahertz thickness measurements. In *2017 47th European Microwave Conference (EuMC)*, pages 1187–1190. IEEE, 2017. 168

[17] F Ellrich, M Bauer, N Schreiner, A Keil, T Pfeiffer, J Klier, S Weber, J Jonuscheit, F Friederich, and D Molter. Terahertz quality inspection for automotive and aviation industries. *Journal of Infrared, Millimeter, and Terahertz Waves*, 41(4):470–489, 2020. 155

[18] James D Taylor. *Advanced ultrawideband radar: signals, targets, and applications*. CRC press, 2016. xi, 156

[19] Liudmyla A Varianytsia-Roshchupkina, Gennadiy P Pochanin, Iryna Ye Pochanina, and Sergey A Masalov. Comparison of different antenna configurations for probing of layered media. In *2015 8th International Workshop on Advanced Ground Penetrating Radar (IWAGPR)*, pages 1–4. IEEE, 2015. xi, 156

[20] Elias Rmeili and Tom Scullion. Detecting stripping in asphalt concrete layers using ground penetrating radar. *Transportation Research Record*, 1568(1):165–174, 1997.

[21] Aleksey K Khamzin, Aleksandra V Varnavina, Evgeniy V Torgashov, Neil L Anderson, and Lesley H Sneed. Utilization of air-launched ground penetrating radar (gpr) for pavement condition assessment. *Construction and Building Materials*, 141:130–139, 2017. 156

[22] Ola Brandt, Kirsty Langley, Jack Kohler, and Svein-Erik Hamran. Detection of buried ice and sediment layers in permafrost using multi-frequency ground penetrating radar: A case examination on svalbard. *Remote Sensing of Environment*, 111(2-3):212–227, 2007. 156

[23] EE Jafarov, AD Parsekian, K Schaefer, L Liu, AC Chen, SK Panda, and T Zhang. Estimating active layer thickness and volumetric water content from ground penetrating radar measurements in barrow, alaska. *Geoscience data journal*, 4(2):72–79, 2017. 156

[24] Jean-Louis Coutaz, Frederic Garet, and Vincent P Wallace. *Principles of Terahertz time-domain spectroscopy*. CRC Press, 2018. 156

[25] Soufiene Krimi, Jens Klier, Joachim Jonuscheit, Georg von Freymann, Ralph Urbansky, and René Beigang. Highly accurate thickness measurement of multi-layered automotive paints using terahertz technology. *Applied Physics Letters*, 109(2):021105, 2016. 156, 160

[26] Andreas Frank, Deran JHC Maas, and JLM van Mechelen. Reliable in-situ thickness monitoring of multilayer paints based on thz time domain spectroscopy. In *Applied Industrial Optics: Spectroscopy, Imaging and Metrology*, pages W4A–2. Optical Society of America, 2019.

[27] Ian S Gregory, Robert K May, Philip F Taday, and Patrick Mounaix. Extending terahertz paint thickness measurements to advanced industry-standard automotive paint structures. In *2016 41st International Conference on Infrared, Millimeter, and Terahertz waves (IRMMW-THz)*, pages 1–2. IEEE, 2016. 156

[28] M Picot, H Ballacey, JP Guillet, Q Cassar, and P Mounaix. Terahertz paint thickness measurements: from lab to automotive and aeronautics industry. In *Proceedings of the 15th Asia Pacific Conference for Non-Destructive Testing (APCNDT2017), Singapore*, pages 13–17, 2017. 156

[29] Q Cassar, CL Koch-Dandolo, Jean-Paul Guillet, M Roux, F Fauquet, JB Perraud, and P Mounaix. Characterization of varnish ageing and its consequences on terahertz imagery: Demonstration on a painting presumed of the french renaissance. *Journal of Infrared, Millimeter, and Terahertz Waves*, 41(12):1556–1566, 2020. 156

[30] Anthony J Fitzgerald, Bryan E Cole, and Philip F Taday. Nondestructive analysis of tablet coating thicknesses using terahertz pulsed imaging. *Journal of pharmaceutical sciences*, 94(1):177–183, 2005. 156

[31] Quentin Cassar. *Terahertz radiations for breast tumour recognition*. PhD thesis, Bordeaux, 2020. 157, 160, 161

[32] JLM Van Mechelen, AB Kuzmenko, and H Merbold. Stratified dispersive model for material characterization using terahertz time-domain spectroscopy. *Optics letters*, 39(13):3853–3856, 2014. 157

[33] Doris L Caballero. A theoretical development of exact solution of reflectance of multiple layer coatings. In *Journal of the Optical Society of America*, volume 36, pages 710–711. AMER INST PHYSICS CIRCULATION FULFILLMENT DIV, 500 SUNNYSIDE BLVD, WOODBURY . . . , 1946. 158

[34] Pierre Lecaruyer, Emmanuel Maillart, Michael Canva, and Jannick Rolland. Generalization of the rouard method to an absorbing thin-film stack and application to surface plasmon resonance. *Applied optics*, 45(33):8419–8423, 2006.

[35] Antonin Vasicek. Sur la réflexion de la lumière sur des verres supportant des couches minces multiples. *Journal de Physique et le Radium*, 11(7):342–345, 1950. 158

[36] H Angus Macleod and H Angus Macleod. *Thin-film optical filters*. CRC press, 2010. 160

[37] Sergey Yulin. Multilayer coatings for euv/soft x-ray mirrors. In *Optical interference coatings*, pages 281–307. Springer, 2003. 160

[38] Quentin Cassar, Adrien Chopard, Frederic Fauquet, Jean-Paul Guillet, Mingming Pan, Jean-Baptiste Perraud, and Patrick Mounaix. Iterative tree algorithm to evaluate terahertz signal contribution of specific optical paths within multilayered materials. *IEEE Transactions on Terahertz Science and Technology*, 9(6):684–694, 2019. 160

[39] Lionel Duvillaret, Frederic Garet, and J-L Coutaz. A reliable method for extraction of material parameters in terahertz time-domain spectroscopy. *IEEE Journal of selected topics in quantum electronics*, 2(3):739–746, 1996. 160

[40] Lionel Duvillaret, Frédéric Garet, and Jean-Louis Coutaz. Highly precise determination of optical constants and sample thickness in terahertz time-domain spectroscopy. *Applied optics*, 38(2):409–415, 1999. 161

[41] P Uhd Jepsen, David G Cooke, and Martin Koch. Terahertz spectroscopy and imaging–modern techniques and applications. *Laser & Photonics Reviews*, 5(1):124–166, 2011. 160

[42] Junliang Dong, Alexandre Locquet, Marcello Melis, and DS Citrin. Global mapping of stratigraphy of an old-master painting using sparsity-based terahertz reflectometry. *Scientific reports*, 7(1):1–12, 2017. 160

[43] Junliang Dong, J Bianca Jackson, Marcello Melis, David Giovanacci, Gillian C Walker, Alexandre Locquet, John W Bowen, and DS Citrin. Terahertz frequency-wavelet domain deconvolution for stratigraphic and subsurface investigation of art painting. *Optics express*, 24(23):26972–26985, 2016. 160

[44] Binghua Cao, Mengyun Wang, Xiaohan Li, Mengbao Fan, and Guiyun Tian. Noncontact thickness measurement of multilayer coatings on metallic substrate using pulsed terahertz technology. *IEEE Sensors Journal*, 20(6):3162–3171, 2019. 160

[45] Osman S Ahmed, Mohamed A Swillam, Mohamed H Bakr, and Xun Li. Efficient optimization approach for accurate parameter extraction with terahertz time-domain spectroscopy. *Journal of Lightwave Technology*, 28(11):1685–1692, 2010. 161

[46] Romain Peretti, Sergey Mitryukovskiy, Kevin Froberger, Mohamed Aniss Mebarki, Sophie Eliet, Mathias Vanwolleghem, and Jean-François Lampin. Thz-tds time-trace analysis for the extraction of material and metamaterial parameters. *IEEE transactions on Terahertz Science and Technology*, 9(2):136–149, 2018. 161

[47] Lucas Saludjian. *Optimisations en electrotechnique par algorithmes génétiques*. PhD thesis, Institut National Polytechnique de Grenoble-INPG, 1997. 162

[48] Ian Goodfellow, Yoshua Bengio, and Aaron Courville. *Deep learning*. MIT press, 2016. 162

[49] Jean-Marc Alliot and Nicolas Durand. Algorithmes génétiques. *Centre d'Etudes de la Navigation Aérienne*, 2005. 162

[50] Gabriel Cormier, Roger Boudreau, and Sylvain Thériault. Real-coded genetic algorithm for bragg grating parameter synthesis. *JOSA B*, 18(12):1771–1776, 2001. 162

[51] Radoslaw Piesiewicz, Christian Jansen, S Wietzke, Daniel Mittleman, Martin Koch, and Thomas Kürner. Properties of building and plastic materials in the thz range. *International Journal of Infrared and Millimeter Waves*, 28(5):363–371, 2007. 164, 166

[52] Steffen Wietzke, Christian Jansen, Tilmann Jung, Marco Reuter, Benjamin Baudrit, Martin Bastian, Sangam Chatterjee, and Martin Koch. Terahertz time-domain spectroscopy as a tool to monitor the glass transition in polymers. *Optics express*, 17(21):19006–19014, 2009. 166

[53] Nina S Schreiner, Wolfgang Sauer-Greff, Ralph Urbansky, and Fabian Friedcrich. All-electronic high-resolution terahertz thickness measurements. In *2018 43rd International Conference on Infrared, Millimeter, and Terahertz Waves (IRMMW-THz)*, pages 1–2. IEEE, 2018. 168

Chapter V

Coherent Diffractive Imaging

«If you want to find the secrets of the universe, think in terms of energy, frequency and vibration.»

Nikola Tesla

V.1 Introduction

As a more prospective approach in this work, this chapter, *Coherent Diffractive Imaging* details advances in the field of lensless imaging in the terahertz spectral domain.

Unlike for real-time full-field, inspection addressed in chapter II, where the coherence of the source is witnessed as a highly degrading factor, coherent imaging fully relies on this characteristic of interest for the extraction of a phase information, in addition of the recorded amplitude. As sensors remain too slow for a direct phase recording, such a process alternatively stands on the assessment of the diffraction pattern resulting from the coherent illumination of an object. Hence, it bridges between incoherent sensing and coherent imaging through the retrieval of the additional phase component via the sole recording of intensity profiles, combined to advanced sensing and processing approaches.

This additional wave front phase profile represents precisely the major advance offered by such lensless approaches, and hence provides a compelling complementary tool for inspection in the terahertz spectral range. Namely, it procures an adequate and sensitive mechanism for the assessment of optical proprieties and inhomogeneities among samples of interest, along with topographic insight accompanied by an accurate depiction of their geometries, thanks to the high achievable resolution levels, often below usual diffraction limited imaging systems. Wave front inspections for sensitive terahertz optical setups also serve as a compelling use-case, well fitted for example to the characterization of compensation adaptive optics [1].

A prior depiction of the theoretical developments of Fourier optics will then be detailed as an introduction to the optical principles behind the diffraction theory. More precisely, it will feature the analytical tools for the depiction of free space propagation, embedded in the subsequent numerical processes, as a key component for the obtention of a focused complex wave front image.

Similarly to the visible range of the electromagnetic spectrum, terahertz coherent imaging from intensity distributions can be applied to achieve phase imaging. A review of such different sensing approaches for lensless imaging will then be drawn. Specifically, as the most widespread solutions, ptycography, holography and multi-plane phase retrieval principles will be addressed along with a state of the art related to those integrations in the terahertz spectral range.

Advances in the thematic of iterative phase retrieval in a reflection configuration will be detailed, featuring a high dynamic range raster scan measurement scheme, implementing a 287 GHz illumination source. A simplified transposition to the transmission configuration will be as well considered for the investigation of phase objects. This approach will be put into perspective with the interferometric off-axis holography process, as to provide a methodology comparison. Subsequently, developments toward the integration of real-time recorded data-sets, through the use of focal plane arrays in the terahertz range, will once again demonstrate a strong improvement of the recording cadences with respect to the standard approach of single point sensing multi-plane intensity profiles based phase retrieval.

V.2 Optical Considerations for Free Space Propagation: Fourier Optics

Prior to the understanding of the algorithmic procedure of the different coherent reconstruction approaches, a depiction of the physical principle behind free space propagation, that governs diffraction fields distributions, is conducted in this section. Indeed, such numerical processes rely on the retrieval of a phase information from amplitude recordings of such diffraction pattern induced by an object under coherent illumination, that can be tied to the Fourier optics theory.

The Fourier theory is closely tied to the Huygens-Fresnel principle [2] in optical wave theory, which states that each point of a given wave front can be considered as emitting an elementary spherical wave. The subsequent waveform, in a given plan, is then constituted of the coherent superposition of the contributions of each one of those propagated spherical waves. The Fourier

approach nevertheless lies on the consideration of plane waves superposition to assess the free-space propagation of a wave front [3, 4]. This physical depiction leads to the extensive use of the Fourier transform integral operations as it is based on the spatial frequency harmonic analysis of a signal. In this case, it considers a 2D reduced depiction of the complex wavefunction in a given plane d as U(x,y,d). The temporal beating consideration detailed in section II.2 can be omitted considering the following time space dissociation: $U(\overrightarrow{r},t) = U(\overrightarrow{r})e^{i\frac{2\pi c_0}{\lambda_o}t}$.

To assess the complex wavefunction in a given plane from the knowledge of a prior wave front, two methods are available to define its complex amplitude after propagation. At first, a spatial-domain approach, where the wave is considered as a superposition of parabolic elementary waves, leads to the spatial convolution with a free space propagation impulse response. A second solution is defined through a spatial-frequency approach in Fourier's space where the wave is broken down as a sum of plane wave, on which, a free-space transfer function can be applied. Those two complementary approaches are summarized in Figure V.1. The later leads to the angular spectrum equation, hereafter depicted in Equation V.1, which defines the evolution of the diffractive transform of the wave front between two given parallel planes. It make use of $H_d(\nu_{0x},\nu_{0y})$, the free-space propagation transfer function, as follows :

$$U(x,y,d) = \mathscr{F}^{-1}\Big(H_d(\nu_{0x},\nu_{0y}) \times \mathscr{F}\big(U(x,y,0)\big)\Big), \tag{V.1}$$

with d the distance between the two subsequent planes, and $U(x,y,0)$ and $U(x,y,d)$ the complex amplitude of the wave front at the source plane and observation plane respectively. Once again, $\mathscr{F}$ and $\mathscr{F}^{-1}$ represents the direct and inverse Fourier transform operators.

In this approach, the general transfer function for free space propagation over a distance +d, $H_d(\nu_{0x},\nu_{0y})$, can be expressed as [3]:

$$H_d(\nu_{0x},\nu_{0y}) = \begin{cases} e^{-i2\pi\tilde{n}d\sqrt{\frac{1}{\lambda_0^2}-\nu_{0x}^2-\nu_{0y}^2}}, & if \quad \nu_{0x}^2+\nu_{0y}^2 \leqslant \frac{1}{\lambda_0^2} \\ e^{-2\pi\tilde{n}d\sqrt{\nu_{0x}^2+\nu_{0y}^2-\frac{1}{\lambda_0^2}}}, & if \quad \nu_{0x}^2+\nu_{0y}^2 \geqslant \frac{1}{\lambda_0^2} \end{cases} \tag{V.2}$$

with, $\nu_{0x} = \frac{k_{0x}}{2\pi}$ and $\nu_{0y} = \frac{k_{0y}}{2\pi}$, the spatial frequency components in the Fourier space, along the $\overrightarrow{x}$ and $\overrightarrow{y}$ directions respectively, and λ_0, the wavelength in vacuum.

Assuming a real refractive index, hence a lossless propagation media, $\tilde{n} = n$, the prior condition $(\nu_{0x}^2+\nu_{0y}^2 \leqslant \frac{1}{\lambda_0^2})$ leads to, $|H_d(\nu_{0x},\nu_{0y})| = 1$, which gives rise a sole phase shift of the wavefunction with no amplitude variation in the Fourier domain. The later condition, on the other hand, $(\nu_{0x}^2+\nu_{0y}^2 \geqslant \frac{1}{\lambda_0^2})$ will lead to an evanescent wave, therefore preventing the propagation of high spatial frequency information above the cut off frequency $\frac{1}{\lambda_0}$.

From this explicit model depiction, two major approximations can be made.

- Fraunhofer Approximation

  The Fraunhofer approximation for far field considerations will induce a link between the wave function in the plane d as proportional to the Fourier transform of the wavefunction in the reference plane, assessed at the spatial frequencies $\nu_{0x} = \frac{x}{\lambda_0 d}$ and $\nu_{0y} = \frac{y}{\lambda_0 d}$ such that [5] :

  $$U(x,y,d) \propto \left\{\mathscr{F}\{U(x,y,0)\} \mid \nu_{0x} = \frac{x}{\lambda_0 d}, \nu_{0y} = \frac{y}{\lambda_0 d}\right\}. \tag{V.3}$$

  This approximation is not applicable for this considered close range terahertz configurations.

- Fresnel approximation

  Analogously, a close range approximation can be reached with the definition of a simplified free space transfer function. It relies on the approximation of a spherical wave front as a

parabolic wave front. In such considerations, if the following condition is satisfied, $\nu_{0x}^2 + \nu_{0y}^2 << \frac{1}{\lambda_0^2}$, a simplified free-space transfer function can be derived from a Taylor expansion as follows [5, 6] :

$$H_d(\nu_x, \nu_y) = e^{-\frac{i2\pi\tilde{n}d}{\lambda_0}} e^{i\pi\tilde{n}\lambda_0 d(\nu_{0x}^2+\nu_{0y}^2)}, \tag{V.4}$$

From this simplified quadratic phase expression, its inverse Fourier transform can be computed as $h_d(x,y) = \mathscr{F}^{-1}(H_d(\nu_x, \nu_y))$, which leads to :

$$h_d(x,y) = \frac{i\tilde{n}}{\lambda_o d} e^{-\frac{i2\pi\tilde{n}d}{\lambda_o}} e^{-i\pi\tilde{n}\frac{x^2+y^2}{\lambda_o d}}, \tag{V.5}$$

This quantity represents the free space impulse response and is used as a convolution kernel for the Fresnel transform. Indeed from Equation V.1 it ensues that $U(x,y,d) = U(x,y,0) * h_d(x,y)$, where $*$ stands for the convolution operator.

The two previously described free space propagation computation methods are synthesized in Figure V.1 where $H_d(\nu_{0x}, \nu_{0y})$ represents the transfer function of free space propagation while $h_d(x,y)$ is the free space impulse response. Their simplified expressions are given in the Fresnel approximation and $\mathscr{U}$ represents the Fourier transform of the spatial wave front.

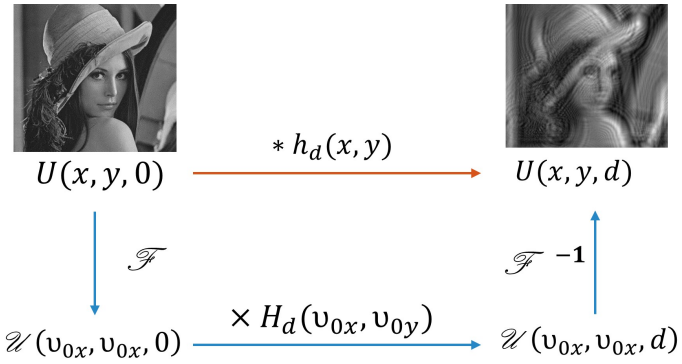

Fresnel approximation :

$$h_d(x,y) = \frac{i\tilde{n}}{\lambda_0 d} e^{-\frac{i2\pi\tilde{n}d}{\lambda_0}} e^{-i\pi\tilde{n}\frac{x^2+y^2}{\lambda_0 d}}$$

$$H_d(\upsilon_{0x}, \upsilon_{0y}) = e^{-\frac{i2\pi\tilde{n}d}{\lambda_0}} e^{i\pi\tilde{n}\lambda_0 d(\upsilon_{0x}{}^2+\upsilon_{0y}{}^2)}$$

Figure V.1: Optical propagation computation scheme with Fourier optics, depicting the direct convolution spatial domain approach and the harmonics spatial frequency decomposition method. It also features a simplified amplitude depiction of a wave front evolution, through free space propagation.

Such an approximation remains quite useful for analytic calculations, with distinct linear spatial dependency and quadratic spatial frequency dependency. It represents an inescapable tool to grasp the mechanics of Fourier optics. It will nevertheless not be considered in this case thanks to the implementation of numerical calculation tools. For numerical computations, the direct application of Equation V.2 is considered as to avoid any model deviation in the reconstructions.

In this convenient modeling approach, beside free-space propagation, the interaction with a planar object, can easily be formulated as a multiplication by a spatial complex pupil function o(x,y), as depicted in Equation V.6, with p(x,y,0) the illumination probe wave front in the object plane and U(x,y,0), the resulting wavefield. The amplitude of this complex object description then represents the attenuation (or amplification if $|o(x,y)| > 1$) caused at the sample crossing while the argument of this distribution stands for the object induced phase shift.

$$U(x,y,0) = p(x,y,0) \times o(x,y) \tag{V.6}$$

V.3 Terahertz Lensless Imaging

From the Fourier optics principles, and especially free space propagation equations, the depiction of diffracted complex wave fronts can be anticipated. As a major limitation however, applicativelly, all detection and imaging devices nevertheless remains too slow for the direct registering of a phase information, leading to the recovery of intensity-only recordings.

As a prospective approach, coherent terahertz imaging aims to recover the complex wave front of a sample, employing the incoherent recording of a sample diffraction fields through intensity-only measurements, hence, in absence of advanced coherent sensing mechanism such as the homodyne detection embedded in the FMCW radar mode of operation. Suiting then the vast majority of available terahertz detectors, this approach does not remain a direct imaging process, as it requires substantial algorithmic considerations, integrating Fourier optics as a fundamental kernel for image refocusing. Additionally to the complex wave front recovery, such approaches to lensless visualization is of great interest thanks to the simplicity of the implementation setups that, beside the probing beam shaping, do not require dedicated complex optical systems such as imaging lenses. It leads as well to high achievable resolution, ensured by numerical post-processing image reconstruction from high NA recorded diffracted fields.

Initially demonstrated in other spectral regions [7–9], and especially X-rays and electronic imaging, the modern approaches of coherent lensless imaging are naturally being extended to the millimeter-waves spectral range [10] through a wavelength and experiment scaling. It indeed represents a viable opportunity to tackle advanced sensing problematics thanks, once again, to the dielectric material penetrability and the sub-millimetric wavelength.

Among coherent imaging, several approaches can be recognized as to recover a complex wave front from the assessment of a diffracted field. Namely, digital holography, ptycography, or intensity profiles iterative phase retrieval demonstrated their capabilities [10].

V.3.1 Digital holography

The coherent wave front extraction of digital holography relies on the recording of an interference pattern between a diffracted object wave front, O(x,y,z), and a unaltered reference probing beam, R(x,y,z) in a measurement plane. As a result of free space propagation, the diffracted object field, O(x,y,z), emerges from Equation V.1 with $\mathrm{O}(x,y,0) = p(x,y,0) \times o(x,y)$, with $o(x,y)$ the object complex pupil function and $p(x,y,0)$ the probing wave front.

Two configurations can be intended from this initial approach [11]. In-line holography aims to generate such an interference pattern through two waves propagating in the same direction. To allow such geometry, the object must be weakly interacting with a unique probing beam. Hence it should induce limited modulation or be smaller than the probing beam as to preserve an unaffected portion of the wave front, considered then as the reference. No further details will be brought to this implementation as it remains highly restrictive to the object geometry, even-though it ensures a compact imaging solution. Several implementations have nevertheless successfully demonstrated this lensless probing scheme in the terahertz range [12, 13].

Oppositely, off-axis holography considers the interference between two wave fronts propagating along different directions as depicted in Figure V.2a. Considering a recording plane perpendicular to the propagation of the object wave front, one can express $\mathrm{O}(x,y) = \mathrm{A_O}(x,y)e^{i\Phi_\mathrm{O}(x,y)}$ with $\mathrm{A_O}(x,y)$ and $\Phi_\mathrm{O}(x,y)$ the respective amplitude and phase profiles of the object wave front. Considering an angle Θ between the two propagation directions, the reference probing complex wave front can then be intended as $\mathrm{R}(x,y) = \mathrm{A_R}(x,y)e^{i\left(2\pi(\nu_{\mathrm{R}0x}x+\nu_{\mathrm{R}0y}y)+\Phi_\mathrm{R}(x,y)\right)}$ with $sin(\Theta_x) = \lambda_0\nu_{\mathrm{R}0x}$ and $sin(\Theta_y) = \lambda_0\nu_{\mathrm{R}0y}$.

The resulting interference intensity profile, in the interfering plane can then be defined as:

$$I(x,y) = |O(x,y) + R(x,y)|^2 = \quad A_R(x,y)^2 + A_O(x,y)^2 + O(x,y)^* R(x,y) + O(x,y) R(x,y)^*, \tag{V.7}$$

$$= A_R(x,y)^2 + A_O(x,y)^2 \quad + A_R(x,y) A_O(x,y) e^{i\left(2\pi(\nu_{R0x}x + \nu_{R0y}y) + \Phi_R(x,y) - \Phi_o(x,y)\right)} \tag{V.8}$$

$$+ A_R(x,y) A_O(x,y) e^{-i\left(2\pi(\nu_{R0x}x + \nu_{R0y}y) + \Phi_R(x,y) - \Phi_o(x,y)\right)},$$

with * the complex conjugate operator [14].

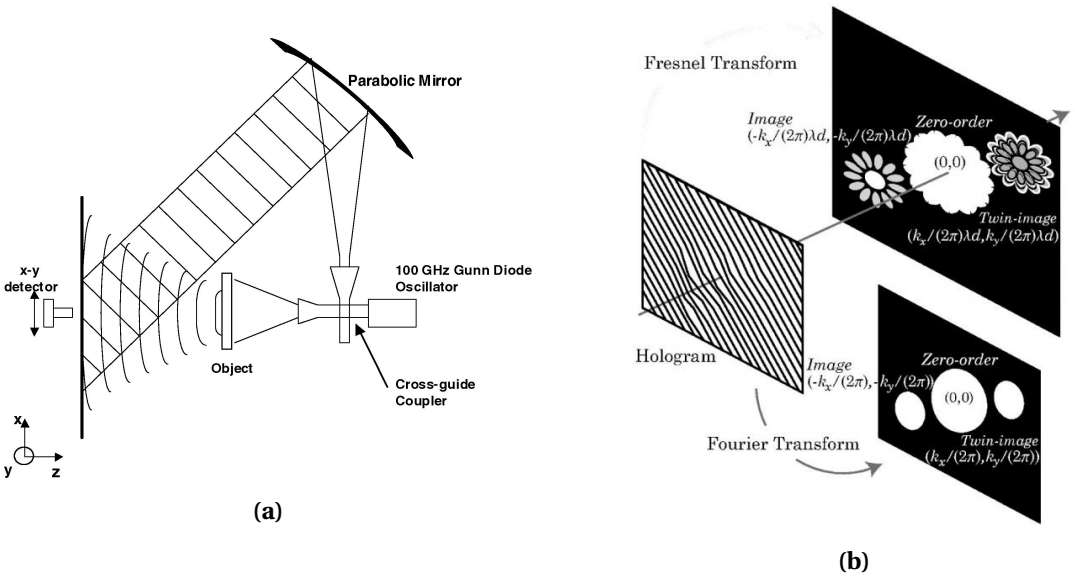

Figure V.2: **(a)** Typical diagram of an off-axis digital holography implementation using a 100 GHz Gunn diode [15], and **(b)** simplified depiction of the order separation induced by off-axis holography interferometric methods [16].

Considering Equation V.7, the sum of conjugate exponentials, equivalent to a cosine function, depict the interference modulation. The two first terms then feature the order 0 of the interference pattern while the two subsequent exponential components relates to the order +1 and -1, respectively centered at the spatial frequencies $\pm[\nu_{R0x}, \nu_{R0y}]$ as depicted in Figure V.2b and featured in Figure V.16c from a millimeter waves experimental measurement. Assuming a large enough interference angle Θ, that would prevent an overlapping of each order, a Fourier space spatial filtering then allows for the retrieval of the +1 order, which incorporates the object wave front, assuming the prior knowledge of the reference wave front, $A_R(x,y)$ and $\Phi_R(x,y)$. Such a methodology has been extensively detailed with the emergence of computation capabilities, for direct digital reconstruction procedure [14, 17, 18]. A variety of work transposed this approach in the terahertz frequency range, providing a scaling of the optical implementation from historical integrations [15, 19, 20]

V.3.2 Ptychography

Unlike off-axis holography, that relies on the use of interferometric investigations, ptycography brings up the recovering of a complex wave front through the sole consideration of intensity diffraction profiles. Through the scanning of the object with a fixed probing beam illumination, a complex wave front can be retrieved through an iterative process over the respective recorded diffraction patterns resulting from a selection of overlapping illuminated sections of the sample as depicted on Figure V.3. After interacting with the sample, such a probing at the position k can be expressed as :

$$U_k(x,y,0) = p(x,y) \times o_k(x - x_k, y - y_k) \tag{V.9}$$

with p(x,y), the probing illumination wave front, $o_k(x,y)$, the object pupil function and (x_k, y_k) the illumination position coordinated.

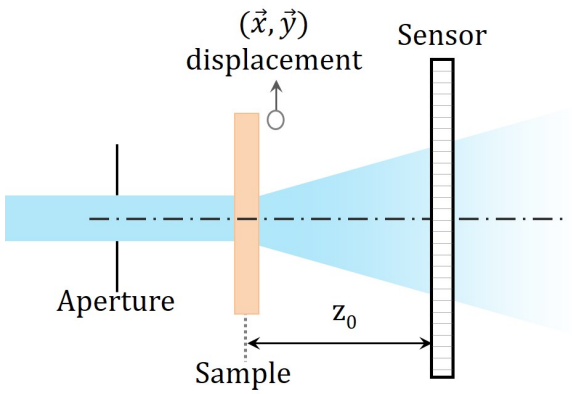

Figure V.3: Diagram of typical ptychographic investigation setup.

From the set of intensity diffraction patterns, $I_k(x,y)$, recorded in a distant plane, emerging from the subsequent displacement of the object, the following iterative corrective procedure [21] leads to the recovering of the complex wave front. After interacting with a given section of the object, the wave front, $U_k(x,y,0)$, can be propagated in the recording plane through free space propagation, as detailed in Equation V.1 to lead to $U_k(x,y,z_0)$. An amplitude constraint can then be used as to fit the intensity diffracted field measurement profile such that $|U_k(x,y,z_0)| = \sqrt{I_k(x,y)}$. A back propagation in the object plan is then practicable where an update of the object illuminated region, $o_k(x,y)$, is performed through a process detailed in [10, 21]. A consideration of the subsequent overlapping illumination region for the $k+1^{th}$ iteration will then repeat the iterative process. A dissociation of the probing beam wave front can as well be operated through an advanced processing method detailed in [22].

V.3.3 Multi-plane Iterative phase retrieval

In a similar fashion, multi-plane phase retrieval will rely on the recording of intensity diffraction patterns to iteratively converge toward the obtention of a complex wave front. Nevertheless, with respect to ptychography the procedure relies on the constant full illumination of the static object hence, ensuring a simplified implementation, coupled to a recording of the diffraction field along different distances.

Typical integrations in transmission and reflection configurations are given in Figure V.10 and V.4 respectively, for single point raster scan recording procedures in the terahertz range. In absence of a reference probing beam, lower requirements are expected for the emission power of the radiation source, an element of importance for terahertz systems. Such use of a single-beam optical layout leads to a large robustness with regard to external perturbations, such as vibrations, in comparison with digital holography. Additionally, phase retrieval stands more efficiently in terms of space-bandwidth product to provide a higher spatial resolution [23].

Beside the optical implementation, the retrieval procedure is of interest for this methodology and rely on the SBMIR (Single Beam Multiple Intensity Reconstruction) algorithmic process [24–26]. From a succession of diffraction intensity fields, $I_{z_k}(x,y)$, recorded along the propagation axis, an iterative, amplitude constrained, procedure can be depicted as follows : an initial estimation of the wave front is performed in the first recording plane, considering the measurement amplitude, complemented by a constant or random phase. A propagation toward the subsequent recording plane is underwent, following Equation V.1. An amplitude constraint, emerging from the recorded intensity profile can then be applied as to generate an estimated hybrid measurement-iterative field when enforcing $|U(x,y,z_k)| = \sqrt{I_{z_k}(x,y)}$, while conserving the previously estimated phase. These steps are sequentially carried out along each ordered plane, and subsequently in the opposite direction, enduring a back-propagation toward the first measurement plane. As to complete an iteration, a final focusing propagation is applied toward the object plane to assess the conver-

gence of the algorithm.

From such ordered iterative retrieval, a minor alteration can be considered. Namely, an unordered plane selection can be applied and demonstrated an improvement of the convergence speed of the algorithm [27]. Inheriting from the operation mode of the SBMIR procedure, namely, after propagation, an amplitude constraint is applied while the phase is preserved, a stochastic selection of the subsequent plane is operated.

Additionally, an extrapolation beyond the spatially limited registration area should be as well applied for non-square recordings, or cropped recorded diffraction fields and for prospection in the vicinity of the recording area. Along the first iteration, the size of the computational grid is extended through zero padding. For each subsequent iteration, the amplitude constraint, from the measurement intensity distribution, is only applied to the central part of the synthesized wave front. To improve the convergence of the algorithm by avoiding side effects, an apodization mask is used, which limits the energy distribution in the region of the object.

Beside such straightforward algorithmic implementations, various adaptations of the SBMIR procedure have been additionally explored. As a first example, the use of a diffuser upstream of the sample ensures the formation of a partially developed speckle structure through probing phase randomization [25, 26]. Phase retrieval, coupled to ptychography have also been applied to imaging problematics behind a moving and scattering barrier [28].

Additionally, in the free space propagation transfer functions depicted in Equations V.2, V.4 and V.5, the $\lambda_0 d$ formulation insight a duality between the propagation distance and the wavelength. From classical coherent imaging, which employs intensity distributions recovered at different distances, a spectral phase retrieval approach can then intuited as to avoid the displacement of the recording plane. Namely, in the terahertz range, pulsed TDS sensing provides such suitable broadband illuminations [29].

V.4 Terahertz Phase Retrieval Through SBMIR Algorithmic Implementation

V.4.1 Sub-millimeter waves investigation in reflection

Its fast iterative phase recovery convergence through a simplified setup implementation in absence of reference interfering arm, allowed the SBMIR algorithm to be successfully demonstrated in transmission [25], diffuse transmission and reflection [26] configurations in the visible range of electromagnetic spectrum. In the terahertz range, on the other hand, only the transmission scheme has yet been investigated [28]. A prior focus on the challenging reflection geometry will then be pursued in this section with an implementation operating at 287 GHz and will be further complemented with a transposition toward a transmission configuration, focused on the inspection of phase objects.

Considering the prior, two methodologies are applicable. The first option rely on the use of beam splitter when the object is illuminated in normal incidence with respect to its surface, as depicted in Figure V.4. It then leads to energy losses, but allows for the use of standard free space propagation models between two planes transverse to the optical axis. The second setup, which features an inclined probing of the sample, is more energy efficient, but additional plane rotational transformations must be applied to the wave front in solving the diffraction equations. Thanks to the availability of a high power source, and the implementation of specific high dynamic range sensing scheme, the more challenging beam splitter integration is assessed in this section [30].

Experimental setup

Figure V.4 provides a descriptive scheme of the implemented experimental setup for the recording of intensity distribution sets for terahertz phase retrieval in a reflection configuration. The previously featured Gunn diode with a Schottky based frequency multiplication chain, emitting at a frequency of f=287 GHz, with an emission power of 14 mW, was used in conjunction with a

Schottky diode (SD) detector, integrated as a single-pixel detector. The removal of the horn antenna from its block integration led to a sensor effective area equivalent to the WR3.4 waveguide aperture.

From the diverging beam emission of the source, shaping optics have been integrated as to generated a suitable large aperture illumination beam. A prior characterization of this beam profile has been performed as to ensure its collimation and suitability of its illumination area, estimated to about 8 cm×8 cm. Via reflection from a 45° BS, the static object was illuminated by the expanded collimated beam. After reflection on the object and subsequent transmission through the BS, the diffracted field was recorded via the acquisition of a sequence of images at multiple distances along the $\vec{z}$ axis. To do so, at each distance of interest z_k a 2D intensity mapping of the diffraction field is recorded through the raster scanning of the plane with the open SD detector. The QCW probing power modulation then resquires the use of LIAs with the subsequently detailed High Dynamic Range (HDR) detection scheme.

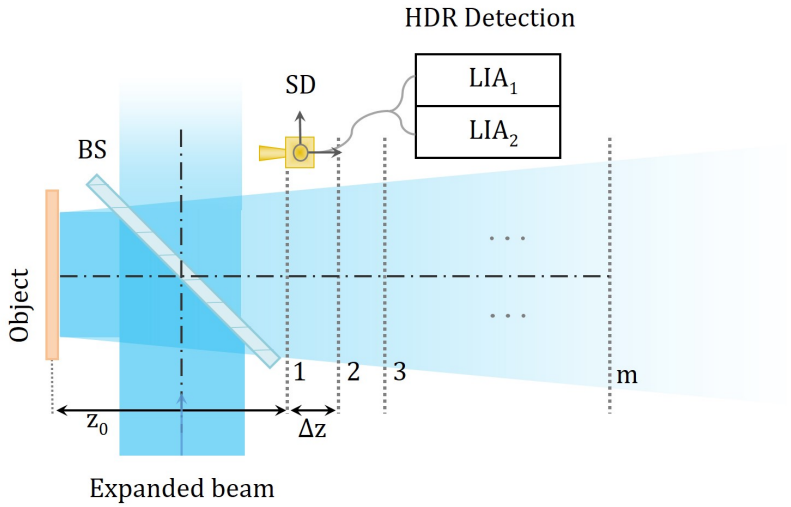

Figure V.4: Diagram of the experimental implementation for phase retrieval measurement in reflection configuration, using HDR detection.

The successive diffracted reflected intensity profiles from the object, $I_{z_k}(x,y)$, were captured at axially spaced m = 27 planes (typically for such implementations m = 20 – 30) with constant separation of $\Delta z = 5$ mm, the first of which was located at a distance $z_0 = 83$ mm from the object plane due to the BS mechanical obstruction. To fit the diffraction pattern dimension, generated from the 8 cm diameter illumination beam, 240×240 pixel images with a lateral pitch of $\Delta x = \Delta y =$ 0.5 mm ($\approx 0.5\lambda_0$) were recorded by the SD during the time-consuming 3D raster scanning operation, leading to a total measurement time above to 36 hours for the recording of 1.6×10^6 pixels, with an integration time of 100 ms.

A metallic shuriken was used as the test reflective object. The illuminated area of the object in the phase retrieval experiment contained several concave Chinese characters, including the king kanji, 王, as showed in Figure V.8c.

HDR detection

In comparison with a transmission geometry, the presence of a beam splitter in the optical path of the reflected wave front imposes a restriction on the minimum permissible distance for recording data between the object and the first measurement plane ($k = 1$ in Figure V.4). Thereby, it drastically restricts the detection capabilities of high spatial frequencies. The beam splitter also induces ineluctable power losses, which exacerbates the main challenge of the practical demonstration of terahertz phase retrieval in reflection configuration. Namely the recording of a weak signal with both limited source emission power and detector sensitivity represents one of the main challenges.

Such diffractive measurements additionally display large disparities in the intensity distribution of the reflected beam, depending on the position and distance of the detector in regard to the object. A large measurement dynamic range is then compulsory to reach adequate reconstructions.

In this experiment, for the QCW sensing operation, the output emitter beam was mechanically modulated using a rotating chopper at 235 Hz, and the SD was connected to LIAs. Commonly, the use of a single LIA leads to a limited dynamic range, usually in such widespread configurations in the order of 60 dB [31] carying an intensity related information, due to intrinsic LIA hardware limitations, then equivalent to a 30 dB dynamic range on amplitude profiles, effectively used in the algorythmis approach. To overcome such a limitation, two distinct LIAs with complementary sensitivity settings have been connected with the SD for HDR detection. Data merging, using the lower sensitivity LIA_2 setting in the case of saturation, and the high sensitivity LIA_1 setting in the case of weak signal levels, was employed to reach an adequate merged dynamic range of over 100 dB in intensity distributions, hence 50 dB on diffracted amplitude profiles, limited by the detectors noise level and source emission power.

Let us denote the signal to be digitized as S, while S_1 and S_2 are its corresponding values after the digitizing with LIA_1 and LIA_2, such that $S_{min1} < S_1 < S_{max1}$ and $S_{min2} < S_2 < S_{max2}$. Complementary LIA sensitivity settings are chosen so that $S_{max1} \gtrapprox S_{min2}$. Then, as displayed on Figure V.5 (b), for each measurement plane one can then consider:

$$I_{z_k}(x,y) = \begin{cases} S_{1k}(x,y) & \text{if} \quad S < \zeta \cdot S_{max1}, \\ S_{2k}(x,y) & \text{otherwise} \quad (S \leq S_{max2}). \end{cases} \tag{V.10}$$

Here, ζ is a regulation factor, which is arbitrarily set to 0.75 for this implementation to avoid data mismatch of LIA's dynamic range extremities. Figure V.6 displays an example of the recorded intensity distributions sets, S_{1k} and S_{2k} from LIA_1 and LIA_2. Maximal voltage settings of S_{max1}=20 mV and S_{max2}=500 mV, were considered respectively, leading to a saturated S_{1k} data set, on the left, and a S_{2k} lowered dynamic range data set, in the center. The resulting merged HDR images set $I_{z_k}(x,y)$ are shown in the right.

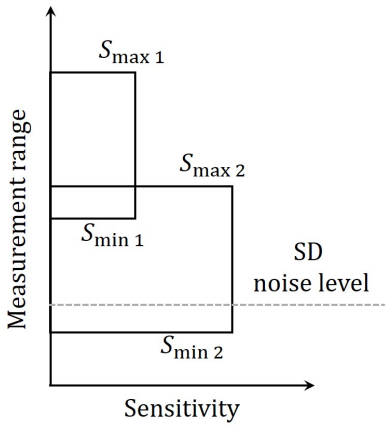

Figure V.5: HDR sensitivity setting diagram for detection.

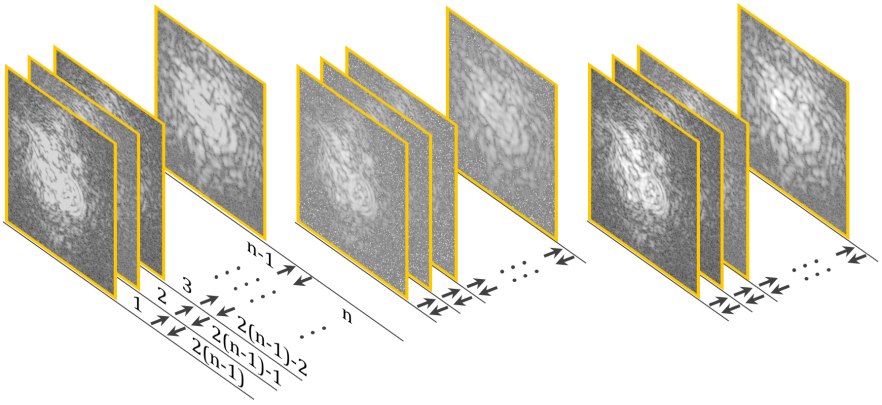

Figure V.6: An example of recorded intensity distribution sets in logarithmic colormap: recorded by LIA_1 (S_{1k}), LIA_2 (S_{2k}) and synthesized HDR images (I_{z_k}). The arrows denote the sequence of propagation based on the ordered SBMIR algorithm.

SBMIR and extracted wave fronts

As demonstrated in Figure V.6, from the recorded intensity distribution set, $I_{z_k}(x, y)$, the field reconstruction, based on Equations V.1 and V.2, following the ordered SBMIR procedure is performed as follows: the initial wave front estimation in the first measurement plane is constructed of the square root from the first intensity measurement plane, accompanied of a random or null phase distribution. This constructed wave front estimation is then propagated in the forward direction toward the second measured plane where the estimated phase is kept, while the amplitude is constrained to the square root from the second measured intensity distribution. In a similar way, this new wave front estimation is subsequently propagated in the forward direction, and the same actions are repeated for each measurement plane. Reaching the last measurement plane, this sequence is repeated in the backward direction. Thus, one iteration encloses $2(n-1)$ propagation steps, as depicted in Figure V.6.

Figure V.7 shows the reconstructed amplitude and phase profiles of the field, focused in the object plane, obtained from the different data sets, which were previously shown in Figure V.6. Due to the high sensitivity setting of LIA_1, the resulting S_1 data set features low-intensity high spatial-frequency components, but suffers from over saturation in a non-negligible portion of the diffracted field. As a result, due to the lack of information from such sections, the SBMIR algorithm is not able to converge toward an acceptable field with such a saturated input data set as demonstrated in Figure V.7a. Oppositely, the signal from LIA_2, S_2, recorded with a non-saturated restricted amplitude dynamic range estimated to 30 dB, clearly demonstrates a lack of sensitivity. The high noise floor in this measurement data set hence drastically limits the recording of high spatial frequency components. Figure V.7b then clearly demonstrates a the very limited, focusing capabilities of the SBMIR procedure in such a limited dynamic range configuration.

In Fine, Figure V.7c reveals the resolution of the reconstructed wave front achieved thanks to the merged HDR data set through the SBMIR algorithm. Indeed, the dynamic range is one of the main limiting factors for such diffraction measurement since the achieved resolution remains bounded to the recording capabilities of low-intensity high spatial frequencies. The self-explanatory reconstructed amplitude profiles of Figure V.7b and V.7c are highlighting the prevalence of this HDR measurement technique with respect to a classical single LIA detection.

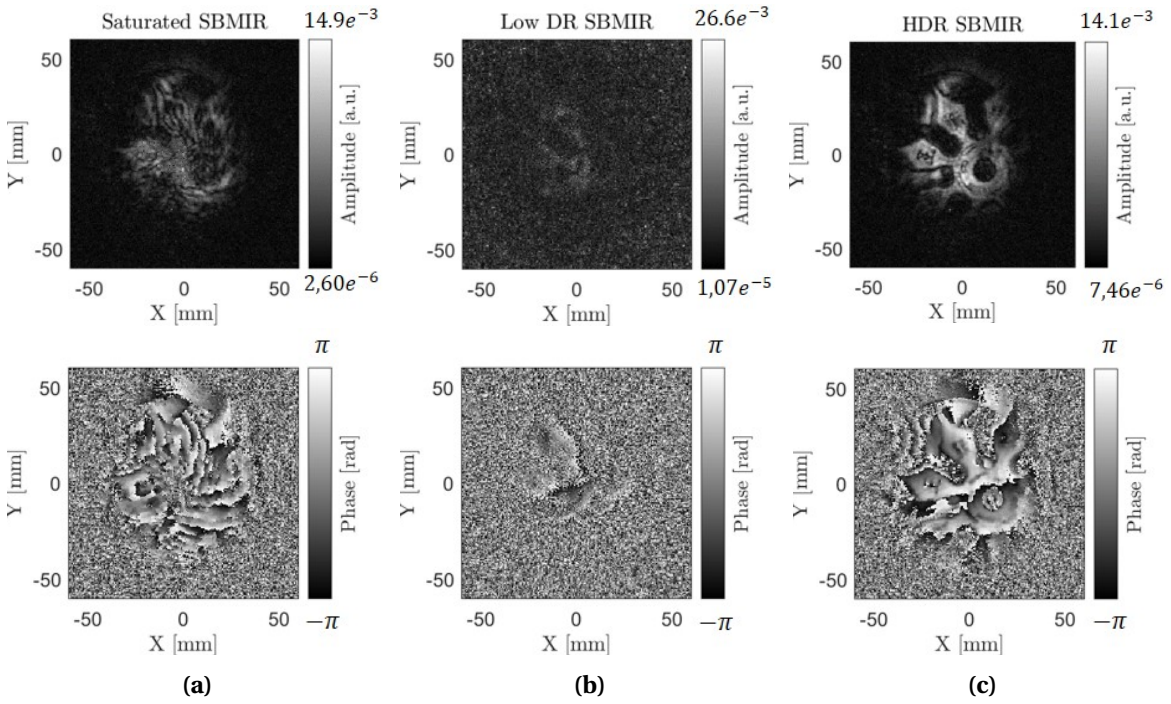

Figure V.7: Typical reconstructed amplitude (top row) and phase (bottom row) distributions from the data sets recorded by **(a)** LIA_1 ,**(b)** LIA_2 and **(c)** HDR measurement data sets.

For comparative purposes, Figure V.8a displays an image obtained at 287 GHz through far field raster-scanning with a numerical aperture of NA = 0.25, as a reference, while an enlarged area of the reconstructed amplitude obtained by through the SBMIR procedure at the same frequency is shown in Figure V.8b. A picture of the investigated object is given in Figure V.8c. Cross-sections in both amplitude profiles are shown in Figure V.8d and demonstrate sharper edges recovering for the SBMIR measurement, testifying in accordance with the high spatial resolution of the proposed approach, achieved through the combination of a HDR measurement data set with the SBMIR algorithm.

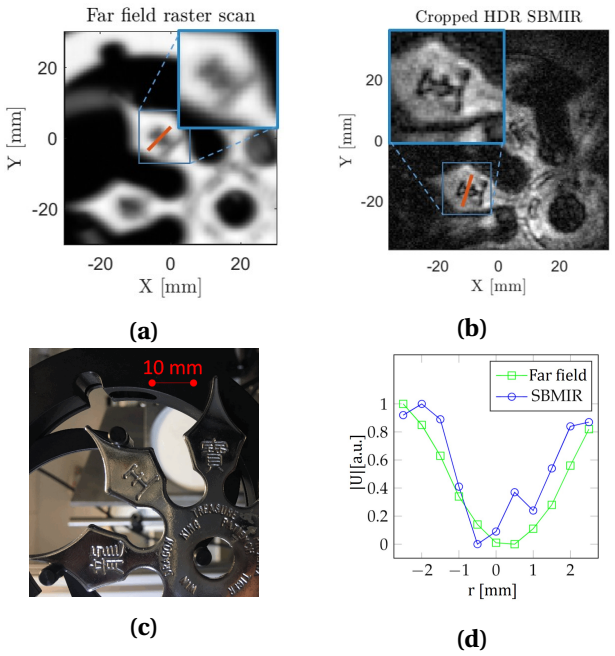

Figure V.8: **(a)** Amplitude distributions of the considered sample obtained through far field assessment at 287 GHz with NA = 0.25 and **(b)** amplitude reconstruction emerging from the SBMIR extraction on HDR measurement sets. **(c)** Picture of the object under inspection and **(d)** cross-sections of the Chinese kanji for both approaches.

Those depictions highlight the advanced capabilities of HDR phase retrieval for sharp resolution imaging with respect to far field imaging, thanks to the inherent lensless ability to provide a high numerical aperture focusing. From the first measurement plane, an estimation to NA = 0.72 is retrieved while for conventional focused point imaging techniques a typical reduction by a factor 1.5 to 3 is expected.

Beside the high resolution amplitude reconstruction, the HDR phase reconstruction provides substantial information to the sample geometry, and especially, in such a reflection configuration, topological insight is retrievable. Indeed, Figure V.7c depicts a slight tilt of the object relative to the imaging planes. The topological profile of the object can as well be noticed with a subtle twist of a shuriken arm.

For further investigation, the obtention of a quantitative height map from the reconstructed reflected object wave front, the following 7-steps procedure has been considered:

- Based on the amplitude image, a binary mask was manually created for the contouring of the object. It should be noted that the mask boundaries were slightly smaller than the irradiated surface area of the shuriken due to its rounded edges.
- This mask was superimposed on the phase image to eliminate the phase noise inherent to undetermined amplitude spatial areas.
- The wave front was over-sampled to subsequently undergo tilt correction by digital interferometric processing with synthesized hologram, as described in [32]. Technically, a sub sampling of 8 was implemented. A subsequent multiplication with an inclined plane reference phase term $e^{\frac{i2\pi}{\lambda_0}(x\cos\beta_x + y\cos\beta_y)}$, where the angle $\beta = (\beta_x, \beta_y)$ is defined such that each fringe spacing matches 8 sub-pixels. Thus, a synthetic off-axis hologram with maximum fringe contrast is simulated.
- The phase distribution is then recovered from the hologram along a slightly different angle, which provided correction of the general surface tilt of the shuriken as depicted in Figure V.9b.
- The background phase of Figure V.9a is then subtracted. This background phase was retrieved through the SBMIR algorithm from preliminary recorded diffraction patterns of a

reference mirror with an additional small reflective bead, introducing a perturbation in the incident field. The phase perturbation induced by the metallic bead has been concealed by a phase averaging over the neighboring values.

- The resulting object area phase was then unwrapped and rescaled to its original size.
- The height map, depicted in Figure V.9c is then obtained as $h(x,y) = \frac{\lambda_0}{4\pi}\arg(\mathrm{U}(x,y))$. This representation displays good agreement with the investigation of topological features conducted by optical microscopy. Namely, the 275 µm deep trench in the 王 kanji is properly retrieved.

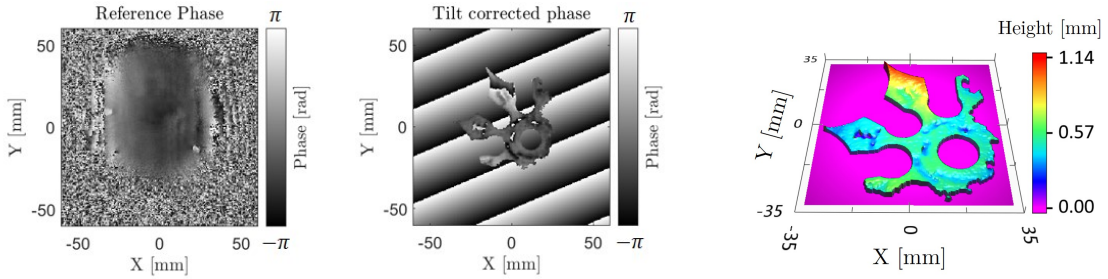

Figure V.9: Numerical post processing with **(a)** reconstructed background phase **(b)** tilt corrected reconstructed phase, and **(c)** subsequently extracted height map.

Such a reflection configuration is especially suitable for highly reflective samples and represents a challenging implementation with the integration of a beam splitter, leading to a large obstruction for the diffracted field recording and non-negligible power losses. Oppositely, a transmission phase retrieval is more suited to transparent phase objects and would lead to a drastic simplification of the optical implementation.

V.4.2 Transmission configuration

In its simplest consideration, one can aim to simply illuminate the sample with a collimated beam of suitable diameter, then retrieving the transmitted diffracted field in a selection of planes along the propagation direction. Figure V.10 depicts this simplified setup which features the previously encountered 8 cm diameter illumination beam as the probing coherent illumination, reducing the need of optical elements requirements to its minimum, with, in this case, the simple addition of a 45° deflection mirror.

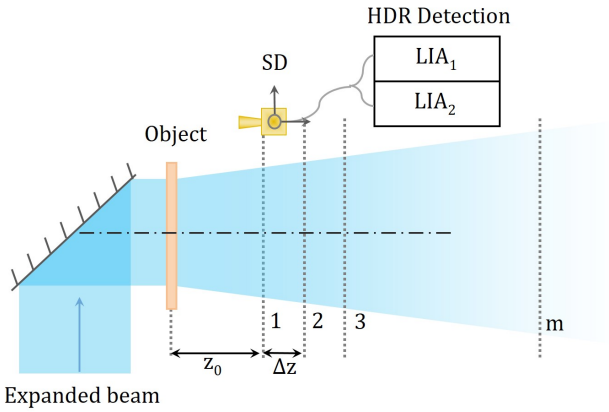

Figure V.10: Diagram of the experimental implementation for phase retrieval measurement in transmission configuration, using HDR detection.

This configuration especially features a non-negligible advantage in comparison with the previously detailed reflection measurement setup. Namely, beside the beam shaping optics, the limited components requirements ensure a simplified setup that leads to a non-obstructed space for the recording of the diffracted field. An optimal proximity of the first recording plane with respect to the sample can then be expected as to ensure the collection of diffracted high spatial frequency components. Large numerical aperture focusing is then possible.

As an ideal phase object, with minimal interface reflection losses and negligible absorption, the previously featured helicoidal HDPE step test chart, displayed in Figure V.11, is considered. Once again, as to ensure optimal recording capabilities, the HDR measurement scheme, featuring two complementary LIAs, is considered. The merged HDR set of intensity diffraction patterns was recorded with a lateral pixel pitch of $\Delta x = \Delta y = 500$ µm with recording planes set $\Delta z = 5$ mm apart. An initial plane distance of $z_0 = 50$ mm was considered due to mechanical constraints and allowed to avoid close range imaging configurations. A selection of the recorded diffracted intensity distribution, $I_{z_k}(x, y)$ along the optical axis is depicted in Figure V.12.

Figure V.11: Polymer step test chart used as a phase sample.

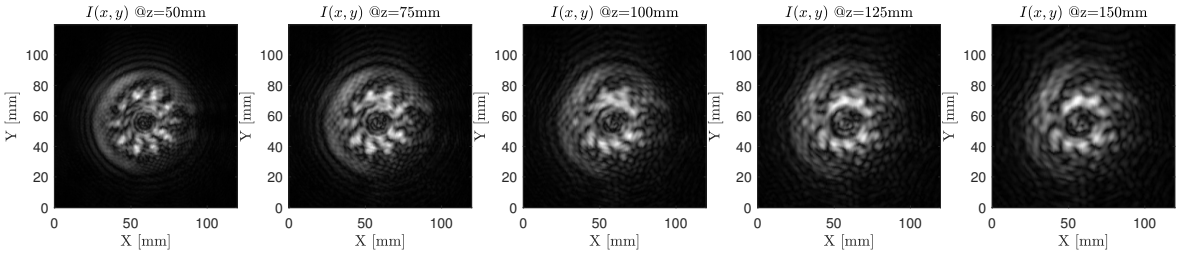

Figure V.12: Raw diffracted field intensity measurements at **(a)** z=50 mm, **(b)** z=75 mm, **(c)** z=100 mm, **(d)** z=125 mm and **(e)** z=150 mm from the object plane.

From such intensity data sets, the unsorted SBMIR algorithm has been considered for the retrieval of the phase information and the focused reconstruction on the object plane. From a randomly selected measurement plane, k, an initial amplitude profile is considered as $U(x, y, z_k) = \sqrt{I(x, y, z_k)}$. Complemented with a zero phase or a random phase spatial distribution, a subsequent back-propagation toward the object plane is conducted and lead to the first object plane reconstruction, featured in Figure V.13a. From there, a consecutive free-space propagation toward a randomly selected plane is performed and allows for the assembly of the hybrid wave front, considering the reconstructed phase in the plane of interest and an update of the amplitude by the measurement amplitude distribution, retrieved from the recorded intensity diffraction field. Such steps can then be subsequently reiterated. Typically, up to 100 iterations are required for the converging of the algorithm toward a stable wave front. No attempt to investigate a convergence criterion has been considered even though a variation coefficient or a correlation coefficient could be estimated between consecutive iterations, as to set an execution threshold. From several extractions, it has been witnessed that initial introduction of a zero phase or a random spatial phase distribution only impacts a few initial iterations, depicting the robustness of the algorithmic procedure to phase perturbations.

A selection of object plane reconstructions are displayed in Figure V.13 along the convergence of the algorithm over 100 iterations.

Additionally, for computational resources considerations, the previously depicted procedure remains unoptimized as a propagation back to the object plane is performed at each iteration.

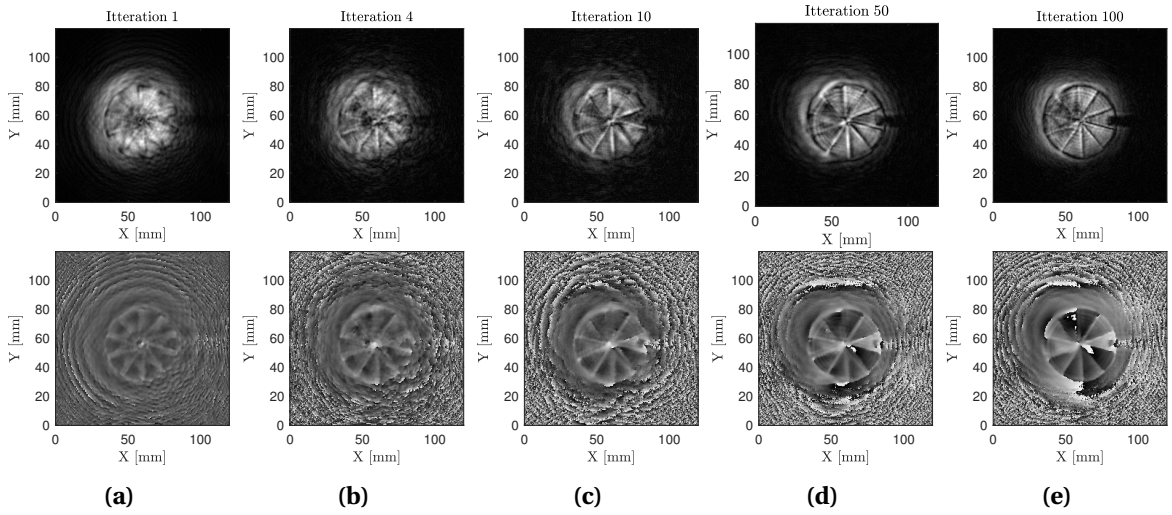

Figure V.13: Amplitude (top row) and phase (bottom row) representation of the focused wave front along the convergence of the SBMIR algorithm at iteration **(a)** 1, **(b)** 4, **(c)** 10, **(d)** 50, and **(e)** 100.

This step is only useful for visualization convenience as to assess the recovering of a stable wave front in the object plane. It nevertheless requires two free space propagation operations, featuring the application of the transfer function $H_{-d_k}(\nu_{0x}, \nu_{0y})$ tied to the back propagation to the object plane and subsequently $H_{d_k+1}(\nu_{0x}, \nu_{0y})$, the forward propagation toward the next plane. Avoiding this propagation to the object plane would lead to the unique consideration of the fully equivalent transfer function $H_{d_{k+1}-d_i}(\nu_{0x}, \nu_{0y})$. After a given number of iterations, a final propagation to the object plane can be conducted to retrieve of the focused wave front, depicted in Figure V.14, for the considered phase object.

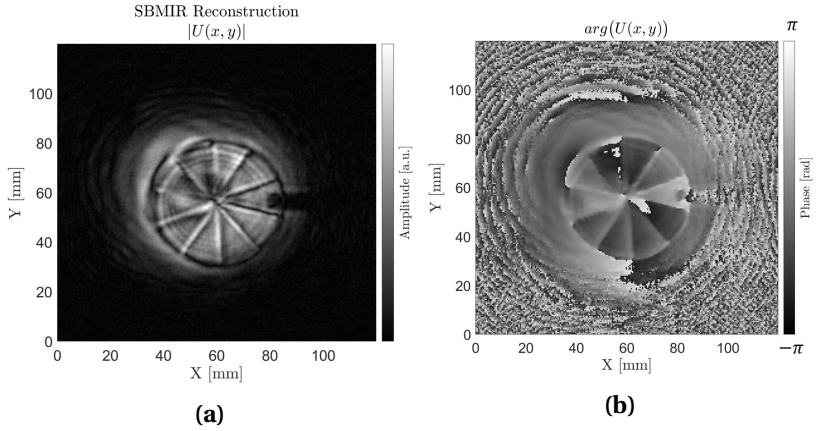

Figure V.14: Recovered complex wave front through iterative phase retrieval using the unsorted SBMIR procedure.

From the final reconstruction, obtained after 100 unsorted SBMIR iterations, a reminiscent diffraction pattern can be witnessed in the amplitude reconstruction. This artifact can be imputed to the non-planar geometry of the sample with the prior diffraction of the flat back interface of this step chart. In addition, a background phase is noticeable and can be attributed to the imperfect illumination beam wave front. This imperfection nevertheless prevents any advanced quantitative phase related inspection. Following Equation V.6, a normalization by the reference probe wave front in the object plane should then lead to sample-only contribution. The recording of a reference wave front, for normalization purposes would then highly improve the phase recovering. Nevertheless, this process remains quite cumbersome and time-consuming as it requires a full intensity set recording, identical to the sample measurement, and should subsequently endure the same process through the SBMIR algorithm to retrieve the reference wave front. For those reasons,

no attempt to apply a wave front normalization on such time consuming measurements have been pursued. This specific wave front correction operation will be addressed in the following section.

Off-axis digital holography in transmission

With a quite similar implementation setup and a simplified recording and algorithmic procedure, the assessment of this same sample has been conducted through transmission off-axis holography as to provide a methodology comparison.

A basic off-axis holography integration has been considered and is detailed in Figure V.15. The reflection arm, ensuing from the BS, provides the normal collimated coherent probing of the sample for the generation of the diffracted field, the object beam, O(x,y). Through the BS, the transmitted power is put to good use for the obtention of the reference beam, R(x,y), as to generate an interfering pattern with the diffracted beam in the recording region. The optimal object-imaging plane distance obviously depends on the size of the object. Indeed, the diffraction pattern should be recorded as close as possible from the object as to be able to record low-amplitudes high spatial frequencies, that would hence lead to a sharper reconstruction or equivalently a higher equivalent diffracted NA recording. On the other hand, the object should not temper with the reference beam. Large incidence angles should then be expected as to allow a diminution of the recording distance.

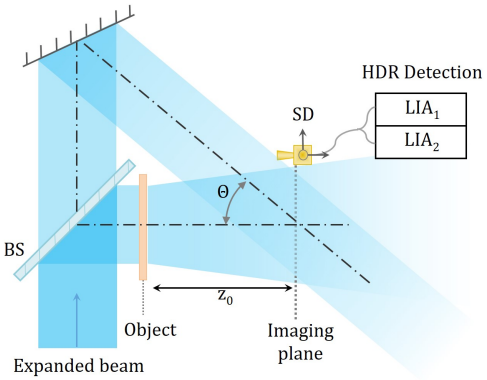

Figure V.15: Diagram of the experimental implementation for holography coherent imaging in transmission configuration, using HDR detection.

However, the larger the incidence angle, the narrower the interfringe distance, then requiring smaller recording pitch and small aperture sensors. From the bases of interference in air-corner configuration, the following relation between the interfering angle Θ [rad], and Λ the spatial interfringe period [m] can be extracted:

$$\Lambda = \frac{\lambda_0}{sin(\Theta)}. \tag{V.11}$$

Accounting for the obstruction generated by the BS and object, an off-axis angle of Θ = 43° was considered, leading to an interfringe distance of 1.41 mm in absence of a diffractive object, according to Equation V.11. Such a reference interferogram is depicted in Figure V.16a and features the expected interfringe as well as a certain inhomogeneity on the respective beam intensity with a donut-shaped profile. The same beam profile was used for the previously described iterative phase retrieval setups. The obtained interfringe distance remains larger than the dimensions of the used open SD integrated WR 3.4 waveguide effective dimensions. Consequently, it ensures a fully contrasted recording of the intereference pattern. Typical lateral recording pitches of 100 µm to 200 µm are considered.

The subsequent Figure, Figure V.16b, depicts the recorded hologram in presence of the previously featured phase sample, depicted in Figure V.11, recorded with a z_0=10 cm object-recording plane distance. From this intensity profile $I_{z_o}(x,y)$, a transposition in the spatial frequency domain of the amplitude distribution, through a two-dimensional FFT, leads to the spatial spectrum in the fourier space, depicted in Figure V.16c. The logarithmic amplitude view depicts the different interfering orders. A spectral filtering, as to recover the +1 order, detailed with the dashed box can then be applied before a subsequent back-transposition in the spatial domain as to recover the wave front on the measurement plane. A final focusing step can then be considered through a back propagation in the object plane, following Equation V.1.

Thanks to the simplified and less demanding recording process with respect to the iterative phase retrieval scheme, the obtention of a probe reference interferogram is facilitated. Subse-

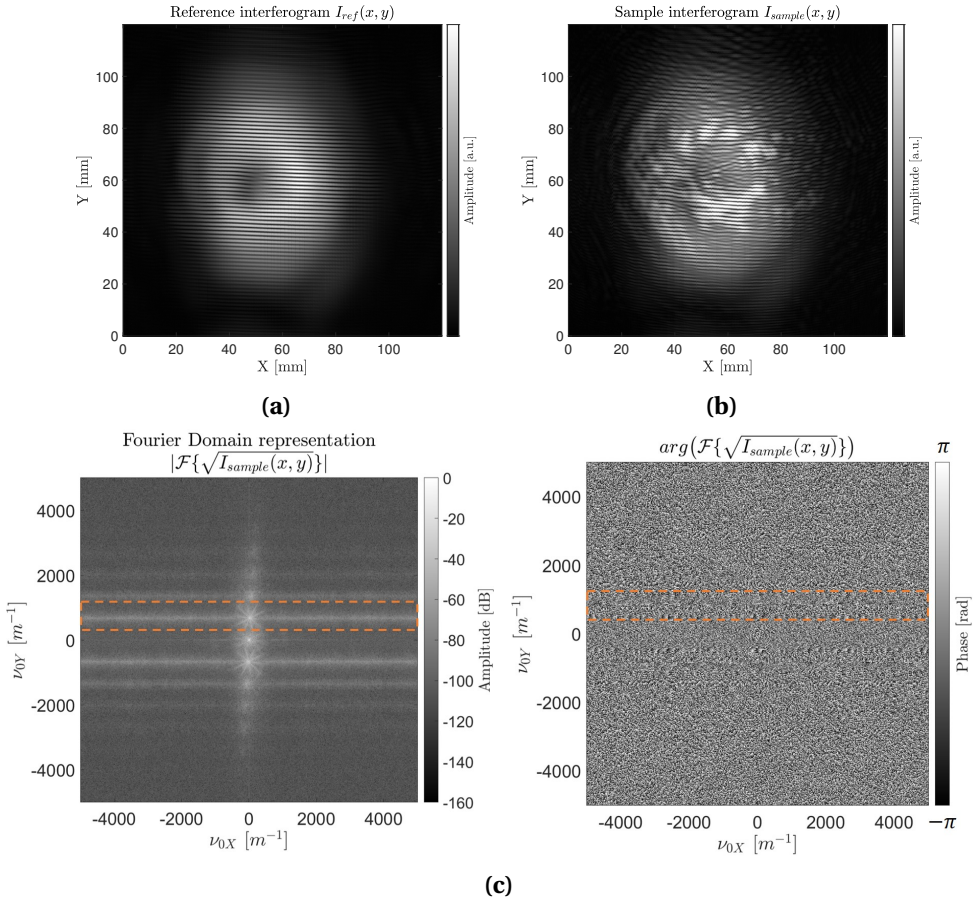

Figure V.16: **(a)** Reference interferogram, collected in absence of sample and **(b)** sample interferogram. **(c)** Amplitude and phase representation of the spatial 2D Fourier transform of the sample interferogram. A dashed frame depicts the subsequent Fourier space order filtering.

quently following an identical data processing, the probe wave front in the object plane, p(x,y,0), can be recovered as to perform a normalization phase adjustment. The resulting recovered wave front is displayed in Figure V.17.

As expected thanks to the probe phase subtraction, it features a homogeneous phase background, allowing to clearly assess the sample induced phase-shift with respect to the raw phase

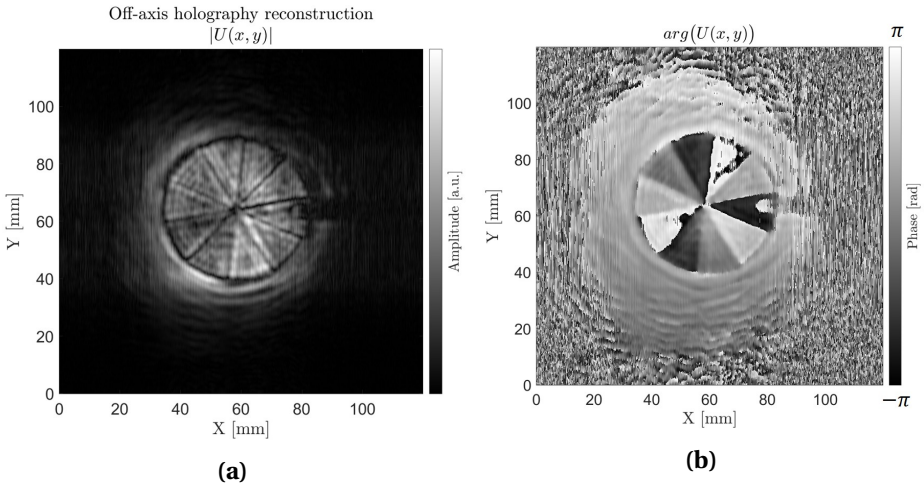

Figure V.17: Recovered complex wave front through off-axis holography inspection and subsequent probing phase subtraction.

retrieval operation of Figure V.14, in absence of reference normalization. The presence of 2 π phase jumps between subsequent steps relates to the induced phase shifts through the crossing of the sample with thickness variations larger than a single wavelength over the whole sample. This aspect hence prevents the direct assessment of the absolute thickness for such a mono-chromatic approach. Nevertheless, with a prior knowledge of the raw sample geometry, the height jumps of 500 to 550 µm, described in section IV.4.4, equivalent to optical thickness difference ranging from 750 to 837 µm when accounting for the sample refractive index $\tilde{n}_{\mathrm{HDPE}} = 1.523 - i1e^{-3}$, would induce 4.6 rad to 5 rad phase shifts, since λ_0=1.045 mm at f=287 GHz. With the unavoidable 2π wrapping featured in Figure V.17b, such phase differences can be reliably retrieved for most steps even though this sample displays step-size optically close to the sensing wavelength. The consideration of smaller steps would grand an absolute step thickness assessment, devoided of such 2π wrapping. From the phase standard deviation obtained in each step ROI, in the order of 0.5 rad, thickness or refractive index deviations leading to optical path variations down to 85 µm should be resolvable.

On the focalization perspective, even though a proper focalization leads to a sub-millimetric resolution, hence sub-wavelength resolution, no additional extensive assessment has been conducted on this point as it will be highly impacted by the object-imaging plane distance, thus, reliant on the object geometry.

V.4.3 Toward real-time phase retrieval in terahertz regime

The previously detailed coherent imaging procedure, featuring the recording of the diffracted field through a single pixel raster scan based scheme, obviously remains an extremely time consuming procedure. Especially for the demanding multi-plane phase retrieval, with recording times over 36 hours a drastic improvement remains necessary to provide a viable development of this method, even in an academic context. Namely, as a first step optimization, the recording of a reference wave front, for the subtraction of a phase background, required for the optimization of Figure V.14, remains a tedious operation. To remedy this time consuming process, once again induced by the integration time required by LIAs, the employment of focal plane arrays is applied to SBMIR Phase retrieval in the following section.

With the quite recent developments of prospective coherent imaging scheme in the sub-millimeter spectral range, little work demonstrated the use of camera arrays for multi-plane intensity phase retrieval schemes. With a fixed implementation, interferometric holography demonstrated the usefulness of such hardware for instantaneous recording or mapped reconstructions of the generated interferogram [15, 20, 33–36]. They mainly relied on pyroelectric cameras or extended LWIR cameras, exploiting a reminiscent sensitivity in the terahertz domain.

Nevertheless, even with the extreme setup simplicity for SBMIR iterative phase retrieval, most work have based multi-plane intensity recording on the previously explored single point raster scan-based detection scheme [30, 37] due to the displacement of the measurement plane. The employment of focal arrays has solely been demonstrated for an application of phase retrieval behind a moving and scattering barrier in [28].

Experimental implementation

From the use of bolometric cameras for full-field imaging applications, detailed in section II.3, devoided of imaging lens, a bare array sensor can be deployed as a direct recording device for the assessment of a diffraction field.

In a straightforward transmission configuration, such a recording setup of the subsequent intensity profiles, $\mathrm{I}_{z_k}(x, y)$, should simply be completed by the illumination source, and eventual beam-shaping elements. In this work, Lytid's teracascade 1000 QCL source, previously featured in section II.3, with an emission power of 1.3 mW at 2.5 THz has been employed in combination with its integrated mirror-based auto-alignment unit to provide a collimated illumination beam through 1" optics, as featured in Figure II.14a. Such a limited illumination finds itself suitable in

comparison to the previously investigated 287 GHz integrations, as an obvious setup rescale with respect to the used the wavelength should be expected when ranging up to 2.5 THz.

In fine, as depicted in Figure V.18, the source, combined with the collimation optics, have been coupled to a simple focal plane array devoided of imaging lens, mounted on a translation stage for the longitudinal scanning of the diffraction pattern along the optical axis.

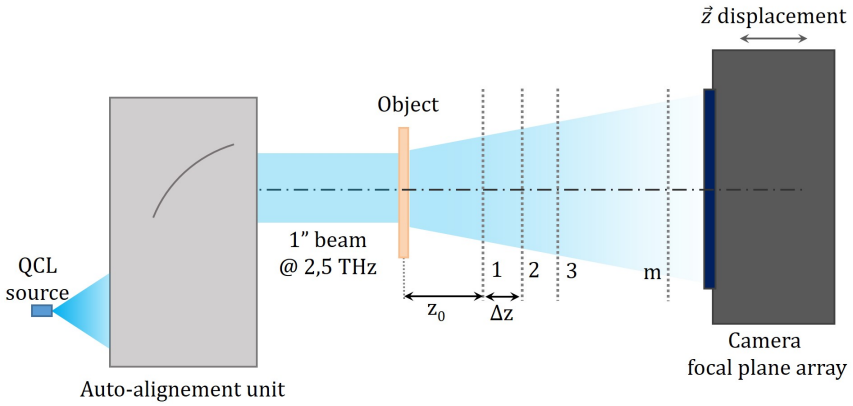

Figure V.18: Diagram of the experimental implementation for real-time phase retrieval measurement in transmission configuration.

Prior experiments have been performed using the first generation INO IRXCAM Camera (288 × 384 pixels matrix with 35 µm pitch), that displayed stability issues over the recording operations, hence, limiting the measurement repeatability. Additionally, a drastic lack of sensitivity, coupled with the mW illumination level, constrained the intensity recording to diffracted low spatial frequencies. The subsequent SBMIR data processing steps then led relevant reconstructions on restricted portions of the illumination field.

The tenfold increase in sensitivity with the I2S camera (240 × 320 pixels matrix with 50 µm pitch) has then been employed for the recording of the data-sets. To assess the longitudinal intensity profile, $I_{z_k}(x,y)$, a continuous displacement, at the speed of 10 $mm.s^{-1}$ is used and, accounting for the 25 FPS recording frame rate, a Δ_z=400 µm longitudinal recording pitch is achieved. A stack of ten images, along a 4 mm range, is considered, hence requiring a recording time below 1 second.

SBMIR phase retrieval

In this transmission configuration, a PP injected phase object sample, displayed in Figure V.19a has been selected such that apparent features would suite the expected resolution. The two specifically investigated topographic elements are highlighted through dashed boxes. From such rectangular images real-time recorded data-sets, partially displayed through Figure V.19b, V.19c and V.19d, a square 240×240 pixel selection of the diffracted field, centered on the sample portion of interest is cropped as to fit the algorithmic approach.

Using such cropped intensity-sets, the unsorted SBMIR procedure is applied to reach the wave fronts displayed in Figure V.20. A precise mechanical assessment of the first measurement plane distance, z_0, is impracticable in such a configuration due to the obstruction of the camera mechanical structure, as well as the unreachable sensor plane, lodged behind a protective window. A direct focused reconstruction on the object plane, following each SBMIR step, remains then inconceivable. The wave front reconstruction has then to be performed at a raw estimated object plane position and further focused in a subsequent effort.

Figure V.20a displays the complex wave front retrieved from the data-set featured in Figure V.19, centered on the UP topographic element, following 100 SBMIR iterative steps, focused at z_0 = 15.5 mm. Figure V.20b demonstrates the results obtained on the PP recycling profile pictogram, at z_0 = 11.9 mm. With the high transparency of this material, the phase profiles bring most insight

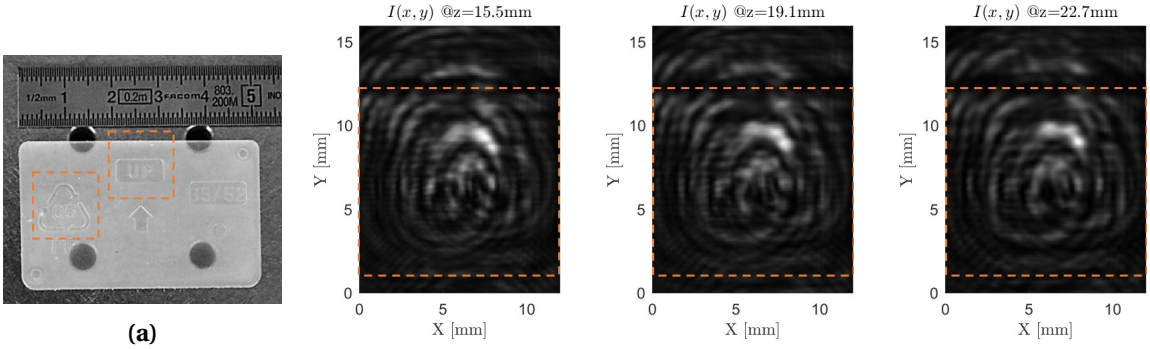

Figure V.19: **(a)** Phase sample under inspection featuring two ROIs. Selected raw measurement diffracted field profiles, $I_{z_k}(x, y)$, for the UP ROI at **(b)** 15.5 mm, **(c)** 19.1 mm and**(d)** 22.7 mm from the object plane.

on the sample event hough the amplitude distribution features well defined refraction impacted topographic edges.

From such recovered wave fronts, large reminiscent artifacts of the background illumination remain noticeable. Indeed, a strong inhomogeneity in the amplitude profile and the phase distribution are highly deteriorating the reconstruction. Those artifacts are partially due to the use of off-axis parabolic mirrors in the beam shaping collimation unit, that can lead to the appearance of high optical aberrations.

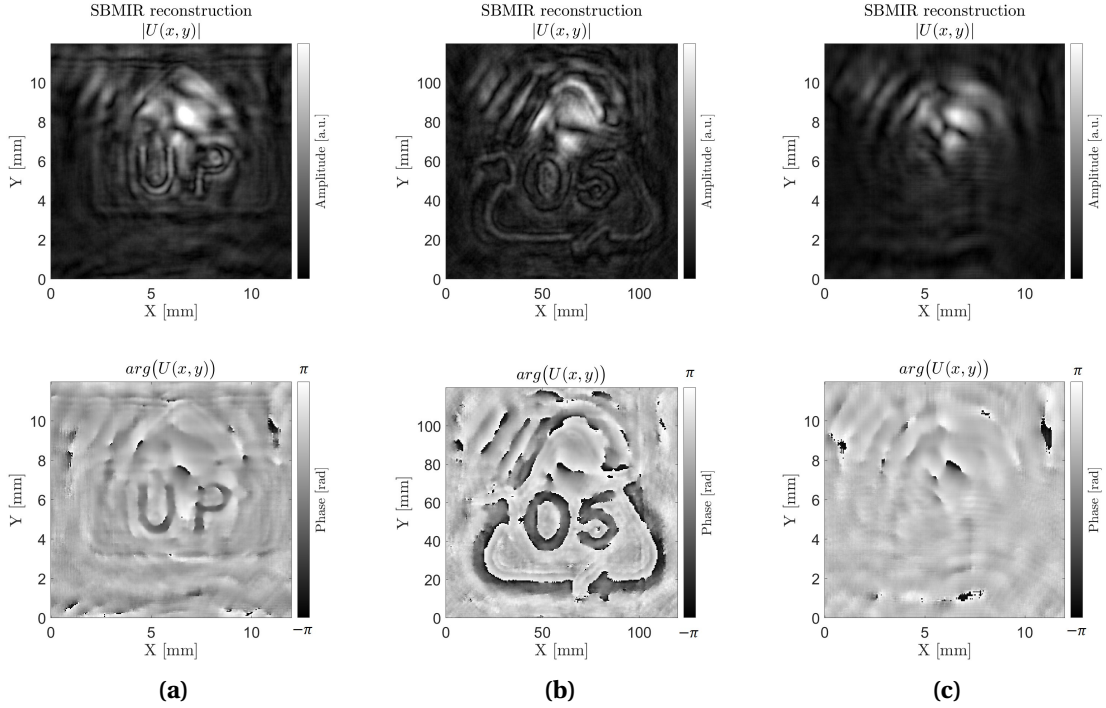

Figure V.20: Reconstructed wave front from the unorded SBMIR procedure for **(a)** the UP ROI and **(a)** the PP recycling sign, focused at $z_0 = 15.5$ mm and $z_0 = 11.9$ mm respectively. **(c)** reconstructed probe reference wave front, in absence of a diffractive sample, for $z_0 = 15.5$ mm.

Following Equation V.6, a reference probe wave front subtraction, p(x,y,0), can then be pursued thanks to the highly reduced recording time, using such a real-time imaging implementations. Indeed, unlike for the single point raster-scan based approach, the obtention of the reference probe profile, depicted in Figure V.20c then becomes quite straightforward for a full diffracted field assessment under a second, and the subsequent application of the SBMIR algorithm. A normaliza-

tion of the wave front under inspection by the probe wave front, propagated in the plane of interest then leads to the sole contribution of the sample.

Figure V.21 displays the subsequent normalized phase for the UP ROI. A much more stable phase profile is obtained, with the mitigation of the major phase inhomogeneities on the top part of the image. A proper reconstruction of the UP topological feature is reached, along with a distinction of the encircling extrusion, as well as the horizontal sample boundary line at y=11 mm.

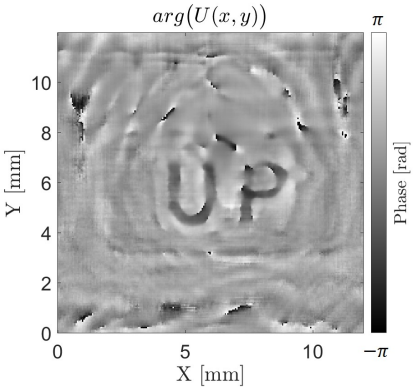

Figure V.21: Phase profile of the normalized reconstruction in the object plane.

A reminiscent phase inhomogeneity, also witnessed on the normalized amplitude reconstruction, remains noticeable and is induced by another major limiting factor. One could notice that the lower part of the reconstructed profile features a more stable reconstruction, with respect to the top half in Figure V.20. This limitation is linked to the previously inferred diffraction field cropping, applied to the recorded data-sets. Indeed, due to the limited coverage of the diffraction field by the sensor area, a non-negligible loss of information is incurred and leads to the appearance of drastic edges artifacts. This effect is especially exacerbated with the cropping of predominant diffracted signal portions, well depicted in Figure V.19 with the non-consideration of the top section of the diffracted field. It will hence impact the sample and reference wave front reconstructions, leading to inaccurate distributions.

In contrast, such artifacts were not witnessed on the previous low frequency raster-scan processes, owing to the adequate recording of large fields. It then ensured the collection of the whole diffracted profiles, leading to limited numerical cropping artifacts.

The deployment of the self-extrapolation algorithm, with a numerical extension of the effectively considered field should then allow the consideration of the whole measurement intensity profiles. From the initial iteration, a spatial zero-padding of the recorded diffraction profiles $I_{z_k}(x,y)$ to an extended square field is performed, followed by an eventual apodization operation. Such considerations are limiting edge effects. In addition, the reference normalization can be performed along the iterative SBMIR steps for visualization purposes and lead to the retrieval of the wave front depicted in Figure V.22.

The phase distribution, along with the amplitude profiles, recovered through such methods features a more precise outlines of the object topological profile, along with a stable background wave front. A convergence in the vicinity of the initial measurement field is as well observed.

Through the intrinsic cropping of the diffraction field by the limited size of the sensor, the previously predominant edge-artifacts remains noticeable but have been warded out of the central feature of interest with respect to the initial reconstructions, on the ground that larger measurement field in the $\vec{y}$ direction have been considered. A larger sensor or an extended mapping through an additional lateral scanning of the array [35] would better suite the initial beam size and hence, subsequent diffraction field for recording.

Beyond those artifacts, from the phase profile, once again, a topological dimensioning can be performed. The element of interest features a depth difference of 100 µm, extracted from microscopy investigations. Once again accounting for the real part of the refractive index of the material, n_{PP}=1.515 [38], and the effective wavelength of 120 µm when operating at 2.5 THz, a 8.1 rad phase difference is expected. Accounting for the 2π phase wrapping, the expected 1.8 rad phase jump is accurately retrieved even though a spatial standard deviation of 0.4 rad is witnessed. With this wavelength scalling, up to 2.5 THz, topological measurement capabilities below 10 µm can be then expected.

In this extremely simplified setup, solely featuring beam shaping optics and a longitudinal displacement of a bare array sensor, a limited diffraction field recording under 1 second allows for the

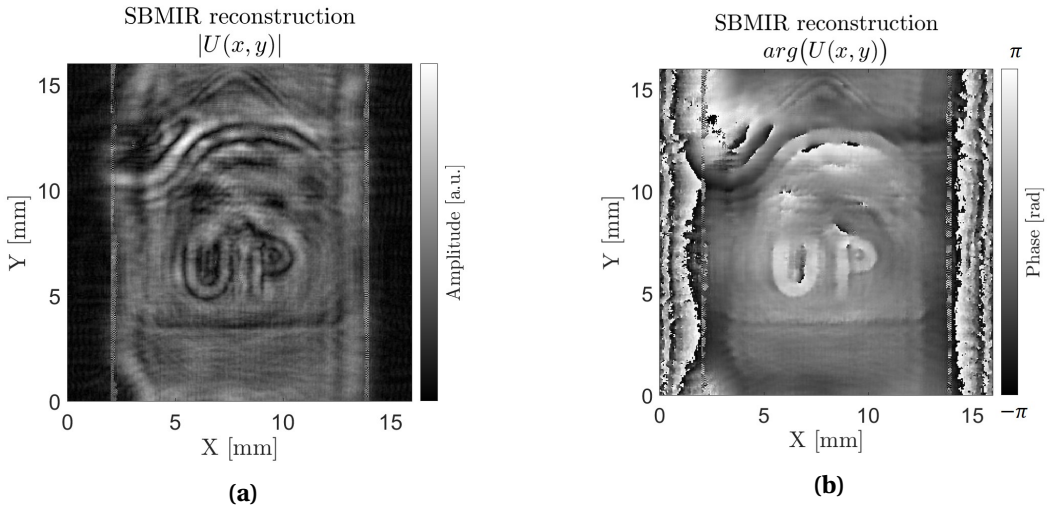

Figure V.22: Recovered complex wave front through iterative phase retrieval using the unsorted self-extrapolation SBMIR procedure along with a reference probe field normalization.

retrieval of a reliable complex wave front through the use of the unsorted self-extrapolation SBMIR algorithmic procedure. It led to the recovering of focused wave front with lateral resolutions in the order of the sensing wavelength and a step resolution below 100 µm from the recovered phase profile.

V.5 Conclusion

Emerging from electron sensing and X-ray imaging through the recording of diffraction scattered fields, coherent imaging activities advocated their usefulness in the limited requirement for optical components, hence overcoming inherent imaging aberration problematics in those fields to reach high resolution levels [7, 39]. Subsequently ranged in the visible and IR spectral domains [40], and based on incoherent sensing schemes, it has been demonstrated to overcome the phase problem through different algorythmic and instrumental processes, as to retrieve the phase of an electric field. Such approaches then represent performant analysis and sensing tools, with enhanced lateral resolutions, through reduced optical complexity and are still witnessing current advances and developments [41].

In the continuity of those developments, this section focused on the specificities of the transposition of coherent imaging in the sub-millimetric spectral range. It unveiled imaging system simplifications, enhanced resolution levels and phase sensitive inspections methods.

As an initial theoretical consideration, diffraction principles, based on free-space propagation operators have been detailed with the recall of Fourier optics bases. Notably, the consideration of the free-space propagation transfer function, $H_d(\nu_{0x}, \nu_{0y})$, with the use of the angular spectrum equation, is featured. Common sensing procedures and related algorithmic approaches for such phase reconstruction have then been reviewed. Namely, the interferometric holography approach has been detailed in off-axis configuration, followed by the a brief depiction of the ptychography mode of operation, and completed by the single beam multiple intensity diffractive approach as the center methodology featured in this chapter.

Ongoing developments in the field of iterative terahertz phase retrieval using the SBMIR algorithmic approach was demonstrated in a reflection geometry using millimeter waves at the frequency of 287 GHz. The synthesis of high-dynamic-range intensity distributions from a single detector with two independent lock-in amplifiers was proposed and experimentally validated as a drastic wave front reconstruction improvement was witnessed. It was established that, in such optimized configurations, SBMIR terahertz phase retrieval provides a non-negligible resolution en-

hancement in the amplitude distribution to reach sub-millimeter resolutions in comparison with the reference widespread technique of raster-scan focused point imaging at the same frequency. A reliable phase distribution reconstructions was as well featured as eligible for quantitative topological assessment.

A radical setup simplification led to similar investigations in a transmission configuration, specifically adequate on the inspection of phase samples. Through such a geometry, the unobstructed access to the sample diffraction wave front in near-field allows for enhanced resolution achievements. However, the tedious and time consuming single pixel detector raster-scan recording process remains a major hindrance to the maturation of this inspection method. Namely, through the consideration of a reference measurement in absence of a sample, a straightforward wave front normalization, for the consideration of the probe beam, remains impracticable in a descent time frame. For methodology comparison, the consideration of the interferrometric holography approach has been depicted. Even though the inspection setup is complexified, the recording of a single diffraction field plane confers a non-negligible advantage from which, the use of a normalization procedure have been demonstrated.

Once again working toward the substitution of the conventional single point data-registration, subsequent advances and system scaling led to the employment of a focal plane array for iterative phase retrieval with the development of a system operating at 2.5 THz in transmission configuration with real time recording. Such full-field lensless field mapping ensures the assessment of a multi-plane measurement diffraction field under one second, as to subsequently consider the SBMIR iterative phase retrieval approach. Due to the intrinsically limited recording array field size, that leads to non negligible spatial distribution signal cropping during recording, substantial artifacts have been witnessed with the use of the conventional unsorted SBMIR procedure. The simplified consideration of a probe wave front subtraction ensure subtle improvements on the phase profile with still cropping related artifacts. The consideration of a numerical field enlargement SBMIR approach then featured a more precise outlines of the object topological profile, along with a more stable background wave front.

Such prospective demonstrations of coherent imaging exposed scalability performances through their transposition in the sub-millimeter waves spectral range with the penetrability of dielectric materials as a favorable characteristic for transmission configurations. In this continuity, further developments for real-time phase retrieval approaches are intended with array based enlarged field mapping and sub-sampling to overcome certain encountered limitations. Such wave front retrieval tasks can be intended as to develop efficient and simplified tools for coherent sensing, optical characterization problematics with beam shaping applications, quasi-optical components performances assessments or phase array and wave front shapers investigations.

V.6 Bibliography

[1] Mathilde Brossard, Jean-François Sauvage, Mathias Perrin, and Emmanuel Abraham. Terahertz adaptive optics with a deformable mirror. *Optics letters*, 43(7):1594–1597, 2018. 178

[2] Bevan B Baker and Edward Thomas Copson. *The mathematical theory of Huygens' principle*, volume 329. American Mathematical Soc., 2003. 178

[3] Edward G Steward. *Fourier optics: an introduction*. Courier Corporation, 2004. 179

[4] Okan K Ersoy. *Diffraction, Fourier optics and imaging*, volume 30. John Wiley & Sons, 2006. 179

[5] Robert K Tyson. *Principles and applications of Fourier optics*. IOP Publishing, Bristol, UK, 2014. 179, 180

[6] Junchang Li, Zujie Peng, and Yunchang Fu. Diffraction transfer function and its calculation of classic diffraction formula. *Optics communications*, 280(2):243–248, 2007. 180

[7] JN Chapman, AB Johnston, LJ Heyderman, S McVitie, WAP Nicholson, and B Bormans. Coherent magnetic imaging by tem. *IEEE Transactions on Magnetics*, 30(6):4479–4484, 1994. 181, 198

[8] Ulf Schnars, Claas Falldorf, John Watson, and Werner Jüptner. Digital holography. In *Digital Holography and Wavefront Sensing*, pages 39–68. Springer, 2015.

[9] John M Rodenburg. Ptychography and related diffractive imaging methods. *Advances in imaging and electron physics*, 150:87–184, 2008. 181

[10] Lorenzo Valzania, Yuchen Zhao, Lu Rong, Dayong Wang, Marc Georges, Erwin Hack, and Peter Zolliker. Thz coherent lensless imaging. *Applied optics*, 58(34):G256–G275, 2019. 181, 183

[11] Dennis Gabor. A new microscopic principle. *nature*, 161:777–778, 1948. 181

[12] Kai Xue, Qi Li, Yun-Da Li, and Qi Wang. Continuous-wave terahertz in-line digital holography. *Optics Letters*, 37(15):3228–3230, 2012. 181

[13] Lu Rong, Tatiana Latychevskaia, Chunhai Chen, Dayong Wang, Zhengping Yu, Xun Zhou, Zeyu Li, Haochong Huang, Yunxin Wang, and Zhou Zhou. Terahertz in-line digital holography of human hepatocellular carcinoma tissue. *Scientific reports*, 5(1):1–6, 2015. 181

[14] Etienne Cuche, Pierre Marquet, and Christian Depeursinge. Spatial filtering for zero-order and twin-image elimination in digital off-axis holography. *Applied optics*, 39(23):4070–4075, 2000. 182

[15] Ronan J Mahon, J Anthony Murphy, and William Lanigan. Digital holography at millimetre wavelengths. *Optics Communications*, 260(2):469–473, 2006. xii, 182, 194

[16] Michael Liebling, Thierry Blu, and Michael Unser. Complex-wave retrieval from a single off-axis hologram. *JOSA A*, 21(3):367–377, 2004. xii, 182

[17] Mitsuo Takeda, Hideki Ina, and Seiji Kobayashi. Fourier-transform method of fringe-pattern analysis for computer-based topography and interferometry. *JosA*, 72(1):156–160, 1982. 182

[18] Kyoji Matsushima, Hagen Schimmel, and Frank Wyrowski. Fast calculation method for optical diffraction on tilted planes by use of the angular spectrum of plane waves. *JOSA A*, 20(9):1755–1762, 2003. 182

[19] Qi Li, Sheng-Hui Ding, Yun-Da Li, Kai Xue, and Qi Wang. Research on reconstruction algorithms in 2.52 thz off–axis digital holography. *Journal of Infrared, Millimeter, and Terahertz Waves*, 33(10):1039–1051, 2012. 182

[20] Haochong Huang, Dayong Wang, Lu Rong, Spozmai Panezai, Donglei Zhang, Peiyao Qiu, Lu Gao, Hua Gao, Haokun Zheng, and Zhiyuan Zheng. Continuous-wave off-axis and in-line terahertz digital holography with phase unwrapping and phase autofocusing. *Optics Communications*, 426:612–622, 2018. 182, 194

[21] John M Rodenburg and Helen ML Faulkner. A phase retrieval algorithm for shifting illumination. *Applied physics letters*, 85(20):4795–4797, 2004. 183

[22] Andrew M Maiden and John M Rodenburg. An improved ptychographical phase retrieval algorithm for diffractive imaging. *Ultramicroscopy*, 109(10):1256–1262, 2009. 183

[23] Igor A. Shevkunov, Nikolay S. Balbekin, and Nikolay V. Petrov. Comparison of digital holography and iterative phase retrieval methods for wavefront reconstruction. *Proc. SPIE*, 9271:927128, nov 2014. 183

[24] Nickolay V Petrov, Victor G Bespalov, and Andrei A Gorodetsky. Phase retrieval method for multiple wavelength speckle patterns. In *Speckle 2010: Optical Metrology*, volume 7387, page 73871T. International Society for Optics and Photonics, 2010. 183

[25] Giancarlo Pedrini, Wolfgang Osten, and Yan Zhang. Wave-front reconstruction from a sequence of interferograms recorded at different planes. *Optics letters*, 30(8):833–835, 2005. 184

[26] Percival Almoro, Giancarlo Pedrini, and Wolfgang Osten. Complete wavefront reconstruction using sequential intensity measurements of a volume speckle field. *Applied optics*, 45(34):8596–8605, 2006. 183, 184

[27] Jonel F Binamira and Percival F Almoro. Accelerated single-beam multiple-intensity reconstruction using unordered propagations. *Optics letters*, 44(12):3130–3133, 2019. 184

[28] Lorenzo Valzania, Peter Zolliker, and Erwin Hack. Coherent reconstruction of a textile and a hidden object with terahertz radiation. *Optica*, 6(4):518–523, 2019. 184, 194

[29] Nikolay V Petrov, Victor G Bespalov, and Mikhail V Volkov. Phase retrieval of thz radiation using set of 2d spatial intensity measurements with different wavelengths. In *Practical Holography XXVI: Materials and Applications*, volume 8281, page 82810J. International Society for Optics and Photonics, 2012. 184

[30] Nikolay V Petrov, Jean-Baptiste Perraud, Adrien Chopard, Jean-Paul Guillet, Olga A Smolyanskaya, and Patrick Mounaix. Terahertz diffractive reflection phase imaging. In *2020 45th International Conference on Infrared, Millimeter, and Terahertz Waves (IRMMW-THz)*, pages 1–1. IEEE, 2020. 184, 194

[31] RF User's Manual Model SR844. Lock-in amplifier standford research systems. *Inc., Sunnyvale, CA*, 1997. 186

[32] A.V. Belashov, N.V. Petrov, and I.V. Semenova. Digital off-axis holographic interferometry with simulated wavefront. *Opt. Express*, 22(23):28363–28376, 2014. 188

[33] Erwin Hack, Lorenzo Valzania, Gregory Gäumann, Mostafa Shalaby, Christoph P Hauri, and Peter Zolliker. Comparison of thermal detector arrays for off-axis thz holography and real-time thz imaging. *Sensors*, 16(2):221, 2016. 194

[34] Sheng-Hui Ding, Qi Li, Yun-Da Li, and Qi Wang. Continuous-wave terahertz digital holography by use of a pyroelectric array camera. *Optics letters*, 36(11):1993–1995, 2011.

[35] Peter Zolliker and Erwin Hack. Thz holography in reflection using a high resolution microbolometer array. *Optics express*, 23(9):10957–10967, 2015. 197

[36] Massimiliano Locatelli, Marco Ravaro, Saverio Bartalini, Luigi Consolino, Miriam S Vitiello, Riccardo Cicchi, Francesco Pavone, and Paolo De Natale. Real-time terahertz digital holography with a quantum cascade laser. *Scientific reports*, 5(1):1–7, 2015. 194

[37] Greg Hislop, Li Li, and Andrew Hellicar. Phase retrieval for millimeter-and submillimeter-wave imaging. *IEEE transactions on antennas and propagation*, 57(1):286–290, 2009. 194

[38] Lu Rong, Fangrui Tan, Dayong Wang, Yaya Zhang, Kunlun Li, Jie Zhao, and Yunxin Wang. High-resolution terahertz ptychography using divergent illumination and extrapolation algorithm. *Optics and Lasers in Engineering*, 147:106729, dec 2021. 197

[39] JM Zuo, I Vartanyants, M Gao, R Zhang, and LA Nagahara. Atomic resolution imaging of a carbon nanotube from diffraction intensities. *Science*, 300(5624):1419–1421, 2003. 198

[40] Christopher J Mann, Lingfeng Yu, Chun-Min Lo, and Myung K Kim. High-resolution quantitative phase-contrast microscopy by digital holography. *Optics Express*, 13(22):8693–8698, 2005. 198

[41] Yair Rivenson, Yichen Wu, and Aydogan Ozcan. Deep learning in holography and coherent imaging. *Light: Science & Applications*, 8(1):1–8, 2019. 198

General Conclusion

As a general guiding thread, this work has been focused on the enhancement of sensing and imaging techniques in the terahertz and millimeter-waves spectral ranges, oriented toward specific topics of interest in the field of non-destructive testing, as to bridge with industrial applications. The origin of this work is based on the recent developments in terahertz instrumentation with the emergence of powerful sources, sensitive detectors, integrated sensor arrays, as well as the investigation of advanced sensing schemes. In this context, this work incorporates three main instrumentation approaches.

As an opening thematic, general imaging considerations have been at the center of these developments, with a focus on continuous wave sensing. From a basic imaging scheme, based on a single point sensing operation, with a raster scanning of the element under inspection, multi-spectral imaging results have been obtained. Spanning over a wide portion of the terahertz down to the millimeter-wave spectral ranges, optimal sample representations are retrieved thanks to the nominal achievable resolution and illumination background power stability. Although not entitled to major breakthroughs, beside technical enhancement implementations, this basic imaging process grasped the inherent problematics at stake for ranging to more complex sensing schemes. Despite its highly adaptable aspect, adequate for prospection works, the unequivocal limitation remained the imaging acquisition speed, preventing any relevant transfer beyond academic testing.

The use of sensor arrays, to move toward full-field real time imaging was shown to be the most adequate alternative to remedy this drawback and ultimately meet the requirements for industrial thematics. To reach a fully operational system, mainly working at 2.5 THz in this implementation, several physical limitations have nevertheless been tackled. Namely, the optical coherence of the illumination beam represents a devastating aspect for quantitative imaging, while power density spreading then also represents a technical constraint when ranging up to full-field illumination. To cope with such aspects, the development of a beam steering galvanometric integration allowed for a drastic mitigation of the coherence induced artifacts, along with the provision of a full control over the illumination pattern, for power handling. It then represents a versatile imaging tool, adaptable for enhanced illumination procedures. It is hence suited for the inspection of wide-field low absorption samples, up to reduced areas considerations for high power density sensing on more opaque items. Resolution levels down to 280 µm at 2. THz and 222 µm at 4.7 THz have been demonstrated, with working distances ranging from 10 to 40 cm and ensuring a 25 FPS full-field recording frame rate. With such capabilities, real-time recorded tomographic reconstructions have then been considered as to highlight the contrast with continuous wave single point recordings.

Beyond such straightforward inspection, the consideration of advanced coherent sensing schemes often provides enhanced capabilities, with high measurement dynamic ranges, high measurement rates along with an additional phase information in most cases. In this scope, with non-destructive inspection as a target application field, the development of a frequency modulation based homodyne sensing scheme, in the millimeter wave spectral range, stood at the central effort of this work.

To meet with several applicative prerequisites, a central frequency in the 150 GHz band has been considered and complemented with a modulation bandwidth of 32 GHz, as to reach lateral resolutions in the millimeter range and an expected longitudinal resolution of 4.6 mm originat-

ing from the Frequency Modulated Continuous Wave mode of operation. As a driving foundation brick, a fast hybrid Phase Locked Loop, able to provide a suitable triangular highly linear full-band sweep in 65 µs has been developed. Subsequently, a mono-static transceiver geometry, based on harmonic mixing has been integrated among a standard single point quasi-optical setup. Substantial development characterizations detailed in this work, corroborated an optimized instrumental implementation, which still demonstrated a significant deviation from the ideal FMCW model. Namely, the probing chirp and local oscillator spectral characteristics led to an alteration of the impulse spectral response of such a system, hence requiring the enforcement of a two-points normalization procedure. A clear description of this algorithmic approach was detailed and supported by analytical considerations, as to highlight the resultant corroboration with the ideal FMCW longitudinal sensing operation. From such resulting coherent signals, dedicated characterizations addressed the capabilities of the developed transceiver. Namely, a raw measurement rate of 7.62 kHz is granted through the embedded FPGA based data-processing. The expected lateral and longitudinal resolutions levels of 4.6 mm have as well been experimentally validated. Thanks to the robustness procured by the integrated Phase Locked Loop, stability measurements established no performance losses over several hours of continuous operation without the need for intermediate recalibrations. Highly impacted by the measurement integration time, the longitudinal precision positioning has been effectively quantified down to 3.6 µm. Finally, an abacus of the achievable measurement dynamic range is provided with SNR levels above 90 dB for few seconds recording windows, and approaching 60 dB when considering the 7.62 kHz full speed measurement rate of 130 µs.

Based on those performance figures, as to entrench the capabilities of the developed FMCW transceiver, targeted proofs of principle were dedicated to current thematics, in accordance with industrialists requirements for niche problematics. A prime consideration of volumetric inspection highlighted the benefits of the FMCW operation, with the embedding of the additional longitudinal inspection dimension. Through raster scan imaging, the prospection toward specific cases of interest, with polymer soldering traces testing and the inspection of pharmaceutical packagings, demonstrated the excellent suitability of this sensing method for such industrial applications.

More specifically centered on the inherent depth sensing of FMCW operations, coupled to materials penetrability, the monitoring of millimetric-level thicknesses in multi-layers structures defines a growing industrial topic of interest. As to provide a technical background, a parallel with terahertz time domain extraction of micrometric-level stratified paint layer thicknesses has been provided. It ensued on the definition of a sample physical model adapted to the coherent homodyne FMCW detection scheme. Extraction approaches have subsequently been considered and led to experimental investigations with optical thickness extractions below 2 mm, hence well under the developed transceiver longitudinal resolution, with relative errors below 1%. A clear identification of the minimal sensible single-layer thickness remains to be specifically addressed. The extension toward multi-layered structures, through the consideration of an optically contrasted three-layers stack, advocates in favor of the adequacy of this monitoring approach, still in its early stage.

Additional topics have as well been explored in the continuity of the applicative technological maturation of the FMCW scheme. Initiated among the aeronautics industrial field, penetrating see-through inspection aims to reduce the requirements for plane dismantlement during preventive maintenance phases. Inspection through an interior plane cover allowed for the depiction of metallic samples, moisture presence and structural defects. In addition, with the goal of providing proof of concept beyond contactless sensing for FMCW systems, an instrumentation development has been investigated for remote sensing through the simplified integration of guided geometries. The enhanced guided sensitivity, provided by the embedded longitudinal discrimination ability, led to the demonstration of end-of-guide imaging capabilities with resolution down to 1.4 mm at 122 GHz and dynamic range up to 27 dB, decorrelated from the embedded sensing along the waveguide.

Lastly, as a more prospective coherent imaging process in the terahertz spectral range, wave front reconstructions has been operated through the transposition of lensless imaging techniques. Such considerations, based on incoherent recordings, provides the expected additional phase information of interest through the assessment of the diffraction patterns, induced by the object under inspection. Specifically, a sub-millimetric integration, operating at 287 GHz focused on an iterative phase retrieval in a challenging normal reflection configuration. From the recording of the intensity diffraction field at different distances, the enforcement of the iterative SBMIR algorithmic procedure led to the recovering of a focused complex wave front, in the object plane. A transposition in a straightforward transmission configuration specifically suits the inspection of phase objects. For comparative purposes, the interference based off-axis digital holography has as well considered in a transmission configuration at 287 GHz. The inspection of phase object highlighted sub-millimetric topographic inspection with the consideration of the wavefront phase along with sub-wavelength lateral resolution. Once again highly restricted by the recording rate of the single point scheme, a scaling to a higher frequency spectral range, for real-time recording operation through the use of a sensor array, has been operated. Namely, at 2.5 THz, real-time iterative phase retrieval in a transmission configuration demonstrated convincing coherent sensing capabilities.

In fine, although the terahertz research field remains in its quite early stage, this work featured an effort dedicated to the obtention of a consistent step toward closing the gap with the industrial technological transposition. Naturally, an aim at specific unsolved niche applications is to be expected, beyond the grasp of well-established NDT technologies. In contrast with the decades of developments that those approaches accumulated, the current advances in the terahertz field mark the premises of terahertz inspection, with still a long path ahead.

Appendix A

Resolution Chart

USAF-1951 Test Chart

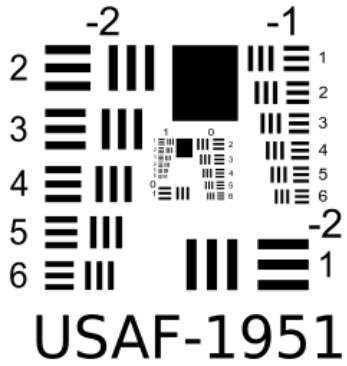

Figure A.1: USAF-1951 Test Chart.

$$Res[lp.mm^{-1}] = 2^{Grp+\frac{El-1}{6}} \tag{A.1}$$

Table A.1: Resolution and line width tables for USAF test chart.

Spatial frequency in USAF Test chart $[lp.mm^{-1}]$						
	Group number					
Element	-4	-3	-2	-1	0	1
1	6.25×10^{-2}	0.125	0.25	0.5	1	2
2	7×10^{-2}	0.14	0.281	0.561	1.12	2.24
3	7.8×10^{-2}	0.156	0.313	0.630	1.26	2.52
4	8.85×10^{-2}	0.177	0.354	0.707	1.41	2.83
5	9.9×10^{-2}	0.198	0.397	0.794	1.59	3.17
6	0.111	0.222	0.445	0.891	1.78	3.56

Line width in USAF Test chart $[mm]$						
	Group number					
Element	-4	-3	-2	-1	0	1
1	8	4	2	1	0.5	0.25
2	7.128	3.564	1.782	0.891	0.445	0.222
3	6.348	3.174	1.587	0.794	0.397	0.198
4	5.656	2.828	1.414	0.707	0.354	0.176
5	5.04	2.52	1.26	0.63	0.315	0.157
6	4.488	2.244	1.122	0.561	0.281	0.140

Appendix B

FPGA Integration : DAQ Design for IF Signal Handling

Appendix B offers a more detailed approach of the FPGA based DAQ design, succinctly adressed in section III.2.2.

FPGA architecture for beating signal recording

A depiction of the chip architecture for Zynq 7000 components family is given in Figures C.1 and C.2 in Appendix B, through detailed block diagrams. On the highest level, the ZYNQ XC7Z010 chip can be separated in 2 main sections with on one side the Programmable Logic (PL) and on the other side, the Processing System (PS) for additional data processing, external communications, and initial Boot handling. A communication between those two distinct architectural regions can be performed through a multitude of AXI (Advanced eXtensible Interface) GPIO and HPIO (High Performance IO) ports.

Additionally, the PS features most of the connections towards the IO peripherals, as well as a clock generation unit. On the other hand, the PL integrates a finite amount of typical Slices FPGA logic gates, DSP48 arithmetic logic units and BRAMs (Block Random Access Memory) [1]. Such a finite amount of logic will obviously limit the amount of data-processing that can be achieved on the logic section of the board, especially for highly demanding operations such as Fourier Transforms or high bit count operations. The logic oriented development has been performed on the Xilinx Vivado Software suite in Verilog and VHDL (VHSIC Hardware Description Language) languages, completed by the use of a SDK (Software Development Kit) for the PS related development, in C language.

This first implementations only targets a data-recording of the IF beating signal, S_{IF}. To do so, an ADC will be put to contribution for data digitalization while the Ethernet port has been considered for data externalization towards the host processing unit, due to the high required data transfer rate. An additional chirp trigger signal will as well be generated to ensure a perfect synchronization between the chirp emission and the data recording process. A depiction of this global architecture is given in Figure III.16. For the sake of simplicity, this simplified representation omits the timing flags handling, namely t_{Valid} and t_{Last}, inherent to FPGA data processing implementations. Those single bit flags, when in high state, respectively indicated the validity of a related data, and the last elements of a data frame. A more complete block diagram depiction of the architecture in the VIVADO environment is given in Appendix B with Figure B.4.

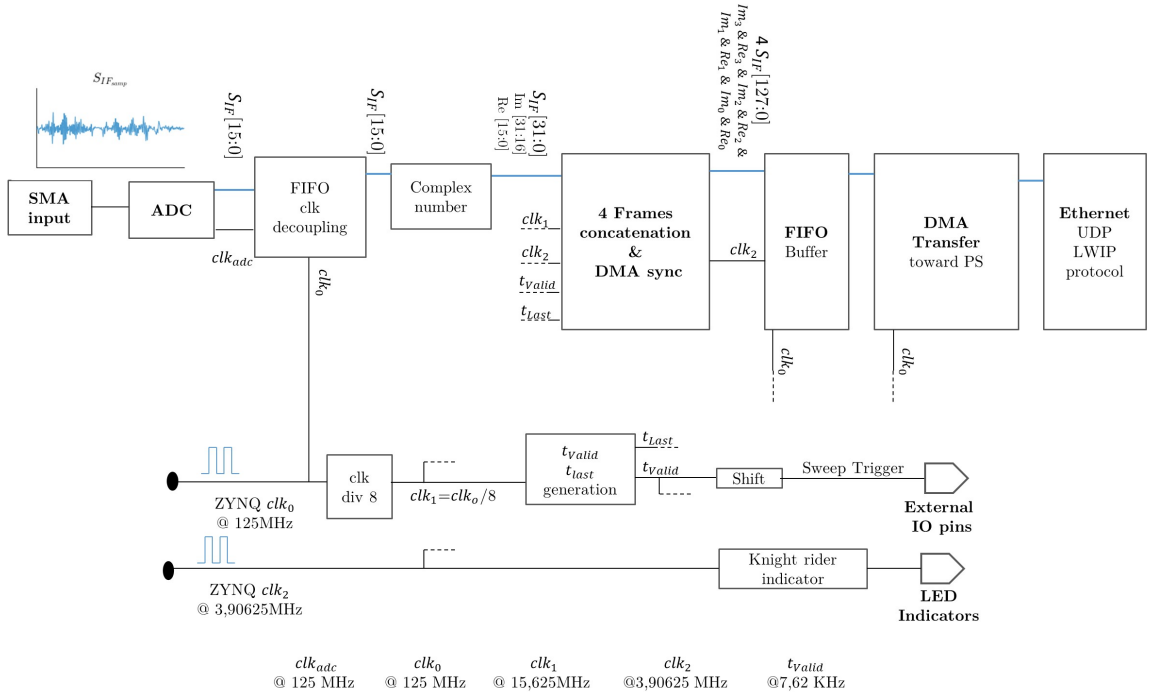

Figure B.1: Depiction of the implemented FPGA architecture as a DAQ module.

Complex data-frame formatting

At first, the ADC will generate 14-bit data streams at a rate of 125 M$sample.s^{-1}$ based on a 125 MHz clock clk_{adc}. To avoid timing issues among the design with the imperfect ADC clock, a proper primary master clock, clk_0 operating at 125 MHz is retrieved from the Zynq PS clock generator. A clock decoupling FIFO (First in, First out) then needs to be considered. All subsequent clocks are inherited from this master clock. Namely, the decimated clock, clk_1, which is used to decrease the effective sampling frequency. Indeed, anticipating further processing and data transfer problematics, the need for a full 125 M$sample.s^{-1}$ remains limited since, for a target at 50 cm, the beating frequency would be expected in the order of 1 MHz. A sampling decimation can then be performed without risking information loss. A clock division by a factor of 8 is then considered to reach an effective sampling frequency of F_s = 15.625 M$sample.s^{-1}$ based on the clk_1 clock signal. Additional room for improvement could be found in integrating a time based data averaging over 8 clk_0 cycles to reach a higher effective bit count resolution and subsequently improved raw signals SNR. A lower decimation factor, typically 4, would have naturally induced a larger amount of data recorded over the course of a chirp. Hence, it would have led to a resource demanding implementation in anticipation of complex operations such as real time Fast Fourier Transform, without providing interesting spectral information above 7.8125 MHz.

Forestalling the following signal processing, 32-bit complex signal handling among the FPGA has been integrated. A prior signed 16-bit conversion from the initial 14-bit resolution is performed. It is then followed in this simplistic case by a concatenation of a null imaginary part such that $S_{IF}[31:0] = S_{Im}[31:16] \& S_{Re}[15:0]$ with & the concatenation operator and S_{Re} and S_{Im} the signed 16-bit real and imaginary signal respectively, with in this case $S_{Re} = S_{IF}$, and $S_{Im} = 0$.

Once again in anticipation of the subsequent signal processing convenience, a signal frame, recorded over a full one-way frequency chirp, should be comprised of a given power of 2 samples. To achieve such minor evolution, from the initial T_s = 100 µs intended initially for the full-sweep rate, a reduction down to T_s = 65 µs is performed, equivalent to an increase of the chirp rate to $\Gamma = 492 \times 10^3$ GH$z.s^{-1}$. This improvement relies on the fact that the PLL can still be operated in locked state at this rate. With this sampling rate, 1024 14-bit samples are recorded over a full one way

sweep. Such an optimization leads to a symmetric chirp repetition rate of 7.62 kHz and so, and so an effective one-way chirp repetition rate of 15.25 kHz. This initial implementation relies on the sole recording of the beating signal only over a rising chirp, leading to a 7.62 kHz measurement rate.

Figure B.2 displays a typical recorded logic waveform for S_{IF}, after complex conversion. It features the decimated clock, clk_1 operating at 15.625 MHz, a signal frame, comprised of 1024 samples, S_{IF}^{j} with j the sample number, and the related t_{Valid} and t_{Last} timing signals. Such signals can be witnessed through the use of an ILA (Integrated Logic Analyzer) among the PL architecture itself as a debug tool.

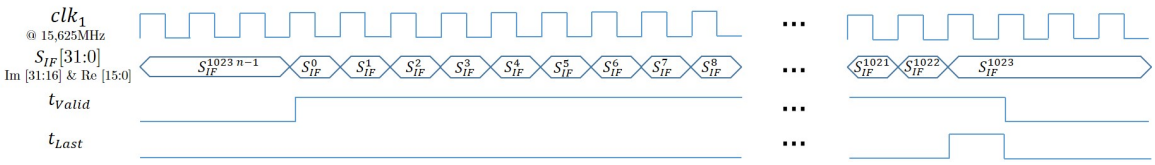

Figure B.2: FPGA logic waveform sequence for the sampled FMCW beating signal, S_{IF}.

Beside simple logic signal handling and formatting, to ensure the best synchronization between the DAQ frame acquisition and the sweep emission delivered by the PLL, a square wave trigger signal is generated among the FGPA board and linked to the DDS sweep generation unit that will drives either the rising or descending chirp. This synchronization signal is generated among the FPGA board to allows for the best reliability when it comes to signal front sharpness and jitter performances. Based on the t_{Valid} flag, the generation of this signal is once again performed through an additional clock division by a factor of 1024 and externalized through a pair of differential IO pins. It is then linked to the DDS card, as depicted on the general architecture of Figure III.20. Similarly, indicators for the proper functioning of the board are sent towards the available 8 LED indicators.

Externalization Ethernet transfer

Following those data formatting steps, the retrieval of those numeric signals toward a central unit for processing and Human-Machine Interface rendering, can be considered. To do so, a prior transfer of those data frames towards the PS memory should be carried out since the Gigabit Ethernet (GigE) IO interfaces are linked to the processing unit (see Figure C.2 and C.2 in Appendix B). As the most appropriate technical solution, due to the high data rate required, a DMA (Direct Memory Access) transfer has been integrated through the HPIO AXI ports. It will allow for the allocation of part of the PS memory where the S_{IF} frames will be subsequently written.

A DMA transfer size limitation nevertheless requires an additional prior data shaping. Indeed, a maximal amount of 256 clock burst frames can be considered for this transfer towards the PS memory. In order to avoid sending multiple data-bursts for a single frame, i.e. slicing out a full frame into 4 subsequent sub-frames, the full data frame length should be reduced. In order to compensate this point, an increase of the bit count of each sample can be considered to ensure an adequate data rate throughput. More precisely a concatenation of 4 subsequent samples is performed to keep a consistent global data frame. A resulting 128-bit signal, with effective clock frequency of clk_2 at 3.90625 MHz, spanned over 256 samples then integrates the initial 1024, 32-bit, complex samples recorded over a full rising frequency chirp. The resulting logic waveform sequence, after data-concatenation, is displayed in Figure B.3.

To allow for a maximal transfer throughput towards the PS in order to make sure that the GigabitEthernet transfer does not limits the system, the DMA transfer should occur at the fastest available clock, clk_o. A clock domain decoupling FIFO, which will then also operate as a data buffer, is inserted.

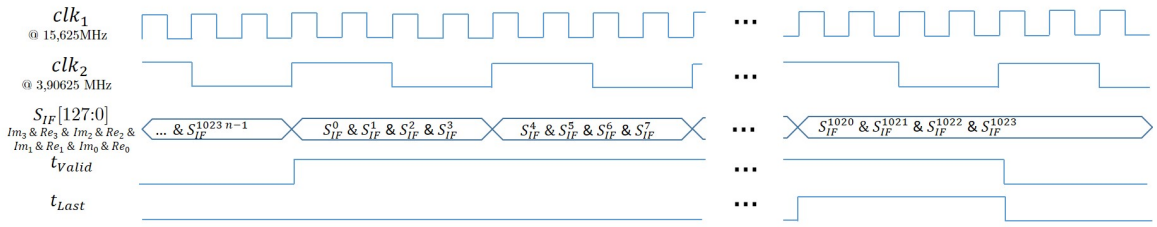

Figure B.3: FPGA logic waveform sequence for the sampled FMCW beating signal, S_{IF} after 4 samples concatenation for DMA transfer.

Once the DMA transfer towards the PS dedicated memory is completed, the Gigabit Ethernet transfer of a whole FMCW frame is performed and initiated on the PS side towards the host unit through the lwIP (lightweight IP) UDP (User Datagram Protocol) protocol. A simplified integration was enable thanks to the existing lwIP package of the Vivado SDK. Board specific amendment has been made to reach a functional Ethernet link, especially concerning the Ethernet PHY (physical layer) integrated on the Red Pitaya board and the large data frames to send. Even though it does not guarantee users data reception due to the absence of handshaking dialogues, the UDP protocol remains reliable thanks to the checksum verification. It then remains a simple solution especially suitable to the unidirectional data transfer that needs to be operated in this specific case. A prior Ethernet link configuration ensure an optimum communication speed setting according to the capabilities of each Ethernet port emitter and receiver. Once the full frame packet Ethernet transfer is performed, a feedback status register is updated on the PS side to allows the PL to initiate the subsequent FMCW frame DMA transfer.

A final expected transfer data rate of 254 M$b.s^{-1}$ is then achieved for the externalization of the raw complex data, where each UDP frame corresponds to a full recording of the beating signal, S_{IF}, over the course of a rising frequency chirp, sampled at the effective sampling frequency of $F_s = 15.625\text{MH}z$.

DAQ FPGA Block diagram Architecture

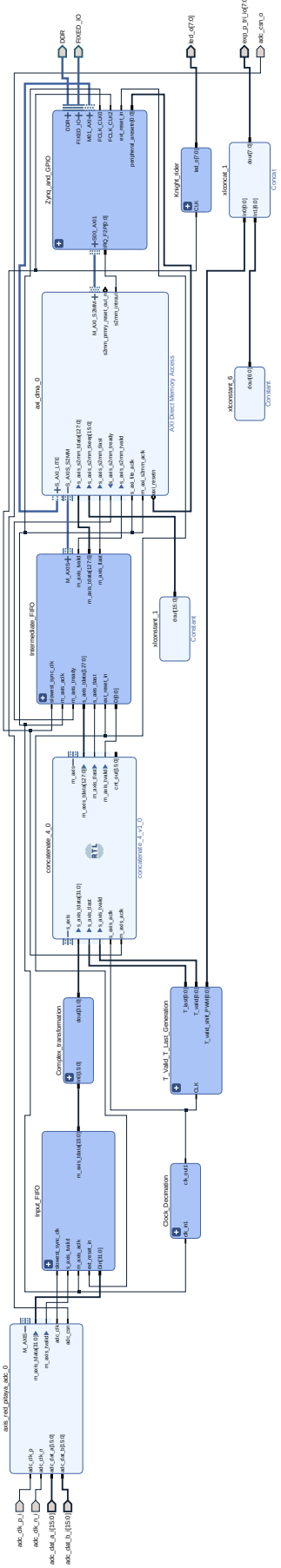

Figure B.4: Vivado architectural block diagram for the Data retrieval FPGA implementation, featuring the data digitalization, complex data handling, Buffer FIFOs, frame length reduction by concatenation, DMA transfer and clock handling for function indicator (Knight rider), and chirp synchronization trigger signal.

Appendix C

Zynq Layout

Zynq 7000 Architectures

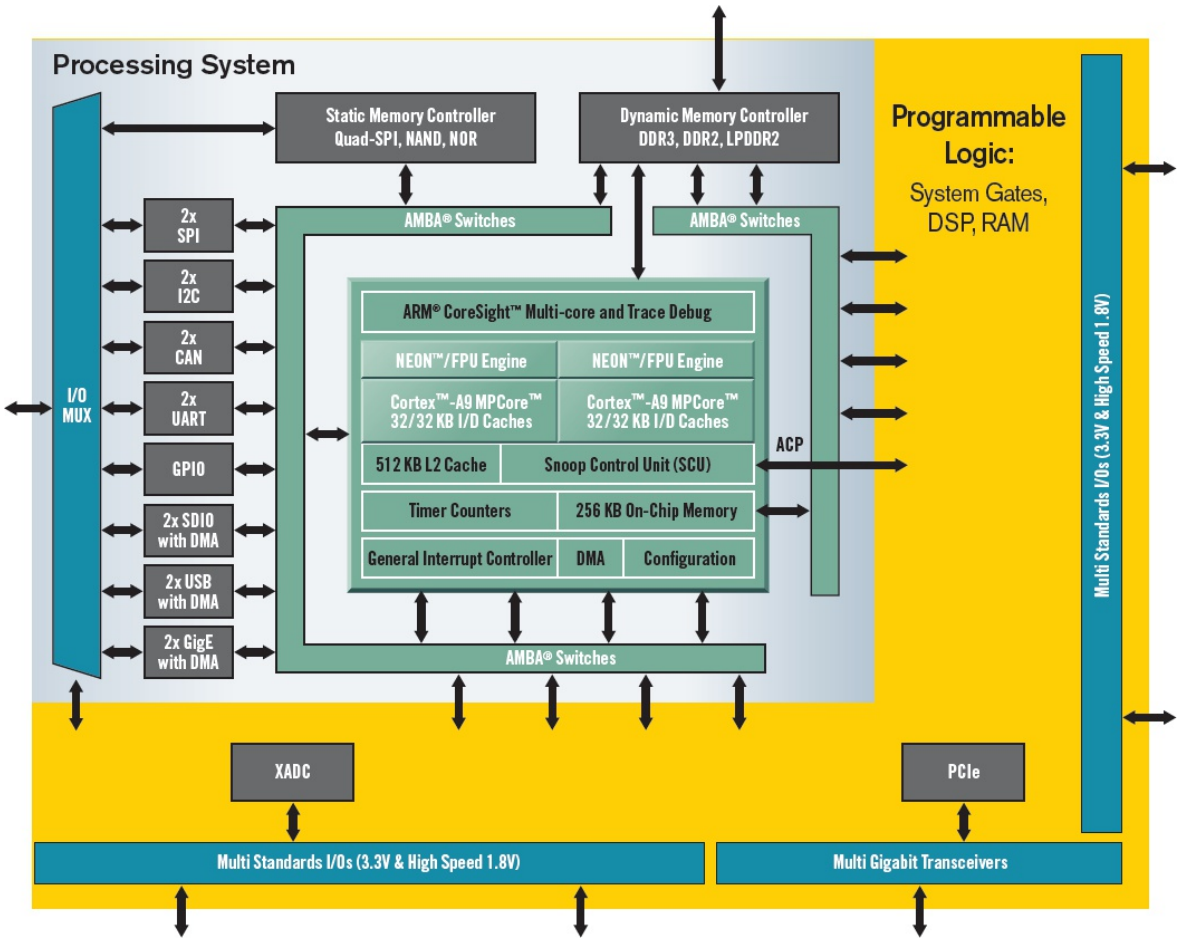

Figure C.1: PS and PL Block diagram representations of the Zynq 7000 offering a global architectural overview.

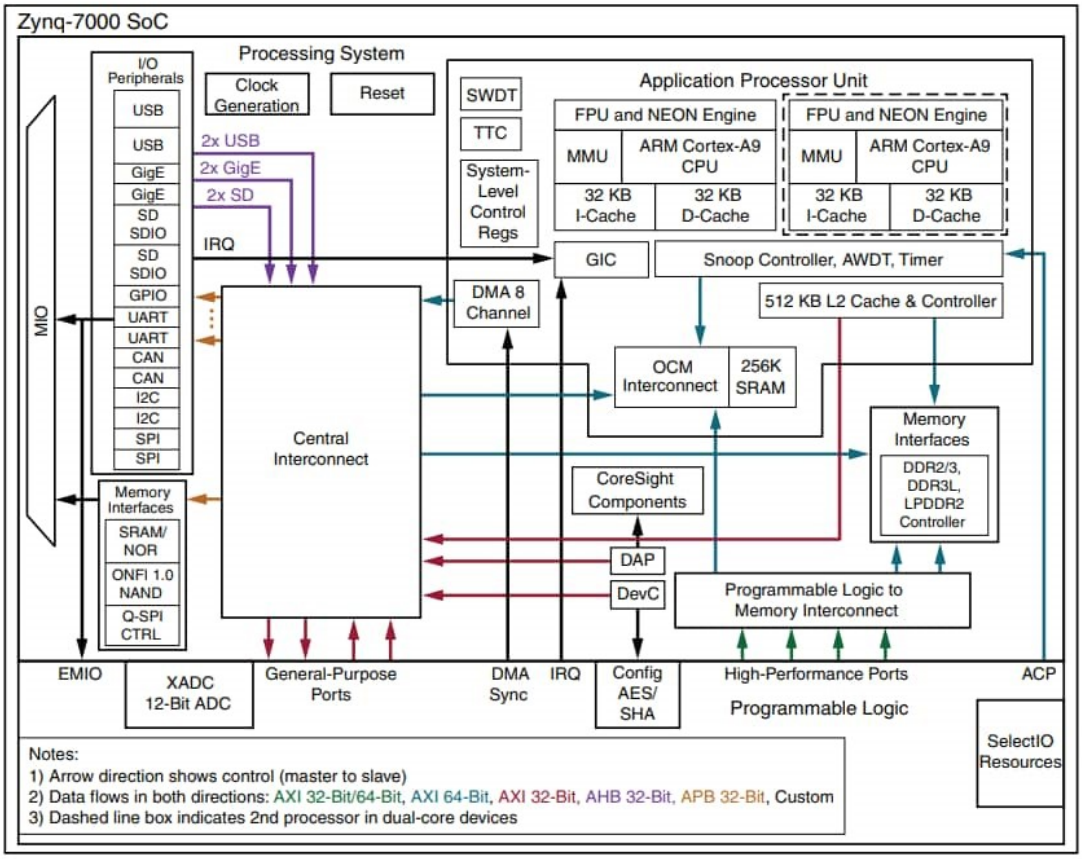

Figure C.2: PS oriented Block diagram representations of the Zynq 7000 offering a detailed PS architectural overview.

Appendix D

FPGA Integration : Full Embedded Data Processing

Appendix D offers a more detailed approach of the FPGA based data processing unit for FMCW signals normalization, succinctly addressed in section III.3.3.

Considering the efficient normalization procedure featured in section III.3, that allows for the deconvolution of the initially un-exploitable FMCW raw signals, a global real-time data processing integration can be considered. The previously described DAQ FPGA unit, detailed in section III.2.2 and Appendix B, initially considered as a simple data retrieval tool, can be complemented to integrate additional processing steps. The reprogrammable logic architecture then ensures an optimization of its capabilities to allow for real-time processing. The global architecture of this FPGA implementation is given in Figure D.1 while the Vivado block diagram for the full processing project integration is given in Appendix D, Figure D.2. This section will be dedicated to the development of this implementation.

The FPGA integration feasibility lies on the suitability of this normalization process with the mode of operation of classical FPGA implementations. In this case it will hence lie on the cascading of distinct logic units for each subsequent operation.

Data collection and formatting

This first operation, lies on the exact same architecture as for the DAQ implementation. A 125 M$sample.s^{-1}$ signal sampling is performed by the ADC and fed in the clock decoupling FIFO. For the integration of the subsequent FFT operation, a complex number signal is then generated by concatenating a zero imaginary part.

In parallel, timing operations are considered with the generation of the factor 8 decimated clock clk_1 from the initial 125 MHz clk_0. The use of this ckl_1 signal as the working frequency input of the FFT will passively operate the sub-sampling operation to the desired frequency of F_s = 15.625 MHz. A proper trigger of the signal through the t_{Valid} and t_{Last} flags (see Figure B.2) is as well of extreme importance for those first step. This operation obviously goes hand in hand with the externalization of the chirp trigger signal though the differential external IO pins. This chirp signal is once again generated from the t_{valid} flag, and follows a symmetrical rectangular signal of frequency $\frac{F_s}{2048}$.

Additionally, the use of LED indicators will detail the proper functioning of the FPGA board and will integrate status indicators for the normalization signals collection.

Single-sided filtering

Due to the complexity of integrating an FPGA Hilbert transform, the analytical signal retrieval will be conducted as detailed in Equation III.7, through the enforcement of an asymmetrical rectan-

gular window modulation in the frequency domain.

The first step then consists in applying a Fourier transform to the input collected signal. The capability to perform this transform fast enough should then be considered in order to avoid a limitation of the achievable measurement rate. Several architectures are offered in the Vivado software suite with specifics resource requirements and computation performances. Unlike the other architecture choices, the Pipelined streaming I/O solution allows for such real time processing thanks the following feature: *"The core has the ability to simultaneously perform transform calculations on the current frame of data, load input data for the next frame of data, and unload the results of the previous frame of data. You can continuously stream in data and, after the calculation latency, can continuously unload the results."* [2]. With respect to the other available FFT architectures, this integration obviously represents a demanding operation in term of required logic resource, nevertheless, each frame can be subsequently processed. The resource limitations of this board hence lead to the limitation of the frame size to 1024 samples by setting the decimation factor to 8.

The complex Fourier transform of the input signal can then be fed in the asymmetrical BPF. To set the filter characteristics, the two cut-off frequencies should be provided. As depicted in Figure D.1, those values are retrieved through an initial value update query from the PS. The operator will then be able to set the desired cut-off values, f_{L} and f_{H} which will be sent to the FPGA PL through GPIO AXI ports and then stored in BRAM memory units. From there, they can be accessed at any moment by the band-pass filter block on the PL side.

Unlike when using Matlab or other interpreted languages, no straightforward vector considerations can be applied for the enforcement of the filter. Instead, the data flow should be considered for this operation. A clock counter is then synchronized with the signal frame. After the FFT, each clock cycle will bring the subsequent frequency component. As the signals transit through the processing block, a comparison of the clock counter value with the related cut off frequencies f_{H} and f_{L} bins number if performed. The asymmetrical filtering operation is then performed by either directly outputting the input value if the current frequency is within the $[f_{\mathrm{L}}, f_{\mathrm{H}}]$ frequency range or nullifying it otherwise. The timing requirement, through once again the t_{valid} and t_{last} flags, is then of drastic importance for this step.

This single sided filtered spectrum can then be back-transposed to the time domain with the integration of an IFFT. Similar consideration as for the prior FFT have been taken into account.

In their fixed point Vivado implementation, for optimized binary dynamics, the two previously detailed Fourier transform operations are accompanied with an additional constant scaling factor for each processed frame. To reach a consistent and quantitative data-processing chain, those two scaling coefficients are integrated in a subsequent re-scale amplitude correction step

Normalization

The sample analytical complex signals will then transit at this point. Hence, the normalization procedure can be considered. Nevertheless, the two reference and background analytic signals should as well be provided for the operation. To do so, a prior recording of those normalization elements, is required. Similarly to the update of the f_{L} anf f_{H} frequencies, at launch an update the reference signal (taken on a perfectly reflective sample placed at the imaging waist) and a background signal, taken in absence of object in the imaging field, is required. upon this update query, generated among the PS, the temporal recording of those 1024 sample traces (equivalent to a full sweep) can be extracted at the output of the single sided filter processing chain where the analytic signal transits. An additional averaging step, typically over 512 frames is performed on each of those two configurations to improve the transfer function effective SNR. The bit growth required for this averaging operation led to the determination of this 512 value. The use of LED indicators for the highlighting of the ongoing recording process for either a reference or background signal has been implemented. Those averaged complex reference and background raw temporal signals are then stored in their dedicated BRAM units and accessed when needed by the background

removal and normalization procedure units as depicted in Figure D.1.

For those two operations, the timing requirement are as well drastic as the background subtraction and normalization procedure are time dependent operations. Specifically, as the sample signal is transiting, the values collected in the BRAM units for the reference and background should correspond with the considered time sample. A counter synchronized with the frames then asses the reference and background samples to be read in the BRAMs and accounts for the BRAM read operation latency of 2 clock cycles.

In addition to those timing considerations, specific precautions have to be taken into account for the normalization procedure due to the integration of a division operation (see Equation III.12). This operation indeed leads to bit grows possibilities as the range of the output signal remains uncertain when the divisor becomes small.

Data externalization

Having then access to the normalized temporal complex signals, their externalization toward the host central unit can be considered. With respect to the simple DAQ architecture previously detailed, the data-stream to transfer displays identical characteristics. Namely, a frame of 1024, 32-bit samples should be sent every 2048 clk_1 cycles. These unchanged cadences and bit counts allows for the use of the exact same transfer mechanism.

A prior requirement for a 4 sample concatenation into a 128-bit signal is achieved and directed toward a buffer FIFO to suite the 256 burst size AXI DMA transfer. The initialization of the DMA transfer then emerges from the PS, and once the PS memory update is done, an Ethernet transfer of a full chirp frame takes place on the PS side. once transfer is over, the subsequent DMA transfer can be triggered. Due to interrupt signals incompatibilities, the Ethernet transfer is initiated once the cut-off frequencies and respective reference and background signals have been updates. No additional update of those values can be performed after the initialization phase.

On the central unit side, the reception of those fully processed complex frames is then possible for every chirp cycle, *i.e.* every 130 µs. Those time domain frames are then equivalent to the $\widehat{\mathrm{S}}_{samp}(t)$ traces featured in Figure III.22.

Nevertheless, considering the zero padding and final spectral conversion rendering FFT, those final processing steps should be performed outside of the FPGA integration for 2 main reasons. At first, the implementation of high sample count FFT after zero-padding would displays large resource requirements, that are not meeting the capabilities of such limited FPGA zynq7010 chips. Secondly, the externalization data-transfer throughput (GigE) needs to be able suite the input data rate. In absence of zero-padding frequency resolution enhancement, transferring 1024 complex samples over 130 µs leads to a 254 $k\mathrm{B}.s^{-1}$ transfer rate. The use of a $\mathrm{N_{ZP}}$ = 4 would already saturate the Gigabit Ethernet link. Nevertheless, when using the radar in a limited range configuration (such as with the far-field sensing), only a small spectral window remains of interest. After normalization, this frequency window is centered around 0 Hz (related to the reference plan position) and spans typically over 500 kHz, for an equivalent region of interest of roughly 15 cm. Only this spectral portion can then be transmitted through the Ethernet port, that will allow larger zero-padding factor considerations.

Additionally, the externalization of the final zero-padding and FFT operations lies on a versatility-oriented decision. More freedom can then be granted to the integrator if those two operation are performed externally. Larger $\mathrm{N_{ZP}}$ could be considered while the window choice for the apodization operation would not be imposed. Finally, the use of normalized temporal signals, is of interest for specific application cases. Namely, thickness assessment problematics, detailed further in section IV.4 On this consideration, the whole thickness determination process is based on temporal error minimization of physical models with respect to the performed measurement. Hence, such approaches would remain incompatible with the use of partial resolution enhanced spectral signals.

As a current integration, the full normalization architecture displayed in Figure D.1 takes up

to 87 % of available logic LUTs elements in the PL section of the FPGA board. Those resources are mainly employed for the FFT and IFFT transform operations as well as the normalization division.

This full data processing implementation relies on the recording of the beating signal over a rising chirp and further data processing over a full symmetrical chirp period. Indeed, even in its most effective configuration, the FFT requires more than a 1024 and less than 2048 clk_1 clock cycles to perform its transform operation. This integration leads to a 7.62 kHz measurement rate for the FMCW radar unit. No attempt to exploit the descending chirp has been pursued in this work. A parallelization on the processing chain, focused on this descending chirp time, could solve this issue and provide a doubling of the radar measurement rate. However, beside requiring twice as much logic resources, this implementation would still be limited by the DMA transfer process and Ethernet link capabilities as bottleneck elements.

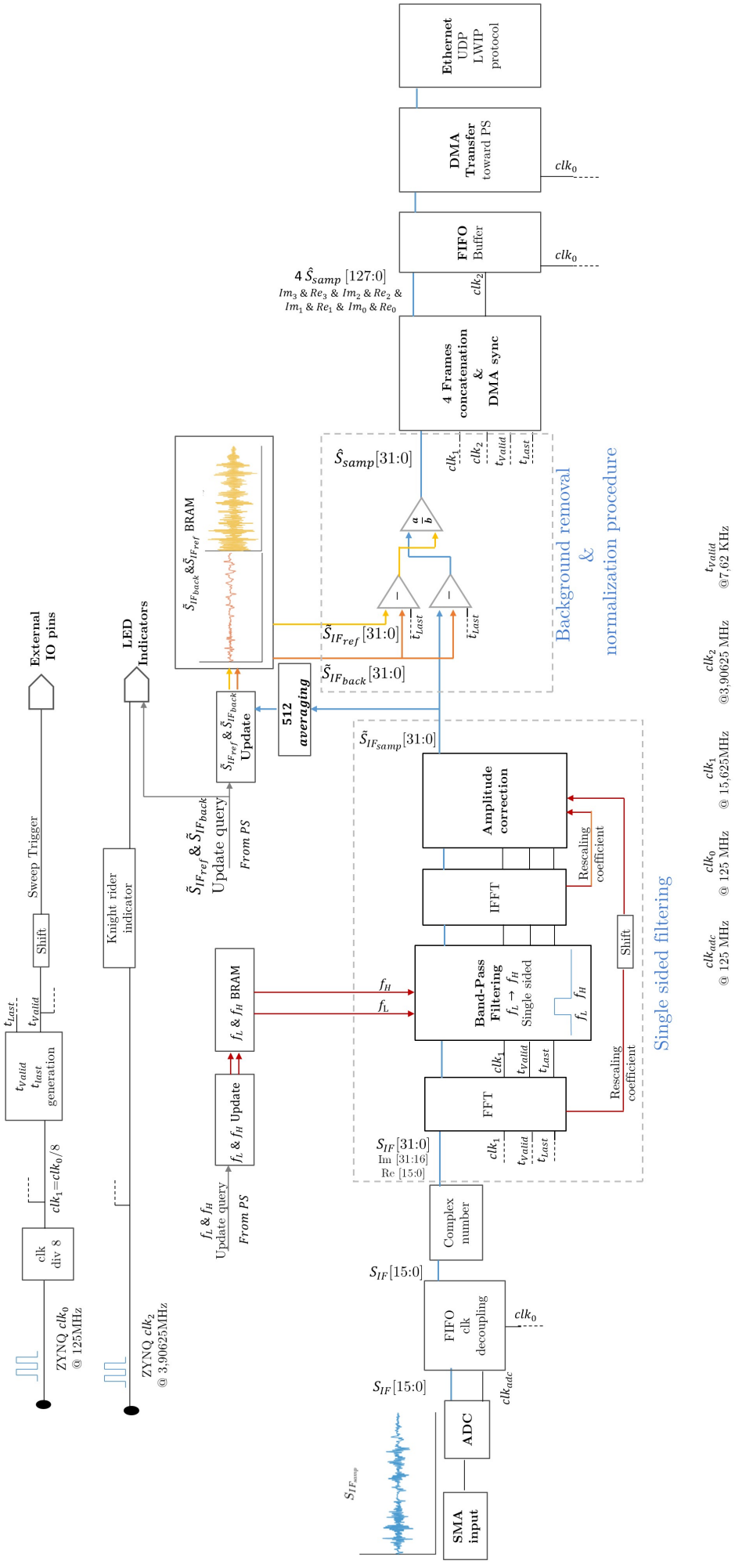

Figure D.1: Depiction of the implemented FPGA architecture as a DAQ module with integrated full FMCW data normalization procedure.

DAQ FPGA Block diagram Architecture, embedded normalization processing

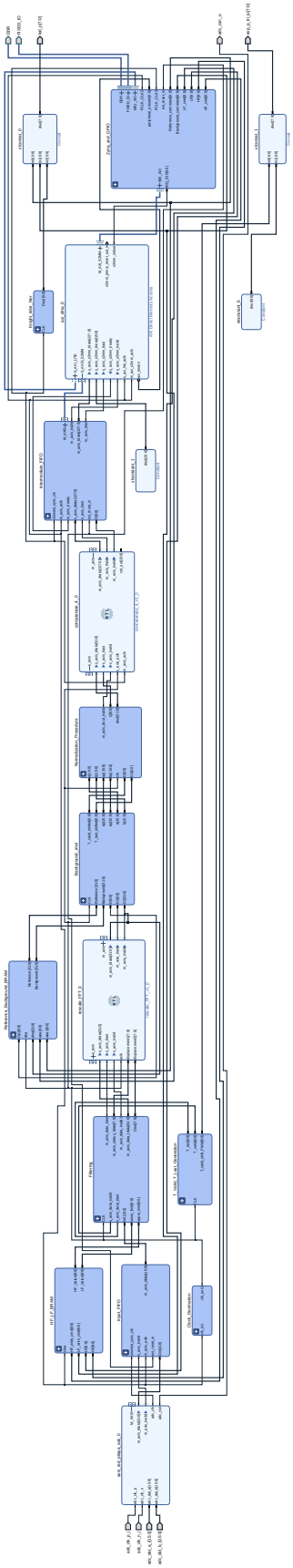

Figure D.2: Vivado architectural block diagram for the Data retrieval FPGA implementation with embedded data processing, additionally featuring a GPIO-based communication process for the definition of the filtering cut-off frequencies, and reception of the queries for reference and background signals recording, a single sided complex data filtering, the normalization procedure and subsequent DMA transfer.

Appendix E

Generalized Low-cost Radar Imaging

As an alternative approach to the high-end FMCW radars developments conducted along this work, a pursue of low-cost systems have as well been initiated with the Teragogic [3] open source project which has been thought as a solution for the democratization of low-budgets terahertz investigation. Once again based on the Si-Ge 122 GHz Silicon radar transceiver, it aims to offer an affordable fully functional millimeter-wave scanning device for a democratization toward a wide field of applications. It is hence integrated in a far field configuration single point sensing unit, mounted on a motion staged, based on a slightly modified, Arduino controlled, $\vec{x}$-$\vec{y}$-Plotter MakeBlock v2.0 [4]. This then offers a low-cost lightweight structure allowing for a 30 × 30 cm scanning area with competitive sensing performances. Obviously, a limitation in term of recording rate and dynamic range is nevertheless witnessed with respect to the established III/V based solutions.

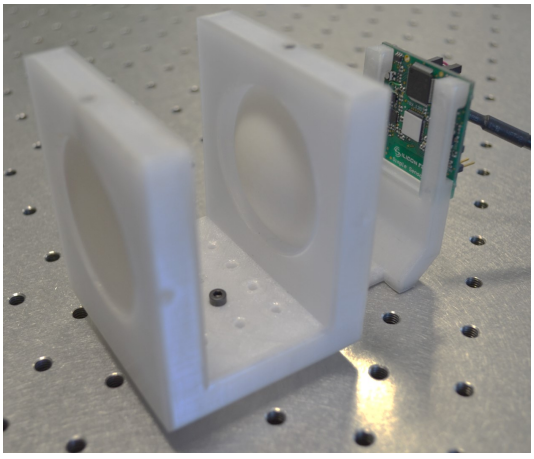

Figure E.1: Lightweight and low-cost 3D printed transceiver support for the Teragogic scanning unit featuring the integration of the 122 GHz silicon radar fmcw PCB integrated chip and dedicated beam shaping optics PTFE lens doublet.

In the pursue of cost minimization, 3D printed pre-aligned optomechanical supports have been designed for a simplified lightweight integration as displayed in Figure E.1. In addition, as mentioned in section III.2, the use of additive manufacturing for the design of optics in the millimeter range [5] then allows for specific customizations. A full depiction of the setup, performances and imaging applications are given in [3] with a focus toward NDT capabilities and art heritage investigations.

E.1 Bibliography

[1] https://www.xilinx.com/support/documentation/selection-guides/zynq-7000-product-selection-guide.pdf. 209

[2] Fast Fourier Transform Xilinx. v9. 1 logicore ip product guide, 2019. 218

[3] Adrien Chopard, Frederic Fauquet, Jing Shun Goh, Mingming Pan, Patrick Mounaix, Jean-Paul Guillet, Anton Simonov, and Olga Smolyanskaya. Teragogic: Open source platform for low cost millimeter wave sensing and terahertz imaging. In *2021 IEEE Radar Conference (RadarConf21)*, pages 1–6. IEEE, 2021. 223

[4] Jason N Pitt, Nolan L Strait, Elena M Vayndorf, Benjamin W Blue, Christina H Tran, Brendon EM Davis, Karen Huang, Brock J Johnson, Keong Mu Lim, Sophie Liu, et al. Wormbot, an open-source robotics platform for survival and behavior analysis in c. elegans. *GeroScience*, 41(6):961–973, 2019. 223

[5] Bing Zhang, Yong-Xin Guo, Herbert Zirath, and Yue Ping Zhang. Investigation on 3-d-printing technologies for millimeter-wave and terahertz applications. *Proceedings of the IEEE*, 105(4):723–736, 2017. 223

Author Publication List

«†: *Peer-reviewed papers.*
‡: *Proceedings and Conferences.*»

---

[1] †Jean-Baptiste Perraud, Adrien Chopard, Jean-Paul Guillet, Pierre Gellie, Antoine Vuillot, and Patrick Mounaix. A versatile illumination system for real-time terahertz imaging. *Sensors*, 20(14):3993, 2020.

[2] ‡JB Perraud, A Chopard, Jean-Paul Guillet, P Gellie, F Fauquet, and P Mounaix. A fast and homogeneous illumination applied to full-field terahertz imaging. In *2020 45th International Conference on Infrared, Millimeter, and Terahertz Waves (IRMMW-THz)*, pages 1–2. IEEE, 2020.

[3] †Mingming Pan, Adrien Chopard, Frederic Fauquet, Patrick Mounaix, and Jean-Paul Guillet. Guided reflectometry imaging unit using millimeter wave fmcw radars. *IEEE Transactions on Terahertz Science and Technology*, 10(6):647–655, 2020.

[4] ‡A Chopard, M Pan, F Fauquet, J-P Guillet, and P Mounaix. Simplified fmcw radars implementation for guided terahertz reflectometry sensing. In *2020 45th International Conference on Infrared, Millimeter, and Terahertz Waves (IRMMW-THz)*, pages 1–1. IEEE, 2020.

[5] †Nikolay V Petrov, Jean-Baptiste Perraud, Adrien Chopard, Jean-Paul Guillet, Olga A Smolyanskaya, and Patrick Mounaix. Terahertz phase retrieval imaging in reflection. *Optics Letters*, 45(15):4168–4171, 2020.

[6] ‡Nikolay V Petrov, Jean-Baptiste Perraud, Adrien Chopard, Jean-Paul Guillet, Olga A Smolyanskaya, and Patrick Mounaix. Terahertz diffractive reflection phase imaging. In *2020 45th International Conference on Infrared, Millimeter, and Terahertz Waves (IRMMW-THz)*, pages 1–1. IEEE, 2020.

[7] ‡Nikolay Petrov, Jean Baptiste Perraud, Adriene Chopard, Jean-Paul Guillet, Olga Smolyanskaya, and Patrick Mounaix. Terahertz phase retrieval imaging with multiple-plane data. In *SNAIA 2020*, 2020.

[8] †Nikolay V Petrov, Jean Baptiste Perraud, Adriene Chopard, Jean-Paul Guillet, Olga A Smolyanskaya, and Patrick Mounaix. Terahertz multiple-plane phase retrieval. In *Digital Holography and Three-Dimensional Imaging*, pages HF4G–8. Optical Society of America, 2020.

[9] †Quentin Cassar, Adrien Chopard, Frederic Fauquet, Jean-Paul Guillet, Mingming Pan, Jean-Baptiste Perraud, and Patrick Mounaix. Iterative tree algorithm to evaluate terahertz signal contribution of specific optical paths within multilayered materials. *IEEE Transactions on Terahertz Science and Technology*, 9(6):684–694, 2019.

[10] ‡Q Cassar, A Chopard, F Fauquet, JP Guillet, M Pan, JB Perraud, and Patrick Mounaix. Iterative tree algorithm for the assessment of optical path contributions within stratified structures. In *2019 44th International Conference on Infrared, Millimeter, and Terahertz Waves (IRMMW-THz)*, pages 1–2. IEEE, 2019.

[11] ‡Q Cassar, A Chopard, F Fauquet, Jean-Paul Guillet, J Perraud, and P Mounaix. 3d painting distribution extracted by time domain spectroscopy. In *SNAIA 2020*, 2020.

[12] ‡A Chopard, J Bou Sleiman, Q Cassar, P Fauché, JP Guillet, P Mounaix, M Pan, JB Perraud, and A Susset. Contactless terahertz paint thickness measurements: specificity of aeronautics industry. 2019.

[13] †A. Chopard, J. Bou Sleiman, Q. Cassar, J.P. Guillet, M. Pan, J.B. Perraud, A. Susset, and P. Mounaix. Terahertz waves for contactless control and imaging in aeronautics industry. *NDT E International*, page 102473, 2021.

[14] ‡Adrien Chopard, Joyce Sleiman, Q Cassar, P Fauché, J Guillet, Patrick Mounaix, Perraud Jean-Baptiste, and A Susset. Millimeter waves radar: A way to see through the airplane covering? In *11 symposium international: NDT in Aerospace*, 2019.

[15] Jean-Paul Guillet, Frédéric Fauquet, Adrien Chopard, Jean-Baptiste Perraud, Marie Roux, and Patrick Mounaix. Comparative study of millimeter wave iii/v semiconductor and integrated silicon based fmcw radars. In *2019 44th International Conference on Infrared, Millimeter, and Terahertz Waves (IRMMW-THz)*, pages 1–1. IEEE, 2019.

[16] ‡Adrien Chopard, Frederic Fauquet, Jing Shun Goh, Mingming Pan, Patrick Mounaix, Jean-Paul Guillet, Anton Simonov, and Olga Smolyanskaya. Teragogic: Open source platform for low cost millimeter wave sensing and terahertz imaging. In *2021 IEEE Radar Conference (RadarConf21)*, pages 1–6. IEEE, 2021.

[17] Jean-Paul Guillet, Adrien Chopard, Frederic Fauquet, Jing Goh, Mingming Pan, Anton Simonov, Olga Smolyanskaya, and Patrick Mounaix. Teragogic: Open source platform for low cost millimeter wave sensing, terahertz imaging and control. In *SNAIA 2020*, 2020.

[18] ‡Jean-Paul Guillet, Frederic Fauquet, Adrien Chopard, Patrick Mounaix, Jean Rioult, and Timo Jaeschke. Augmented reality terahertz (ar-thz) interface for imaging and sensing. In *IRMMW-THz 2021, 46th International Conference on Infrared, Millimeter and Terahertz Waves*, page 1p, 2021.

Introduction en Français

Le Contrôle Non-Destructif (CND) est un domaine lié à l'automatisation de méthodes d'inspection et de monitoring, tendant à s'appliquer à un large panel de domaines applicatifs. Il inclut ainsi une variété de problématiques allant, pour n'en citer que quelques-unes, de la détection d'inclusions, de défauts, de fissures et de traces d'impacts, jusqu'à l'inspection de marques de soudures, ou l'évaluation de densités ou encore du taux d'hydrométrie d'échantillons spécifiques.

Une récente automatisation des productions, a induit une inévitable croissance dans la demande de moyens de détection d'imperfections, dans le but de pouvoir garantir la fiabilité des produits finis. Une telle évolution des exigences industrielles, en parallèle du développement de procédés de fabrications toujours plus perfectionnés, mène à une large variété de produits devant faire l'objet de tels tests de conformité. Dans cette dynamique de fort développement, le marché du CND est amené à évoluer d'une valorisation à 16.72 Milliards de Dollars en 2020, vers une estimation atteignant 24.64 Milliards de Dollars en 2026, selon les chiffres prospectifs d'un rapport de Mordor Intelligence.

Les principales technologies établies, faisant appel aux méthodes radiographiques, d'inspection ultra-sonique, de thermographie Infrarouge ou encore par courants de Foucault, ont déjà fait l'objet de plusieurs décennies de développement. Elles ont ainsi mené à des procédés CND poussés proposant des capacités de détection de défaillances avancées, sur une large gamme de domaines applicatifs.

En tant que technologie concurrente émergente, l'évaluation sans contact térahertz apporte plusieurs avantages, en comparaison aux méthodes évoquées, pouvant ainsi être appliquée à certaines thématiques niches. En particulier, les résolutions submillimétriques atteignables, en parallèle de la capacité de pénétration dans les matériaux diélectriques pour offrir une inspection volumique, couplées au caractère non-ionisant et donc sans danger pour la santé des opérateurs, renforcent l'intérêt croissant observé envers la plage spectrale des ondes térahertz.

Néanmoins, dû au caractère relativement récent de ce domaine, un manque certain de fondements technologiques en comparaison aux méthodes établies, contraint le térahertz à proposer des solutions complémentaires à l'état de l'art CND existant ou visant des problématiques très spécifiques. En particulier, une des transpositions technologiques marquantes, observée récemment, est relative au sujet de niche du contrôle d'épaisseur de peintures stratifiées, dans les domaines aéronautiques et automobiles, au travers d'approches d'inspection térahertz résolues en temps.

Entourées de méthodes de contrôle établies, les ondes submillimétriques cherchent ainsi à résoudre des besoins spécifiques dans le domaine du CND, au travers de l'intégration des dernières avancées observées sur les sources, détecteurs, et méthodes de détection. Ce travail se place ainsi parfaitement dans cette thématique, avec pour but d'asseoir certaines capacités des systèmes térahertz envers des problématiques de contrôles spécifiques. En particulier, plusieurs approches d'imagerie et de détection ont été abordées avec succès, aux travers de solutions d'instrumentation, faisant appel aux récentes avancées technologiques.

Le premier chapitre cherche donc à proposer une vue d'ensemble sur les technologies submillimétriques au sein du domaine applicatif de l'inspection, de manière à définir le fondement de ce travail. Une première section sera donc dédiée aux principaux systèmes de CND établis, en détaillant leurs avantages et inconvénients, afin de mettre en lumière les performances inhérentes aux technologies émergentes du domaine térahertz. En particulier, la pénétrabilité d'une vaste gamme

de matériaux, la capacité de mesure sans contact, et le caractère bénin de ce type de radiation envers l'organisme humain ont contribué à en faire un candidat d'intérêt au cours des dernières décennies. Afin d'illustrer ces récentes avancées, un état des lieux quantitatif des sources et méthodes de détection accessibles est proposé et est accompagné d'un passage en revue des domaines applicatifs explorés. Ces détails permettront ainsi au lecteur de situer les choix technologiques effectués au cours de ce manuscrit. En complément, un approfondissement plus spécifique sur le principe de fonctionnement du radar FMCW (Radar à ondes continues, modulées en fréquence), dans le domaine spectral des ondes millimétriques, accompagné d'un état de l'art technologique et applicatif, seront proposés pour soutenir la problématique centrale abordée au sein de ce travail.

Le second chapitre se focalisera ainsi sur les approches d'imagerie en régime continu. Les principes optiques d'interactions macroscopiques en jeux seront donc rappelés comme fondements théoriques aux méthodes d'imagerie standard. En particulier, basée sur l'imagerie raster-scan, la méthodologie de détection point par point est déclinée sous deux configurations, au travers d'un système d'imagerie transmission-réflexion simultanée, et d'une géométrie bi-fréquence concomitantes. De par la résolution et stabilité optimale atteignable, cette implémentation de référence représente typiquement un outil prospectif d'inspection, appliqué à une large bande spectrale allant de 75 GHz à 2.5 THz dans ce manuscrit. Au travers de considérations tomographiques, des capacités de reconstruction 3D ont été démontrées. L'imagerie temps réel est ensuite abordée dans le but de surmonter les limitations intrinsèques de temps de mesures, imposées par ce type de setup d'inspection point par point. Néanmoins, trois problématiques restent à prendre en considération, au travers de la densité de puissance d'illumination, l'homogénéité de l'éclairage ou encore la cohérence des sources, pouvant mener à une forte limitation des capacités d'imagerie. Le système d'illumination galvanométrique, développé pour travailler à 2.5 THz, relié à un imageur bolométrique dédié, équipé d'un objectif plein champs, permet ainsi d'obtenir un système d'imagerie palliant à ces trois restrictions rédhibitoires. En effet, un tel système débloque l'accès à un motif d'illumination contrôlable, induisant un lissage des artefacts de cohérence. Les résultats d'imagerie temps-réel obtenus sont donc ainsi exposés, et enrichis de méthodes complémentaires d'illumination optimisées, pour l'obtention de performances accrues, basées sur la versatilité du système. De par l'amélioration drastique du temps d'acquisition, des reconstructions tomographiques sont aussi abordées.

Au centre de ce travail, le troisième chapitre fournira le détail du développement de l'architecture de détection homodyne FMCW dans le domaine spectral des ondes millimétriques. Les choix technologiques préliminaires pour la mise en place de ce radar monostatique III-V, opérant un mixeur harmonique sur la gamme spectrale de 150 GHz seront discutés. Sur la base de certaines caractéristiques préliminaires, l'architecture complète du transceiver est abordée et appuyée par des caractérisations dédiées de chaque brique principale. En particulier, pour la détection cohérente proposant une capacité de détection longitudinale, l'unité de génération de la modulation en fréquence, basée sur une Phase Locked Loop (PLL) est détaillée de manière extensive. Elle permet ainsi l'atténuation de effets non-linéaires observées sur un élément de base du radar FMCW, pouvant jouer un rôle néfaste sur ses performances. L'architecture haute fréquence est précisée par la suite, et accompagnée du détail de la configuration optique. A ce point, une procédure algorithmique additionnelle sur les signaux collectés est nécessaire. Une opération de normalisation et soustraction de background permet de mettre en lumière la détection longitudinale conférée par le mode de fonctionnement FMCW. Dans l'optique d'une transition vers un système intégré, autorisant une optimisation de la cadence de mesure, visant ainsi une adéquation avec l'inspection point par point, le développement d'une unité de traitement FPGA sera abordée succinctement. Afin de fournir une vue d'ensemble quantitative des performances du radar, la cadence de mesure, les résolutions latérales et longitudinales pour l'inspection 3D, la précision et la justesse longitudinales, ainsi que la stabilité ou encore la plage dynamique atteignable sont abordés et chiffrés.

Aux vues des capacités du système radar FMCW précédemment détaillées, le chapitre quatre démontrera les performances applicatives de ce type d'architectures, transposées dans le do-

maine des ondes millimétriques. Plus spécifiquement, représentant l'application principale envisagée, le contrôle volumétrique sera abordé au travers d'échantillons spécifiques, reliés à des problématiques industrielles d'intérêts. En particulier, l'inspection de pièces polymères, ou de traces de soudures et collages plastiques, ainsi que des considérations d'échantillons pharmaceutiques sera détaillée, en tant que preuve de fonctionnement pour l'unité radar développée. L'imagerie pénétrante, au travers de panneaux opaques, sera aussi abordée en tant que thématique d'intérêt pour l'aéronautique, dans le cadre du suivi de l'état de santé des appareils. Une approche d'instrumentation sera aussi détaillée avec l'intégration d'une géométrie radar guidée simplifiée, visant des problématiques de détection à distance. Les avantages du mode de fonctionnement FMCW seront ainsi soulignés dans ces configurations. D'autre part, basée sur les capacités de détection longitudinale, une thématique applicative porteuse sera plus spécifiquement abordée avec l'extraction sans contact d'épaisseur pour le contrôle d'échantillons stratifiés. Sur ce point, une forte analogie sera observée avec les systèmes et méthodologies de l'approche térahertz résolue en temps, pour l'inspection de déposes stratifiées submillimétriques de peintures. L'application de problèmes inverses électromagnétiques, adaptés au principe de fonctionnement de l'approche cohérente FMCW, couplé à un modèle descriptif de tels échantillons, sera abordée. Au travers de l'utilisation du radar précédemment développé, l'extraction d'épaisseur sur échantillons monocouches, au-delà de la résolution longitudinale intrinsèque sera démontrée. Une extension toute naturelle vers des échantillons multicouches sera abordée et démontrera des résultats tout aussi prometteurs.

Au-delà de la méthode de détection cohérente obtenue par le principe FMCW radar, le dernier chapitre se penchera sur une méthode d'imagerie plus prospective au travers de la transposition de l'imagerie sans lentille dans le domaine térahertz. Considérant ainsi des profils d'intensité enregistrés par un procédé de détection incohérent, de telles méthodes apportent une information supplémentaire de phase sur le front d'onde, bénéfique pour de nombreuses applications de contrôle. En premier lieu, les principes d'imagerie diffractive seront rappelés au travers de l'holographie, la ptychographie et la reconstruction de phase itérative, et accompagnés d'un état de l'art de leurs développements respectifs. La mise en place d'un système de reconstruction de phase itératif, travaillant en réflexion à 300 GHz fera l'objet des développements initiaux, suivie par une considération plus simpliste d'une approche en transmission. L'holographie hors axe, sera aussi abordée dans le but de proposer une base comparative. Toujours avec la volonté de contourner la limitation intrinsèque de temps de mesure imposée par les méthodes point par point, ce travail est conclu autour d'une transposition vers des enregistrements en temps réel dédiés à imagerie diffractive à 2.5 THz.

Les résultats collectés au sein de ce manuscrit sont le fruit d'une collaboration résultant d'une conventions CIFRE entre l'entreprise Lytid, sous la supervision du Dr. Pierre GELLIE, avec l'Université de Bordeaux, sous la tutelle des Dr. Patrick MOUNAIX et Dr. Jean-Paul GUILLET.